UNIVERSITY OF CALIFORNIA
Santa Barbara

Search for supersymmetry at CMS in events with b-tagged jets and missing transverse energy at 8 TeV

A Dissertation submitted in partial satisfaction
of the requirements for the degree of

Doctor of Philosophy

in

Physics

by

Kristen Flowers

Committee in Charge:

Professor Jeffrey Richman, Chair

Professor David Stuart

Professor Steve Giddings

March 2015

The Dissertation of
Kristen Flowers is approved:

Professor David Stuart

Professor Steve Giddings

Professor Jeffrey Richman, Committee Chairperson

March 2015

Search for supersymmetry at CMS in events with b-tagged jets and missing transverse energy at 8 TeV

by

Kristen Flowers

Acknowledgements

I would like to thank my parents, as well as all my teachers who helped me get this far.

Curriculum Vitæ

Kristen Flowers

Education

University of California, Santa Barbara

- Ph.D., Physics **2011-2015**
  - Advisor: Jeffrey Richman
- M.A., Physics **2008-2011**

Northeastern University

- B.S., Physics (minor in Mathematics) (*summa cum laude*) **2003-2008**

Awards and Fellowships

Graduate Assistance in Areas of National Need (GAANN) Fellow **2008-2009**
University Honors Program Distinction **2008**
Presidential Scholarship (full tuition at Northeastern University) **2003-2008**
Provost's Office Undergraduate Research Grant **2008**

Research Experience

Graduate Student Researcher, University of California, Santa Barbara **2008-2015**
Supported by GAANN fellowship (2008-2009), as Graduate Student Researcher (2009-2014) with Jeffrey Richman

- Developing searches for supersymmetry involving b-tagging
- Calculating data-driven background estimations in SUSY searches

Undergraduate Research Assistant, Northeastern University (at CERN) **July-Dec. 2007**

- *Calibration and testing of cathode strip chambers in the CMS end-cap muon system*

Honors Thesis Project, "The Stuekelberg Z' at D0" ..... **Jan.-June 2007**

- *Emulating predictions and detector acceptance of the Stuekelberg extension in Z' Monte Carlo*

INFN Summer Student, Laboratori Nazionali di Frascati ..... **Oct.-Dec. 2006**

- *Studying detector performance and updating tracking algorithms at KLOE and KLOE2*

Undergraduate Research Assistant, Lawrence Berkeley National Lab ....**July-Oct. 2006**

- *Testing and modeling effects of radiation on silicon pixel prototypes for the ILC*

Faculty/Undergraduate Research Initiative Fellowship (at NU) .....**Jan.-April 2006**

- *Updating top quark charge measurements at D0 to include b-tagging*

Undergraduate Research Assistant, Northeastern University ..... **July-Dec. 2005**

- *Modeling PDT performance and testing/installing electronics in the D0 muon system*

Publications

- "Search for supersymmetry in events with b-quark jets and missing transverse energy in pp collisions at 7 TeV", Phys. Rev. D 86, 072010 (2012)
- "Search for gluino mediated bottom- and top-squark production in multijet final states in pp collisions at 8 TeV", Phys. Lett. B 725, 243 (2013)

Talks and Posters

- "CMS search for supersymmetry in events with b-jets and MET: data driven top quark, W boson, and QCD background estimation", APS April meeting 2013

Abstract

Search for supersymmetry at CMS in events with b-tagged jets and missing transverse energy at 8 TeV

Kristen Flowers

This dissertation presents results from a search for physics beyond the Standard Model, using 19.39 pb^{-1} of data collected by the CMS detector at the Large Hadron Collider, during its 2012 operation at $\sqrt{s}$=8 TeV. It focuses on models of supersymmetry that lead to final states with multiple jets, especially those from b-quark decay, and a large amount of missing transverse momentum. The amounts of background from top-quark, W+jets, $Z \to \nu\bar{\nu}$, and multi-jet production are determined from data-driven techniques. In particular, this includes a novel estimation of the $E_{\text{T}}^{\text{miss}}$ spectrum from semi-leptonic $t\bar{t}$ decay, which takes advantage of the precise knowledge of the W boson polarization. Predicted yields are consistent with simulated Standard Model processes and the observed data. Since no evidence of new physics is observed, limits are placed on the rate of gluino pair production to a final state with four b-quarks and two neutralinos. This process is excluded at 95% CL for a gluino with mass 1225 GeV and a neutralino with mass up to 350 GeV.

Contents

List of Figures

List of Tables

Chapter 1

Introduction

The study of high energy particle physics is the endeavor to understand the most fundamental objects and processes of the universe. While our current understanding of physics is a beautiful description of most of what we observe, and has been found to be incredibly accurate, there are also major mysteries in the field. For hundreds of years, theorists have been proposing solutions to the mysteries of the day, and the job of the experimentalist is to test the limits of our current understanding for unexplainable phenomena or support for new theories. The author of this thesis was lucky enough to be involved in a search for a potentially undiscovered property of the universe which may hold the answer to several outstanding mysteries. This theory is called supersymmetry. Searches for evidence of new physics at the TeV scale, including supersymmetry, are a main focus for the Large Hadron Collider and the CMS experiment located there. The high energy environment and vast quantity of data offer a new frontier for as yet unobserved phenomena. The title

of this thesis describes some properties of the data analyzed in this search. The quantity 19.39 fb^{-1} defines the amount of data used, and "final state with b-jets and missing transverse momentum" describes properties of the data that offer a promising experimental signature for some models of supersymmetry.

The search for evidence of supersymmetry in a final state with b-jets and missing transverse energy at the CMS experiment was developed from 2009 to 2013. It has been a collaborative effort involving scientists from the University of Colorado at Boulder, the University of California at Riverside, Cornell University, and the University of California at Santa Barbara. The parameters of the study detailed in this thesis are consistent with the analysis developed by the group and published in several papers [17] [18] [13]. However, the background predictions (important elements of which are published in [18]) and interpretation of the result in this thesis is a largely independent study. This result is compared with other searches having hadronic activity in the final state.

The next chapter is a brief discussion of the theoretical foundations of this analysis. It introduces basic concepts in particle physics, such as types of particles and forces, as well as simple explanations of concepts important to the experimental methods, such as parity violation in the weak interaction. Additionally, it describes the experimental motivation and phenomenological characteristics of supersymmetry as an extension of our current understanding of the universe, and the type of supersymmetry model which is the focus of this study.

The third chapter describes the experimental apparatus used to obtain the data. The Large Hadron Collider (LHC), which accelerates protons to speeds close to the speed of light and then smashes them together, is perhaps the largest piece of scientific equipment ever built. Several international collaborations have built apparatus to observe collisions at the LHC, which are independent experiments. This chapter details the characteristics of the CMS detector, which collected the data used in this thesis. Finally, the types of objects observed by the detector are described. This section is important because it defines many of the terms used throughout this thesis. It describes how objects mentioned in Ch. 2 are actually observed and studied.

The search for supersymmetry is introduced in Ch. 4. It outlines the parameters of the search used by the CMS group studying hadronic events with b-jets. To this effect, the chapter describes important properties of the data and compares them with simulations of fundamental processes. While the parameter space is defined to select collisions with very rare properties characteristic of the existence of supersymmetry, known processes may also (very rarely) have the same features. The resulting rates of a few supersymmetric models are compared with those from known processes, which are the underlying background to the potential signal.

The understanding of rare processes that look like supersymmetry is the topic of Ch. 5, as well as the bulk of the work for this study. Since we do not know the precise features of any new physics, we look for an excess in the rate of rare processes. Therefore, it is crucially important to understand and be able to predict the rate of the background.

A novel approach for understanding a major source of background is described in Sec. 5.1. This chapter describes the physics behind each background process, how their rates are predicted, and with how much uncertainty.

Once the rates of backgrounds are established, we look for the possibility of new physics from a particular class of supersymmetry models in Ch. 6. Since no evidence of signal is observed, a well-established calculation is presented that takes into account all of the uncertainties associated with the background predictions and determines how inconsistent the simplified models of supersymmetry are with the collected data. The results are similar to other hadronic searches with b-jets and missing transverse energy.

Chapter 2

Theoretical Motivation

This chapter presents a brief overview of particle physics for the layperson, and the motivation for the study described in this thesis. First, an outline of the fundamental particles is provided, including deeper discussion of topics relevent to this study. This is followed by a a discussion of a few of the key questions in the field. The theory of supersymmetry is introduced as a possible answer to some of these questions, and I describe how it will be tested experimentally.

2.1 The Standard Model of particle physics

The Standard Model of particle physics is the most complete description of fundamental processes that scientists have to date. In one unified picture, it describes almost everything at the subatomic scale, with a few notable exceptions such as gravity and dark matter. Experimental measurements testing the predictions of this theory have validated

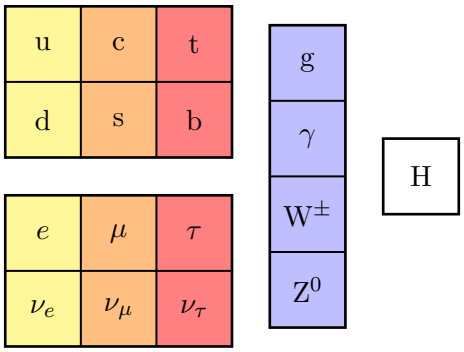

Figure 2.1: Fundamental particles in the Standard Model. The two orange boxes on the left include all the fermions, which have half integer spin, the quarks (top box) and leptons (bottom box). Blue box contains the spin 1 gauge bosons. The white box contains the recently discovered spin 0 Higgs boson.

it to a very high precision, and the newly discovered Higgs boson confirms its remarkable power. This section provides a brief overview of particle physics as it is currently understood.

The reductionist effort in physics is the scientific approach of breaking down the physical world into its smallest components. This approach attempts to explain all physical phenomena as interactions between these fundamental components. Figure 2.1 shows the types of fundamental particles present in the Standard Model. This simple table, like the periodic table of elements, contains deeper information about the relationship of the particles with respect to each other.

Three columns of boxes contain (left to right) fermions, gauge bosons, and Higgs boson(s). The fermions in the orange boxes have half-integer spin, in units of $\hbar$. Each fermion square actually contains two entries, the particle and anti-particle. The anti-particle has oppositely-signed quantum numbers with respect to the particle, including charge, spin,

and lepton/baryon number. The gauge bosons have integer spin, with a magnitude of 1. They are the fundamental particles responsible for mediating three of the four forces: strong, electromagnetic, and weak.

Fermions

The upper box of fermions in Fig. 2.1 contain the quarks. They interact with each of the four forces. All quarks have fractional electric charge. The top row of *up-type* quarks have charge +2/3 (in units of e, the electron's charge), and the bottom row of *down-type* quarks have -1/3 charge. In addition, they have a different type of charge, color, which is associated with the strong force. There are three color "charges", creatively named: red, green, and blue. Like any other quantum number, anti-quarks have opposite values of color charge. Quarks can only exist in *colorless* bound states – that is, the composite particle must be a color-neutral combination of all three colors or a color/anti-color pair.

The lower box of fermions contain the leptons. The upper row are charged leptons, including the electron and its heavier cousins the muon and τ-lepton. Each is partnered with a neutral lepton with the same flavor, the neutrinos, which only interact via the weak force. Since they only interact via the weak force, they are difficult to study in general purpose experiments. The arrangement of the leptons below the quarks indicates their grouping in three *generations*. Each generation is composed of an up-type quark, a down-type quark, a charged lepton, and a neutrino. The yellow boxes are the first generation, which contains the lightest and therefore (mostly) stable objects. The orange and red boxes can be considered heavier copies of the first, as seen in Table 2.1. With the exception of

Table 2.1: Masses of fundamental particles in the Standard Model.

Quarks		Leptons		Bosons	
u	2.3 MeV	e	0.51 MeV	g	0
d	4.8 MeV	ν_e	<2 eV	γ	0
s	95 MeV	μ	105.6 MeV	$W^{\pm}$	80.4 GeV
c	1.28 GeV	ν_μ	<0.2 MeV	Z	91.2 GeV
b	4.18 GeV	τ	1777 MeV	H	125.9 GeV
t	173 GeV	ν_τ	<20 MeV		

Table 2.2: Characteristics of fundamental forces.

Force	Strength	Range
strong	1	10^{-15} m
EM	$\frac{1}{137}$	infinite
weak	10^{-6}	10^{-18} m

the neutrinos, particles in the higher generations have short lifetimes and eventually decay to those in the first generation. The mechanisms of these decays involve the force carriers, and are described in more detail below. While there is strong evidence against the existence of a fourth generation, the Standard Model does not demand three. The reason for three generations remains an open question within the Standard Model.

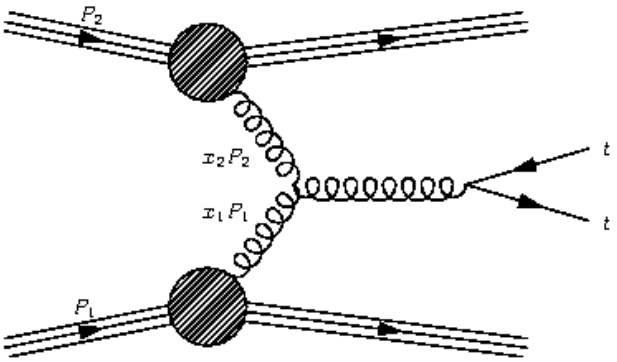

Figure 2.2: The production of a top/anti-top quark pairs from proton-proton collisions. A gluon from each proton carries momentum $x_{1,2}P_{1,2}$, where the momentum fraction of the proton is determined by the parton distribution function for gluons.

Gauge bosons

The bosons listed in Fig. 2.1 mediate all forces between quarks, leptons, and each other. The gravitational and electromagnetic forces are reponsible for most of the forces we interact with on a daily basis. Since it is beyond the scope of this thesis, gravity is not described in this section. However, the characteristics of the other forces have extremely powerful effects as well.

The blue column in Fig. 2.1 contains the gauge bosons: photon, gluon, W and Z. First, the photon (γ) is the familiar mediator of the electromagnetic force. The photon has no mass, has an infinite lifetime, infinite range, and travels at the fastest possible speed, c. It couples to oppositely charged particles (the photon is neutral and charge must be conserved), provided that no other conservation laws are violated.

More powerful than the electromagnetic force is the strong force, mediated by eight gluons. Like photons, gluons are also massless with no electric charge. Only quarks

and gluons have color, and gluons only couple to colored particles. The theory of the strong force is called quantum chromodynamics, or QCD.

As a proton–proton collider, the strong force plays a major role in physics at the LHC. In addition to the three valence quarks (uud), the proton contains a "sea" of gluons and quark/anti-quark pairs that are produced through particle interactions. The parton distribution function (PDF) is the probability density function of a parton to have a certain fraction of the hadron momentum. Studies of the proton PDFs indicate that the quarks carry about half the total momentum, with gluons responsible for the rest. Since the valence quarks do not annihilate in proton-proton collisions, the LHC is to a large extent a gluon collider. The principle of *asymptotic freedom* in QCD, means that the bonds between partons are weak at high energy and short distances. Within the relativistic proton, quarks and gluons jostle about freely. As partons are pulled apart, the strength of the bond increases until it is energetically favored to produce a quark/anti-quark pair, in a process called hadronization. In this way, high-energy collisions of individual quarks and gluons result in the production of other colorless particles. Because the strong force dominates, the cross-section (rate) of these types of interactions is very large.

Since they can not be isolated, the masses of quarks may be difficult to define, especially for the first generation. Table 2.1 lists the masses of the fundamental particles in the Standard Model. Bottom and charm quarks are more easily measured since they are very heavy with respect to the first generation, so that bound states with lower-mass quarks are dominated by heavy quark mass. Interestingly, the top quark so massive, it

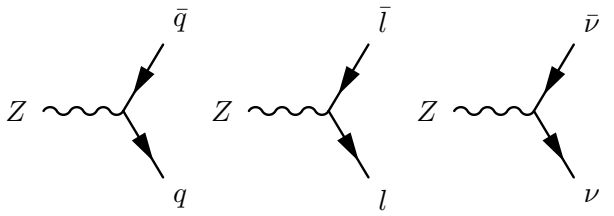

Figure 2.3: Coupling of Z boson to fermions.

decays before it hadronizes, within 5×10^{-25} s. It is the only colored object that has been observed "bare". Figure 2.2 shows the production of top and anti-top quark pair from the collisions of protons at the LHC. Gluons from within the protons, having momenta x_1P_1 and x_2P_2, provide the energy for the heavy quarks. The top quark has many fascinating properties and is an important part of this analysis, as discussed in Ch. 4 and Ch. 5.

Two more gauge bosons are shown in Fig. 2.1, the W and Z, which are responsible for mediating the weak interaction. As shown in Table 2.1, the W and Z are the only massive gauge bosons, which makes their appearance as a virtual particle mediating interactions relatively very rare. As a result, the weak force has the smallest coupling (shown in Table 2.2) and weakly-mediated processes have small cross-sections. The strength of this force is so small that it does not produce any bound states, and particles that can decay only via the weak force have relatively long lifetimes. Since neutrinos only interact via the weak force, they are hardly affected by any matter, and are very difficult to detect.

The Z boson, which is neutral, is its own antiparticle. As a force mediator, it behaves almost exactly like a photon, but its large mass suppresses the rate for Z-mediated processes. Unlike the photon, it couples to neutrinos, and can therefore create charged or neutral lepton pairs of any flavor, as seen in Fig. 2.3. The W^+ and W^- are a particle/anti-

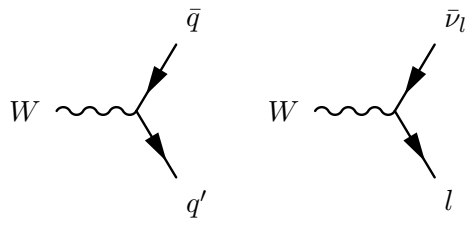

Figure 2.4: Coupling of W boson to fermions.

particle pair. Because the W boson is charged, it is the only particle that couples quarks of different flavors together and charged leptons to neutrinos (Fig. 2.4). Due to its presence in the top-quark decay chain, the W boson is important for this analysis.

2.1.1 Important properties of the weak force

The quarks that interact with the W boson do so on a different basis than those listed in Fig. 2.1. Instead, the W couples to a mixture of those states, in which they are rotated by various mixing angles. The particle that couples to the up quark via the charged-current weak interaction is a superposition of down-type quarks, $d' = V_{ud}d + V_{us}s + V_{ub}b$. The flavor composition of this new basis is determined by the CKM matrix,

$$\begin{bmatrix} d' \\ s' \\ b' \end{bmatrix} = \begin{bmatrix} V_{ud} & V_{us} & V_{ub} \\ V_{cd} & V_{cs} & V_{cb} \\ V_{td} & V_{ts} & V_{tb} \end{bmatrix} \begin{bmatrix} d \\ s \\ b \end{bmatrix}.$$

As a result, the squared elements of the CKM provide the probability for an up-type quark to couple to a down-type quark. This is especially relevent when considering the weak decays of hadrons, such as neutrons and charged pions. Since these particles only decay via the weak interaction, they have a relatively very long lifetime with respect to other unstable

particles. The values of the CKM elements are listed in Eq. 2.1.1. The squared entry in the bottom right, $|V_{tb}|^2 \approx 1$, tells us that the top quark decays almost exclusively to a W boson and b-quark,

$$\begin{bmatrix} |V_{ud}| & |V_{us}| & |V_{ub}| \\ |V_{cd}| & |V_{cs}| & |V_{cb}| \\ |V_{td}| & |V_{ts}| & |V_{tb}| \end{bmatrix} = \begin{bmatrix} 0.974 & 0.225 & 0.004 \\ 0.225 & 0.973 & 0.041 \\ 0.009 & 0.040 & 0.999 \end{bmatrix}.$$

The law of parity conservation is observed to be respected by gravitational, electromagnetic, and strong interactions. In 1957, experimentalist Chien Shiung Wu discovered that the weak interaction violates parity in the beta decay of cobalt atoms. It is the only force which does not preserve parity symmetry (P). In fact, parity is *maximally* violated by the weak force. The W boson only couples to the left-handed components of the fermions (or right-handed components of the anti-particles) in Fig. 2.1. Rewriting the fermions in terms of their left- and right-handed chirality projections, $\psi_{L,R} = \frac{1}{2}(1 \mp \gamma_5)\psi$, the coupling of the W to fermions is proportional to this left-handed part. The projection operator is included in the expression of the charged weak current, and when expanded, gives $\frac{1}{2}(\bar{u}\gamma^\mu u - \bar{u}\gamma^\mu\gamma^5 u)$. This shows that the current contains a Lorentz vector in the first term and an axial vector in the second term, causing it to be dubbed the V–A interaction. Since a vector flips sign under a parity transformation and an axial vector does not, this results in the characteristic parity violation of the weak force.

The Glashow-Weinberg-Salam theory describes the fields responsible for the combination of the weak and electromagnetic forces. According to this theory, at very high energies, the universe has four massless gauge boson fields. At lower energies, the gauge

symmetry is spontaneously broken, causing three of the fields to acquire mass through the mechanism of spontaneous symmetry breaking. These fields consist of an isotriplet of vector fields (W^1, W^2, W^3), and a single vector field, B. The four fields are not mass eigenstates, instead, the physical fields are rotated by Weinberg angle, θ_W. For example, the massive Z boson and massless photon are a linear combination of the two neutral fields [19]:

$$\begin{pmatrix} \gamma \\ Z^0 \end{pmatrix} = \begin{pmatrix} \cos\theta_W & \sin\theta_W \\ -\sin\theta_W & \cos\theta_W \end{pmatrix} \begin{pmatrix} B \\ W^3 \end{pmatrix}$$

Furthermore, the mass eigenstates of the W bosons are a combination the two charged vector fields, $W^{\pm} = \sqrt{\frac{1}{2}}(W^1 \mp iW^2)$. The masses of the W and Z bosons are related very simply by the Weinberg angle, $\cos\theta_W = \frac{M_W}{M_Z}$. From this relationship, the theory provided a prediction for the masses of the two bosons. Their discovery and subsequent measurement of their masses was a tremendous victory for the predictive power of the Standard Model. As discussed in the following section, the concepts of symmetry breaking and field mixing are important in the supersymmetric extension of the Standard Model.

2.1.2 Questions in particle physics

While the Standard Model is an extremely successful description of nature, there are several key mysteries about the universe that scientists are trying to understand today. Some of the big questions are:

1. Why is the universe full of matter, with very little anti-matter, even though anti-matter is usually produced in equalamounts with matter in nearly all known processes?

2. Why do the neutrinos have the masses we measure?

3. How does gravity fit into our knowledge of particle physics?

4. Are the 19 free parameters (which can only be determined experimentally) in the Standard Model really arbitrary?

5. What is dark energy?

6. What is dark matter?

7. How is the electroweak scale stabilized against quantum corrections to the Higgs mass?

8. Why do the running couplings of the forces **almost** converge at the GUT scale? Should they meet?

To answer any of these questions, a major new theory to explain the universe will need to be introduced. Certain supersymmetric theories attempt to answer the last three questions. Two prominent issues are discussed below.

Dark matter was first discovered from observing the rotation of galaxies. By considering the gravitational effect of luminous matter at the center of galaxies (determined by x-ray measurements), astrophysicists predicted the rotational velocity of the galaxy at large radii. Surprisingly, measurements of the rotation showed that the amount of matter was greatly undermeasured in the center. There must be additional unseen matter within galaxies which can not be detected. Since no direct observations of these particles or their decay products have ever been made, this dark matter is expected to be weakly

interacting particles which must be stable on a cosmological timescale. Neutrinos are weakly interacting, but their masses are far too tiny to create the proper mass density. All other known particles would decay into visible products. Other observations via gravitational lensing have supported the conclusion that the majority of the mass of galaxies is dark matter. According to cosmological measurements, baryonic matter only makes up 4.6% of the energy in the universe, dark matter is responsible for 22.7%, and dark energy is the dominant component (72.8%) [20]. The nature of dark matter and dark energy is an open question in particle physics.

A theoretical issue known as the hierarchy problem is a perplexing issue in the Standard Model. In field theory, perturbative expansions are used to calculate the rate of certain processes. For example, to calculate the Higgs mass involves tree-level, one-loop, and higher order terms. Since the Higgs field most strongly couples to mass, the largest contribution is a closed top/anti-top loop. As a result of the Higgs boson having spin 0, the one loop correction, $\Delta m_H^2 = -\frac{|\lambda|^2}{8\pi^2}\Lambda^2 + ...$, is quadratically divergent [21]. Here, λ is the self-interaction of the field, and Λ is the cutoff scale. If there is no new physics to be discovered in the intervening energies, the cutoff for the field theory would be the Planck scale, at 10^{19} GeV. Quantum field theory (QFT) is expected to break down at this energy because the quantum fluctuations in the gravitational fields would become important, demanding a new theory to explain them. If QFT is the only physics, having this huge value of Λ would require a correction term to cancel it out and leave the Higgs mass at the correct value, and therefore would have to be accurate to one part in 10^{32}! This scenario is unpleasant

Table 2.3: First generation fermions and their superpartners.

	Spin $\frac{1}{2}$	Spin 0
Quarks	$(u_L \; d_L)$	$(\tilde{u}_L \; \tilde{d}_L)$
	u_R	$\tilde{u}_R$
	d_R	$\tilde{d}_R$
Leptons	$(\nu_L \; e_L)$	$(\tilde{\nu}_L \; \tilde{e}_L)$
	e_R	$\tilde{e}_R$

to most theorists, which is why they try to construct new theories of physics which would be consistent with Standard Model observations, but would remove the need for a very precisely tuned parameter. Such a parameter would be unnecessary if new physics presents itself at the TeV scale, which happens to be the energy probed by the LHC!

2.2 Motivation for the supersymmetry hypothesis

Supersymmetry provides possible solutions to the dark matter, hierarchy, even unification questions in particle physics. Fundamentally, this theory introduces a new symmetry between fermionic degrees of freedom and bosonic degrees of freedom. In the simplest models, which will be the only scenario considered here, each particle in the Standard Model has a partner whose spin differs by 1/2. The symbols of the supersymmetric partners are distinguished by a tilde.

Table 2.4: Gauge particles and their corresponding gaugino mass eigenstates.

Particles	Spin	NDOF	SUSY Fields	Spin	NDOF	Sparticles	Spin	NDOF
W^+	1	3	$\tilde{W}^1$	1/2	2	$\tilde{\chi}_1^+$	1/2	2
W^-	1	3	$\tilde{W}^2$	1/2	2	$\tilde{\chi}_1^-$	1/2	2
Z	1	3	$\tilde{W}^3$	1/2	2	$\tilde{\chi}_2^+$	1/2	2
γ	1	2	$\tilde{B}$	1/2	2	$\tilde{\chi}_2^-$	1/2	2
H	0	1	$\tilde{H}$	1/2	2	$\tilde{\chi}_1^0$	1/2	2
h	0	1	$\tilde{h}$	1/2	2	$\tilde{\chi}_2^0$	1/2	2
H^+	0	1	$\tilde{H}^+$	1/2	2	$\tilde{\chi}_3^0$	1/2	2
H^-	0	1	$\tilde{H}^-$	1/2	2	$\tilde{\chi}_4^0$	1/2	2
A	0	1						
Total		16			16			16

In order for the number of states to be consistent, the quarks and charged leptons each have two supersymmetric partners, one each for their left-handed and right-handed chiral components. These are listed for the first generation in Table 2.3, with the pattern repeated for the second and third generation. The scalar partners, called squarks and sleptons, maintain consistent color and lepton number properties.

The supersymmetric partners to the gauge bosons are collectively called gauginos, listed in the third column of Table 2.4. Only the gluon's partner corresponds to a gaugino mass eigenstate. In the same way that the photon, W, and Z bosons are mixtures of the electroweak fields, gauginos are mixtures of the bino ($\tilde{B}$), wino ($\tilde{W}_i$), and higgsino ($\tilde{H}$) fields, shown in the second column of the table. The result is four electrically charged states, charginos, with degenerate mass for each pair, and four electrically neutral mass states, called neutralinos. Table 2.4 also shows that the number of degrees of freedom available to particles in the electroweak sector (including five Higgs bosons) are equivalent to the corresponding supersymmetric fields, as well as the mass eigenstates of the supersymmetric fields.

In many supersymmetric theories, in particular the ones of most interest at the CMS experiment, a new conserved quantity (like baryon or lepton number) is introduced to govern particle interactions. This quantity, *R-parity* is defined as $R = (-1)^{3(B-L)+2J}$, where J is spin, B is baryon number, and L is lepton number [21]. By requiring the number of sparticles to be conserved, the proton can not decay through a virtual sparticle, which is crucial to maintain consistency with current observations. As a result, supersymmetric

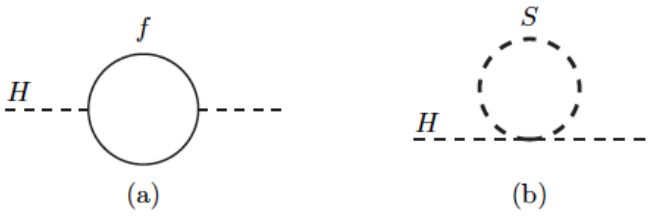

Figure 2.5: One-loop corrections to the Higgs boson mass, involving fermions (left) and a scalar (right).

particles must be produced in sparticle/anti-sparticle pairs, and the lightest sparticle is stable, since there is nothing for it to decay to. If this lightest sparticle (LSP) only interacts via the weak force (a neutralino), it is a natural candidate for dark matter.

Simple models of supersymmetry have other convenient features. If the new particle masses are on the order of a TeV, the divergent terms in the Higgs mass, described above, are cancelled out. This is because the one-loop correction now has an additional scalar component in addition to the fermionic one, as shown in Fig. 2.5. This enters the calculation with the opposite sign as the fermion term, cancelling it out. In fact, this occurs at all higher order corrections as well, without requiring the adjustment of any parameters. In addition, this extension of the Standard Model may allow the coupling constants to converge at an energy $\sim 10^{16}$, where all the forces become one. This would be a very pleasing feature of nature!

If supersymmetry were an unbroken symmetry in nature, the supersymmetric sparticles would have the same masses as their Standard Model partners. However, since we know this is not the case, minimal models of supersymmetry are based on a softly broken symmetry, whereby the sparticle masses have been pushed above the TeV scale, but all

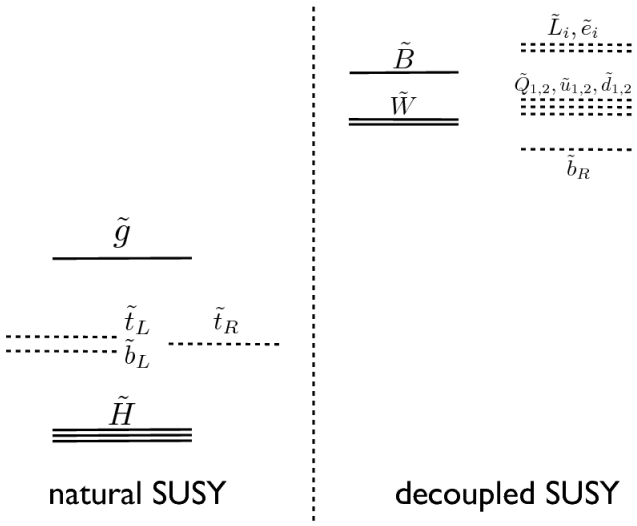

Figure 2.6: Sketch of a possible supersymmetric particle relative mass spectrum, with mass increasing upwards. Models in which the supersymmetric particles on the left (at minimum) are near the electroweak scale have desirable properties. The remaining supersymmetric particles on the right may have large masses beyond the reach of the LHC [1].

other properties remain shared. Figure 2.6 shows a possible mass spectra for supersymmetric particles. Since the third generation squarks are convenient for solving the hierarchy problem discribed above, we are interested in models in which they have relatively low mass, but the masses of most other sparticles are free (decoupled) to be too heavy to be detected. In these scenarios, either the $\tilde{t}_R$ has the smallest mass, the degenerate $\tilde{t}_L$ and $\tilde{b}_L$ are lightest, or all three are light. The figure shows the LSP as a pure higgsino, but it is possible for it to be a mixture of other gaugino fields, as well.

With a mass spectrum like the one proposed in Fig. 2.6, there are several ways in which supersymmetric particles could be created and decay at the LHC. At the LHC, the most probable production of sparticles is through the strong force. Figure 2.7 shows how gluino pairs could be produced. The mass of the gluinos determines its production

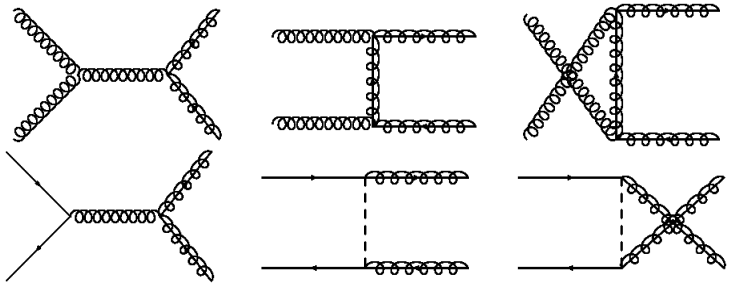

Figure 2.7: Diagrams of gluino pair production via gluon-gluon (top) and quark-quark (bottom) fusion. Production from gluon interactions dominate at the LHC.

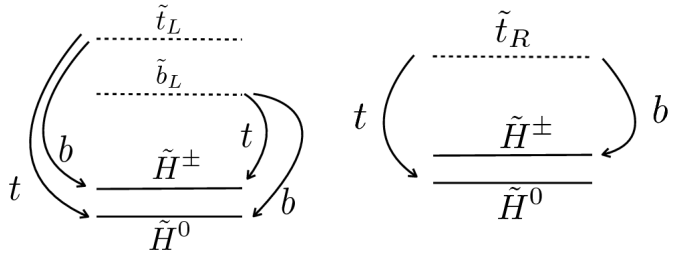

Figure 2.8: Decay of light third generation squarks to the LSP [1].

cross-section, so that the heavier the gluino is, the rarer it will be. To conserve R-parity, the gluino must decay to a lighter sparticle. Since interactions are determined by the gauge group in the same way as in the Standard Model, a third generation squark-quark pair would be produced. Those squarks would then decay to a quark and the LSP, as shown in Fig. 2.8. As a result, models with this simple mass spectra would involve the production of many third generation particles. For this reason, the detection of top and bottom quarks are extremely interesting in searches for supersymmetry.

2.2.1 Simplified models

Over the past several decades, theorists have developed many different scenarios involving the principle of supersymmetry. Even in the minimal extensions to the Standard Model described above, in which each known particle has only one supersymmetric partner, the number of free parameters governing these models can range from 5 to dozens. Depending on the values of the parameters, the resulting physical phenomena can be dramatically different. Scientists at the CMS experiment need to know what phenomena they should be looking for, and be able to test for evidence of thousands of very different models.

It is clearly impossible to individually look for evidence of every supersymmetric model the theorists concieve, along with the full parameter space of each. Instead, experimentalists use a simplification of supersymmetry which depends on only a few parameters. In this framework, specific production and decay chains of supersymmetric particles are studied individually. By varying the masses of the sparticles, experimentalists can proceed with a very general search that does not depend on the parameters of any particular theory.

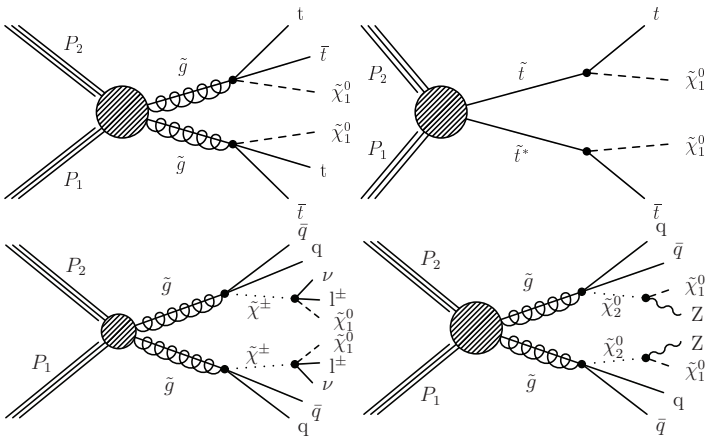

Figure 2.9: Decay chains to top-quarks via gluino and squark pair production (top row). Examples of more complicated decay chains involving gauge bosons (bottom row) [2].

They then provide a generic interpretation that can be applied by the theorist to their favorite models that involve the process. These *Simplified Models* are collectively referred to as the Simplified Model Spectra (SMS). They range in complexity from very simple direct decays to the LSP, to long decay chains involving multiple charginos and sleptons, where the choice of intermediate particle masses can alter the kinematics of the process dramatically. Figure 2.9 shows some examples. The top row of the figure shows the production of top-quarks in the final state through either gluino or squark pair production. The bottom row shows more complicated scenarios, in which the final state depends upon the mass of intermediate charginos and neutralinos in the decay chain.

Experimentalists tailor their approach according to the final state topologies of the SMS model(s) they are interested in. This allows them to take phenomenological similarities amoung the many SUSY models and calculate limits on each topology. Many groups of analysts are put to work to focus on almost every possible final state in which supersymmetry

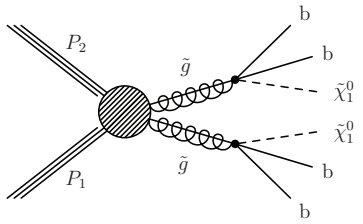

Figure 2.10: Decay of gluinos to bottom quarks and the LSP through a virtual b-squark, T1bbbb [2].

may present itself. Generally speaking, within each SMS model the sparticle production cross-section and masses are allowed to vary according to the type of process being studied, and usually the branching ratios are set to one, or allowed just a few possibilities. Individual limits are placed for each possible value of these parameters, called a scan of the parameter space.

This analysis studies gluino pair production in which the third generation squarks are light and the LSP is neutral. A hadronic search for supersymmetry is suitable for exploring squark decay to b-quarks, since multiple top-quarks would be likely to produce a lepton in the final state. In particular, a limit is set on the SMS model in which the branching fraction of $\tilde{g} \rightarrow b\bar{b}\tilde{\chi}_0$ is 100%. This signature, shown in Fig. 2.10, is called T1bbbb. The masses of the gluino and neutralino are scanned. Since there are no leptons in the final state, this analysis has many unique challenges, as described in Ch. 4.

Chapter 3

Experimental Tools

3.1 The Large Hadron Collider

The Large Hadron Collider is the largest particle accelerator ever built, located at the European Organization for Nuclear Research (CERN). CERN employs thousands of scientists and engineers to maintain the functioning of several accelerator systems, shown in Fig. 3.1, to deliver particle beams to dozens of scientific experiments. In the underground tunnel originally built for the LEP electron-positron collider, the LHC accelerates oppositely circulating beams of protons (and occasionally lead ions) close to the speed of light, and then collides them at the center of large particle detection apparatuses. The purpose of this enormous scientific instrument is to explore the Standard Model and beyond, and to answer major questions about dark matter, the matter-antimatter imbalance, and the early universe.

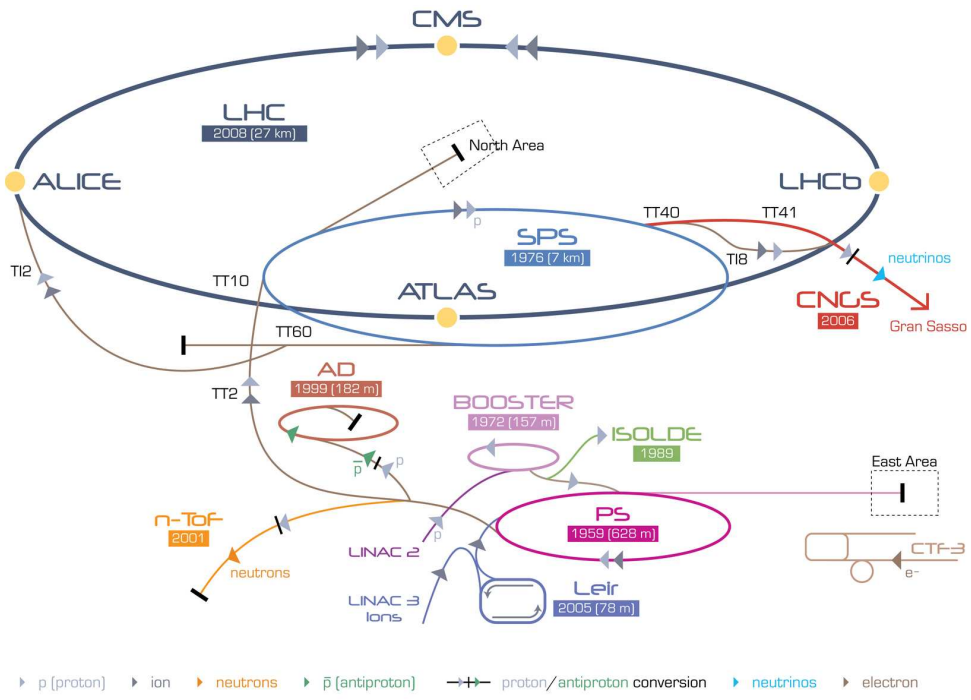

Figure 3.1: Schematic drawing of the accelerator complex at CERN, including the Large Hadron Collider. Image: CERN.

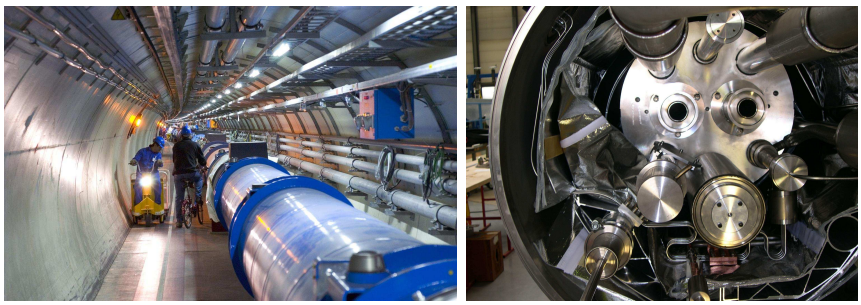

Figure 3.2: Photographs of the LHC. A view of the accelerator inside the underground tunnel (left), and a cross-sectional view of a dipole magnet (right). Photos: CERN.

Table 3.1: Major components of the LHC machine.

	Number	Size	Purpose
Total magnets	9593		
Main dipole magnets	1232	15 m	Bending beams
Main quadrupole magnets	392	5–7 m	Focusing beams
RF cavities	16		Accelerating & shaping bunches

The tunnel that houses the accelerator is 27 km in circumference, with a mean depth of 100 m underground. In it, a series of magnets accelerate clusters of particles, called bunches, in an ultrahigh vacuum. Figure 3.2 is photographs of the accelerator, showing it in the underground tunnel, with a person shown for scale. The second photograph is a cross-sectional view of a typical portion of the accelerator, showing the two beamlines for the oppositely traveling particles within the magnet, along with the delivery of support systems like power and cooling.

A total of 9593 magnets are used for controlling the proton beams, each one several meters long. The main types of elements used to bend and accelerate the beams are listed in Table 3.1. The dipole magnets, with a cross-sectional view shown in Fig. 3.3, keep the beams in their circular trajectory. For a given circumference, the strength of the magnetic field they produce is proportional to the maximum attainable energy of the beams. To maintain a high field of 8.33 T, the dipoles require an enormous current of 11850 A, which necesitates supplying the current from superconducting cables to avoid energy loss.

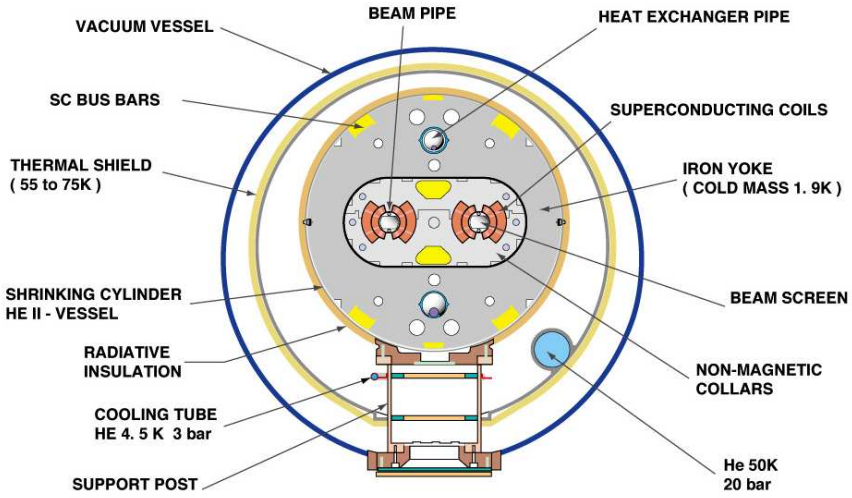

Figure 3.3: Diagram showing a cross-sectional view of an LHC dipole magnet, with important components labeled. Image: CERN.

It is important to keep the beams focused very tightly, so that protons in a bunch arrive together at the appropriate beam crossing and are focused enough to increase the probability of a hard proton-proton collision. For this purpose, focusing magnets keep the beam collimated. Radio frequency cavities give a "kick" to the bunches at eight locations along the ring. The oscillations of these electromagnetic resonators accelerate the protons while pushing them together within the bunch. The bunches make 11245 turns around the ring every second, and are focused to a diameter $\sim$16 μm near the interaction regions.

Figure 3.3 shows a transverse view of a typical portion of the accelerator. The two proton beams circulate in beampipes down the center. They are surrounded by superconducting coils that generate the magnetic field to bend the trajectory of the particles. To allow the superconducting magnets to conduct a large amount of current without energy

loss, they must be kept at very cold temperatures. This is achieved with a liquid helium cooling system, which brings the magnets to −271.3 Celsius, colder than outer space. In turn, the cryostat system requires a vacuum to insulate it. This portion of the vacuum system is incredibly large, ∼9000 m^3.

3.1.1 Production and acceleration of proton beams

To begin, protons are obtained from hydrogen gas, which is stripped of its electrons by an electric field. They are first boosted by the Linac, the linear accelerator shown in violet in Fig. 3.1, which starts the proton beam with an energy of 50 MeV. Then the beam is transfered through a series of synchrotrons to increase its energy. Figure 3.1 traces its path through increasingly powerful circular accelerators, the Proton Synchrotron Booster (in violet), then the Proton Synchrotron (in magenta), and to the Super Proton Synchrotron (in blue). Finally, the protons injected into the LHC at an energy of 450 GeV. Two proton beams, separated into bunches, travel in opposite directions around the ring as they are accelerated to an energy of 4 TeV. It takes ∼45 minutes to fill the ring, ramp up the beam to 4 TeV, squeeze it to the appropriate narrowness, and be ready for collisions. Once collisions begin, the beams are stable for typically six hours, providing important data to the experiments where the interactions take place. During 2012, the LHC provided collisions to the CMS and ALTAS experiments over the course of 201 days, during which a tremendous amount of data was collected.

The probability of observing a very rare and undiscovered new particle at the LHC experiments is directly dependent on the properties of the LHC beam. The rate of

occurance for a process is:

$$\frac{dN}{dt} = \mathcal{L}\sigma \tag{3.1}$$

$$\int \mathcal{L}dt \times \sigma = N \tag{3.2}$$

The first term, $\mathcal{L}$, is the (instantaneous) luminosity of the beam. It is a measure of the probability of collisions, in units of $\mathrm{cm}^{-2}\mathrm{s}^{-1}$, and is constructed according to the aspects of the beam. The second term, σ, is the cross-section for the physics process of interest (measured as an area). It is an intrinsic property of the process, dependent on coupling strengths and masses of the particles involved. For example, the cross section of proton-proton interactions is $\sigma_{pp} \sim$100 mb.

The instantaneous luminosity for the head-on collision of two beams is [22]:

$$\mathcal{L} = \frac{N_1 N_2 f n_b}{4\pi\sigma_x\sigma_y}. \tag{3.3}$$

Here, N_1 and N_2 are the number of protons per bunch in beam 1 and beam 2, respectively. The quantity f is the revolution frequency of the beam, which contains n_b bunches. In the denominator, a kinematic factor and the sizes of the beams appear. This expression assumes that both beams are gaussian and have the same spread in the x-direction and the same spread in the y-direction. To increase the probability of proton-proton collisions, we can not change the cross section for this process, but we can effect the luminosity by tightly collimating the beam, inserting as many protons in each bunch as possible, and including as many bunches as possible. To be successful in providing the best conditions for scientific study, the LHC must deliver not just proton beams with high energy, but also with high luminosity.

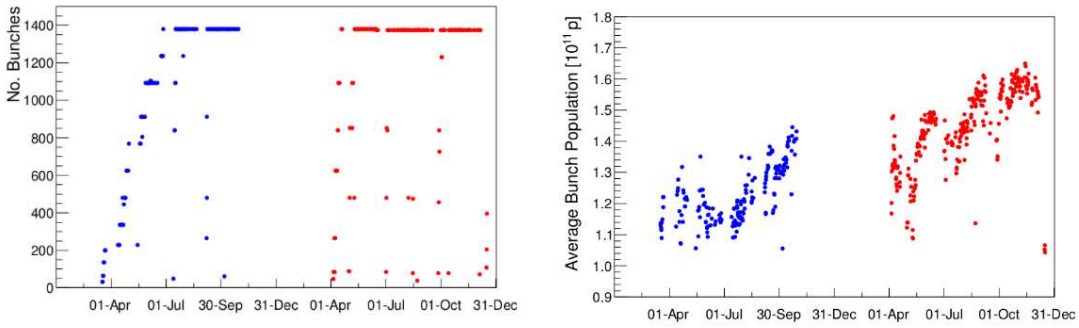

(a) Number of bunches per fill.

(b) Number of protons per bunch.

Figure 3.4: Properties of proton bunches during Run 1, for 7 TeV collisions in 2011 (blue), and 8 TeV collisions in 2012 (red) [3].

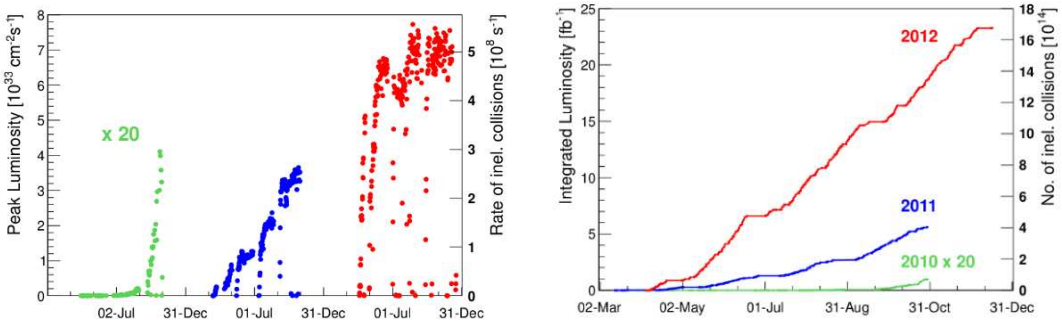

(a) Maximum instantaneous luminosity.

(b) Integrated luminosity.

Figure 3.5: Instantaneous and integrated luminosity during Run 1. Early data-taking in 2010 (green), 7 TeV collisions in 2011 (blue) and 8 TeV collisions in 2012 (red) [3].

Figure 3.4 shows some properties of the proton bunches, comparing the conditions in 2011 with the high intensity conditions provided in 2012. The first figure shows that for the most part, the maximum number of bunches were inserted for each fill. Fig. 3.4(b) shows that as the operation of the machine became better understood, it became possible to insert many more protons in each bunch. By the end of 2012, almost an order of magnitude more protons were present in each bunch with respect to early running in 2011. The result of improvements in the beam during the first few years of operation is shown in Fig. 3.5(a), where the maximum instantaneous luminosity is shown to increase.

As seen in Eq.3.2, luminosity can be used to provide a measure of the amount of data delivered to the experiments. The instantaneous luminosity measured during running can be integrated over time to provide the integrated luminosity,

$$\mathcal{L}_{INT} = \int L\, dt. \tag{3.4}$$

The integrated luminosity from three periods of data-taking is shown in Figure 3.5(b). Experiments need a large amount of data to search for rare events, therefore, they are interested in datasets with large integrated luminosity. Of the amount delivered by the LHC in Fig. 3.5, the CMS experiment collected 19.39 fb^{-1} of data in 2012. As seen in Eq. 3.2, the collected integrated luminosity is proportional to the number of events, N. This is critically important for the study of rare processes, as the production of supersymmetric particles is expected to be. The importance of luminosity is apparent when σ in Eq. 3.3 is replaced with a very small cross section, and the expected number of observations of a rare process increases with luminosity.

Table 3.2: Properties of the collisions provided by the LHC during its 2012 operation.

Proton beam energy	4 TeV
Center of mass energy	8 TeV
Bunches per fill	∼1380
Bunch intensity	$1.6–1.7\times10^{11}$
Bunch spacing	50 ns
Peak event pile-up	∼40
Peak inst. luminosity	7.7×10^{33} $\mathrm{cm}^{-2}\,\mathrm{s}^{-1}$

Table 3.2 summarizes important quantities related to the amount of data-taking possible for CMS. The bunch intensity is the number of protons in each bunch, and the bunch spacing is the amount of time between the arrival of bunches. The latter is critical for detector design and performance. The time between beam crossings should be small to keep luminosity high, but long enough to allow detector response, efficient triggering, and the distinction of overlapping interactions (called *out-of-time pile-up*). The LHC and its experiments were designed to operate with a 25 ns bunch spacing. Table 3.2 also shows the typical number of interactions occuring at the same beam crossing, the peak event pile-up, also known as *in-time pile-up*. These conditions create a challenge for the experiments to disentangle detected particles from multiple proton–proton interactions not associated with the hard scatter, but is a necessary consequence of pushing the limits on deliverable luminosity.

3.1.2 Particle physics experiments at the LHC

The LHC beams collide at four points along the ring, at the locations of four major large physics experiments. They are listed in Table 3.3. ATLAS and CMS (Compact Muon Solenoid) are the two main multi-purpose detectors. While they are both based on the similar barrel and endcap design, a striking difference is in the choice of producing the magnetic field for bending charged particles. ATLAS has eight long superconducting magent coils forming a cylinder around the beam pipe, giving the detector the largest volume of any collider experiment. The CMS detector is arranged around a central large superconducting solenoid. Data from CMS is used for this analysis, so it is discussed in detail in the following section.

There are two specialized major experiments, as well as two other small detectors that study the beam. ALICE (A Large Ion Collider Experiment) takes data from lead ion collisions to study the quark-gluon plasma. In this state, the partons are no longer confined inside hadrons, and conditions of the early universe can be studied. The LHCb experiment studies the slight asymmetry in matter and antimatter through the decays of b-mesons. The detector is designed to catch mostly forward particles from glancing proton interactions. Two additional smaller experiments, TOTEM (TOTal Elastic and diffractive cross section Measurement) and LHCf (LHC forward) are located in the CMS and ATLAS caverns, respectively. They study the proton-proton cross-section and properties of the circulating beam.

Table 3.3: Main particle physics experiments at the LHC. Locations are in France unless otherwise stated.

	CMS	ATLAS	LHCb	ALICE
Dimensions [m]	21×15×15	46×25×25	21×13×10	26×16×16
Weight [t]	12500	7000	5600	10000
Location	Cessy	Meyrin, CH	Ferney-Voltaire	St. Genis-Pouily

3.1.3 Future goals

After a successful period of comissioning and delivering collisions from 2010 to 2012, the LHC began its first long shutdown. The shutdown is being used to perform much needed upgrades and maintainence on the machine, including fixing magnet interconnects that were damaged in a major quench in 2008. The LHC experiments, including CMS, also use this time to perform upgrades on the detectors. The accelerator is scheduled to restart in 2015, providing collisions with a center of mass energy of 13 TeV.

3.2 The CMS Detector

The CMS detector is a large, general-purpose particle detector located at the LHC. It is designed to efficiently record information on final state particles that result from high-energy, high-rate proton-proton collisions.

The primary motivations for this international effort are the study of physics at the TeV scale and the discovery of the mechanism for electroweak symmetry breaking [23]. The search for evidence of a Higgs boson guided some of the design goals by prioritizing the performance of detector elements that are critical for the probing well motivated decay channels. These design choices proved advantageous in creating a scientifically strong document claiming evidence of a Higgs boson discovery in 2012. With the start of 13 TeV collisions in 2015, there are many important avenues of research to explore. Additional studies of the Higgs boson are needed, as well as searches for additional Higgses. Groups of CMS physicists are dedicated to exploring the properties of the very rare B_s meson, which is a sensitive probe of new physics. In addition, with the increased beam energy, the hunt becomes even more exciting for evidence of the production of black holes, additional heavy bosons, extra dimensions, and supersymmetric particles.

To provide quality data for physics analysis, the CMS detector has four main requirements. First, it must provide good muon identification and momentum resolution over a wide range of muon momenta and angles. Second, an inner tracker system must provide good momentum resolution of charged particles, which is necessary for the reconstruction of primary vertices and identification of b-quarks. Additionally, identification of photons and

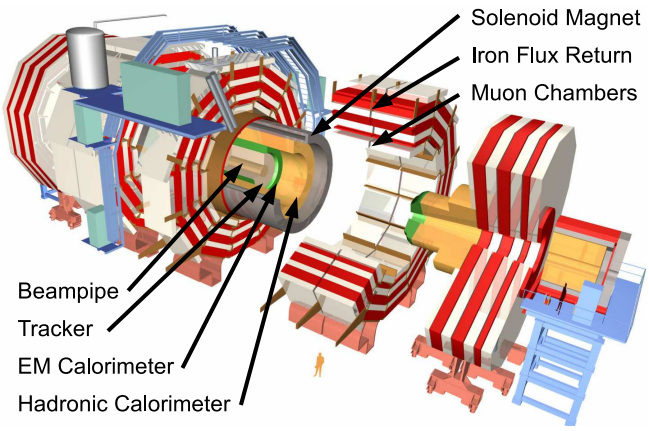

Figure 3.6: Drawing of the CMS detector with major subdetectors and components labeled, and a person for scale. Image modified from CERN.

electrons is needed, along with good electromagnetic energy resolution. Finally, a finely-segmented and hermetic hadronic calorimeter system is essential for calculating the energy of particle showers.

CMS is unique among particle physics detectors for its high-field solenoid, fully-silicon inner tracker, and weight of 12,500 tons. Figure 3.6 is an illustration of the detector, with portions removed to show the inner components. The center of the CMS design is the superconducting solenoid magnet, a hollow cylinder (shown in dark grey) surrounding the beampipe and centered on the interaction region where collisions occur. It provides a powerful and uniform field for bending the trajectories of charged particles in order to accurately measure their momentum at high energy. Within its inner volume 6 m in diameter and 12.5 m long, it produces a 3.8 T field. Here, the particle tracking and calorimetry systems are housed, surrounding the beampipe. Outside the solenoid, the magnetic flux is returned through a 10,000 ton iron yoke, layered with muon spectrometers. As seen in

the figure, five massive "wheels" of iron yoke and muon chambers encircle the solenoid (the red and grey cut-away ring). They are complemented by two enormous "disks" of iron and muon chambers on either end of the solenoid, with additional calorimeter instrumentation close to the beamline (the orange and green "plug").

The coordinate system of the detector has its origin at the nominal interaction point. The layout of a quadrant of CMS is shown in Fig. 3.7, with the subdetectors and important coordinates labeled. The beam line defines the z-axis, with the $x-y$ plane lying in the transverse direction. The r-direction indicates the distance from the z-axis, so this figure is a slice of CMS in the $r-z$ plane. The angular coordinate ϕ lies within transverse plane, while θ is the angle with respect to the beamline in the $r-z$ plane.

Pseudorapidity, η, is a very important coordinate in collider experiments. It is based on the lorentz-invariant quantity, rapidity,

$$y \;=\; \frac{1}{2}\,\ln\,\frac{E+p_z}{E-p_z}. \tag{3.5}$$

This definition of rapidity uses the z-components of particle momenta, such that the angle is being measured relative to the beam axis. Therefore, it represents the boost which translates from the lab frame to the frame where the particle momentum is perpendicular to the beam. The pseudorapidity is an approximation of this quantity, based on the angle θ,

$$\eta \;=\; -\ln\left(\tan\frac{\theta}{2}\right). \tag{3.6}$$

As seen in Fig. 3.7, η=0 is at 90°, and increases rapidly as it approaches the beamline. This is particularly useful for collider experiments since equal segments of η contain roughly

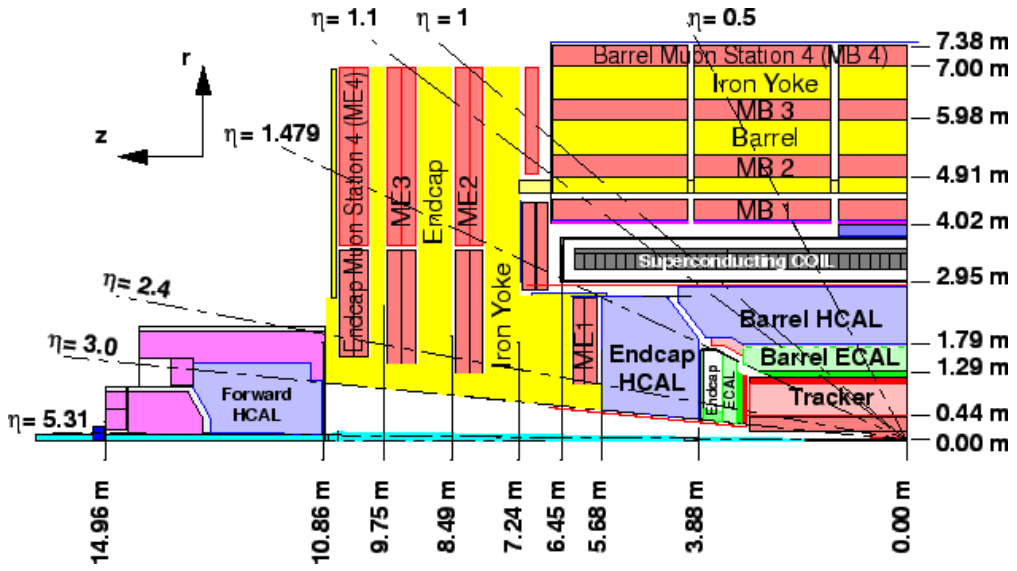

Figure 3.7: Schematic drawing of a quadrant of the CMS detector, in the $r - z$ plane, with important components and coordinates labeled. Image: CERN.

equal fluxes of outgoing particles from the interaction point. The forward regions of the detector, at high $|\eta|$, are affected by very large flux, and the central regions where $|\eta|$ is small have lower occupancy. This is an important consideration in detector design.

Detector components which wrap around the beampipe for a particular region in r are characterized by their "barrel" geometry. They measure the position of particles with low $|\eta|$. The "endcap" geometry describes subdetectors at particular regions in z, covering an area in the transverse plane. They are important for detecting forward particles, and in most cases, operate in a harsher radiation environment. The gaps between barrel and endcaps are carefully planned not to allow passage of particles along a given direction in η to go undetected. An end-on view of the CMS barrel is shown in Fig. 3.8, showing the concentric layers of subdetectors. Also in the figure is a photograph of the entire CMS

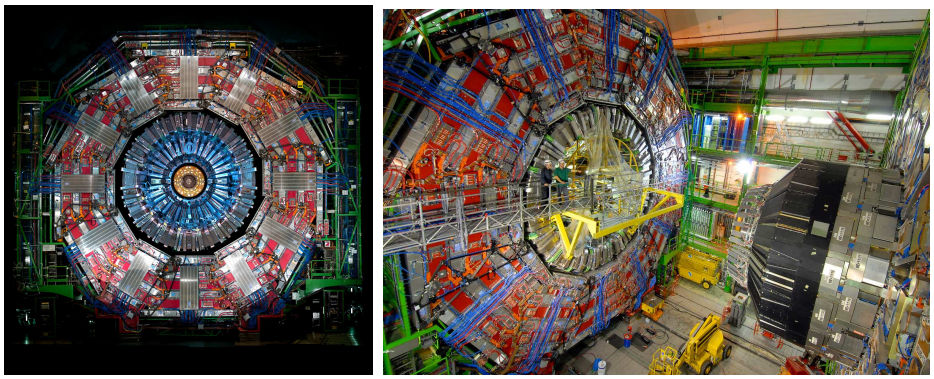

Figure 3.8: View inside the CMS detector during installation. An end-on view of the barrel, showing the layers of subdetectors (left), and the installation of the endcap, with the forward portion of the calorimeter visible. Photos: CERN.

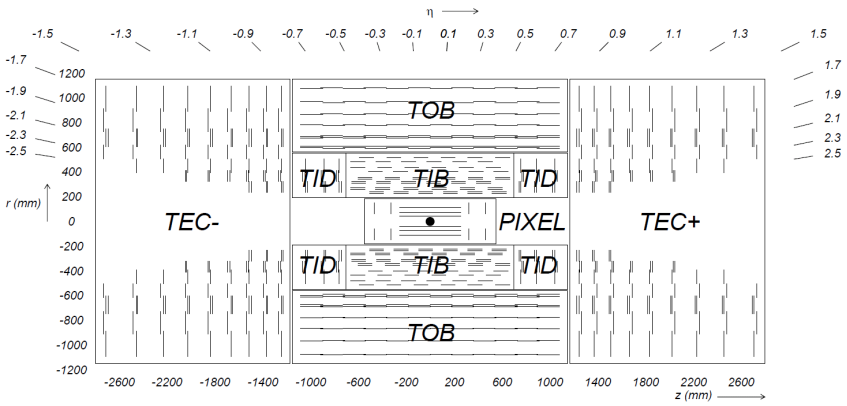

Figure 3.9: Diagram of the silicon tracking system in the $r - z$ plane. The pixels are at the center, closest to the interaction region. The strips comprise the majority of the tracker, with inner (TIB and TID) and outer (TOB and TEC) regions [4].

endcap being moved into position in front of the barrel. Only the calorimeter "plug" is visible, which will fit inside the grey solenoid, with the massive red iron disk barely in view. The following sections describe the subdetector systems of CMS, starting with the components closest to the beampipe.

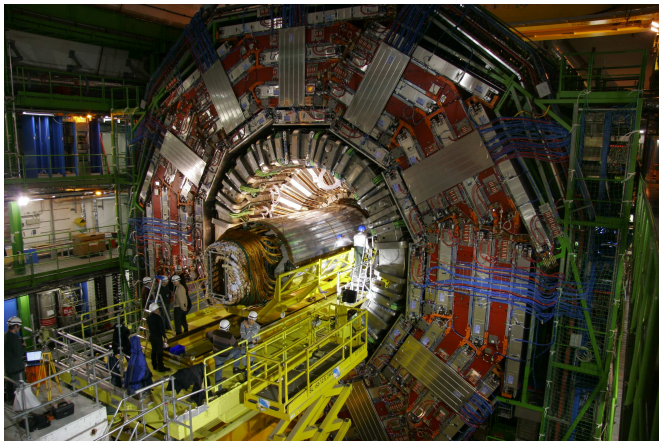

Figure 3.10: Insertion of the tracking system into the center of the detector. Photo: CERN.

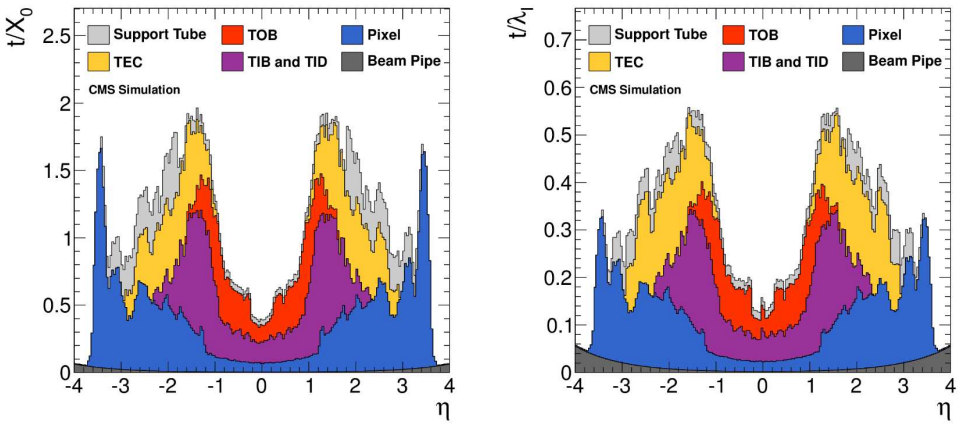

(a) Radiation lengths.

(b) Interaction lengths.

Figure 3.11: Thickness of the tracker in terms of energy loss, for electromagnetic (left) and hadronic (right) interactions [4].

3.2.1 Inner Tracker

The inner tracker is the first layer of active material encountered by particles from the interaction point. Figure 3.10 shows the insertion of the full tracker assembly into the center of the CMS barrel. It is designed for the precise and efficient measurement of the trajectories of charged particles and of the position of primary and secondary vertices.

The physical layout of the tracker in the $\eta - z$ plane is shown in Fig. 3.9. The tracker is a cylindrically-shaped assembly 5.8 meters long and 2.5 meters in diameter, with the silicon pixel detector at its core. Surrounding the pixels are layers of silicon strips, arranged in an inner barrel and disks (TIB, TID) and outer barrel and endcaps (TOB, TEC). The performance of these separate trackers are described below. The entire subsystem is composed of a total of 200 m^2 of silicon, making it the largest silicon tracker ever built. The silicon semiconductor releases electron-hole pairs when traversed by a charged particle. An electric field causes them to drift in opposite directions. The silicon is doped in such a way that once the charge threshold on the surface is reached, an analog signal transmits the amplitude and location of the hit.

The inner tracker is designed for optimum performance in a very harsh environment, where the instantaneous luminosity at almost 10^{34} $cm^{-2}s^{-1}$ produces an average of 20 proton-on-proton interactions at every bunch crossing. To operate in this high flux, the tracker material needs fine granularity, and fast response. Since a very large number of channels are needed, it needs a large number of on-detector electronics which in turn requires efficient cooling and support structures, while limiting the amount of non-sensitive material

which would produce multiple-scattering. Figure 3.11 shows the amount of material in the tracker in terms of how it effects passing particles. As the number of radiation lengths increases, so does the probability for Coulomb scattering, as well as bremmstrahlung and electron-positron pair production. More interaction lengths correspond to a higher probability of hadrons to scatter off nuclei in the material.

The occurence of bremsstrahlung, photon conversion, and nuclear interactions all create a harsh environment for the silicon. Additionally, neutrons backscattered from hadronic interactions in the electromagnetic calorimeter can contribute to the flux of particles in the outer layers of the tracker. Secondly, damage to the electronics can occur when positive holes from the passage of an ionizing paricle get trapped in the silicon oxide layer. Non-ionizing energy can create damage to the silicon bulk by creating additional energy levels in the band gap, leading to an increase in the leakage current and additional trapping centers that both reduce the signal and can lead to dangerous overheating. Finally, ionizing particles passing through electronic circuitry can affect the read-out, an occurance called a *single event upset*.

The performance of the inner tracker during the 2012 data-taking period was very good. During this period, 96.3% of the pixels and 97.5% of the strips were fully operational. Together, they demonstrate a very high tracking efficiency, >99.5%. This was measured with $Z \rightarrow \mu\mu$ events, in events with an average of 20 primary vertices.

Table 3.4: Tracker geometry and performance [16].

	Pixels	Strips
$\|\eta\|$ coverage	<2.5	<2.5
Location in r	4.4 – 10.2 cm	20 – 110 cm
Location in $\pm z$	<46.5 cm	<280 cm
Spatial resolution	9.4 μm	13 – 55 μm
Number of channels	66 $\times 10^6$	9.3 $\times 10^6$

Figure 3.12: Installing the pixel detector into the center of the tracker assembly. Photos: CERN.

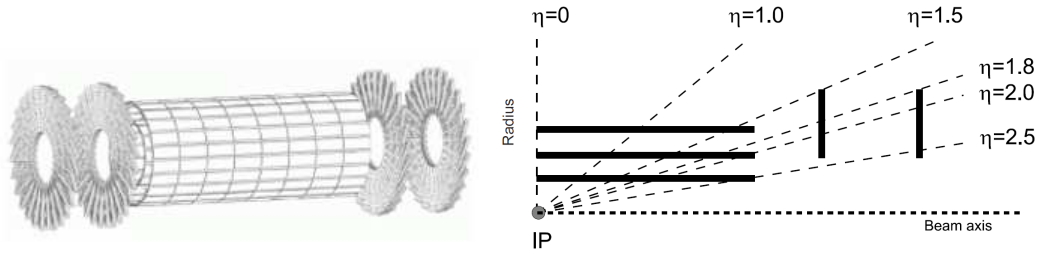

Figure 3.13: Schematic diagrams of the silicon pixel subdetector. A 3-dimensional view from the outside (left) and the locations of the layers and disks for a quadrant in the $r-z$ plane (right). Images: CERN.

Pixel Detector

Since the pixel detector is the closest to the interaction region, it is the most important for measuring the primary and secondary vertices, and for associating particles to the correct one. The pixel detector is used to form seed tracks for the reconstruction of complete trajectories in the tracker, as well as for high-level triggering. Fig. 3.12 is a photograph of a portion of the pixel barrel and disks modules being inserted into the tracker assembly.

Figure 3.13 shows a three-dimensial exploded view of the outside of the sensitive material, showing the geometry of the barrel and endcaps. The three barrel layers and two disks at each end have the measurements listed in Table 3.4. A quadrant of the subdetector showing the positions of these elements in the $r - z$ is shown in Fig. 3.13. For almost the full range in η, particles pass through at least three pixel modules. Combined, these layers and disks cover an area of 1.1 m^2, totalling about 66 million pixels.

The silicon pixels are n^+ doped pixels, 100×150 μm in size, and are implanted in n-type bulk with p-type backing underneath. Signal charge is read-out as an analog pulse, and along with the charge-sharing between pixels, interpolating between them allows good signal to noise separation and discrimination between large hit clusters and overlapping tracks. As a result, while the pitch is about $10\times$ larger, resolution down to $\sim$10 μm is achieved. Read-out chips located on the detector amplify the signal, check the Level-1 trigger, send out hit information, and are responsible for adjusting various operating parameters such as voltages and currents.

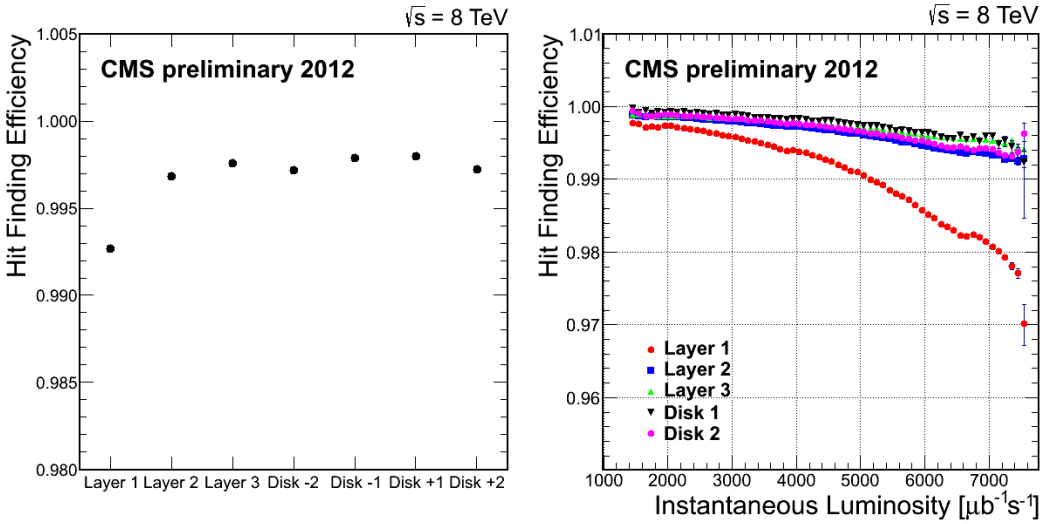

(a) Efficiency with respect to module.

(b) Efficiency with respect to luminosity.

Figure 3.14: Efficiency of finding hits in the pixel detector according to module and instantaneous luminosity [5].

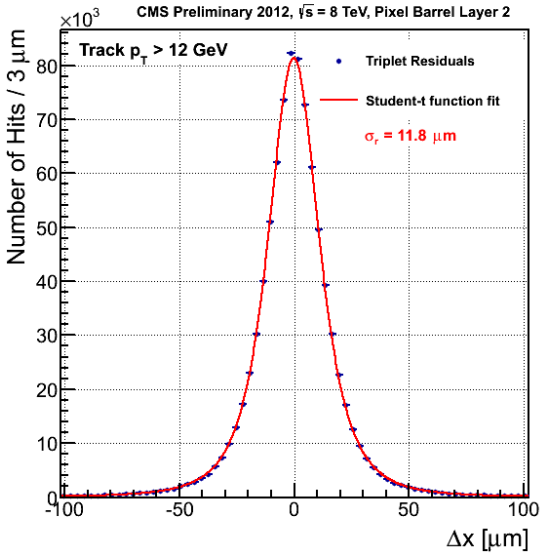

Figure 3.15: Spatial resolution of hits in the pixel detector, for the second barrel layer [5].

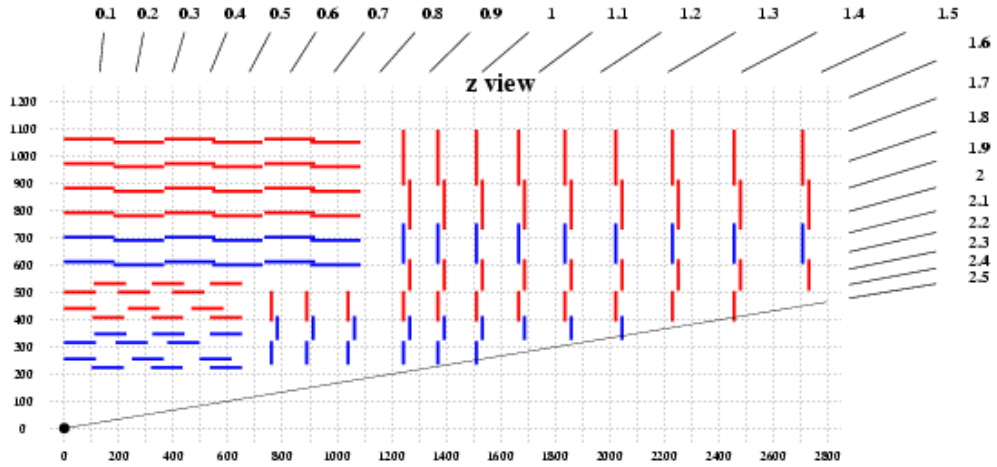

Figure 3.16: Schematic diagram of the silicon strip subdetector, showing the locations of the barrel and endcap modules for a quadrant in the $r - z$ plane. Image: CERN.

The efficiency of detecting a hit on the pixels is given in Fig.3.14. It is calculated by taking the trajectory determined from two or more layers/disks, and predicting the position of a hit on another module. If a hit is found within 500 μm of the prediction, it is counted as a successful detection. Figure 3.14 shows the efficiency of the three layers and four disks, as well as how it changes with increasing instantaneous luminosity. As the occupancy of the pixels increases, the efficiency of finding a particular hit decreases, especially in the innermost layer. The hit efficiency for all active modules is above 99%. The pixels achieve excellent track resolution in both the $r - \phi$ and z-directions, shown for the second layer in the barrel in Fig. 3.15.

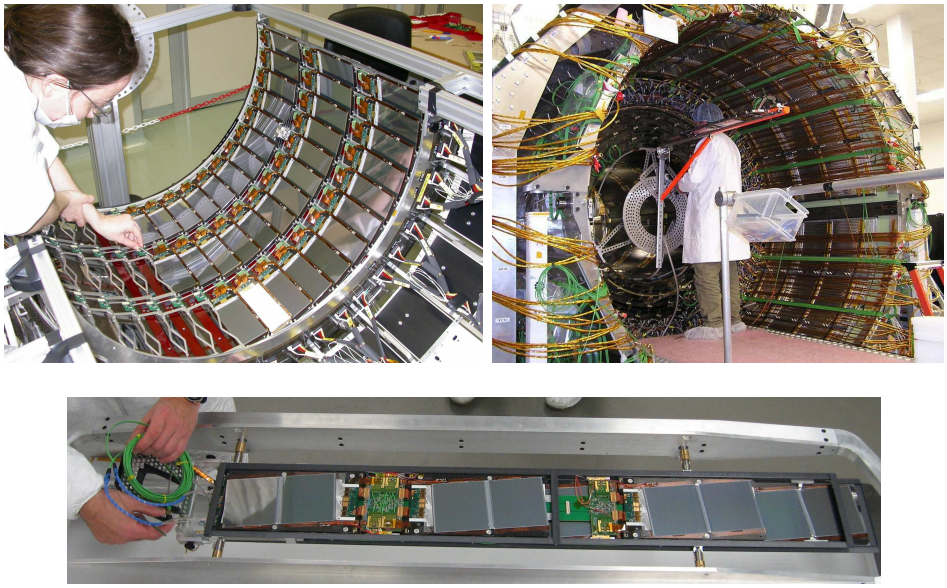

Figure 3.17: Inner (top left) and outer (top right) barrels of silicon strips. To assemble the barrel, modules are mounted on rods (bottom). Photos: CERN.

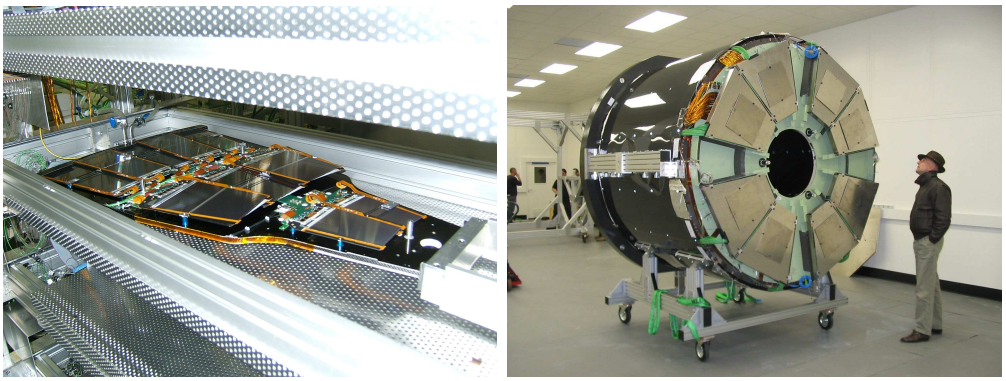

Figure 3.18: Endcap silicon strip modules mounted on petals for disks and endcaps (left), and a complete outer tracker endcap (right). Photos: CERN.

Silicon Strip Tracker

Surrounding the silicon pixels is the silicon strip tracker, which operates in a similar, but more cost-effective way. The layout of a quadrant of this subdetector in the $r - z$ plane is shown in Fig. 3.16. Ten layers of overlapping silicon sensors make up the cylindrical barrel out to a radius 1.1 meters from the beamline, four in the inner region, and six in the outer region. Endcap layers on each end of the barrel extend to the highest possible η, providing nearly hermetic coverage.

To give a sense of scale, Fig. 3.17 and Fig. 3.18 show photographs of the inner and outer silicon strip assemblies. The former shows the production and installation installation of the smaller inner barrel and larger outer barrel. Modules in the barrel are mounted on rods, as shown in the photograph. The endcaps require a very different geometry, and modules are mounted on petals as shown in Fig. 3.18. These are used to form disks that make up the endcaps, and one of the two large outer endcaps (TEC) is shown as well.

The entire subdetector comprises 9.6×10^6 p^+ strips implanted in the n-type bulk with an n-type backside. Depending on location, the pitch varies from 80 μm to 205 μm. The strips are aligned with a relative angle of 100 mrad between them, to aid in the three-dimensional measurement.

The hit finding efficiency is measured by taking hit in multiple silicon strip layers, and observing if a hit is recorded in an expected module. This is shown for each module in Fig 3.19, taken from 2011 data. Among operational elements, the efficiency is above 99%.

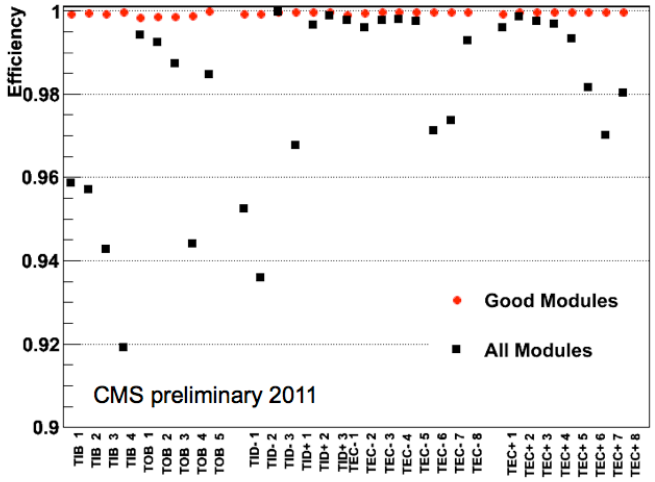

Figure 3.19: Efficiency of the silicon strip subdetector with respect to module.

Hadrons from the interaction region or backscattered off the electromagnetic calorimeter cause radiation damage to the silicon tracker. The radiation causes leakage current, leading to noise and excess heat, which lowers the efficiency of charge collection on the strips. To counter this, a cryogenic system circulates nitrogen gas to keep the entire subsystem at a temperature of –24 C. The full volume of the tracker subsystem, 25 m^3, is circulated every hour. While efficient systems for cooling, powering, and supporting the tracker are crucial, the position resolution of the pixel and strip sensors are degraded by the multiple scattering of hadrons off these inactive materials. In addition, the photon conversion and bremming from multiple scattering can enter the electromagnetic calorimeter. The detector support structure is designed to be light and minimal to reduce this effect.

3.2.2 Electromagnetic Calorimeter

Like most general-purpose detectors for collider experiments, CMS uses an electromagnetic calorimeter to efficiently capture and measure the energy from charged particles and photons from the interaction point. To achieve this, a hermetic, homogenous medium

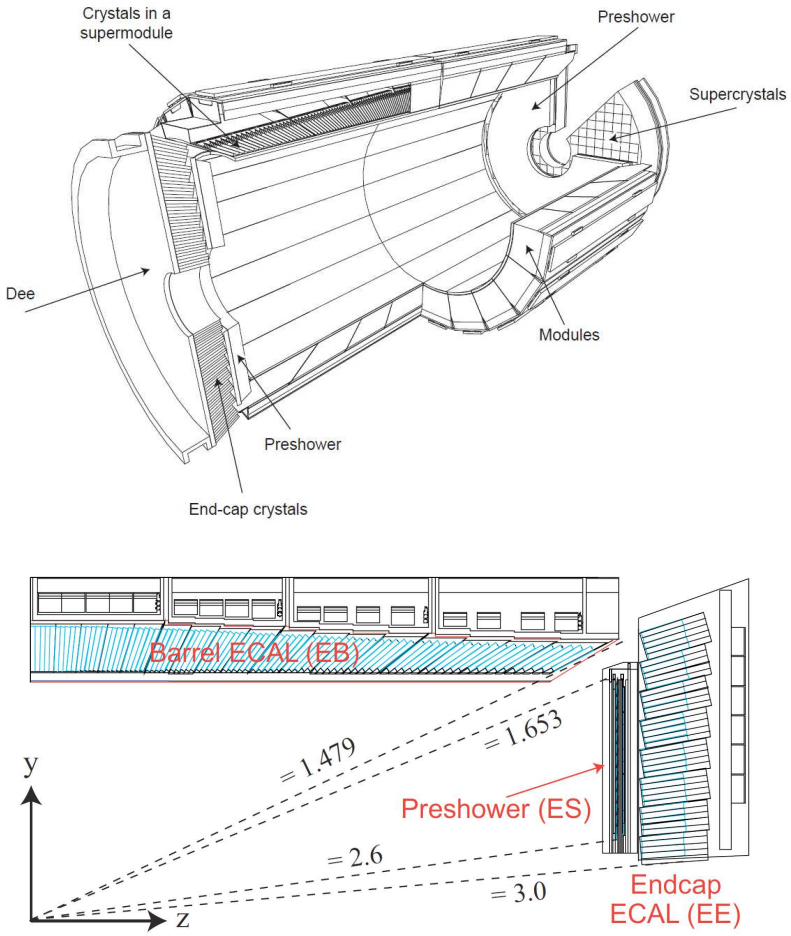

Figure 3.20: A 3-dimensional exploded view of the electromagnetic calorimeter (top), and a quadrant of the subdetector in the $r - z$ plane (bottom). Images: CERN.

Table 3.5: Electromagnetic calorimeter geometry and performance. Position resolution is calculated from electrons including information from tracker [16].

	Barrel	Endcap	Preshower
$\|\eta\|$ coverage	<1.479	1.479 – 3.0	1.653 – 2.6
Location in r	1.29 – 1.77 m	<1.77 m	<1.29 m
Location in $\|z\|$	<3.0 m	3.14 – 3.88 m	3.0 – 3.14 m
Radiation lengths	25.8 X_0	24.7 X_0	3.0 X_0
$\Delta\phi$ resolution	3 mrad	5 mrad	
$\Delta\eta$ resolution	1×10^{-3}	2×10^{-3}	
Timing resolution	0.2 ns	0.3 ns	

of high-density scintillating material is required. Lead tungstate crystals were chosen for their fine granularity and radiation resistance, and the light induced by the crystals are collected by photodetectors. Figure 3.20 has two views of the electromagnetic calorimeter, showing the locations of the barrel, endcap, and preshower components. The geometric properties and performance of these components are shown in Table 3.5.

Both the number of photons emitted by the crystals and the amplification of the photodiodes are temperature dependent, getting less efficient at lower temperatures. The cooling system needed to extract heat from the readout electronics must therefore maintain a very precise balance within 0.05 C. Furthermore, there are 1 – 2 radiation lengths of material in front of the electromagnetic calorimeter, due to the silicon tracker

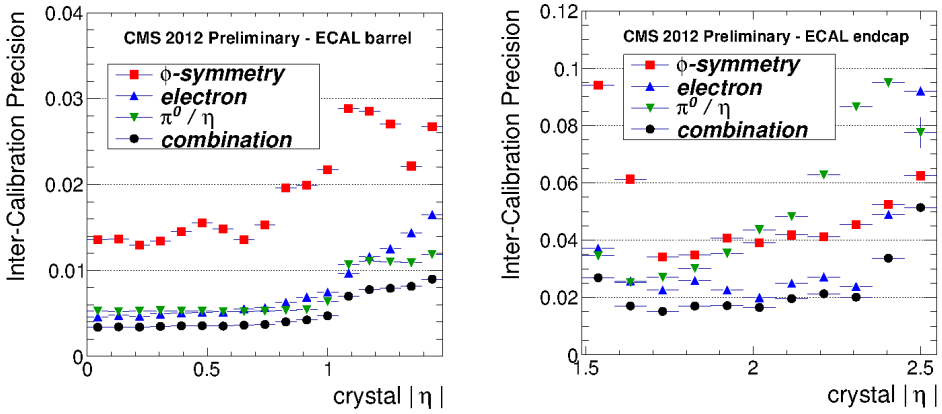

(a) Precision in barrel.

(b) Precision in endcap.

Figure 3.21: Uncertainty of main calibrations of the electromagnetic calorimeter with respect to $|\eta|$ [6].

and its structural support. This causes multiple scattering which degrades the performance of the calorimeter.

The energy resolution of the electromagnetic calorimeter is parameterized by three terms as described by

$$\begin{aligned} \frac{\sigma(E)}{E} &= \frac{S}{\sqrt{E}} \oplus \frac{N}{E} \oplus C \\ &= \frac{2.8\%}{\sqrt{E}} \oplus \frac{12.8\%}{E} \oplus 0.3\%. \end{aligned} \tag{3.7}$$

The three components are a stochastic term, a noise term, and a constant. The stochastic term includes event-to-event fluctuations in shower containment, noise from the process of increasing gain in the photodetectors, and fluctuations in the energy deposited in the preshower. The noise term considers all effects from from electronics, digitization, and pileup. The constant term takes into account the non-uniformity of light collection, calibration errors, and leakage of energy from the back of the crystal. The values for each were

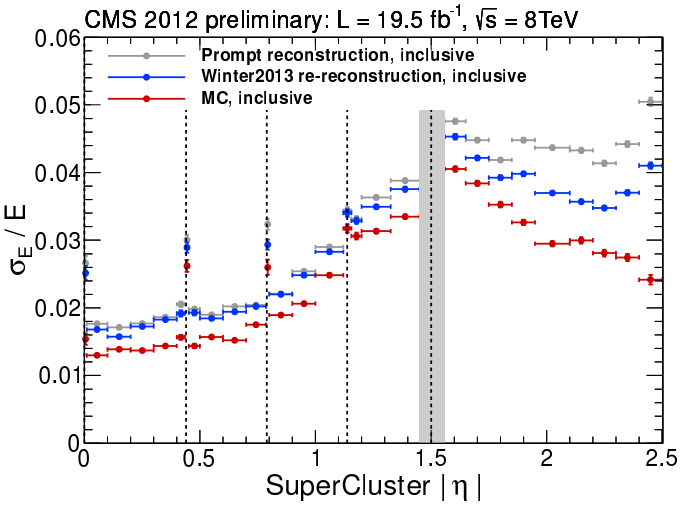

Figure 3.22: Resolution of the energy measurement in the electromagnetic calorimeter, measured from electrons from W and Z bosons, in 2012 data without (gray) and with (blue) calibrations applied [6].

measured under ideal conditions with a test beam. Additional calibrations to account for several different effects are performed on the calorimeter measurements, which contribute to the uncertainty of the energy measurement.

Figure 3.21 shows the precision of three major inter-calibration constants determined from three procedures in 2012. They are shown with respect to the absolute value of pseudorapidity for the barrel and endcaps separately. The first accounts for the ϕ-symmetry expected for a given value of η. Next, energy deposits from isolated electrons from W and Z boson decay can be compared with the measured values in the tracker. Also shown is the calibration obtained from measuring the π^0 and η invariant mass. Figure 3.22 shows the energy resolution measurement with respect to $|\eta|$ without and with the calibration corrections applied to data. With these corrections, the resolution improves significantly, especially in the endcaps, to a total resolution from 2 – 5%.

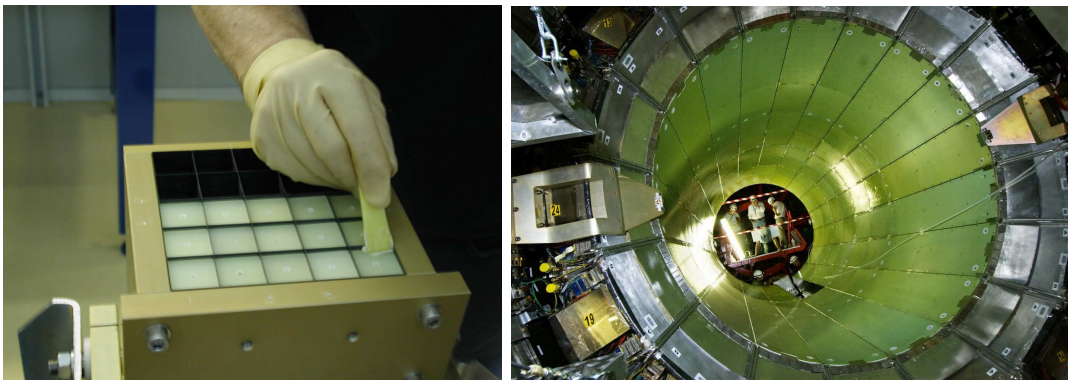

Figure 3.23: Assembling a crystal supercluster for the endcap (left) and installing the barrel of the electromagnetic calorimeter (right). Photos: CERN.

Lead Tungstate Crystals

The scintillating material of the electromagnetic calorimeter comprises 61,200 lead tungstate crystals in the central barrel, and 7,324 crystals in each endcap. A single crystal with photo detector attached is shown in Fig 3.24, along with a visualization of an electromagnetic shower induced by the crystals. They are read out in groups of 5×5, called *towers*. Each cell is mounted at a quasi-projective angle, offset by 2-8 degrees from with respect to the beamspot, to prevent the occurence of particles slipping through cracks between the towers. Each crystal in the barrel is actually shaped as a truncated pyramid, having a smaller face in front. This translates to a granularity of 0.0174×0.0174 radians^2 in the $\eta - \phi$ directions.

The choice of scintillating material allows the electromagnetic calorimeter to be quite compact. This is due to the high density (8.28 g/ cm^3) and short radiation length (0.89 g/ cm^2) of this material. Each crystal has a length of 220 or 230 mm, corresponding to 24.7 and 25.8 radiation lengths for the endcap and barrel, respectively. An endcap tower is being

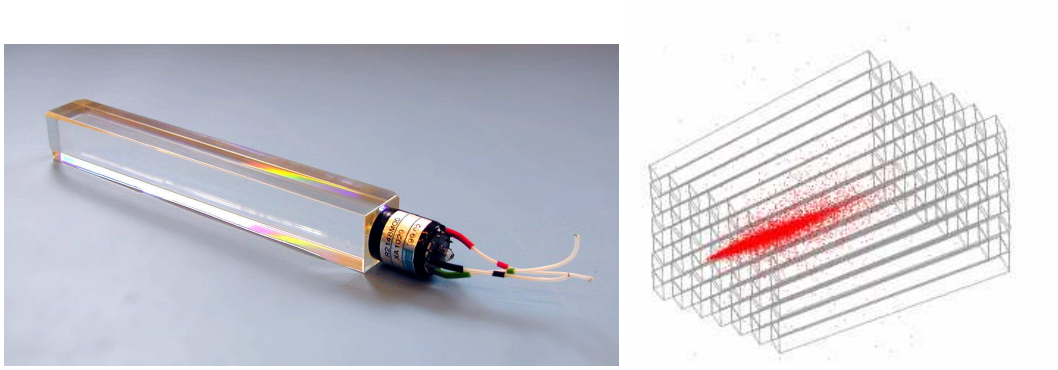

Figure 3.24: Lead tungstate crystal with attached photodetector (left), and a visualization of energy deposits amoung crystals in the electromagnetic calorimeter (right). Images: CERN.

assembled in Fig. 3.23(a). Figure 3.23(b) is a view inside the electromagnetic calorimeter barrel, lined with crystals.

The crystals are mass-produced efficiently to be fast, optically clear, and radiation tolerant. The length of the scintillation decay time is crucial since the LHC bunch crossings will occur as closely as 25 ns apart after the long shutdown (LS1). Within this period of time, the crystals transmit ∼80% of the light signal to the photodetectors. The crystals are carefully polished for total internal reflection and optimal light collection at the photodetectors. Ionizing radiation produces oxygen vacancy impurities in the lattice, causing a wavelength-dependent loss of transparency. However, this effect is characterized and accounted for during running.

Avalanche photodiodes

Light from the lead tungstate crystals is transmitted to photodetectors, the surfaces of which are silicon semiconductors, designed to be fast and radiation tolerant. Due

Figure 3.25: The preshower detector, to be installed in front of the crystals in the electromagnetic calorimeter endcap. Photo: CERN.

to the low light yield of crystals, the diodes must amplify the signal, while being insensitive to the effects of particles transversing them. In the barrel, the photodiodes provide a gain of 50, and are mounted in pairs for each cell, as seen in Fig. 3.24. Endcap phototriodes operating in the higher flux environment provide a factor of 5 less gain. The amplification is affected by temperature, voltage, and direct ionization within the electronics.

Preshower Detector

The preshower detector is an important addition to the electromagnetic calorimeter. It has two locations at the front of each calorimeter endcap, as shown in the diagrams of Fig. 3.20. A photograph of a complete preshower disk is shown in Fig. 3.25. Each disk is composed of two layers of lead and silicon strips. It helps to identify electrons and photons in the range $1.653 < |\eta| < 2.6$. For example, a forward π^0 can decay to two photons with very minimal angular separation that could mimic a single photon. The lead layer causes showering, and the particularly fine granularity of the silicon sensors (with respect to the

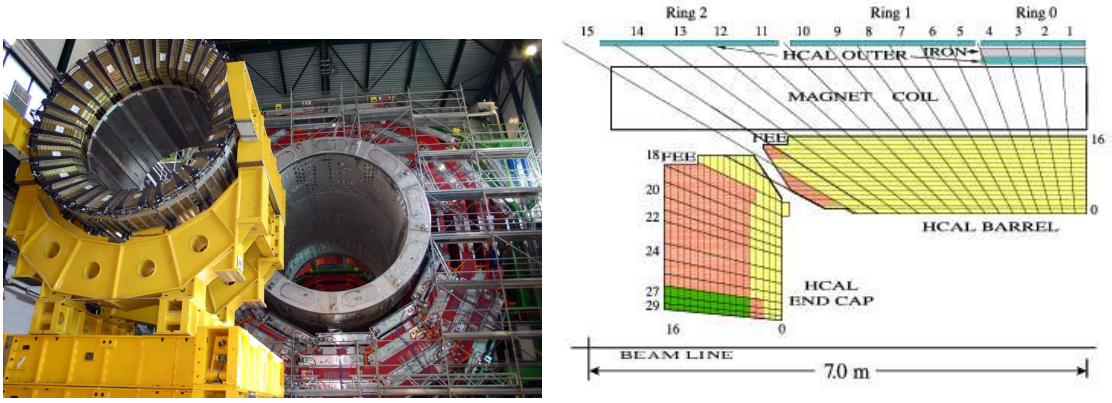

Figure 3.26: Installating the hadronic calorimeter inside the solenoid, showing the gold-colored lead absorbers (left). A diagram of a quadrant of the hadronic calorimeter in the $r - z$ plane, showing the barrel and endcap inside the solenoid, and the outer calorimeter (in blue) outside (right). Images: CERN.

endcap crystals) allows these photons to be distinguished. The preshower is very effective, causing ∼95% of photons to begin showering before reaching the second layer of silicon.

3.2.3 Hadron Calorimeter

As with all hadronic calorimeters, the purpose of this component of CMS is to efficiently contain hadronic showers and measure their energies. A very dense material is used, causing passing hadrons to interact with its nuclei. This absorbs energy and induces particle showering. Layers of the absorber are interspersed with active scintillating material and fibers, which transmits the light for readout. This type of design is often called a sampling calorimeter, since not all of the energy is deposited in active material, as opposed to the homogenous material in the electromagnetic calorimeter.

With a total thickness of 10.6 – 11.8 interaction lengths, the entirety of the calorimeter system is successful in stopping the vast majority of particles from the inter-

Table 3.6: Hadronic calorimeter geometry and performance. Interaction lengths are calculated for electromagnetic and hadronic calorimeters combined [16].

$\|\eta\|$ coverage	<3
Location in r	1.81 – 2.9 m (HB), $<$2.9 m (HE)
Location in z	$<$4.33 m (HB), 3.9 – 5.68 m (HE)
Interaction lengths	10.6 – 11.8
$\Delta\phi$ resolution	10 mrad
$\Delta\theta$ resolution	30 mrad

action region. The granularity of the hadronic calorimeter provides an angular resolution of $\sim$10 mrad in the ϕ-direction, and $\sim$30 mrad in the η-direction, for showers of at least 100 GeV. The calorimeter is calibrated with LEDs to measure the gain and ϕ-symmetery corrections of the detector. Energy from particle showers across both calorimeters is interpreted by sophisticated algorithms which associate the response of groups of cells with the passage of a particle. Therefore, the resolution and efficiency of reconstructing particles from the calorimeter system depends on the algorithm used. This is discussed in Sec. 3.3. Each component of the hadronic calorimeter is designed for the particular geometric region it covers, in order to prevent leakage of particles in the most vulnerable areas. Some properties are listed in Table 3.6

The photograph and diagram shown in Fig. 3.26 show the size and layout of most of the hadronic calorimeter. The barrel (HB) and endcap (HE) are the final active detector components within the solenoid. However, a narrow layer of calorimetry lines the outside

of the solenoid, called the outer hadronic calorimeter, and an additional component, the forward hadronic calorimeter, is located far down the beam pipe, as shown in Fig. 3.7.

Barrel

The barrel region of the hadronic calorimeter is constrained by the outer radius of the electromagnetic calorimeter, at 1.77 meters, and the inner radius of the solenoid magnet, at 2.95 meters. The absorber material is 40 mm of steel plate, followed by eight layers of 50.5 mm brass plates and a final 75 mm steel plate. This system has a total thickness of 5.8 to 10.6 interaction lengths, depending upon η. Sandwiched between the absorbers are 70,000 plastic scintillator sampling tiles. Wavelength-shifting fibers, embedded in the tiles, carry the light signal to photodiodes for read-out. This subdetector covers up to an $|\eta|$ of 1.3, with no projective gaps of dead material.

Endcap

Extending to $1.3 < |\eta| < 3.0$, the endcap region of the hadronic calorimeter is responsible for stopping about one third of the final state particles from collisions. Like the barrel region, it is composed of brass and scintillator layers to sample the energy deposits, staggered in such a way to be hermetic. Along with the purpose of sampling energy, the hadronic calorimeter endcap adds important absorber material to minimize the cracks between the barrel and endcap, to reduce the leakage of particles. Including the electromagnetic calorimeter in front of it, its thickness is at least 10 interaction lengths over its η range.

Outer Calorimeter

In the central region of the detector, the combination of the electromagnetic and hadron calorimeters are not sufficient to adequately contain hadronic showers. Therefore, an outer hadron calorimeter was installed outside the solenoid magnet, within the first layer of the iron yoke, as shown in Fig. 3.26. It uses the solenoid itself as an additional absorber. A layer of scintillator and wavelength-shifting fibers, common to the rest of the hadronic calorimeter, determines the energy of showers being stopped in this material. Even though the outer calorimeter is very limited in radial size, it is crucial for stopping leakage of particles that might otherwise contribute to a mismeasurement of energy.

With this additional material, the total depth of calorimeter in the barrel region is about 11.8 interaction lengths. The coverage of active material is broken in some places by steel beams holding up the iron barrel rings, cryogenics, powercables and other necessary service components. The outer calorimeter was found to have an excellent reconstruction efficency of $\sim$99.3%, as measured with cosmic muons.

Forward Calorimeter

Special care is taken in the design of the forward hadronic calorimeter, to measure the tremendous particle flux at the highest rapidities. It is located 11.2 meters away from the interaction region, in the z-direction. Quartz fibers are chosen as the active medium because they are resistant to the high radiation environment. The electromagnetic component of incident showers produces Cherenkov light in the quartz, of which a small fraction is col-

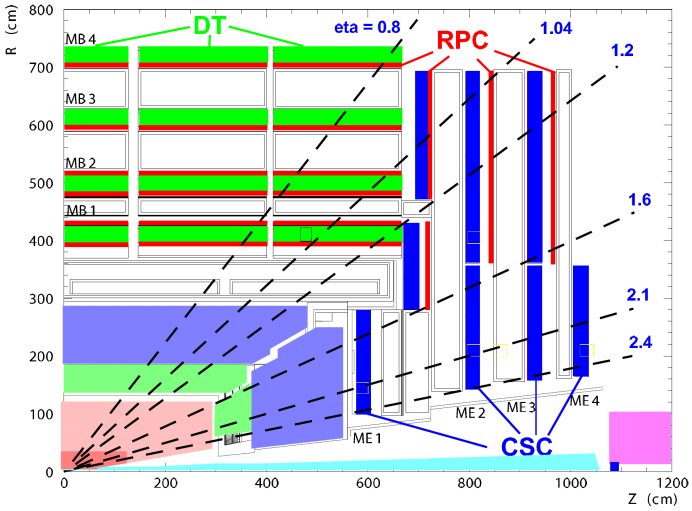

Figure 3.27: Schematic diagram of a quadrant of the CMS muon system, in the $r-z$ plane. The location of gas chamber assemblies are shown in the barrel are green (drift tubes), and blue in the endcap (cathode strip chambers). Interspersed between them are resistive plate chambers (in red) and white space where the iron yoke is located. Image: CERN.

lected. Some amount of disambiguation between particles is achieved because electrons and photons deposit most of their energy within the first 22 cm, whereas hadronic showers are more evenly distributed in the longitudinal direction. These particles are stopped with steel absorbers, 5 mm thick. The entire subsystem is housed in twin radiation-shielded cases of steel and concrete, to protect the read-out photomultipliers and front-end electronics from neutrons and other low energy particles saturating the area around the beampipe.

3.2.4 Muon System

Muon detection is a key focus of the CMS experiment. Muons are convenient objects to study because they are less affected by radiative losses in the detector materials than electrons are, providing the best mass resolution for the parent particle. The system

goals are muon identification, momentum measurement, and triggering. The momentum measurement is aided by the high-field magnet and the return yoke iron, which doubles as a hadron absorber to aid in muon identification.

The muon detector design is mostly based on the typical ionizing gas chamber. Individual cells are filled with gas and permeated by an electric field created by anode wires down the center and cathode strips along the walls of the cell. A passing muon ionizes the gas, and electron-positron pairs drift to the appropriate surface from which the signal is transmitted. Depending on the geometry and layout of the chambers, this can provide 2- or 3-dimensional position measurements as well as timing measurements.

The muon system is separated into two distinct regions, using three types of particle detection strategies to achieve all the system's goals. Figure 3.27 is a diagram of a quadrant of the system. The barrel region consists of five rings of detectors on the iron yoke surrounding the solenoid and covering $|\eta| < 1.2$. In this area, the hadronic background and muon rates are both low, and the field from the solenoid are uniform and low (<0.4 T). Here, drift tube chambers are used, as described below. Covering the endcaps of calorimeter and adjacent to the solenoid are the disk-shaped end-cap muon subsystem, which is also sandwiched between layers of iron. This is a much more complicated measurement environment at a high $|\eta|$, where background and muon rates are high, and the magnetic field is large and non-uniform. The cathode strip chambers here must provide a fast response time, fine segmentation, and radiation hardness. Combined, the barrel and endcap subsystems cover $|\eta| < 2.4$ with no gaps. A station is an assembly of chambers around a fixed r (in

the barrel) or z (for the endcaps) location. There are four stations in the barrel, forming concentric rings in each of the 5 wheels, and four stations in each endcap, forming layers of disks, as shown in Fig. 3.27.

Hadron *punch-through* occurs when colored particles are not contained by the calorimeter. This is negligible in CMS because there is a distance of 16 interaction lengths (including the solenoid magnet) of material in front of the muon system. However, multiple scattering in front of the muon system affects the momentum resolution, so tracks in the muon system are matched to those in the tracker, which provides the best momentum measurement. An important feature of the drift tubes and cathode strip chambers is that they can trigger on the transverse momentum of muons independently of the rest of the detector. In addition, the resistive plate chambers provide a complementary triggering system of an independent, fast trigger on even low momentum muons that do not reach the outer layers.

Table 3.7 lists the properties of each type of muon chamber. Overall, the efficiency for reconstructing hits and tracks within the muon system is 95–98%.

Drift Tubes

The central region of the muon system uses five massive iron rings from the magnetic flux return as a support structure. As illustrated in Fig. 3.28(a), each wheel contains 4 concentric layers (or stations) of 12 drift tube chambers. Each chamber contains 12 layers of individual drift tubes: 8 layers measuring position in the bending plane (in $r - \phi$) and 4 layers in the longitudinal plane (for the $r - z$ coordinate). Each rectangular cell has has a

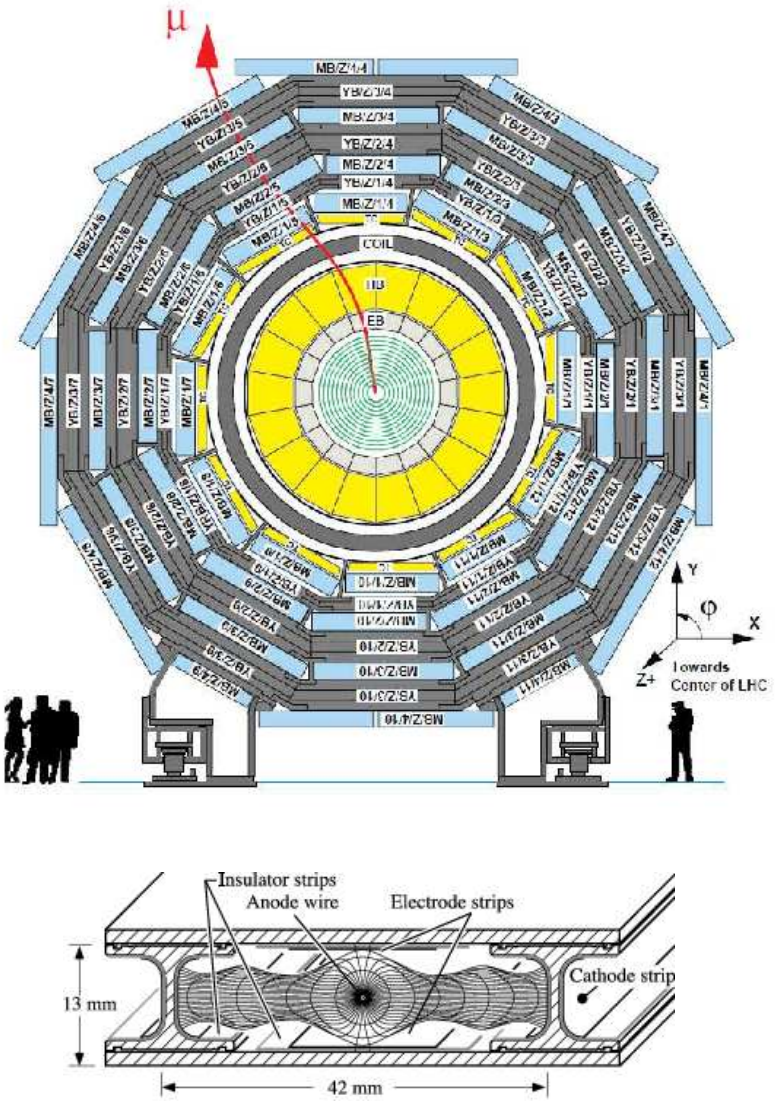

Figure 3.28: Diagrams of the drift tube chambers in the barrel of the muon system. A transverse view of the layout of a wheel in the barrel (top), shows the arrangement of drift tube chambers (blue) on the iron yoke (gray). Below, a cross-sectional view of a drift tube cell shows the important components and electric field lines. Images: CERN.

Table 3.7: Muon system geometry and performance [16].

	DTs	CSCs	RPCs
$\|\eta\|$ coverage	<1.2	0.9 – 2.4	
Location in r	400 – 730 m	<730 m	
Location in $\|z\|$	<650 m	5.6 – 10.6 m	
Spatial resolution	80 – 120 μm	40 – 150 μm	0.8 – 1.2 cm
Number of chambers	250	540	610

cross-section of 13×42 mm, and is up to 2.4 meters long. Lining the cells are 5 electrodes, 2 field shaping strips, and 2 cathode strips, threaded down the center by an anode wire. Figure 3.28(b) shows a single cell lined with strips and threaded with an anode wire.

The timing resolution of the drift tubes is a few ns, which can efficiently match the muon to the appropriate bunch crossing, but is delayed by the drift time of the electrons and positrons through the gas. The maximum drift path is 21 mm, taking up to 400 ns to deposit the charge on the anode and cathodes. The drift time is affected by the size of the tube, the electric field, and the properties of the gas filling the chambers. For accurate timing, the electric field within the cells is carefully shaped to have a drift time linear with the drift path. Each chamber is filled with a gas mixture 85% Ar and 15 %CO_2, chosen to allow fast drift speed of electrons produced from ionization.

Cells in the drift tube chambers are small enough to have negligible occupancy, but large enough to limit the number of active channels requiring read-out. Front end

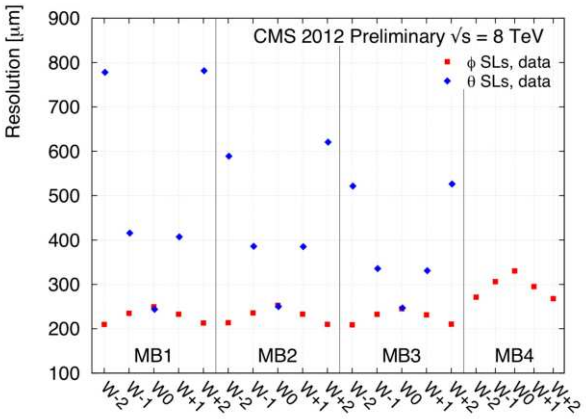

Figure 3.29: Spatial resolution of the muon system drift tube chambers in the ϕ (red) and θ (blue) directions, with respect to station.

electronics amplify signals produced by the detector, compare them with a threshold, and send the results to the trigger and read-out electronics.

Figure 3.29 shows the resolution measurement of the drift chambers from 2012 data, according to the station. The four MB layers are at increasing r location, starting closest to the beam line, and the 5 W locations indicate which of the 5 wheels (in the z-direction). Measurements from superlayers providing the θ measurement are in blue, and the much better ϕ measurement is in red.

Cathode Strip Chambers

The endcap of the muon system is made of large trapezoidal chambers each covering 10 or 20 degrees in ϕ, overlapping to provide continuous ϕ coverage. Redundacy in the muon system is important, so between $1.2< |\eta| <2.4$, a muon crosses 3 or 4 cathode strip chambers, and from $0.9< |\eta| <1.2$, a muon is detected by both drift tubes and cathode strip

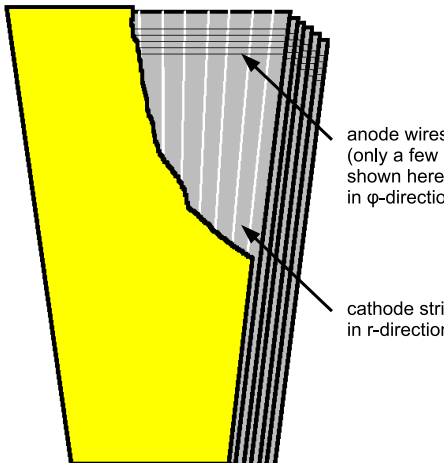

(a) Layout of a cathode strip chamber.

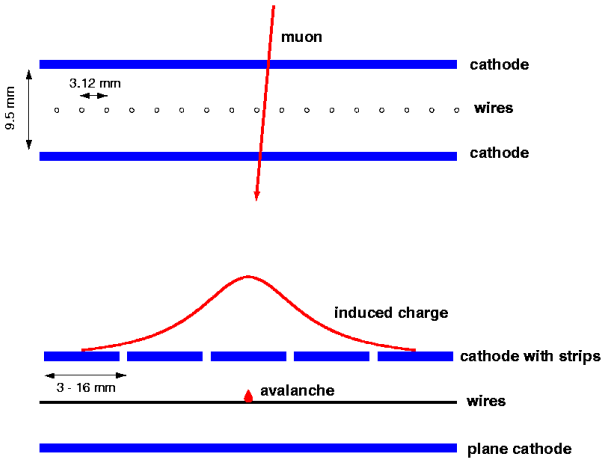

(b) Two views of the orthogonal cathode and wire planes.

Figure 3.30: Illustrations of the cathode strip chambers in the endcap of the muon system. The diagram of the cathode strip chamber (top) shows the layers of cathode strips in the r-direction. A few representative anode wires which lie between the layers in the ϕ-direction are also shown. The effect of a passing muon (bottom) causes an avalanche of charge on the wire, as well as an induced charge across a few cathode strips. Images: CERN.

chambers. As seen in Fig. 3.27, the first station is located within the solenoid magnet, just behind the hadronic calorimeter endcap.

The cathode strip chambers are multiwire proportional chambers with 6 azimuthal anode wires (for ϕ measurement) interleaved among 7 cathode panels arranged lengthwise at constant a constant $\Delta\phi$ width. This layout is shown in Fig. 3.30(a). The position along the wires (ϕ) of a passing muon is obtained by interpolating charges induced on the strips. This is illustrated in Fig. 3.30(b), where a muon creates an avalanche of electrons at a particular location on the anode wire, as well as a mirror charge across a few cathode strips.

The largest chambers have gas volume more than 50 cubic meters, containing up to 2 million anode wires. In total, 220,000 cathode strip readout channels and 180,000 anode wire readout channels are used. The subsystem provides both precise muon momentum measurement and fast triggering in the challenging high rate environment and non-uniform magnetic field. Because of the higher occupancy at large $|\eta|$, the maximum drift time must be much shorter than that in the drift tubes in the barrel region. This reduction in the maximum drift time is achieved with a fast gas mixture (40% Ar, 50% CO_2, 10% CF_4) and shorter drift path. As a result, the maximum time for a drift charge to traverse a plane in a chamber is about 60 ns. In addition, the cathode strip chambers have very good timing resolution of $\sim$5 ns. In early tests using cosmic rays, the hit and track reconstruction efficiency for these chambers were above 99%.

Resistive Plate Chambers

Figure 3.31 shows the double-gap RPC, where each gas gap is created using 2 mm thick resistive plates covered with a conductive coating. The passing muon ionizes both gas volumes, which is picked up by the readout strips shown. Layers of resistive plate

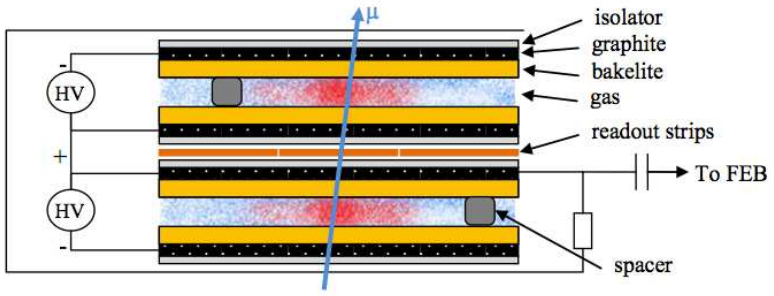

Figure 3.31: Diagram of a resistive plate chamber used throughout the muon system. A passing muon ionizes two layers of gas sandwiched between graphite plates. Image: CERN.

chambers are interspersed in the both the barrel and endcap of the muon system. They are gaseous parallel-plate detectors providing moderate spatial resolution with a time resolution comparable to what is achieved with scintillators. They are chosen because they can tag the timing of an ionizing particle with a resolution of 3 ns, which is much shorter than the designed bunch spacing of 25 ns. As a result, an independent bunch crossing assignment and momentum measurement for triggering is achieved.

As seen in Fig. 3.27, six layers of resistive plate chambers are embedded in the iron yoke of the detector barrel, two in the first and second stations, and one each in the third and fourth stations, for redundant measurement of low p_{T} muons. Here, readout strips are aligned with the beam direction, and each chamber has two or three layers of read-out. In the endcaps, the chambers are trapezoidal-shaped, arranged in 3 concentric rings in the $r - \phi$ direction. The efficiency for observing a hit in the RPCs is good, measured to be 95-98%.

3.2.5 Trigger and data acquisition

As discussed in Sec. 3.1, the LHC delivered proton-proton collisions to the center of the CMS detector at a rate of almost 500 MHz, corresponding to a peak instantaneous luminosity of 7.7×10^{33} $\mathrm{cm}^{-2}\,\mathrm{s}^{-1}$. It would be impossible to store full event information for every collision, since they occur too quickly to be processed, and would consume a tremendous amount of storage space. In fact, doing so would be undesirable, since the vast majority of collisions result from the protons only glancing past each other, with minimal energy transfer. These *minimum bias* events are of no use for studying rare or undiscovered processes. To quickly discard minimum bias events and store events with interesting properties, CMS uses a two-level trigger system for filtering the data during a run.

The Level 1 (L1) trigger is the first level of event filtering. The calculations are performed with custom-designed hardware processors. To keep up with the incoming data, they have only 3.2 μs to make a decision whether to keep an event or throw it away. Of the 3.2 μs, only 1 μs is actually used for processing, the rest is used for the data to be sent to and from the processor. To this end, the L1 trigger only uses information from the calorimeter and muon systems, which do not involve complex track reconstruction in the inner tracker, and uses simple algorithms to make the decision. During the high luminosity running of the LHC during 2012, the L1 trigger brought the event rate down to about 100 kHz.

The next level of event filtering is the High Level Trigger (HLT). Since it has a longer latency, more complicated algorithms can be run to determine if an event should be kept based on the value of one or more measurements in any of the detector subsystems. Based on which L1 conditions were satisfied, (for example, finding a track in the muon system or large amount of calorimeter energy) the algorithm follows a modular trigger *path*. The trigger path involves a sequence of reconstruction and filtering stages, which increase in complexity as they continue to be satisfied. If an event fails a filter, it is immediately thrown out of that particular trigger path, which is why the fastest quantities to reconstruct are filtered first. The events are sorted by which family of paths was taken, so that analysts do not have to process the entire 2012 dataset, but may instead focus on the final states of interest. Using a computing farm with 13000 CPUs, the HLT reduces the data-taking rate to 1 kHz.

Even though the HLT algorithms are quite good and may perform calculations on multiple objects, they are not as sophisticated as the algorithms used for offline processing of the data. Therefore, analysts must consider how the rate of offline identified particles compare with the number of trigger objects observed above the trigger thresholds. In 2012, the *particle flow* algorithm was implemented at the HLT level, to provide better online reconstruction of jet and missing energy. The procedure is discussed more in the following section. It improved the energy resolution of trigger objects, provided ways to reduce the presence of pile-up in the calculations, and increased the efficiency of trigger objects with

respect to offline reconstructed objects. Offline reconstruction, including the particle flow algorithm, is discussed in the next section.

The trigger system of CMS is a fundamental part data acquistion and physics analysis. It is designed to be both efficient and flexible, to balance the needs for speed of computing and accuracy of preliminary reconstruction. As the year went on and luminosity increased, the rates for many triggers became too large to be processed. Similar triggers with higher thresholds were introduced to allow analyses with those channels to continue, and the original triggers were *prescaled*, meaning they were only recorded a certain fraction of the time they passed HLT thresholds. Additionally, the average processing time was found to increase linearly with pile-up, leading to new algorithms designed to reject its effects. During 2012 running at 8 TeV, the CMS detector collected on average 400 Hz of data for reconstruction and analysis.

3.2.6 Conclusion

Having described the design and performance of the CMS detector, the next section presents how the CMS collaboration uses the measurements to identify particles from the hard scatter of protons and determine the processes that created them.

3.3 Object reconstruction

As described in Sec. 3.1, the LHC collided protons at a center of mass energy of 8 TeV during its 2012 operation. Collimated beams of protons are brought together at the center of the CMS detector. At high energy, the hard scatter of protons is in fact the interaction of partons that comprise the hadron, in particular, the gluons. Figure 3.32 is a sketch of top-antitop pair production from the hard scatter event.

The environment of the collision is far messier than this simple diagram would imply. The other partons interact with each other as they pass by, producing soft showers of additional partons, called the *underlying event*. Figure 3.32 shows these spectators as the additional lines in the incoming and outgoing protons. In addition, the highly energetic partons associated with the hard scatter may split or radiate a gluon. This is called intial state radiation when it occurs before the main energy transfer, (or final state radiation if it occurs after), and can potentially have large momentum. Outgoing partons from the hard scatter or other sources hadronize as a result of quark confinement, producing highly collimated sprays of hadrons. As these particles pass through the detector material, they undergo fragmentation and develop showers of additional hadrons.

As the signature of strongly interacting particles, these showers are very common in hadron collisions. In addition, they are an important part of any search for heavy gluino pair production. This section describes how hadronic showers are identified and measured in the CMS detector.

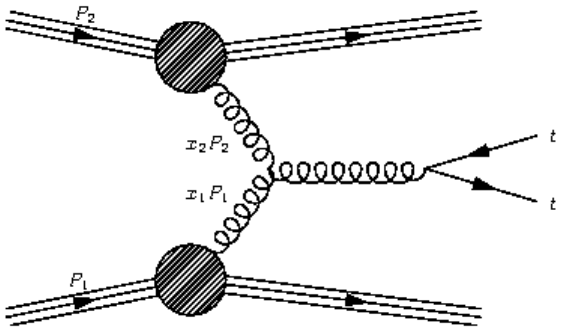

Figure 3.32: Illustration of a proton-proton collision.

Electro-weak processes are rarer at the LHC. They are the source of charged leptons and neutrinos. Since the latter of the two does not interact with the detector materials, it is the source of imbalance in the visible energy in an event. This is precisely the signature of neutralinos, therefore, any search for weakly-interacting stable particles will be difficult to distinguish from Standard Model weak processes. For this reason and the purpose of constructing control samples for this analysis, the understanding of weak processes and reconstruction of leptons is important.

It is critically important for this analysis to have a thorough understanding of how the balance of energy in an event is determined. This section describes the algorithm that takes into account every particle in the final state and calculates the direction and magnitude of a momentum imbalance.

3.3.1 Physics object definitions

As described in Sec. 3.2, each subdetector contributes to the identification of the different particles that are produced in the collision. Particle reconstruction refers to the

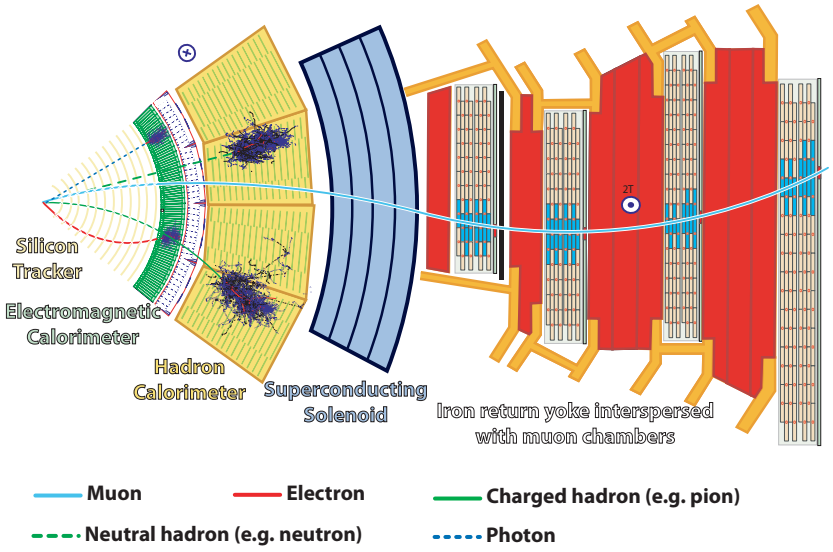

Figure 3.33: Drawing of an octant from the barrel of the CMS detector, with the interactions of particles through each subdetector shown. Image:CERN.

Table 3.8: Identification of particles based on their interactions with the subdetectors.

Subdetector	Physics Objects	Important examples
Tracker	charged	$l^{+/-}$, $\pi^{+/-}$
Electromagnetic Calorimeter	electromagnetic	e, γ, π^0
Hadronic Calorimeter	strongly-interacting	K, $\pi^{+/-}$, ρ, etc
Muon system	μ	μ

process of identifying particles and measuring their various properties using their signatures left in the detector. A diagram of an octant of the CMS detector is shown in Figure 3.33, along with representative paths taken by different particles and the interactions of the particles with material in the subdetectors.

Any charged particle will ionize the material as it passes through the silicon tracker, leaving hits in each layer. Its trajectory will bend in response to the magnetic field, which is essential for determining the momentum of these objects. The reconstructed path of a charged object through the tracker is called a *track*, which is shown as a solid line in the figure.

The electromagnetic calorimeter will stop any electrons or photons, causing them to undergo bremmstralung and produce electron-positron pairs until all the energy of the incoming particle has been expended. These electromagnetic showers are shown in Fig. 3.33 as a somewhat compact *cluster* of energy contained in the electromagnetic calorimeter. The energy takes the form of light in the crystals, which is collected by photomultiplier tubes as described in Sec. 3.2.2. Similarly, the hadronic calorimeter will stop any strongly-interacting objects. The dense lead absorber causes a cascade of interactions as the incoming hadron undergoes fragmentation. As described in Sec. 3.2.3, scintillating tiles sample the energy losses through the absorber. Neutral hadrons will leave no signature in the tracker or electromagnetic calorimeter, so the hadronic calorimeter is critical for measuring the energy of these particles. Together, clustered energy deposits from electromagnetic or hadronic showers in either calorimeter are referred to as *jets*. Since the LHC is a hadron collider, the vast majority of events involve the production of jets.

Finally, as minimum ionizing particles, muons traverse the entire detector. While tracks are the most sensitive measurement for muon momentum, the large system dedicated to measuring the timing and position of muons in the magnetic return flux is important

for redundancy and unambiguous identification. Table 3.8 provides examples of how each subdetector system contributes to the discrimination of various particles.

Since the initial momentum of incoming protons in the $x-y$ plane is zero, the total momentum of all outgoing particles in the transverse plane should balance. If the visible energy of the total event is unbalanced, then one or more particles were produced unseen by the detector. The energy necessary to balance the event is called the *missing transverse energy*, or $E_{\mathrm{T}}^{\mathrm{miss}}$. Large amounts of $E_{\mathrm{T}}^{\mathrm{miss}}$ usually indicates the presence of a particle that only interacts weakly, namely, the neutrino. If supersymmetry is a valid extension of the Standard Model, is R-parity conserving, and has only weakly-interacting particles as its lightest stable particle (*LSP*), we expect a large amount of $E_{\mathrm{T}}^{\mathrm{miss}}$ in the detector. Therefore, the measurement of the transverse balance of an event is very important to supersymmetry searches and must exploit as much information as possible from a combination of all subdetectors.

An illustration of how these reconstructed objects appear in a real event from the early running of the LHC is shown in Fig. 3.34. The production of top-antitop pairs at CMS is interesting for many reasons, but one is shown here to demonstrate a variety reconstructed objects, including multiple jets, a lepton, and $E_{\mathrm{T}}^{\mathrm{miss}}$. The view is in the x–y plane down the center of the detector, such that the magnitude and direction of transverse quantities can be visible. The green curved lines at the center of the figure represent tracks left in the tracker. The circle around these tracks represents roughly the layer of calorimeters, with deposits of energy shown as blue and red columns at the appropriate location in ϕ. Red and blue

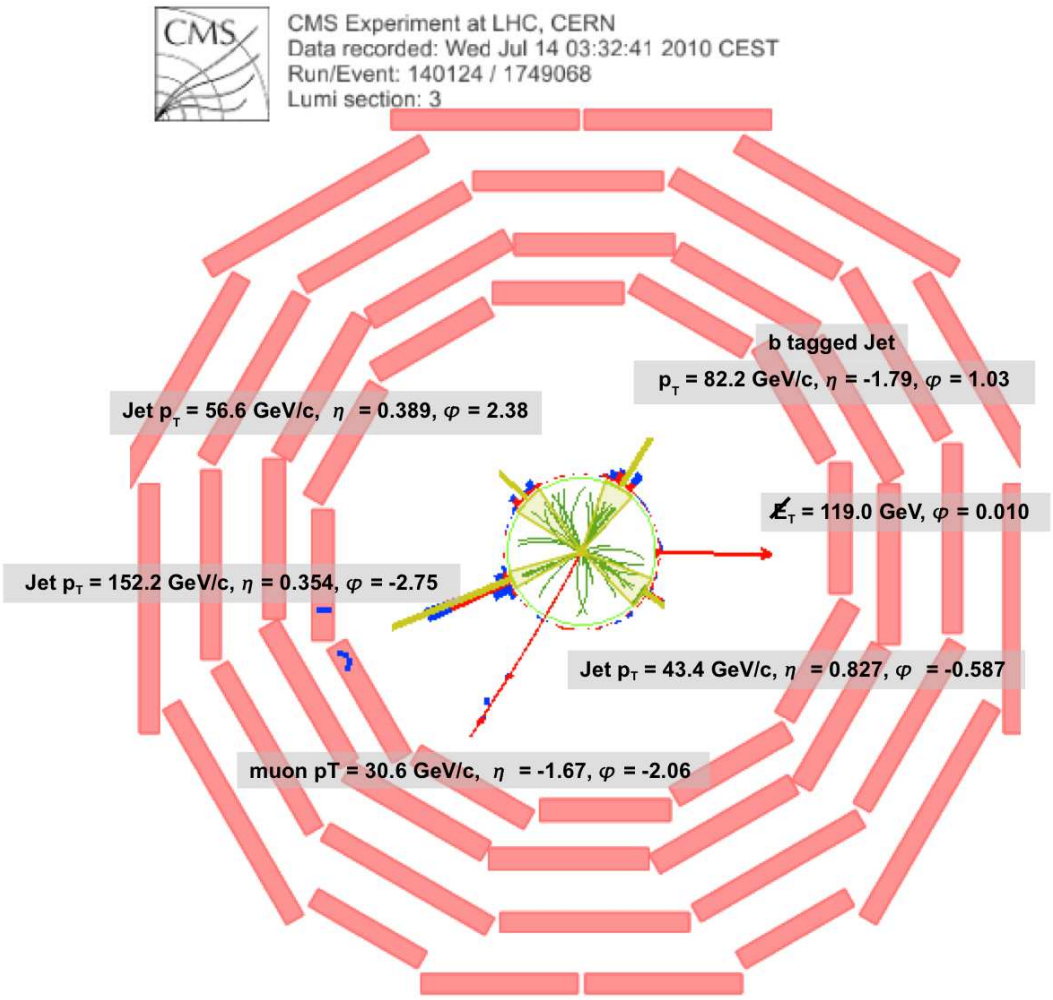

Figure 3.34: Display of a likely top/anti-top event produced at CMS. Image: CERN.

bars indicate the location and magnitude of energy in the electromagnetic and hadronic calorimeters, respectively. As described later in this section, tracks and energy deposits from a single cluster are identified, and the momentum of the total jet is calculated. The yellow shaded areas in the tracker delineate a cone-shaped area circumscribing a single jet, with the total jet momentum drawn as a yellow column in the calorimeter region. There are four jets present, from the hadronization of both b-quarks and the two quarks from a hadronic W boson decay. The second W boson decayed leptonically, as evidenced by the red line indicating a muon. The neutrino is inferred by the presence of 119 GeV of $E_{\mathrm{T}}^{\mathrm{miss}}$ pointing to the right to balance the energy of the event. Additionally, it is very likely that this event involved top-antitop production because one of the jets is labeled a "b-tagged jet". The algorithm for determining which jets in an event are likely to have originated from the hadronization of a b-quark is described later in this section. As discussed in Sec. 2.2, third generation quarks are the focus of several searches for supersymmetry, including this one. Therefore, identifying jets from a b-quark is a critical component of this analysis. Since $t\bar{t}$ events often contain many features in common with gluino decays to b-quarks and LSPs, this process is a significant source of events in the analysis.

3.3.2 The particle flow algorithm

The particle flow algorithm is a detector-wide procedure for identifying physics objects in CMS and correcting their energies based on measurements in multiple subdectors [24]. It is developed and implemented by a dedicated team, and the resulting measurements of final state quantities are used by many physics analyses, including this one. The goal is

to optimize the resolution, fake-rate, and efficiency of identifying electrons, muons, photons, charged hadrons, and nuetral hadrons, and to then use them to construct more complicated objects like jets, b-jets, τ-leptons, and $E_{\mathrm{T}}^{\mathrm{miss}}$. Within a quark or gluon jet of p_{T} $\sim$500 GeV, the average momenta of the stable constituent particles is on the order of 10 GeV. This means that the particle flow algorithm must identify many individual final state particles often with very low energies. In fact, it achieves a small fake rate for particles down to 150 MeV, out to $|\eta|$ <2.6. By spatially associating small features like charged tracks and calorimeter deposits, the goals of this algorithm are achieved.

Particle identification begins with the track fitter, which helps determine the energy of charged leptons and most of the energy within jets. The algorithm employs an iterative tracking strategy, in which tracks are first seeded and reconstructed using very tight criteria with a moderate tracking efficiency and, importantly, negligible fake rate. Then, hits which can be unambiguously assigned to the tracks are removed from consideration, the seeding criteria is loosened, and the track fitting procedure is repeated. This allows the fake rate to remain low, since the combinatorics of the track fitting is reduced with every iteration. After the first 3 iterations, isolated muons are measured with 99.5% efficiency, and charged hadrons with >90% efficiency. The following iterations continue to relax selection criteria, allowing identification of particles displaced from the primary vertex, such as those from photon conversions, interactions with detector material, and decays of long-lived particles. The procedure is so effective that even particles with only 3 hits, and p_{T} as low as 150 MeV, have a fake rate of $\sim$1%.

Identifying clusters of energy in the calorimeters is critical for jet reconstruction. A sucessful algorithm must be able to separate charged and neutral hadron energy deposits, determine the direction and energy of neutral stable particles, and be able to associate photons from bremstrahlung with their parent electron. Furthermore, calorimeter energy deposits are important for measuring the energy of charged particles where reconstructed tracks have low quality or high p_{T}. The $anti - k_T$ clustering algorithm is designed to have high efficiency even for low energy particles, and is able to distinguish deposits with very low separation. First, clusters are seeded independently in the electromagnetic and hadronic calorimeters, when a cell energy is above a certain threshold, 80–300 MeV for the former and ∼800 MeV in the latter. Next, cells above a threshold adjacent to the seed are aggregated. Using an iterative procedure of checking nearby cell energies, one energy cluster is created for each seed. Since the hadronic calorimeter is 25× coarser than the electromagnetic calorimenter, there is no spatial separation between charged and neutral hadrons about 100 GeV. Combining the two subdetectors, the total hadron energy resolution is ∼10% at 100 GeV.

The particle flow algorithm takes reconstructed tracks and energy clusters, called elements, and links them together according to spatial separation. The linking algorithm measures the distance between elements (in ϕ-η) and quantifies the quality of that association. Linked elements among the tracker, electromagnetic calorimeter, and hadronic calorimeter are called blocks. Due to the fine detector granularity, the performance of creating blocks is independent of the complexity of the event. A track is linked to a cluster

if its extrapolated path through the calorimeter is within the boundary of the cluster. To accomodate for inefficiencies, the cluster envelope may be enlarged to allow more tracks, or the hadronic calorimeter envelope may be enlarged to accomodate the more fine-grained electromagnetic calorimeter clusters.

There are several situations where the association of links are less obvious. For example, there are two main reasons why a track may be associated with more than one electromagnetic calorimeter clusters. First, they could be the result of hadronic shower flucations, in which case the energy should be associated with the track. Or, it could be the result of overlapping photons, in which case there should be no link to the track, and a determination is made according to the energies of the clusters as well as their spatial closeness to the track. If energy deposits linked to a track are much larger than the track momentum beyond the calorimeter uncertainty, these may be assigned to photons and neutral hadrons. For example, if the combined cluster excess above the track momentum is greater that the energy in the electromagnetic calorimeter, the electromagnetic energy is assigned to a photon and the remaining excess beyond the tracker measurement is assigned to a neutral hadron. Clusters having no link to a track are called photons, ultimately comprising $\sim$25% of the jet energy. Remaining clusters with a poor link to tracks are taken to be neutral hadrons.

The particle flow linking procedure is also used to identify leptons. The procedure identifies electrons using tracks left by the lepton itself and calorimeter energy deposits from the bremmstrahlung photons created as it passes through the tracker material. The tracks

and clusters associated with the electrons are removed from further processing. Muons are constructed using information from both the tracker and muon system. Tracker and muon system tracks may be linked according to the χ^2 of a fit through their hits. A particle-flow muon must have tracks in both subdetectors, and the combined momentum must be compatible with tracker-only momentum within three standard deviations. As with electrons, the muon energy deposits are removed from association with any other blocks.

3.3.3 Selection criteria

This analysis uses particle flow (PF) objects to construct a region in parameter space in which to search for evidence of supersymmetry. The selection criteria listed in this section are based on recommendations from dedicated studies on the efficency and misidentification of each type of object.

Jets

As described above, the particle flow algorithm incorporates information from multiple subdetectors to compile a collection of jets for analysis. A number of corrections are applied to the jet energy, to account for the presence of energy from pile-up, the effect of the relative (η-dependent) and absolute (p_{T}-dependent) energy scale, residual corrections, and flavor-based corrections (the latter is discussed later in this section). Figure 3.35 shows the resulting uncertainty on the jet energy. In general, the uncertainty is a function of p_{T} and η, while the pile-up uncertainty also depends on the number of vertices in the event and flavor uncertainty obviously depends on the flavor of the jet. While the uncertainty varies

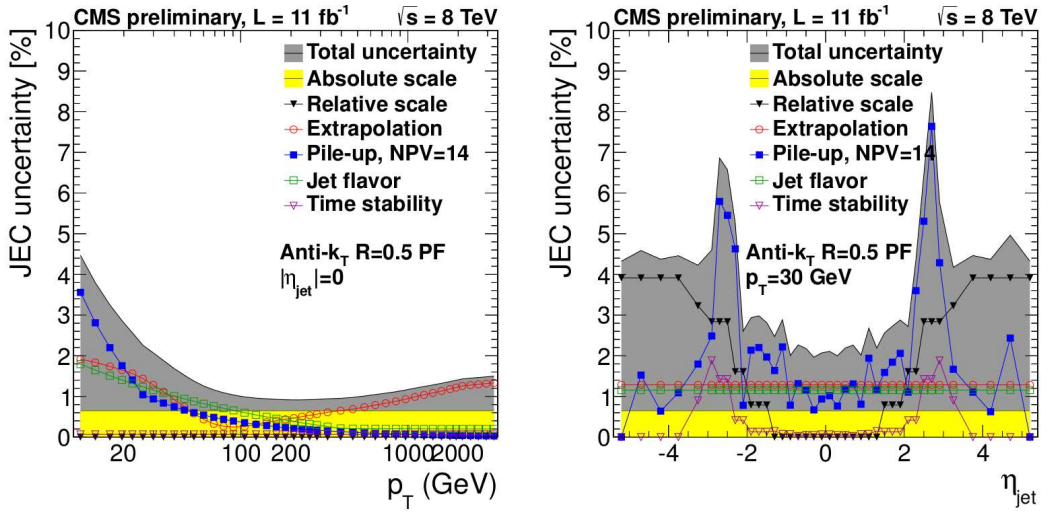

Figure 3.35: Jet energy scale uncertainty with respect to p_{T} (left) and η (right) [7].

dramatically with p_{T} and η, it remains mostly <5% for the jets used in this analysis, down to a resolution of ∼1% for central, high p_{T} jets. Since the jet energy is such an important part of this analysis, its uncertainties are considered an important potential source of bias.

In this analysis, we use standard quality criteria to identify jets with problematic properties and eliminate those events from consideration. Only jets with p_{T} >30 are considered for these quality criteria.

Table 3.9 lists the conditions under which an event may be rejected for having a poorly measured jet. Most jets are comprised of 60% charged particles Therefore, limits are placed on the neutral hadron energy fraction (NHF) and photon energy fraction (PEF) of any jet in the event. Next, we need to reject events in which a high momentum jet has gone through the crack between the barrel and endcap of the calorimeter. For any jet with p_{T} >50 GeV within the geometry of the crack (0.9< $|\eta|$ <1.9), the event is rejected if the

Table 3.9: Jet-based event vetoes.

Measurement	Requirement
Particle-based noise rejection	NHF>0.9 || PEF>0.95 (ANY jet p_{T})
Edge rejection	$p_{\mathrm{T}} > 50$ GeV , $0.9 < \|\eta\| < 1.9$, CM–NM ≥ 40
Bad jet rejection, any η	NEF>0.99 || CM+NM ≤ 1
Bad jet rejection, $\|\eta\| < 2.4$	CHF=0 || CEF>0.99 || CM=0

Table 3.10: Definition of good jet.

Measurement	Requirement
p_{T} ($\Delta\phi_N^{\mathrm{min}}$, b-tag mult.)	30 GeV
p_{T} (H_{T}, jet mult.)	50 GeV
$\|\eta\|$	2.4

charged multiplicity is at least 40 more than the neutral multiplicity. Finally, an event veto is applied if a jet is found with $p_{\mathrm{T}} > 30$ GeV and failing any of the quality requirements. The neutral electromagnetic energy fraction (NEF) must not be close to one, and the sum of the charged and neutral multiplicities must be at least two. Furthermore, any jet with $|\eta| < 2.4$ must have some charged hadronic energy and not total charged electromagnetic energy, with a charged multiplicity of at least one.

Table 3.10 lists the p_{T} and η requirements for all jets considered in this analysis. Any jet with $p_{\mathrm{T}} > 30$ GeV is used in calculating the quantity $\Delta\phi_N^{\mathrm{min}}$ (defined in Sec. 4.4) and b-tag multiplicity of the event. However, only jets with $p_{\mathrm{T}} > 50$ GeV enter the calculation of

the the total energy of the event, H_{T}. The lower threshold ensures we are including resolution effects from all jets in the event for $\Delta\phi_N^{\mathrm{min}}$, and for identifying as many b-jet candidates as possible. Since we expect a large number of high p_{T} jets from gluino production, we pay particular attention to how those objects contribute to the event.

Muons

As described above, it is important to remove events from the analysis sample that include charged leptons, which would indicate that the $E_{\mathrm{T}}^{\mathrm{miss}}$ present is the result of a neutrino. To identify particle flow objects that are very likely to be muons, several properties of the muon candidate are considered.

First, the muon should appear to have originated from the primary vertex, and not a secondary decay. The quantity d_{xy} is the smallest distance in the transverse plane between the muon track and primary vertex. Its value is corrected for the measured position of the beamspot for that event. Similarly, d_z is the distance between the primary vertex and the muon track's closest approach. Secondary muons are often embedded within a jet, having a substantial amount of calorimeter energy around it. The isolation of a muon is calculated by summing the deposited energies within a cone of ΔR <0.4 around the extrapolated muon track. The construction of the relative isolation of a muon with respect to its own momentum is:

$$\text{RelIso} \;=\; (\; E_T(\text{charged hadron}) \;+ E_T(\text{neutral hadron}) \;+ E_T(\gamma) - \frac{1}{2}\, p_{\mathrm{T}}^{PU} \;) \,/\, p_{\mathrm{T}}^{\mu}. \quad (3.8)$$

Table 3.11: Definition of good PF muon.

Measurement	Requirement
p_{T}	>10 GeV
$\lvert\eta\rvert$	<2.4
Rel. Iso.	<0.2
d_{xy}	<0.2
d_z	<0.5
Matched stations	≥2
Valid pixel hits	≥1
Tracker layers	≥6

The final term is a correction that takes into account tracks from pile-up. A measurement is made of the charged tracks in the cone around the muon that do not originate from the primary vertex. Then, using the average fraction of neutral to charged particles, as measured in jets in general, the total energy present from pile-up is subtracted out.

The definition of a good quality muon is given in Table 3.11. If an event contains a muon satisfying these criteria, it is removed from the analysis sample. However, these same criteria are used to define the muons needed in certain control samples.

Figure 3.36 shows the efficiency of reconstructing a PF muon satisfying the conditions listed in Table 3.11. As a result of the great care in designing the tracker and muon system, the efficiency is very high for this tight selection, with some expected decrease at

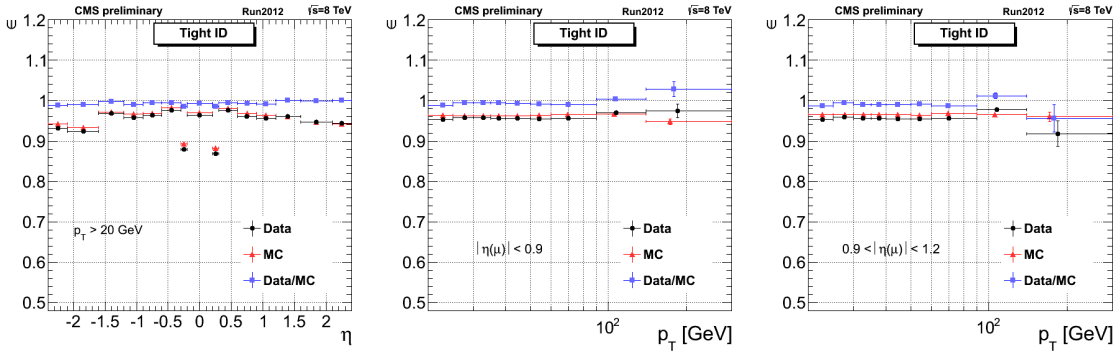

Figure 3.36: Muon reconstruction efficiency with respect to η (left) and p_{T} for two η regions (center and right) [8].

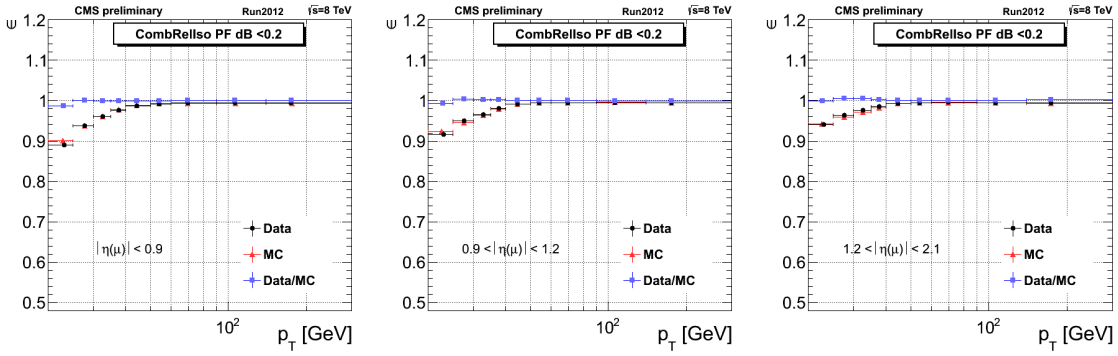

Figure 3.37: Muon isolation efficiency with respect to p_{T} for three η regions [8].

high η. The efficiency of the muon isolation is very important for distinguishing prompt leptons from an electroweak process and secondary leptons from heavy quark decay. This efficiency with respect to the momentum of the muon for different regions of η is shown in Fig. 3.37. The behavior is modelled very well in simulated events.

Electrons

As with muons, it is important for this analysis to be able to veto events with a prompt, isolated electron. Selection criteria for electrons are slightly more complicated than for muons. The same definitions for d_{xy} and d_z, apply, but the relative isolation is calculated in a slightly different way, within a cone of size R=0.3. This is expressed as:

$$\text{RelIso} = (E_T(\text{charged hadron}) + E_T(\text{neutral hadron}) + E_T(\gamma) - \rho \times AE) / p_{\text{T}}^{e}. \quad (3.9)$$

The final term is an area-based subtraction of the effect of neutral particles which depends on the η of the electron.

As in the definition of a good muon, the good electron is useful for vetoing events that should not be included in our analysis sample, as well as helping to define control samples. The criteria for a good electron are listed in Table 3.12. Since the detector response varies greatly between the barrel and endcap, different thresholds are placed based on the geometric location of the electron. A few of the less familiar quantities are shown in Fig. 3.38 and Fig. 3.39. $\Delta\eta_{IN}$ and $\Delta\phi_{IN}$ are the distance in η or ϕ between the supercluster position and the track direction at the innermost tracker layers. Like those quantities, the

Table 3.12: Definition of good electron.

Measurement	Barrel Req'	Endcap Req'
p_{T}	$>$ 10 GeV	
$\lvert\eta\rvert$	-	$<$2.5
Rel. Iso.	$<$0.15	$<$0.15
d_0	$<$0.2	$<$0.04
d_z	$<$0.2	$<$0.2
$\Delta\eta_{IN}$	$\leq$0.007	$\leq$0.01
$\Delta\phi_{IN}$	$\leq$0.8	$\leq$0.7
$\sigma_{I\eta I\eta}$	$\leq$0.01	$\leq$0.03
Had/EM E	$\leq$0.15	-

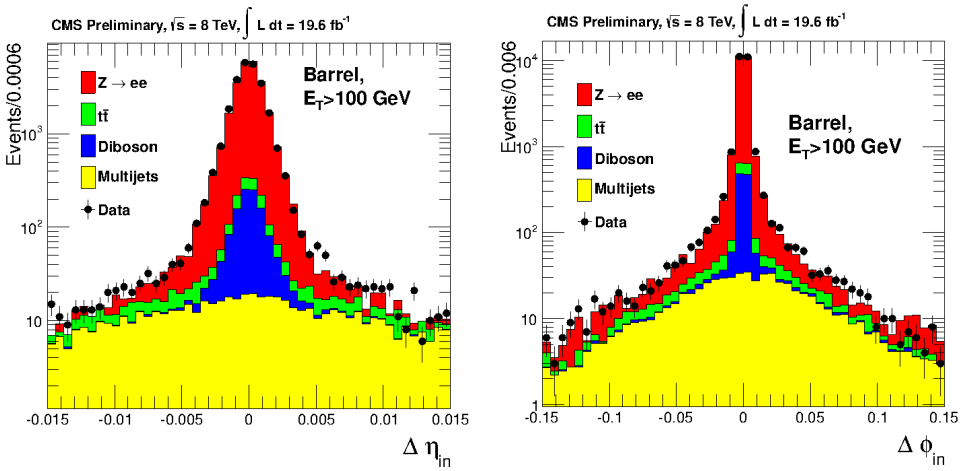

Figure 3.38: Distribution of quantities used for electron identification. The distance between a calorimeter superclusted and inner tracker hits in η (left) and ϕ (right) [9].

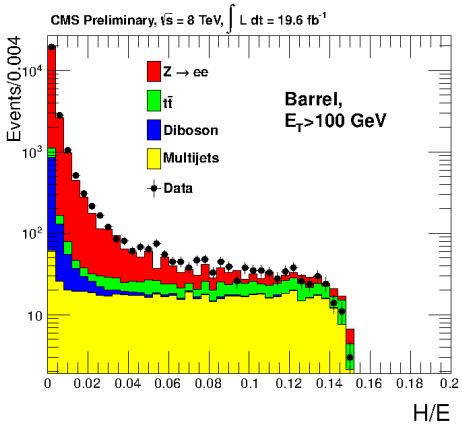

Figure 3.39: Distribution of quantities used for electron identification. The ratio of energy deposited in the hadronic calorimeter with respect to the energy deposited in the electromagnetic calorimeter [9].

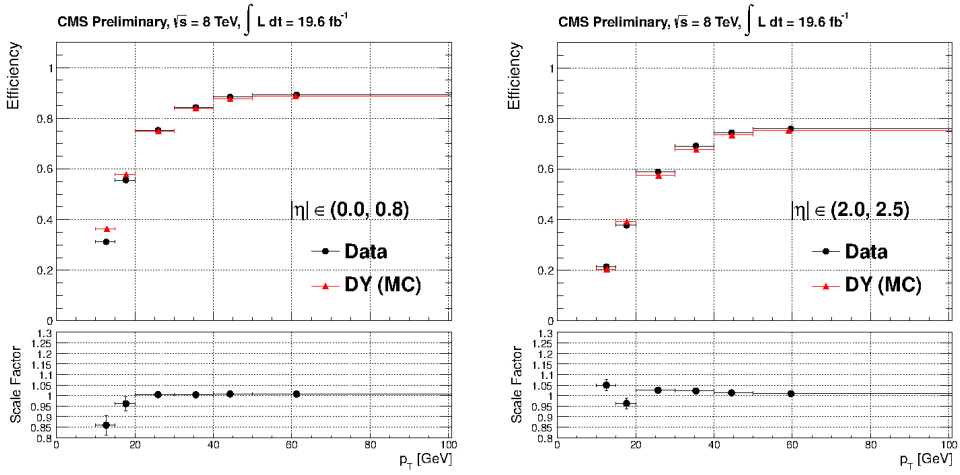

(a) Barrel region.

(b) Endcap region.

Figure 3.40: Electron reconstruction efficiency with respect to p_{T} for two η ranges [9].

fraction of energy in the hadronic calorimeter (H/E) should be close to zero. The quantity $\sigma_{I\eta I\eta}$ is the covariance matrix of the electromagnetic calorimeter cluster in the η direction.

The electron reconstruction efficiency is slightly lower than that for muons, since they can be harder to distinguish in the crowded tracker and calorimeter environments. Figure 3.40 shows this efficiency with respect to electron p_{T} in two regions of η. As expected, the identification of electrons becomes more difficult at high η. The efficiency is better at higher p_{T} and lower η.

3.3.4 Missing Transverse Energy

Among the tremendous benefits of the particle flow algorithm is the accurate measurement of missing transverse energy in an event. This quantity is defined as the negative vector sum of the transverse momenta of all final state particles, as calculated from particle flow. $E_{\mathrm{T}}^{\mathrm{miss}}$ is sensitive to detector and reconstruction errors, such as momentum mismeasurement, particle misidentification, and pile-up. Using out-of-the-box PF quantity, it tends to be underestimated due to energy thresholds in the calorimeters, p_{T} thresholds in tracker, and the non-linearity of calorimeter response.

Known corrections applied to PF jets accounting for bias from non-linearity of calorimeter response and event pile-up need to be considered in the $E_{\mathrm{T}}^{\mathrm{miss}}$ calculation [25]. These jet energy scale corrections can be factorized and we can propagate its effect to the $E_{\mathrm{T}}^{\mathrm{miss}}$,

$$E_{x,y}^{miss,CORR} \;=\; E_{x,y}^{miss,RAW} \;-\; \Sigma(p_{x,y}^{CORR} - p_{x,y}^{RAW}). \tag{3.10}$$

In addition, a second correction is applied to account for the effect of unclustered energy in the event.

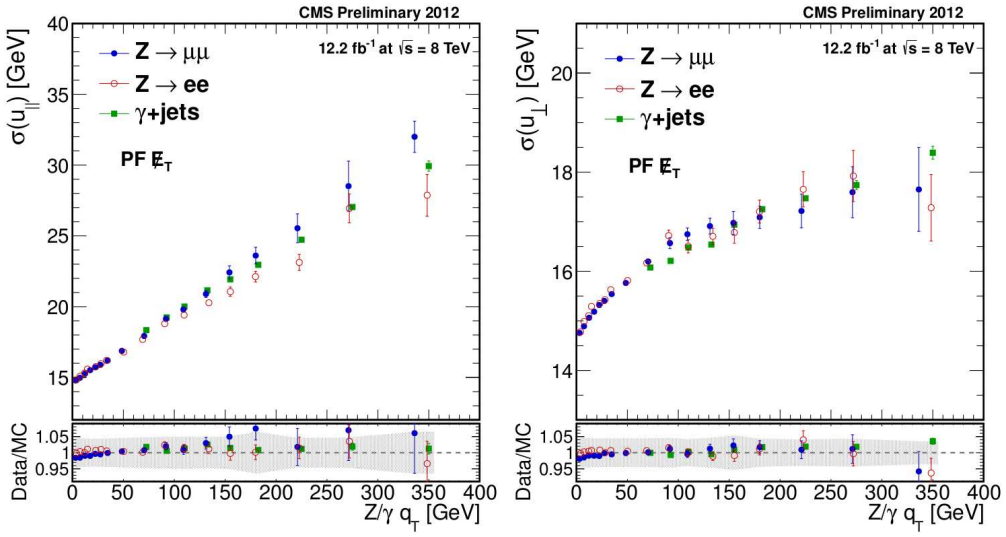

Figure 3.41: Resolution of $E_{\mathrm{T}}^{\mathrm{miss}}$ with respect to boson energy from three different methods. Shown for uncertainty parallel to (left) and perpendicular to (right) boson momentum [7].

Due to the effects of thresholds described above, $E_{\mathrm{T}}^{\mathrm{miss}}$ tends to point in direction of neutral particles. This can be corrected by considering the minimum bias interactions present in pile-up, which should be balanced in the transverse plane. The sum of charged particles associated with pile-up vetices can be used to estimate this effect.

There is an additional, not fully understood ϕ-dependence in the detector response. This has been observed in simulated events, and found to be correlated with the number of vertices. It creates a shift in the E_x and E_y components which is linear with the number of primary vertices, and therefore straighforward to correct.

Lastly, the $E_{\mathrm{T}}^{\mathrm{miss}}$ can be dramatically mismeasured due to misfires in the calorimeter and noise in the tracker resulting in fake tracks. A number of distinctive scenarios have been identified, and through a process called event cleaning, events that have unreasonable detector response are removed from the data sample.

Ultimately, the resolution of $E_{\mathrm{T}}^{\mathrm{miss}}$ depends on the resolution of jets, and can be measured in events with Z bosons. The amount of hadronic recoil is measured parallel ($u_{\parallel}$) and perpendicular ($u_{\perp}$) to the reconstructed boson momentum. The uncertainty of this measurement with respect to the boson energy in the transverse plane is shown in Fig. 3.41 for three different channels.

3.3.5 Combined secondary vertex algorithm

As described in Sec. 2.2, third generation quarks have a particular importance in natural supersymmetry models. This analysis expoits the properties of reconstructed tracks to identify jets associated with the presence of a b-quark, using well-established tools.

The unique properties of b-quarks make possible the distinction of their associated jets from those involving only light flavor partons. Since the b-quark only decays through the weak interaction, it has a relatively very long lifetime, ∼1.5 ps, This lifetime translates to a flight distance of $c \times t = 450\ \mu$m at high energies. When the b-quark decays (Fig. 3.42), it produces tracks within a hadronic jet which originate from a displacement incompatible with the primary vertex. With its very fine spatial resolution, the pixel tracker is able to

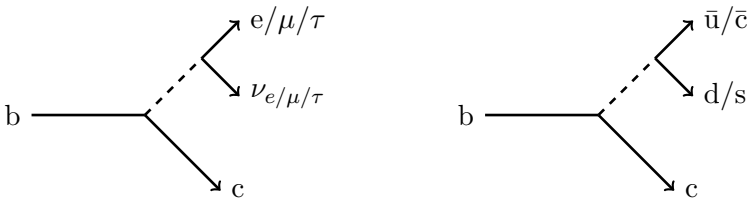

Figure 3.42: Decay of the b-quark via the weak force leptonically (left) and hadronically (right).

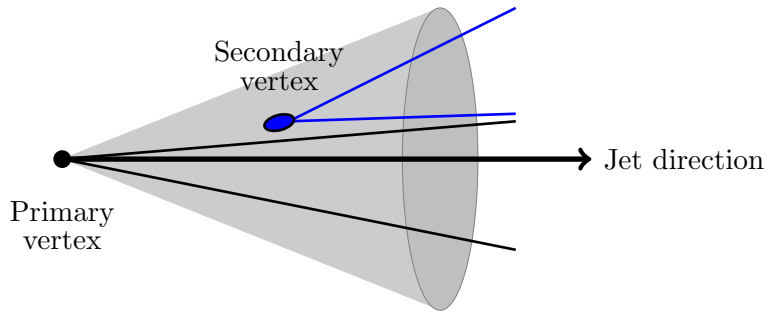

Figure 3.43: Simple diagram of linearized tracks within a b-jet. Intersecting tracks form a secondary vertex within the jet cone, displaced from the primary vertex.

distinguish tracks originating from this *secondary vertex* from the primary vertex at the scale of the b-quark flight distance. Another useful property of the b-quark is its large mass, $\sim$5 GeV. With its large energy and hard fragmentation function, the b-meson contains a large fraction of the jet energy, and tends to produce many (about five) charged tracks. The W boson branching fractions determine that $\sim$20% of b-jets have an electron or muon within or very close to the jet cone. These leptons from secondary decays are not considered "true" leptons for the purposes of most analyses, and are ignored. However, these non-isolated leptons are useful for studying the efficiency of various b-tag algorithms. Figure 3.43 shows a jet cone surrounding tracks associated with a b-jet. The blue tracks are originating from a secondary vertex within the jet. The properties of tracks within a jet are important for determining if a jet is likely associated with a b-quark.

The combined secondary vertex (CSV) algorithm is commonly used for identifying jets associated with b-quark decay [26] [27]. Using information from the tracker, it assigns a value between 0 and 1 to each jet, based on the likelihood that it is associated with a b-quark. To be used in the algorithm, tracks must be good quality, having >1 GeV of

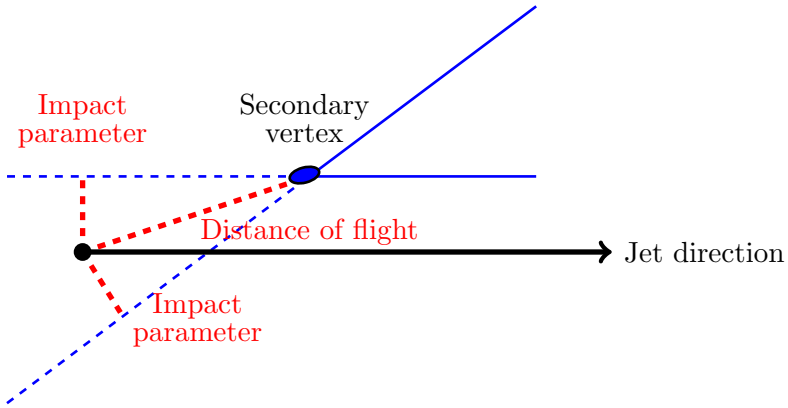

Figure 3.44: Simple diagram showing linearized tracks associated with a secondary vertex, which are extrapolated back towards the primary vertex to determine important quantities.

energy and with at least eight hits in the tracker, two of which in the very precise inner pixel layers. Furthermore, the extrapolated trajectory of the track is very important, so the fit of the hits must be successful, having a χ^2/ndof<5. Within the very busy environment of the tracker, it is important that the track is indeed associated with the particular jet from the hard scatter, so additional cuts are placed on its proximity to the jet axis and primary vertex.

The most important characteristic of a b-quark decay is the presence of a secondary vertex within the jet. Secondary vertices are found using a trimmed kalman vertex finder, which starts with all the tracks in the jet and rejects outliers until intersecting ones are found. For many b-jets, less than 65% of its tracks originate from the primary vertex [27]. The distribution of secondary vertex multiplicity according to jet flavor in multi-jet events is shown in Fig. 3.45(a). Jets from c or light flavor partons (in blue and green) overwhelmingly have no reconstructed secondary vertices, while the distribution of b-jets (in red) peaks at one and has a broad tail. The distance between the primary vertex and

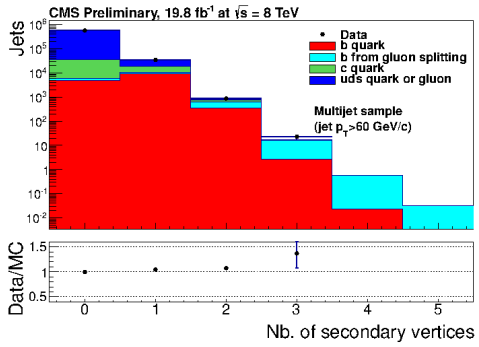

(a) Number of secondary vertices within a jet.

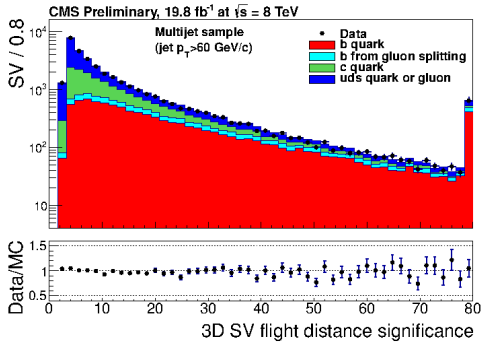

(b) d_0 significance of secondary vertices.

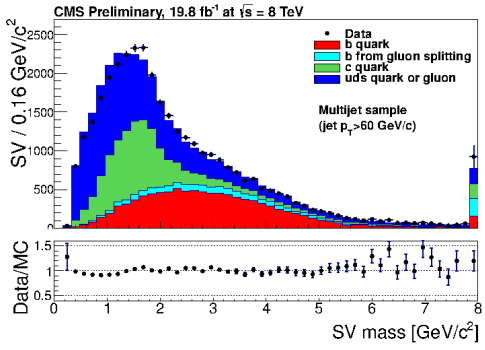

(c) Total mass of tracks in secondary vertices.

Figure 3.45: Properties of reconstructed secondary vertices within a jet, multiplicity (a), $d_0$sig (b), and mass (c) [10].

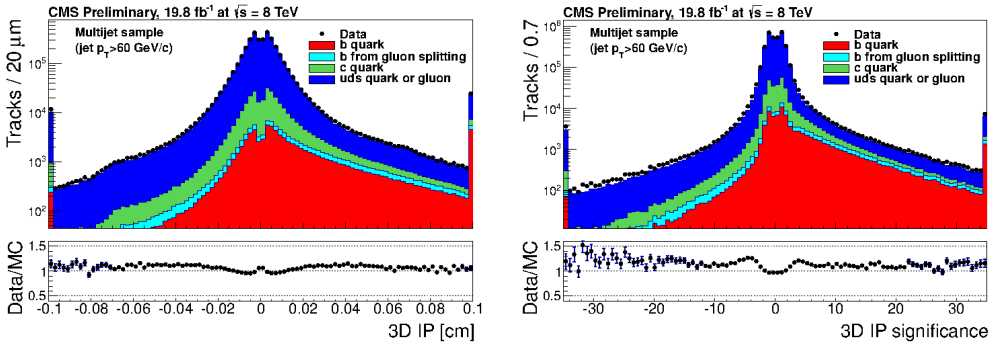

Figure 3.46: The impact parameter (left) and its significance (right) for tracks within a jet [10].

a secondary vertex, shown as a dashed red line in Fig. 3.44, is called the *distance of flight*, d_0. To account for uncertainties in the track measurement, this quantity is divided by its uncertainty to measure the significance of the flight distance, d_0sig, shown in Fig. 3.45(b). This quantity is important because the long lifetime of the b-quark should translate to a relatively far distance of travel before it decays, well beyond the resolution uncertainty of the tracker. Figure 3.45(b) shows that the lighter partons peak sharply at low values, at which the secondary vertex is close to the primary vertex.

Another important property is the *impact parameter*, IP, which is the distance of closest approach of a track to the primary vertex when the track is extrapolated back towards it. These are shown as dashed blue lines in Fig. 3.44, which can be measured for any track regardless of the presence of a secondary vertex. The IP is a signed quantity which is positive if the track is downstream from the primary vertex with respect to the direction of the jet. Figure 3.46 shows the distribution of IP according to jet flavor in multi-jet events. This figure also shows the impact parameter signficance, IPsig, which is the signed value of

Table 3.13: Inputs to combined secondary vertex likelihood algorithm, according to jet category.

RecoVertex	PseudoVertex	NoVertex
d_0 sig.	track mult.	IPsig at c mass
track mult.	track mass	
track mass	tk. energy frac.	
tk. energy frac.	tk. rapidity	
tk. rapidity	IPsig at c mass	
IPsig at c mass		

the impact parameter divided by its uncertainty. Tracks from b-quark decay strongly favor large positive values of IPsig.

The CSV algorithm takes in the values of the quantities described above, as well as a few others based on the tracks and secondary vertices, and constructs a likelihood for each jet to have come from b-quark decay. Each jets falls in one of three categories:

1. RecoVertex: $\geq$1 good secondary vertex
2. PseudoVertex: no secondary vertex, but require $\geq$2 tracks with IPsig>2
3. NoVertex: everything else

When a reconstructed secondary vertex is found (the RecoVertex category), the jet is likely to involve a b- or c-quark, and inputs associated with the secondary vertices are available for the likelihood. However, the purpose of this algorithm is to assign a b-jet probability to every jet regardless of whether a secondary vertex is present, therefore, other

quantities are exploited for the PseudoVertex and NoVertex jets categories. The inputs are listed in Table 3.13 and discussed below.

For jets with a secondary vertex within them, there are many quantities that help determine if the jet is from b-quark hadronization and fragmentation. As discussed above, the significance of the flight distance between the primary and secondary vertex, $d_0$sig, should be large. The individual tracks themselves also provide important information, even if they do not form a good secondary vertex but simply have IPsig>2 for jets in the PseudoVertex category. First, there should be a large multiplicity of charged tracks associated with the secondary (or pseudo) vertex. Also, the invariant mass of these tracks is expected to be significantly above the charm mass ($\sim$1.3 GeV). The fraction of jet energy associated with the tracks from the secondary vertex with respect to the energy of all tracks in the jet is also important. Since b- and c-quarks both have hard fragmentation, they are expected to carry a large fraction of the jet energy. A somewhat less important quantity is the rapidities of each track from the secondary vertex with respect to the full jet direction. The rapidity of tracks from b-quarks with respect to the jet is usually smaller than those from c-quarks.

A quantity common to all three categories is the IPsig of the first track exceeding the charm threshold, which achieves a good rejection of jets from charm. First, the tracks are sorted by decreasing IPsig. Going down the list, the masses of the tracks are summed together until the total mass is greater than 1.5 GeV. The IPsig of that track is added to

the CSV likelihood. For jets in the NoVertex category, this is the only quantity entering the algorithm.

From these inputs, two likelihood ratios are constructed, one discriminating between b- and c-jets, and the other between b- and light flavor jets. This is because the distribution of the input quantities are much different for light flavor jets than for charm. The likelihood function for each flavor of jet (b, c, or light flavors q) is defined as [26]:

$$\mathcal{L}^{b,c,q} = f^{b,c,q}(\alpha) \times \prod_i f^{b,c,q}_{\alpha}(x_i). \tag{3.11}$$

Taking α to denote the vertex category (RecoVertex, PseudoVertex, or NoVertex), $f^{b,c,q}(\alpha)$ is the probability of a jet of a particular flavor to be in category α. This probability is multiplied by each of the probability density functions for the input parameters x_i, for a category α and flavor b, c, or q. The discriminating variable, uses a combination of the ratios of these likelihoods, each weighted by a factor for the relative contributions of the background flavors:

$$\text{CSV output} = frac(c) \times \frac{\mathcal{L}^b}{\mathcal{L}^c + \mathcal{L}^b} + frac(q) \times \frac{\mathcal{L}^b}{\mathcal{L}^q + \mathcal{L}^b}. \tag{3.12}$$

The fractions of the charm and light flavor backgrounds are set to 0.25 and 0.75, respectively, since the expected fraction of c-jets from hadronic W boson decay (which are a main source of jets in this analysis) is about 25%.

The distribution of the CSV output value is shown in Fig. 3.47. This multi-jet sample is vastly dominated by light flavor jets, as expected, but the simulated events show that the b-jet component is peaked at high values. Several different procedures exist for

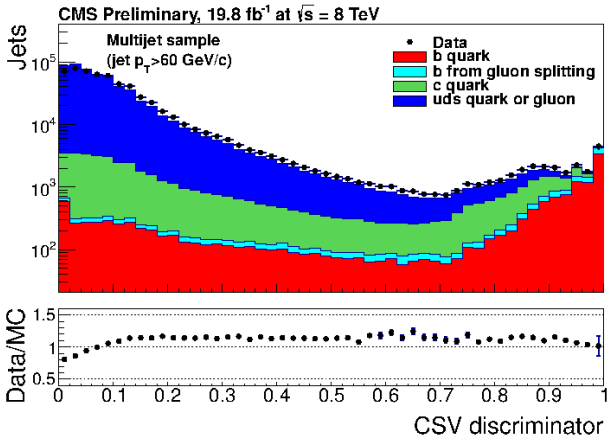

Figure 3.47: Distribution of the combined secondary vertex algorithm output from multi-jet events. A "loose" b-tag requires a CSV value greater than 0.244. A "medium" b-tag requires a CSV value greater than 0.679 [10].

measuring the efficiency of this and other b-tag algorithms. For example, this can be done by finding a muon inside a jet, which almost certainly comes from a b-quark decay, and looking for the anti-b-quark jet. From these studies, the b-tag efficiency with respect to jet p_{T} and η is measured in data, and simulated jets can be corrected with scale factors based on the flavor of the generated jet. The uncertainty on these scale factors is a source of systematic uncertainty in analyses involving b-jet identification, including this one. Table 3.14 shows these scale factors, SF_b, provided for three different values of CSV output. The CSV loose, medium, and tight working points are the discriminant values resulting in a mistag rate of 10%, 1%, and 0.1%, respectively. Figure 3.48 shows the performance of the CSV algorithm, including a typical efficiency curve as a function of CSV value, and the mistag rate of the

Table 3.14: Corrections to the CSV b-tag efficiency applied to events in simulation, based on the working point being used (loose, medium, or tight). The correction was calculated from data in multi-jet and $t\bar{t}$ samples separately.

CSV	SF_b multi-jet sample	SF_b $t\bar{t}$ sample
Loose	0.985 ± 0.070	0.987 ± 0.018
Medium	0.964 ± 0.071	0.953 ± 0.012
Tight	0.920 ± 0.104	0.926 ± 0.036

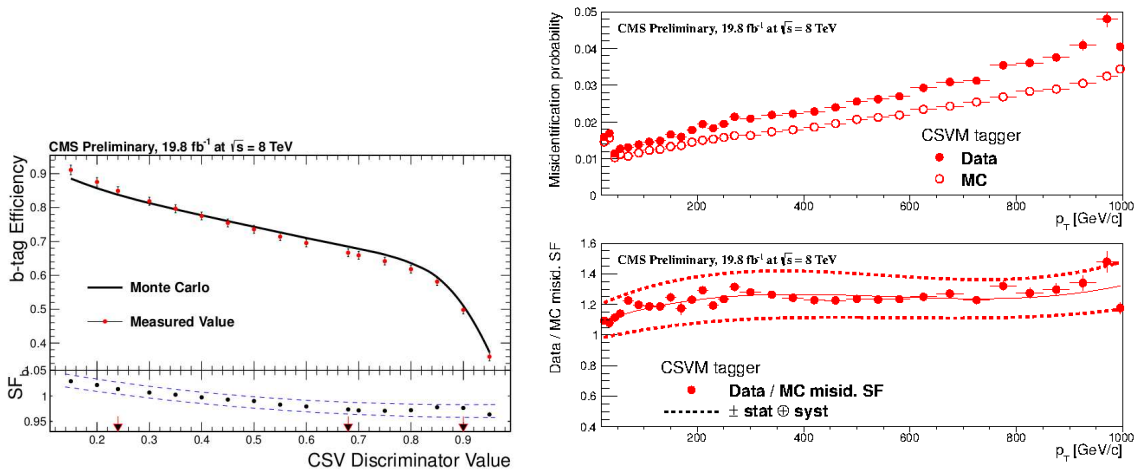

Figure 3.48: Efficiency of correctly identifying a b-jet with respect to CSV value (left). Rate of mis-tagged b-jets at the medium CSV working point with respect to p_{T} (right) [10].

CSV medium working point as a function of jet p_{T}. Among other, older, algorithms, it is the best choice for identifying jets associated with b-quark production at CMS.

The performance and uncertainty associated with the CSV algorithm is critical for this analysis, which relies on events with high b-jet multiplicity as a well-motivated feature of potential supersymmetry signatures. We use the CSV medium working point (CSVM), which requires that a jet have a CSV discriminator value of at least 0.679 to

be considered "b-tagged". This requirement has a misidentification rate of 1%, and an efficiency for identifying a b-jet of about 67%, over a large range of p_{T} and η.

Along with b-tag multiplicity, this analysis uses other selection criteria to create a subset of the CMS data which would include the signal events we are interested in. The requirements for events included in this search for supersymmetry are described in the next chapter.

Chapter 4

Triggers, Event Selection, and Signal Regions

This analysis is designed to search for evidence of supersymmetric particles whose decays lead to multiple b-jets in the final state. If gluinos are light and R-parity is conserved, collisions of protons at the LHC would produce pairs of gluinos via the strong force. As discussed in Sec. 2.2, natural models of supersymmetry favor light third generation squarks (stop and sbottom), to which the gluino may directly decay. This analysis is designed to probe the particular signature in which each gluino decays through a virtual bottom-squark to two b-quarks and a neutralino, seen in Fig. 4.1. The final state of such a process is four jets associated with b-quarks and missing transverse energy from the inability to detect the weakly-interacting neutralinos. This simplified model of gluino decay is referred to as T1bbbb. The T1bbbb simplified model is used in this analysis as a reference signature for

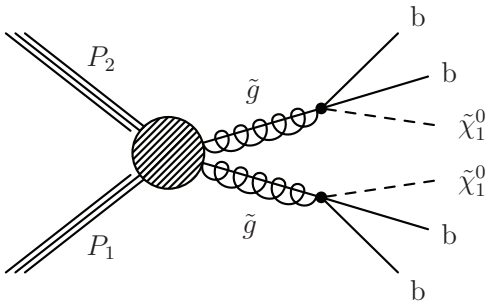

Figure 4.1: Diagram of the gluino pair production and three-body decay in the T1bbbb simplified model, resulting in four b-jets and two LSPs.

what is a fairly general search for supersymmetry with hadronic final states and large b-jet multiplicity. Using simulated signal and Standard Model events, we select a subsample of data events with small background yield and the possibility of significant signal yield.

4.1 Simulated event samples

Simulated T1bbbb and Standard Model physics events are used to design the analysis and aid in understanding the data. Each sample contains a large number of events for a particular process, which are weighted by the appropriate cross-section and luminosity of collected data. It is useful to compare samples of simulated events (also called *Monte Carlo* samples, or simply MC) to data, in particular for understanding the composition of a sample in data, and the distributions of individual processes. However, this analysis does not rely on simulation to determine the presence or absence of signal in the data. Instead, control samples in the data are used to predict the yield of each Standard Model process in the regions of parameter space where signal is expected. A list of Monte Carlo samples used for this analysis is given in Tables 4.1, 4.2, and 4.3.

An important benefit of using simulated event samples is the ability to examine the properties of particles upstream of the final decay. We are able to directly identify the path of decay chains resulting in different event topologies. In addition to a fairly accurate representation of the detector effects, the kinematic properties of all particles from the hard scatter can be examined, without the influence of detector reconstruction. These are referred to as the *generator-level*, or *true*, properties of the objects. Consideration for the particular decay chains and generator-level particle properties of simulated events is an important part of understanding the backgrounds of this analysis and constructing the data-driven predictions.

All Monte Carlo samples have corrections applied to ensure that they accurately describe the data. The effect of pile-up depends on conditions of the beam throughout the run. The weight of individual simulated events are adjusted to match the distribution of primary vertices observed in the data. The p_{T} of all jets are corrected to reflect the performance of the calorimeters. Events in the $t\bar{t}$ sample are reweighted according to the p_{T} of the top-quarks at generator level, in order to reconcile this distribution with reconstructed quantities in data. As described in Sec. 3.3, the weights of simulated events are adjusted to correctly reflect the Combined Secondary Vertex algorithm efficiency, according to the p_{T} and η of each jet. In addition, to get the maximum statistical power from these samples, no direct cut on the number of CSV medium working point jets are made. Instead, the probability of observing any particular number of CSVM b-tags in an event is calculated according to the CSV values of all jets. Then, the yield of events at each b-tag multiplicity

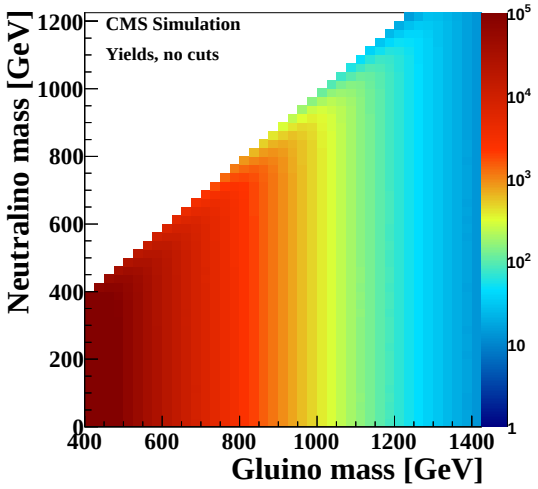

Figure 4.2: Total number of events produced by the T1bbbb SMS model in the gluino–neutralino mass plane, with 19.4 fb^{-1} of integrated luminosity from 8 TeV collisions.

is the sum of all event weights, each multiplied by its probability of observing that number of b-tags. Finally, some processes are given an additional scale factor, listed in Tables 4.1, 4.2, and 4.3, to more closely match event distributions in data from the kinematic regions we are interested in.

4.2 Characteristics of signal

The 2-dimensional parameter space of the T1bbbb simplified model is shown in Fig. 4.2. Simulated events span a gluino mass range from 400 to 1400 GeV, with a corresponding neutralino mass between 0 and 1200 GeV. The z-axis indicates the total expected event yield in 19.4 fb^{-1} of 8 TeV data. The figure clearly shows that the cross-section depends only on the gluino mass, not on the neutralino mass.

Table 4.1: Samples of simulated boson production used for constructing the analysis.

Process	MC sample name	Size [pb]	SF
W+jets	WJetsToLNu_HT-250To300_8TeV-madgraph_v2/Summer12_DR53X-PU_S10_START53_V7A-v1	57.26	
	WJetsToLNu_HT-300To400_8TeV-madgraph_v2/Summer12_DR53X-PU_S10_START53_V7A-v1	45.68	
	WJetsToLNu_HT-400ToInf_8TeV-madgraph_v2/Summer12_DR53X-PU_S10_START53_V7A-v1	30.08	
$Z \to \nu\bar{\nu}$	ZJetsToNuNu_100_HT_200_TuneZ2Star_8TeV_madgraph/Summer12_DR53X-PU_S10_START53_V7A-v1	205.2	0.9
	ZJetsToNuNu_200_HT_400_TuneZ2Star_8TeV_madgraph/Summer12_DR53X-PU_S10_START53_V7A-v1	53.1	0.9
	ZJetsToNuNu_400_HT_inf_TuneZ2Star_8TeV_madgraph/Summer12_DR53X-PU_S10_START53_V7A-v1	5.274	0.9
Drell-Yan	DYJetsToLL_HT-200To400_TuneZ2Star_8TeV-madgraph/Summer12_DR53X-PU_S10_START53_V7A-v1	23.43	
	DYJetsToLL_HT-400ToInf_TuneZ2Star_8TeV-madgraph/Summer12_DR53X-PU_S10_START53_V7A-v1	3.36	
Diboson	WW_TuneZ2star_8TeV_pythia6_tauola/Summer12_DR53X-PU_S10_START53_V7A-v1	55	
	WZ_TuneZ2star_8TeV_pythia6_tauola/Summer12_DR53X-PU_S10_START53_V7A-v1	32.3	
	ZZ_TuneZ2star_8TeV_pythia6_tauola/Summer12_DR53X-PU_S10_START53_V7A-v1	5.196	

Table 4.2: Samples of simulated top quark production used for constructing the analysis.

Process	MC sample name	Size [pb]	SF
$t\bar{t}$	TTJets_FullLeptMGDecays_8TeV-madgraph-tauola/Summer12_DR53X-PU_S10_START53_V7C-v2	13.43	0.9
	TTJets_SemiLeptMGDecays_8TeV-madgraph-tauola/Summer12_DR53X-PU_S10_START53_V7C-v1	53.2	0.9
	TTJets_HadronicMGDecays_8TeV-madgraph/Summer12e_DR53X-PU_S10_START53_V7A_ext-v1	104.1	0.9
Single-top	T_s-channel_TuneZ2star_8TeV-powheg-tauola/Summer12_DR53X-PU_S10_START53_V7A-v1	3.79	
	T_t-channel_TuneZ2star_8TeV-powheg-tauola/Summer12_DR53X-PU_S10_START53_V7A-v1	56.4	
	T_tW-channel-DR_TuneZ2star_8TeV-powheg-tauola/Summer12_DR53X-PU_S10_START53_V7A-v1	11.1	
	Tbar_s-channel_TuneZ2star_8TeV-powheg-tauola/Summer12_DR53X-PU_S10_START53_V7A-v1	1.76	
	Tbar_t-channel_TuneZ2star_8TeV-powheg-tauola/Summer12_DR53X-PU_S10_START53_V7A-v1	30.7	
	Tbar_tW-channel-DR_TuneZ2star_8TeV-powheg-tauola/Summer12_DR53X-PU_S10_START53_V7A-v1	11.1	

Table 4.3: Samples of simulated multi-jet production used for constructing the analysis.

Process	MC sample name	Size [pb]	SF
QCD	QCD_Pt-120to170_TuneZ2star_8TeV_pythia6/Summer12_DR53X-PU_S10_START53_V7A-v3	156293	1.35
	QCD_Pt-170to300_TuneZ2star_8TeV_pythia6/Summer12_DR53X-PU_S10_START53_V7A-v2	34138	1.35
	QCD_Pt-300to470_TuneZ2star_8TeV_pythia6/Summer12_DR53X-PU_S10_START53_V7A-v2	1759.5	1.35
	QCD_Pt-470to600_TuneZ2star_8TeV_pythia6/Summer12_DR53X-PU_S10_START53_V7A-v2	113.88	1.35
	QCD_Pt-600to800_TuneZ2star_8TeV_pythia6/Summer12_DR53X-PU_S10_START53_V7A-v2	26.99	1.35
	QCD_Pt-800to1000_TuneZ2star_8TeV_pythia6/Summer12_DR53X-PU_S10_START53_V7A-v2	3.550	1.35
	QCD_Pt-1000to1400_TuneZ2star_8TeV_pythia6/Summer12_DR53X-PU_S10_START53_V7A-v1	0.7378	1.35
	QCD_Pt-1400to1800_TuneZ2star_8TeV_pythia6/Summer12_DR53X-PU_S10_START53_V7A-v1	0.0335	1.35
	QCD_Pt-1800_TuneZ2star_8TeV_pythia6/Summer12_DR53X-PU_S10_START53_V7A-v1	0.001829	1.35

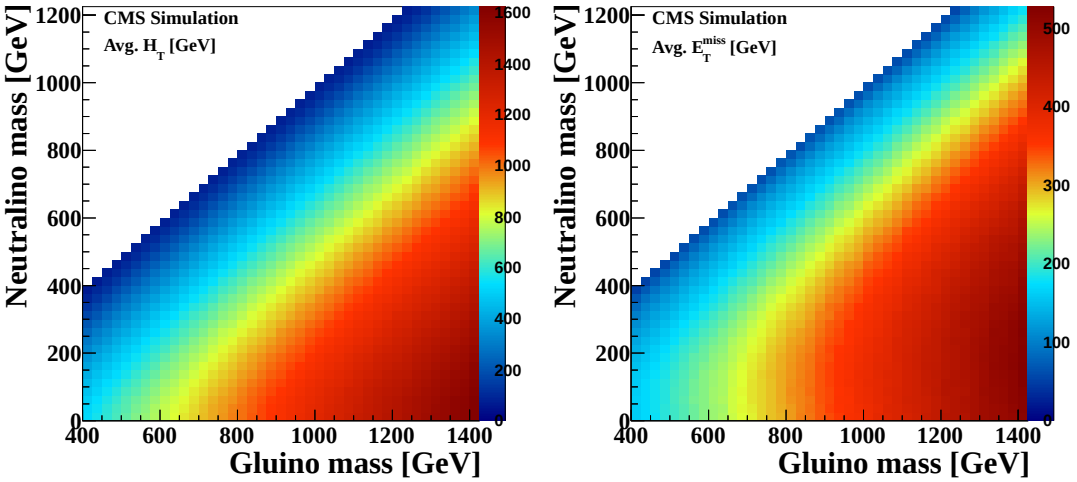

(a) Average H_{T}.

(b) Average $E_{\mathrm{T}}^{\mathrm{miss}}$.

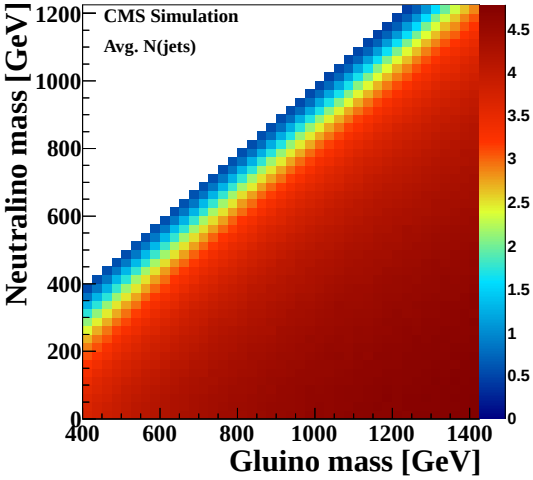

(c) Average number of jets.

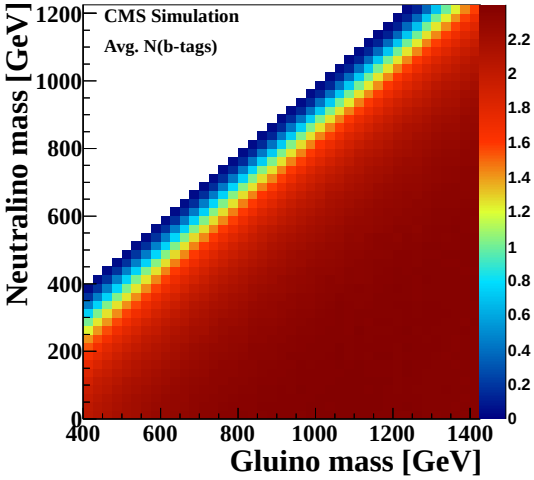

(d) Average number of b-tag jets.

Figure 4.3: Average values of kinematic quantities in T1bbbb events in the gluino–neutralino mass plane.

As a purely hadronic final state with missing transverse momentum, the T1bbbb simplified model has several interesting kinematic properties. The average values for important event quantities in the gluino – neutralino mass plane are shown in Fig. 4.3. The z-axis of Fig. 4.3(a) shows the average H_{T} (the scalar sum of jet p_{T} in an event) for each mass point. For T1bbbb, this quantity is determined by the energy available from the mass of the gluinos after subtracting the mass of the neutralinos, whose energy not deposited in the detector. This results in the diagonal pattern of increasing average H_{T} with increasing mass difference between the gluino and neutralino. The average $E_{\mathrm{T}}^{\mathrm{miss}}$ behaves in a similar way with increasing masses, but increases more slowly at lower neutralino masses, where there is relatively less of the energy from the collision going to the invisible particles. Every simulated event in the T1bbbb model has at least four jets arising from the decay of the two gluinos, as well as additonal jets from initial-state and final-state radiation. The average number of reconstructed jets is plotted in Fig. 4.3(c). For most of the mass plane, we observe the average number of reconstructed jets is indeed four, but drops dramatically close to the diagonal line where the gluino mass is close to the neutralino mass. In this region, there is not enough visible energy to produce jets over the p_{T} threshold defined in Sec. 3.3. Since the momentum spectra of jets from the hard scatter are soft here, the observed energy in the event is especially sensitive to jets from initial state and final state radiation.

A main feature of T1bbbb is the generation of four jets associated with b-quark fragmentation (*b-jets*). The presence of multiple jets satisfying the medium working point criteria of the Combined Secondary Vertex algorithm (described in Sec. 3.3) are an impor-

tant feature that is characteristic of many natural models of supersymmetry. Figure 4.3(d) shows the average number of reconstructed CSVM b-tagged jets in the gluino–neutralino mass plane. Once the threshold for reconstructing a jet is satisfied, the average number of reconstructed b-jets is largely determined by the efficiency of the CSV algorithm. With an efficiency of tagging a b-jet at about 65%, this results in an average of roughly 2.4 identified b-jets for most of the parameter space.

The features of T1bbbb events across the gluino–neutralino mass plane inform the selection criteria used in this search. First, a subset of the data that includes multiple jets and missing transverse energy is defined by choosing the appropriate trigger paths. This is discussed in the next section.

4.3 Triggers and datasets

As discussed in Sec. 3.2.5, triggers are necessary to keep the rate of data-taking at manageable levels, so events must have interesting properties before being fully processed and stored. As the year progresses and improvements to the beam are made, the number of protons per bunch increases, causing the instantaneous luminosity to increase. This means an increase in not only the rate of hard-scatter events, but also in the number of particles from low energy collisions of protons in the same beam crossing (*in-time* pile-up) or spray from other beam crossings (*out-of-time* pile-up). At higher instantaneous luminosity, some triggers must use the coincidence of multiple objects in order to keep thresholds low, known as *cross-triggers*.

Table 4.4: Triggers used to construct the main analysis sample of events.

Runs A, B	Runs C, D
HLT_PFHT350_PFMET100	HLT_PFNoPUHT350_PFMET100
HLT_PFHT650	HLT_PFNoPUHT650
HLT_DiCentralPFJet50_PFMET80	HLT_DiCentralPFNoPUJet50
	_PFMETORPFMETNoMu80

Triggers are designed based on the type of final state of a particular analysis. Since this analysis is focused on both a moderate number of high energy jets and missing transverse energy, the data sample is constructed from a logical "OR" of triggers to fully span the desired parameter space. These are listed in Table 4.4. The first two triggers used across all four runs (HLT_PF∗HT350_PFMET100, HLT_PF∗HT650) are based on the scalar sum of transverse energy of all particle-flow objects with moderate p_{T} in the event. HLT_PF∗HT350_PFMET100 is also known as a cross-trigger, since it requires a relatively large amount of missing transverse energy in the event, which keeps the rate of events passing the trigger small, given its relatively low cut on H_{T}. The third trigger requires at least two jets with moderate p_{T} in the barrel of the detector, along with a moderate amount of transverse momentum. As the instantaneous luminosity increases for Runs C and D, an algorithm for reducing the effect of pile-up energy is applied.

During its 2012 run, CMS collected a total of $19.4\,\mathrm{pb}^{-1}$ of integrated luminosity. For each period of data-taking, events are stored based on the triggers they pass. For

example, events satisfying any of a number of H_{T}-based triggers are stored in the H_{T} dataset. Due to the changing triggers, the dataset definitions used in the analysis change over the course of the year. They are listed in Table 4.5, along with the corresponding luminosity for each period of data-taking. With the increased need for cross-triggers after Run A, the H_{T} dataset is split into two datasets. Some events passing H_{T} triggers appear in multiple datasets, so care is taken to remove duplicates from the sample.

Since event triggering is based of fast calculations often not based on the full detector, the (*online*) quantity on which it makes its decision does not precisely match the final reconstructed (*offline*) quantity with all known corrections applied. Figure 4.4 shows the efficiency of triggering on online H_{T} and $E_{\mathrm{T}}^{\mathrm{miss}}$ with respect to offline quantities. To obtain this efficiency, I begin with an independent dataset. This means that all events must pass a trigger unrelated to $E_{\mathrm{T}}^{\mathrm{miss}}$ or H_{T}. The ratio of events passing the trigger of interest with respect to the total is the trigger efficiency, which varies with respect to the more accurate offline reconstruction value of that quantity. An offline selection in which the trigger efficiency is both high and uniform with respect to offline measurement is desirable.

To obtain the efficiency of the PFHT650 trigger, and the H_{T} component of the PFHT350_PFMET100 cross-trigger, we take a sample of events in the SingleMu dataset where a muon is reconstructed. This ensures that the dataset is not biased with respect to H_{T}. From Fig. 4.4(a), we see that the triggers achieve their maximum efficiency when the offline value is slightly above the online value of H_{T}. This is because the trigger uses a very fast algorithm for reconstructing the objects before deciding whether to keep an event. On

Table 4.5: Datasets used for the analysis sample, constructed from events passing hadronic triggers.

Sample name	$\mathcal{L}$ (fb^{-1})
/MET/Run2012A13Jul2012v1/AOD /HT/Run2012A13Jul2012v1/AOD	0.807
/MET/Run2012B13Jul2012v1/AOD /HTMHT/Run2012B13Jul2012v1/AOD /JetHT/Run2012B13Jul2012v1/AOD	4.421
/MET/Run2012C24Aug2012v1/AOD /HTMHT/Run2012C24Aug2012v1/AOD /JetHT/Run2012C24Aug2012v2/AOD	0.495
/MET/Run2012CPromptRecov2/AOD /HTMHT/Run2012CPromptRecov2/AOD /JetHT/Run2012CPromptRecov2/AOD	6.402
/MET/Run2012DPromptRecov1/AOD /HTMHT/Run2012DPromptRecov1/AOD /JetHT/Run2012DPromptRecov1/AOD	7.273

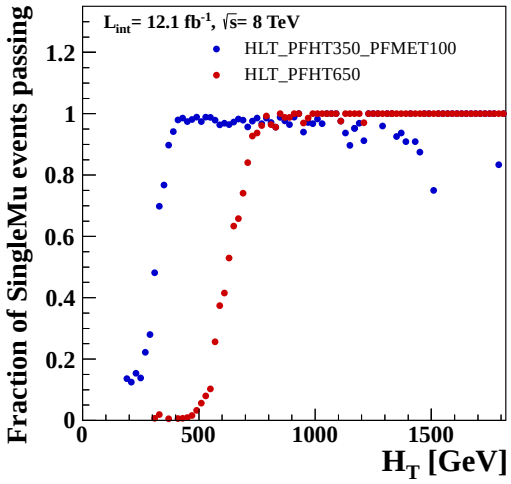

(a) Efficiency of H_{T}.

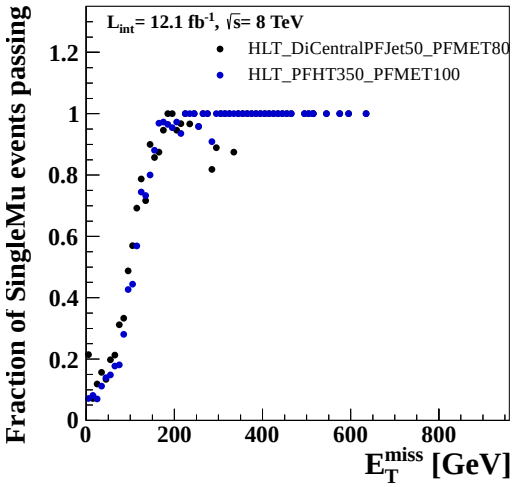

(b) Eff. $E_{\mathrm{T}}^{\mathrm{miss}}$ with 1 lepton.

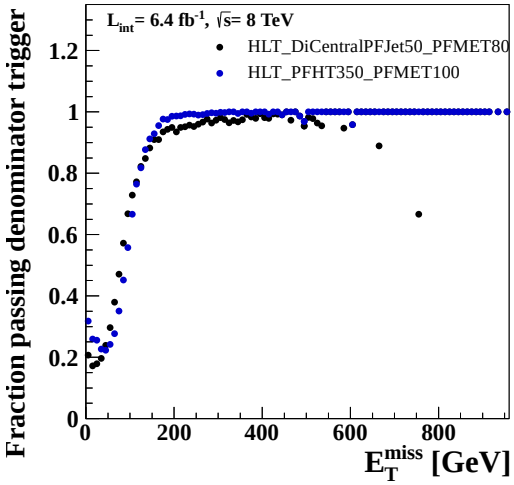

(c) Eff. $E_{\mathrm{T}}^{\mathrm{miss}}$ with 0 leptons.

Figure 4.4: Efficiency of $E_{\mathrm{T}}^{\mathrm{miss}}$ and H_{T} trigger selection, with respect to the reconstructed quantity.

the other hand, the offline quantity is more accurate. The H_{T} component (or *leg*) of the PFHT350_PFMET100 trigger becomes fully efficient at an offline value of H_{T} of 400 GeV. All events shown in this curve require offline $E_{\mathrm{T}}^{\mathrm{miss}}$ >200 GeV, to be sure they are well above the trigger threshold for the $E_{\mathrm{T}}^{\mathrm{miss}}$ leg of this trigger, and that it is not adding any inefficiency to this curve. To ensure that the data-taking rate is consistent across the chosen phase space for this analysis, we must apply a cut H_{T} >400 GeV to all events considered. In this way, the trigger limits the amount of phase space that can be considered for any one analysis.

The other important component to the triggers for this analysis is the $E_{\mathrm{T}}^{\mathrm{miss}}$ leg. $E_{\mathrm{T}}^{\mathrm{miss}}$ can occur in a Standard Model event due to the presence of neutrinos or through the mismeasurement of jets. The resolution of $E_{\mathrm{T}}^{\mathrm{miss}}$ is poorer when it arises from jet mismeasurement, rather than the presence of weakly-interacting particles. The resulting smeared $E_{\mathrm{T}}^{\mathrm{miss}}$ spectrum is responsible for a broad increase in the efficiency of online $E_{\mathrm{T}}^{\mathrm{miss}}$ in multi-jet events. Therefore, we calculate the efficiencies of the $E_{\mathrm{T}}^{\mathrm{miss}}$-based cross-triggers separately for a QCD enriched sample and for a sample with a reconstructed lepton, the presence of which indicates an electroweak process. For the single lepton case, we again turn to the SingleMu dataset, selecting events with one reconstructed muon, H_{T} >400 GeV, and at least two jets with p_{T} >70 GeV. From this sample, unbiased with respect to $E_{\mathrm{T}}^{\mathrm{miss}}$, we plot the efficiency of the $E_{\mathrm{T}}^{\mathrm{miss}}$ legs of the PFHT350_PFMET100 and DiCentralPFJet50_PFMET80 triggers with respect to the offline $E_{\mathrm{T}}^{\mathrm{miss}}$. The efficiency of the selected events passing these triggers is shown in Fig. 4.4(b). We expect the increase in efficiency to be broader for multi-

jets events, therefore requiring a higher offline $E_{\mathrm{T}}^{\mathrm{miss}}$ before the maximum efficiency of the $E_{\mathrm{T}}^{\mathrm{miss}}$ legs of the triggers are reached. This is calculated using a jet sample from a portion of the dataset, in which events pass a prescaled H_{T} trigger much lower than the one used in this analysis. As before, events in the efficiency calculation must have H_{T} >400 GeV and 2 jets with p_{T} >70 GeV. Figure 4.4(c) shows that an online trigger threshold at $E_{\mathrm{T}}^{\mathrm{miss}}$ =100 GeV does not attain a flat, stable efficiency until 200 GeV of offline $E_{\mathrm{T}}^{\mathrm{miss}}$ is required. This value sets the lower bound on the search region for this analysis. However, since the efficiency only falls off slightly between 150 and 200 GeV, we can use data in this region for validation, provided we accurately account for the loss of events due to the trigger. When considering the full suite of triggers, we find that this inefficiency only effects events at low H_{T}, and since we later split the data sample into two regions of H_{T}, we must correct the yield of simulated events in the lower region. All simulated events with $E_{\mathrm{T}}^{\mathrm{miss}}$ 150–250 GeV and H_{T} 400–800 GeV receive a trigger efficiency correction of 12% for multi-jet samples and 1.66% for all other samples.

Figure 4.5 shows the yields and efficiencies of T1bbbb with the minimum $E_{\mathrm{T}}^{\mathrm{miss}}$ and H_{T} cuts applied. Due to the constraints of the triggers described above, all events considered in this analysis are required to have H_{T} >400 GeV, and $E_{\mathrm{T}}^{\mathrm{miss}}$ >150 GeV. The efficiency of these cuts in the T1bbbb mass plane is very high when the mass difference of the gluino and neutralino is more than a few hundred GeV. The shape of the total yields in this mass plane reflects the decrease in cross-section at increasing gluino mass, which drops more steeply where the mass difference is low, as expected. Overall, the minimum H_{T} and

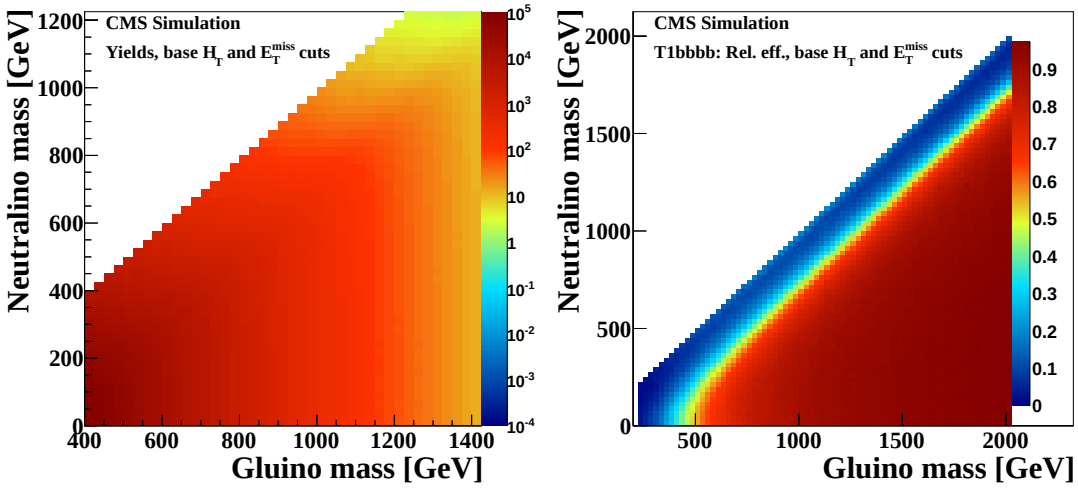

(a) T1bbbb yield with baseline cuts.

(b) T1bbbb efficiency after baseline cuts.

Figure 4.5: Effect of the minimum H_{T} and $E_{\mathrm{T}}^{\mathrm{miss}}$ selection criteria on T1bbbb events in the gluino–neutralino mass plane, with H_{T} >400 GeV and $E_{\mathrm{T}}^{\mathrm{miss}}$ >150 GeV. Shown is the total yield with 19.4 fb^{-1} of integrated luminosity from 8 TeV collisions (left), and the efficiency of events passing the selection criteria (right).

$E_{\mathrm{T}}^{\mathrm{miss}}$ requirements have only a small effect on this search away from the diagonal. With these triggers chosen, more selection criteria can be defined to reduce the yields of Standard Model processes while preserving signal efficiency.

4.4 Selection criteria

In addition to the trigger-based cuts on H_{T} and $E_{\mathrm{T}}^{\mathrm{miss}}$ described above, additional cuts are applied to obtain a data sample targeting events from b-rich hadronic models of supersymmetry, while suppressing backgrounds. Figure 4.6 shows a comparison of the H_{T} and $E_{\mathrm{T}}^{\mathrm{miss}}$ shapes for three points in the T1bbbb gluino–neutralino mass plane and three

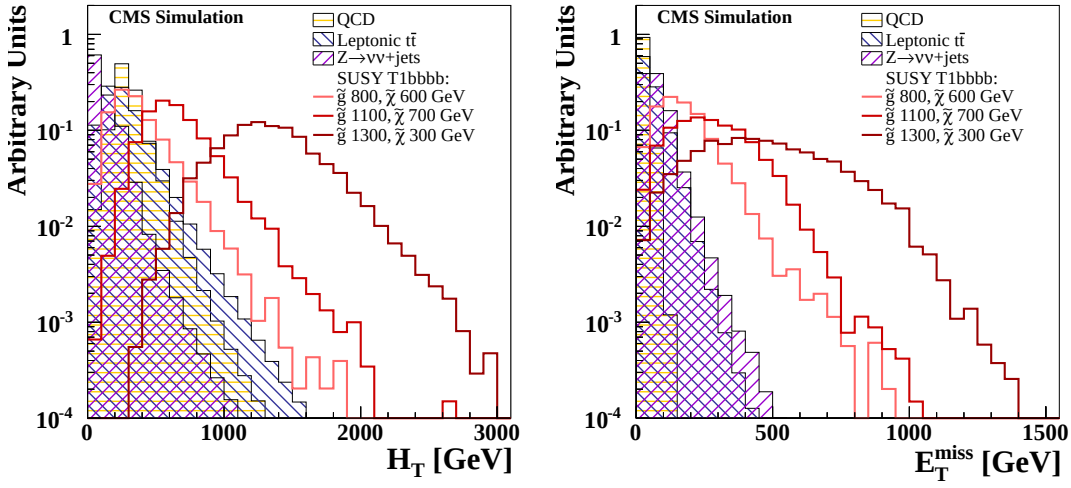

Figure 4.6: Shape comparison of H_T (left) and E_T^{miss} (right) between the major Standard Model backgrounds (hatched, colored histograms) and a few representative T1bbbb scenarios (red lines). No selection criteria are applied, and each sample is normalized to unity.

important Standard Model backgrounds in this analysis. In general, the distributions of both quantities from T1bbbb samples are broader than the Standard Model processes.

The contributions from multi-jet (QCD) processes are shown in yellow, which produce a moderate amount of H_{T}. The H_{T} distribution of multi-jet events peaks at zero and falls exponentially, but it is artificially truncated at low H_{T} in this figure for the purpose of demonstration. The $E_{\mathrm{T}}^{\mathrm{miss}}$ spectrum for these events is very steep, since missing transverse energy only occurs in these events from the mismeasurement of jets. Even though high-$E_{\mathrm{T}}^{\mathrm{miss}}$ QCD events are relatively rare, the cross-section of multi-jet production is very large, so these events must be considered carefully.

Distributions involving a Z boson decaying to two neutrinos are shown in violet. The Z+jets contribution has fairly low H_{T} since jets are produced via final state radiation,

as seen in Fig. 4.6(a). In contrast, Fig. 4.6(b) demonstrates that it has a relatively broad $E_{\mathrm{T}}^{\mathrm{miss}}$ spectrum, due to the presence of two weakly interacting particles in every final state.

The final, and most important, background shown is top-quark pair production, shown in blue. These events are particularly important because they always involve the production of two b-quarks. These jets, and others produced from the W boson decay or final state radiation, contribute to the broad H_{T} spectrum. The final state has between zero and two neutrinos, which contributes to the broad $E_{\mathrm{T}}^{\mathrm{miss}}$ spectrum. Much of this analysis involves controling and understanding the $t\bar{t}$ background.

The three T1bbbb models shown in Fig. 4.6 represent a range of cross-sections and sparticle mass differences close to the expected limit of sensitivity of this analysis. The mass point shown here with the smallest gluino mass and gluino–neutralino mass difference has the gluino at 800 GeV and neutralino at 600 GeV. Although this model has a relatively large cross-section, the small mass difference means that there is little visible energy available to the jets, resulting in an H_{T} spectrum very similar to Standard Model processes. The other two T1bbbb models included in the figures have increasing gluino mass and mass difference: one scenario has a gluino mass of 1.1 TeV and neutralino mass of 700 GeV, and the other has a gluino mass of 1.3 TeV and neutralino mass of 300 GeV. Each of these models has a higher average H_{T} and $E_{\mathrm{T}}^{\mathrm{miss}}$ spectrum than the one before it.

Ultimately, one of the truly distinctive features of T1bbbb is the shape of the $E_{\mathrm{T}}^{\mathrm{miss}}$ spectrum. Along with the number of b-jets, these quantities represent the strongest discriminators between signal and Standard Model background events. While the definition

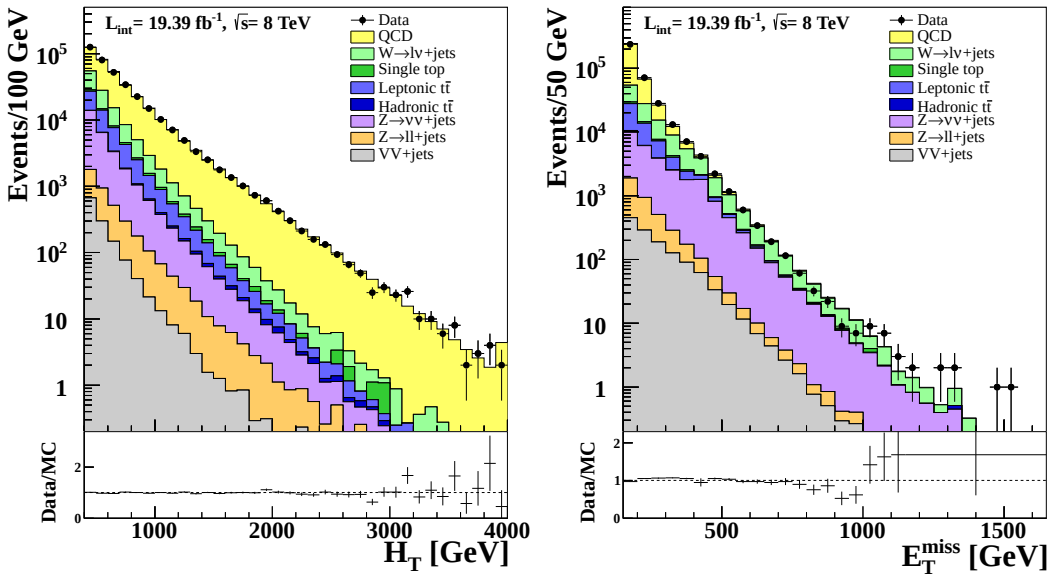

Figure 4.7: Distributions of H_{T} (left) and $E_{\mathrm{T}}^{\mathrm{miss}}$ (right) with baseline cuts, H_{T} >400 GeV, $E_{\mathrm{T}}^{\mathrm{miss}}$ >150 GeV, and $\geq$1 b-tag. Black points with error bars are data. Stacked, colored histograms are simulated events.

of $E_{\mathrm{T}}^{\mathrm{miss}}$ is not itself a complicated quantity, the high tail of the $E_{\mathrm{T}}^{\mathrm{miss}}$ spectrum, which we are interested in probing, is not perfectly understood, and may be sensitive to fluctuations. As a result, the goal of this analysis is to examine the high $E_{\mathrm{T}}^{\mathrm{miss}}$ tails of our data sample, and to use data-driven methods to characterize the expected shapes of the Standard Model processes, especially $t\bar{t}$.

The H_{T} and $E_{\mathrm{T}}^{\mathrm{miss}}$ distributions from the data sample defined above are shown in Fig. 4.7(a) and Fig. 4.7(b), respectively. These events satisfy the minimum H_{T} and $E_{\mathrm{T}}^{\mathrm{miss}}$ values determined by the performance of the triggers as previously described, along with at least one CSVM-tagged jet. The data are represented by black dots, and simulated Standard Model samples are shown as colored and stacked histograms. The simulated samples are used to demonstrate that the composition of the data is well understood, by

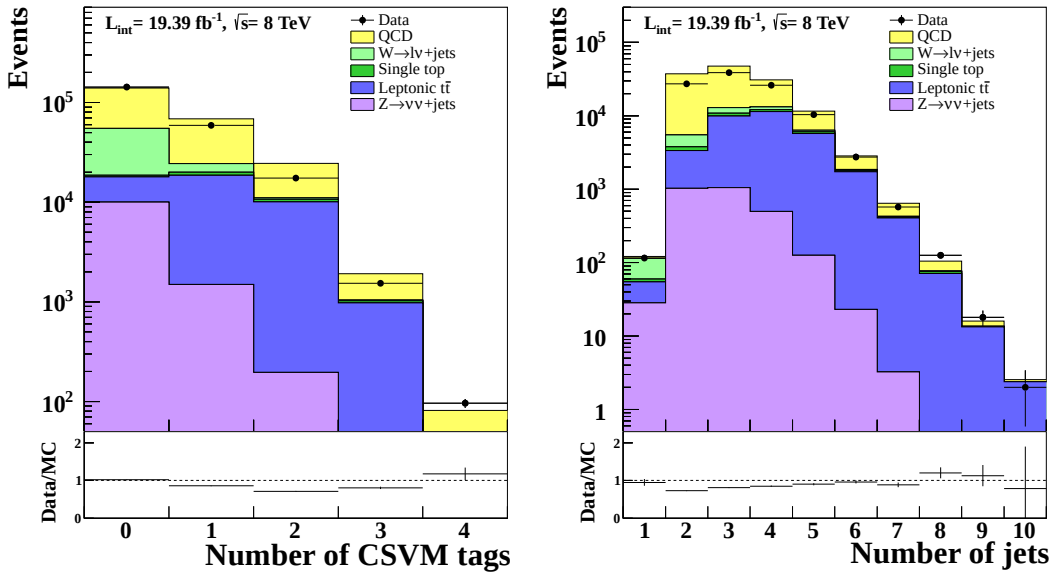

Figure 4.8: Distributions of CSVM b-tag multiplicity (left) and jet multiplicity (right) with H_{T} >400 GeV and $E_{\mathrm{T}}^{\mathrm{miss}}$ >150 GeV. Right plot requires ≥1 CSVM b-tag. Black points with error bars are data. Stacked, colored histograms are simulated events.

the close matching of its total shape to the observed distribution in data. This data sample is dominated by QCD events, which are highly peaked at low values of $E_{\mathrm{T}}^{\mathrm{miss}}$. The event yields in data and for each SM process are shown in the first row in Table 4.6. This table lists their yields after the successive application of several other requirements to the data and MC samples, which are discussed one by one below.

Since we are only interested in events with b-tagged jets, we require at least least one CSVM b-tag in every event. The yield in data after this requirement is listed in the second line of Table 4.6, and the distribution of the number of CSVM jets in data is shown in Fig. 4.8, with the baseline H_{T} and $E_{\mathrm{T}}^{\mathrm{miss}}$ cuts applied. The effect of this cut on signal is shown in Fig. 4.9. Since a b-tagged jet is allowed to have a p_{T} as low as 30 GeV, this cut has excellent efficiency even to the very smallest mass difference between the gluino

Table 4.6: Comparison of yields from data and simulation with increasing event selection requirements. The events in the second row pass the baseline selection.

Requirement	Purpose	Data	Total MC	QCD	$t\bar{t}$	$Z \to \nu\nu$
$E_T^{miss} > 150$ GeV	Above trigger	364399	366320	246732	31082	24229
$H_T > 400$ GeV	thresholds					
≥1 CSVM b-tag	Loosest b-tag requirement	105909	132468	90809	30398	3173
2 jets p_T >70 GeV	Signal includes	78008	93799	58830	27667	1665
3rd jet p_T >50 GeV	multiple jets					
E_T^{miss} >250 GeV	Signal includes invisible LSPs	9381	11105	3784	5230	579
$\Delta\phi_N$ >4.0	Reduces QCD	6435	6716	549	4387	529
e/μ veto	Not in signal,	4267	4161	542	2407	529
Iso. track veto	reduces t, W	3181	3120	513	1646	508
=2 CSVM b-tags	Signal includes	690	783	104	565	55
=3 CSVM b-tags	multiple b-tags	67	65	5	55	2
≥4 CSVM b-tags		9	2.4	0.07	2.2	0.06

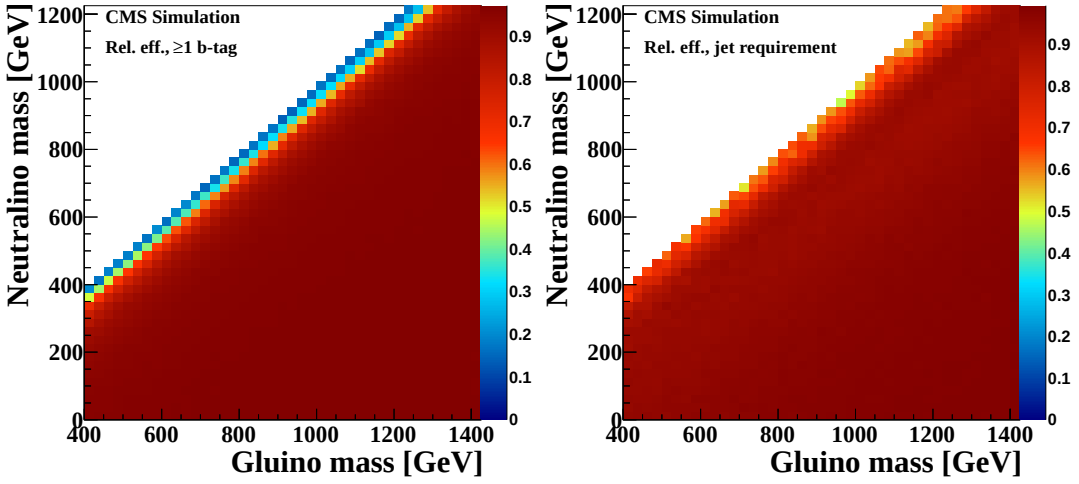

(a) ≥1 b-tagged jet.

(b) ≥3 jets.

Figure 4.9: Relative efficiency of applying b-tag (left) and jet (right) requirements in the gluino–neutralino mass plane. Left plot shows efficiency with respect to requiring only H_{T} >400 GeV and $E_{\mathrm{T}}^{\mathrm{miss}}$ >150 GeV. The right plot adds ≥1 b-tag to the demoninator, showing the relative efficiency of requiring 2 jets with p_{T} >70 GeV, and a third with p_{T} >50 GeV.

and neutralino, along the diagonal in the plot. Tightening this selection is discussed in the following section.

We then require at least three jets, two of which with p_{T} greater than 70 GeV, and a third with p_{T} >50 GeV. The T1bbbb models involve at least four jets in the hard scatter, so we focus on data with moderate jet multiplicity. The choice of p_{T} is based on a general optimization across the gluino–neutralino mass plane. The distribution of jet multiplicity is shown in Fig. 4.8, for jets with p_{T} >50 GeV in data and simulated events. The requirement of at least three jets removes some QCD, W+jets, and $Z \to \nu\bar{\nu}$ background. At the same time, it eliminates hardly any T1bbbb events, as seen in Fig. 4.9. Here, you can see the effect of initial and final state radiation on events on the diagonal with H_{T} >400 GeV, where producing 50 GeV jets is fairly common.

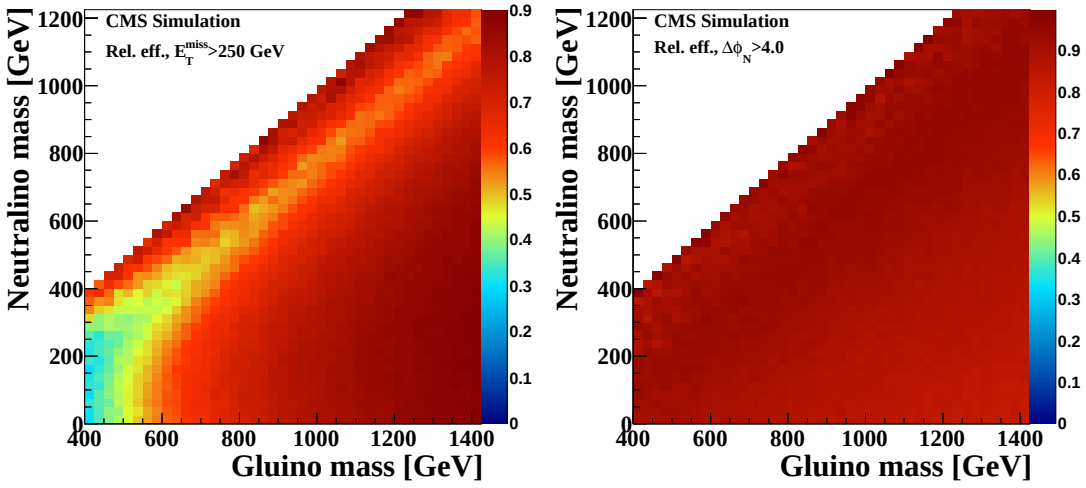

(a) $E_{\mathrm{T}}^{\mathrm{miss}}$ >250 GeV (b) $\Delta\phi_N^{\mathrm{min}}$ >4.0

Figure 4.10: Relative efficiency of applying tighter $E_{\mathrm{T}}^{\mathrm{miss}}$ (left) and $\Delta\phi_N^{\mathrm{min}}$ (right) requirements in the gluino–neutralino mass plane. Each plot includes all selection criteria listed above that quantity in Table 4.6.

Next, the cutflow table, Table 4.6, shows the result of increasing the $E_{\mathrm{T}}^{\mathrm{miss}}$ cut to 250 GeV. This removes a large amount of Standard Model background, in particular QCD events. As discussed above, it is not expected to dramatically decrease the signal yield, and Fig. 4.10(a) shows this. The $E_{\mathrm{T}}^{\mathrm{miss}}$ actually increases close to the diagonal in the gluino–neutralino mass plane. This is because to have the necessary H_{T} and jet requirements, these events must have significant initial state radiation. This causes a dramatic imbalance in the energy of these events. The effect disappears when the mass difference is around 400 GeV, when jets from the hard scatter are sufficient to pass the H_{T} cut.

Even with a fairly tight $E_{\mathrm{T}}^{\mathrm{miss}}$ cut at 250 GeV, the MC yield in Table 4.6 indicates that there is a significant fraction of QCD in the sample. In these events, large missing transverse energy appears when the magnitude of the p_{T} of a jet has been greatly mismea-

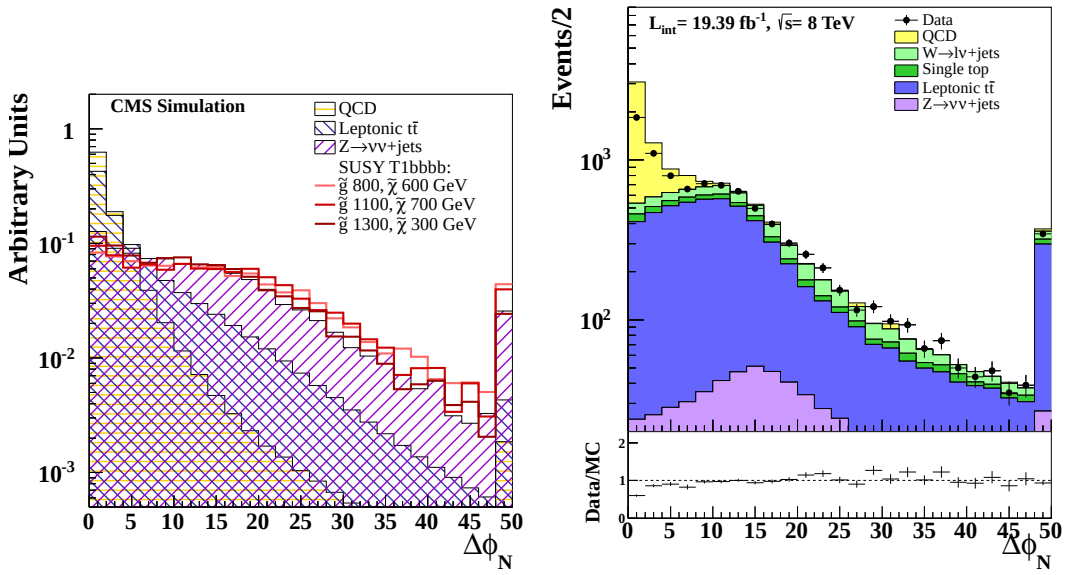

(a) Shapes with no selection criteria.

(b) All previous cuts applied.

Figure 4.11: Distribution of $\Delta\phi_N^{\min}$, the smallest normalized angle between one of the three leading jets and the E_T^{miss}. The shape comparison (left) shows backgrounds (hatched, colored histograms) and T1bbbb signal (red lines), with no selection criteria applied, and normalized to unity. The data and MC comparison (right) indicates data with black points with error bars, while the stacked, colored histograms are simulated events. All selection criteria above the $\Delta\phi_N^{\min}$ requirement listed in Table 4.6 are applied.

sured, giving the appearance of an imbalance in the transverse plane. In these cases, the measured $E_{\mathrm{T}}^{\mathrm{miss}}$ aligns with the mismeasured jet. Many analyses use the angle between the $E_{\mathrm{T}}^{\mathrm{miss}}$ and any of the highest p_{T} jets as an indicator of this effect, and apply a cut on that measurement. This analysis constructs a similar quantity, $\Delta\phi_N^{\min}$, which has the advantage of being independent of $E_{\mathrm{T}}^{\mathrm{miss}}$. First, the quantity $\Delta\phi_j$ is calculated for each of the three jets with highest p_{T}, j,

$$\Delta\phi_j = \frac{\Delta\phi(j, E_{\mathrm{T}}^{\mathrm{miss}})}{\sin^{-1}(\Delta_{Tj}/E_{\mathrm{T}}^{\mathrm{miss}})}, \tag{4.1}$$

where

$$\Delta_{Tj} = 0.1 \times \frac{\sqrt{\Sigma_{i \neq j}[p_x^j p_y^i - p_y^j p_x^i]^2}}{p_T^j}. \tag{4.2}$$

The quantity $\Delta\phi_j$ takes the angle between the $E_{\mathrm{T}}^{\mathrm{miss}}$ and jet j, $\Delta\phi(j, E_{\mathrm{T}}^{\mathrm{miss}})$, and scales it according to the effect of the resolution of all other jets in the event. This is done by assigning a resolution of 10% to each of the reconstructed jets, and summing their components transverse to jet j. The minimum value of $\Delta\phi_j$, is called $\Delta\phi_N^{\mathrm{min}}$, and it is discussed in greater detail in Sec. 5.5. For the purposes of event selection, we observe that shape of $\Delta\phi_N^{\mathrm{min}}$ is very different according to the number of weakly interacting particles in the event, Fig. 4.11(a). Multi-jet processes have no neutrino, so their distribution is sharply peaked at zero. Most $t\bar{t}$ events include zero or one neutrino in the final state, so its distribution is broader, but still maintains a peak at zero. In contrast, $Z \to \nu\bar{\nu}$ always produces two neutrinos, therefore its shape is the broadest, with no peak at low values. Similarly, signal events have two neutralinos, and all three scenarios shown have the same shape as $Z \to \nu\bar{\nu}$. The $\Delta\phi_N^{\mathrm{min}}$ variable is an excellent way of filtering events with missing energy from jet mismeasurement.

Figure 4.11(b) compares the distribution of $\Delta\phi_N^{\mathrm{min}}$ in data and simulated events. All selection criteria discussed up to this point are applied. The plot shows that the remaining QCD is indeed pushed to low values. The distributions of all other backgrounds decrease at low values of $\Delta\phi_N^{\mathrm{min}}$, since they involve the weak interaction and contain leptons. A threshold at $\Delta\phi_N^{\mathrm{min}} > 4$ is applied, to remove events with jet mismeasurement responsible for the high $E_{\mathrm{T}}^{\mathrm{miss}}$. The effect of this threshold on signal is shown in Fig. 4.10(b). It

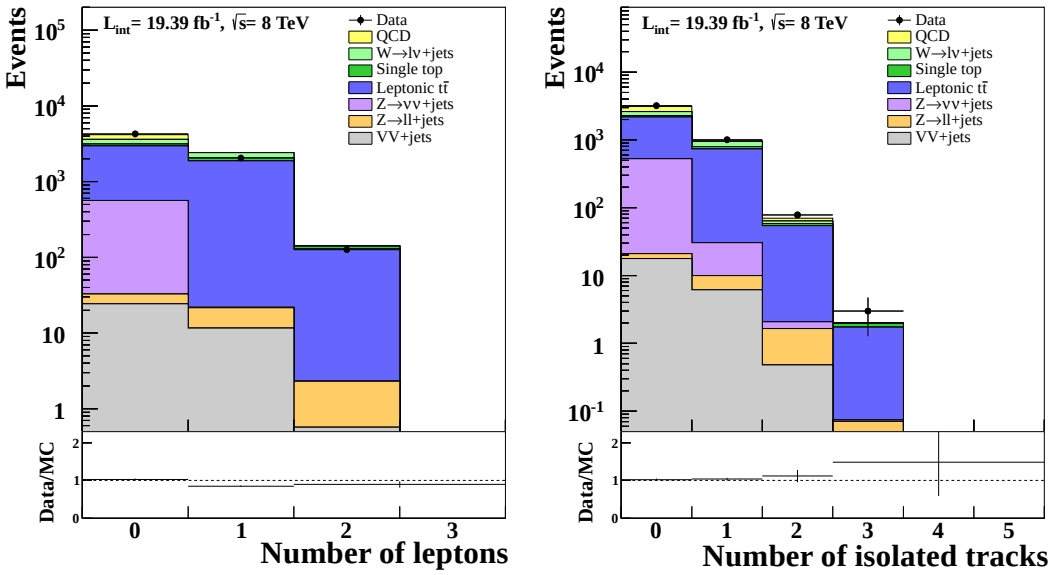

Figure 4.12: Distribution of electron and muon yields (left) and isolated track yields (right) for each event passing all selection criteria listed above that quantity in Table 4.6. Black points with error bars are data. Stacked, colored histograms are simulated events.

is almost perfectly efficient across the entire gluino–neutralino mass plane. A very slight decrease in efficiency occurs at high mass difference between the gluino and neutralino, because at this extreme we might expect additional hadronization causing some jets to be accidentally close to a neutralino. At this point, the background is dominated by $t\bar{t}$, with some small contributions from W+jets and $Z \to \nu\bar{\nu}$.

The simplified model of supersymmetry that we are interested in does not include any charged leptons in the final state, therefore these events are removed from the signal sample. Electrons and muons are reconstructed as particle-flow objects, and are defined using the criteria discussed in Sec. 3.3. The multiplicity of electrons and muons is shown in shown in Fig. 4.12. Applying a veto to events with reconstructed electrons or muons with p_{T} greater than 10 GeV not only provides a signal region statistically independent

from searches for supersymmetry with leptons in the final state, it also serves as a good suppressor to some backgrounds. Events with a charged weak decay produce a neutrino, appearing as significant $E_{\mathrm{T}}^{\mathrm{miss}}$ in the detector, along with a charged lepton. Requiring zero charged leptons reduces the contributions of top-quark and W+jets events in the signal sample. In fact, the largest Standard Model background in this analysis is $t\bar{t}$ production in which a charged lepton from W boson decay is not observed in the detector or did not pass the quality requirements necessary for the veto. An additional veto rejects events with isolated charged particles in the tracker, Fig. 4.12. This veto further removes electrons and muons that might not have been well reconstructed, and removes some isolated taus, which are notoriously difficult to reconstruct due to the similarity of their decay products to ordinary jets. Both plots show that each multiplicity of charged leptons and tracks are well understood in data. Inverting the charged lepton veto and removing the isolated track veto provides a very important control sample with which to study top-quark and W boson backgrounds, as described in Ch. 5.

With these requirements, the composition of the analysis sample has changed dramatically compared to the loose baseline selection on H_{T} and $E_{\mathrm{T}}^{\mathrm{miss}}$. Figure 4.13 shows the relative yields of Standard Model backgrounds in pie charts for three stages of the cutflow. At first, the data is dominated by multi-jet processes. Figure 4.13(b) shows the composition after all the selection criteria, one of the last lines in Table 4.6. At this point, $t\bar{t}$ dominates, but there is still significant amounts of QCD, W+jets, and $Z \to \nu\bar{\nu}$ events. In

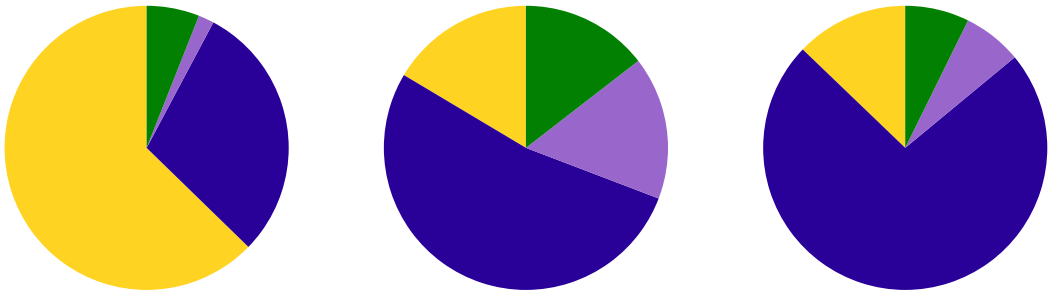

(a) Baseline selection. (b) Full selection, ≥1 CSVM. (c) Full selection, ≥2 CSVM.

Figure 4.13: Composition of Standard Model backgrounds with increasing selection criteria, determined from simulated events. The yellow section represents the relative yield of multi-jets (QCD) events, the blue section represents $t\bar{t}$, and violet represents the yield from $Z \to \nu\bar{\nu}$. The green section represents the remaining backgrounds, almost entirely W+jets and single-top production. Left: Requiring H_{T} >400 GeV, $E_{\mathrm{T}}^{\mathrm{miss}}$ >150 GeV, 2 jets with p_{T} >70 GeV, a third jet with p_{T} >50 GeV, and ≥1 CSVM b-tagged jet. Center: Additional requirements of $E_{\mathrm{T}}^{\mathrm{miss}}$ >250 GeV, $\Delta\phi_N^{\mathrm{min}}$ >4, e/μ veto, and isolated track veto. Right: Additional requirement of ≥2 CSVM b-tagged jets.

order to simplify the background composition while maintaining a high efficiency for signal, we can increase the b-tag multiplicity, as seen at the bottom of Table 4.6.

Figure 4.13(c) provides an estimate of the relative yields of each background with ≥2 b-tagged jets. We see that $t\bar{t}$ production is over 70% of the sample, roughly 10% each coming from QCD and production of a Z boson decaying to two neutrinos, and the final 10% from other sources, notably W boson and single top-quark production. While we observe good agreement between shapes and yields from MC simulation and data in this section, we do not want to rely on simulation for the yields in the high tail of the $E_{\mathrm{T}}^{\mathrm{miss}}$ distribution. The total efficiency of signal and the effect of tightening the b-tag selection is shown in Fig. 4.14. Both plots in this figure include all of the selection criteria. As expected, the efficiency of signal increases with the difference between the gluino and neutralino masses,

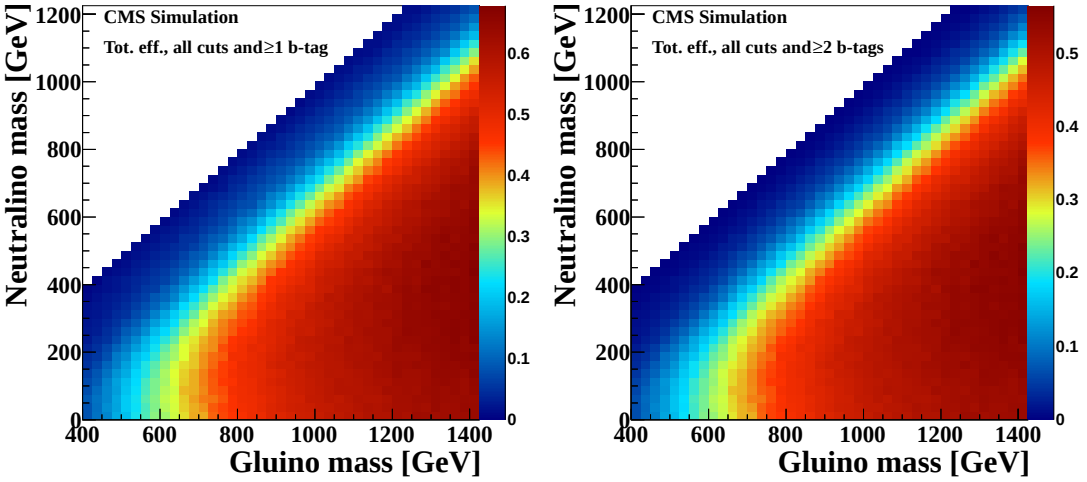

(a) ≥1 CSVM b-jet.

(b) ≥2 CSVM b-jets.

Figure 4.14: Total efficiency of T1bbbb in the gluino–neutralino mass plane, using the selection criteria from Table 4.6.

as more energy becomes available in jets and $E_{\mathrm{T}}^{\mathrm{miss}}$. In the region where the mass difference is greater than 400 GeV, the efficiency is good, between 15-70%. Requiring a second b-tag only reduces the overall efficiency by about 10%.

4.5 Definition of signal region

With the selection criteria for the analysis established, we further refine the sample into several signal regions. Since T1bbbb has multiple b-jets, we require two or more in the signal region. Any signal with one reconstructed b-jet would be overwhelmed by Standard Model background. Therefore, the selection criteria discussed above with only one b-jet is an important validation region. It is kinematically very similar to the signal region, with significant amounts of each background. All studies and data-driven predictions will be

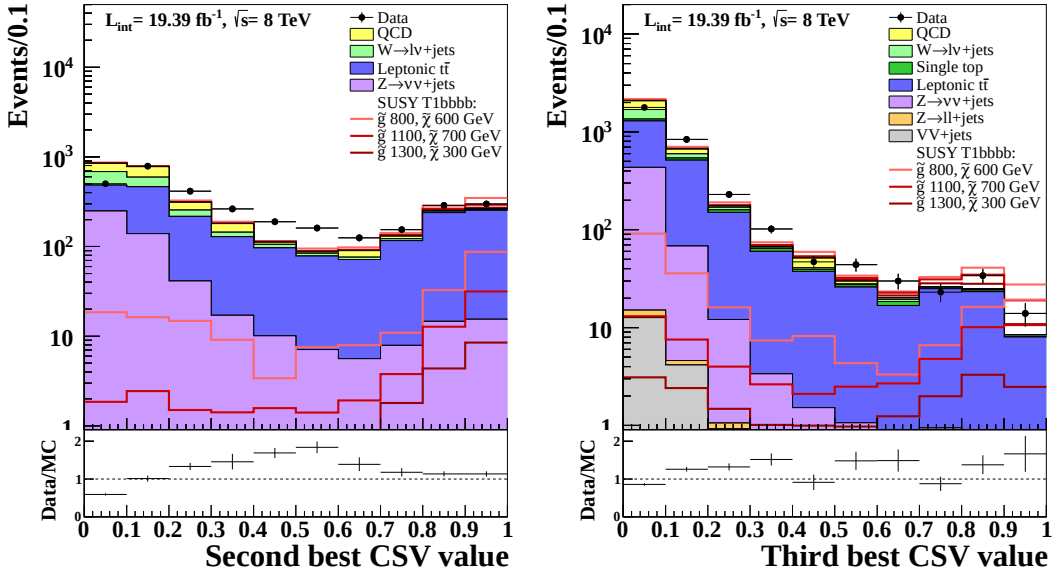

Figure 4.15: Distribution of CSV for the second best (left) and third best (right) jet in the event, ranked by CSV value. All selection criteria from Table 4.6 are applied, including requiring at least one b-tag. Black points with error bars are data. Stacked, colored histograms are simulated events. Red lines are three T1bbbb scenarios, both stacked above the simulated background and shown unstacked.

done on this sample in addition to the signal region, as a way of ensuring the methods are performing as expected.

Standard Model backgrounds very rarely have more than two b-quarks, mostly limited to $t\bar{t}$ events with an additional jet mistagged as a b-jet. Figure 4.15 shows the CSV distribution for the second best and third best jets in the event, ranked by their CSV value. All events above 0.679 would pass the additional CSVM selection. Events with real b-jets, such as $t\bar{t}$ and T1bbbb, are concentrated to the right side of the plot. By requiring at least 3 b-tags, only a small amount of the $t\bar{t}$ background remains, which is comparable in yield to the T1bbbb scenarios shown. Figure 4.16 shows the relative efficiency of tightening the b-tag requirement on signal in the gluino–neutralino mass plane. A second b-tag is almost

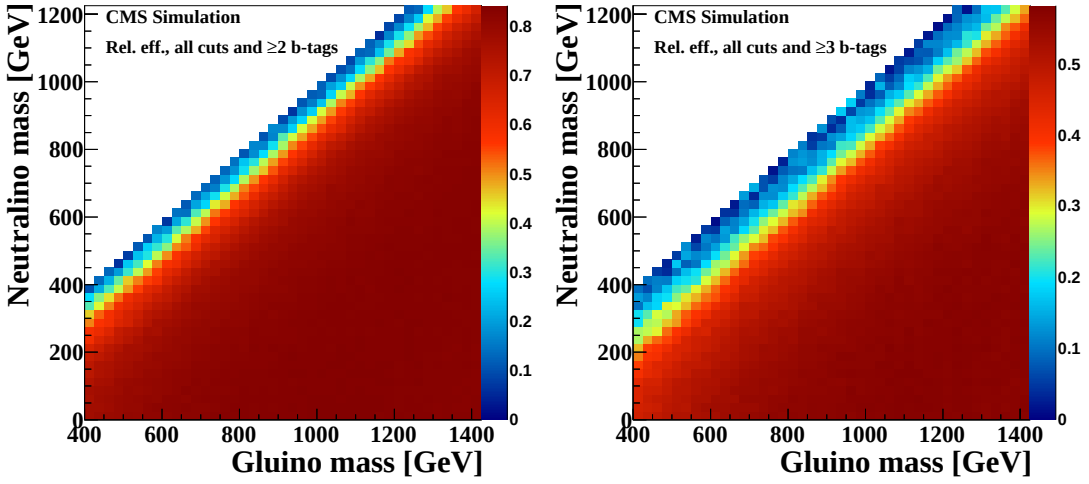

(a) ≥2 CSVM b-jets.

(b) ≥3 CSVM b-jets.

Figure 4.16: Relative efficiency of tightening the b-tagging selection for T1bbbb in the gluino–neutralino mass plane, with respect to all other selection criteria from Table 4.6.

Figure 4.17: Yields of events with full event selection for T1bbbb in the gluino–neutralino mass plane for two b-tag multiplicities.

80% efficient for most of the mass plane, with respect to requiring only one b-tag. A third b-tag is more costly, leaving about half the events that passed the single b-tag selection. However, the background suppression provided is valuable.

Yields and efficiencies for three mass points in T1bbbb are shown for different stages of the cutflow in Table 4.7. The mass points are chosen for their different gluino mass and mass splitting between the gluino and neutralino. The first has the lightest gluino mass (800 GeV), and smallest splitting (200 GeV). This results in a large cross-section for gluino production, but since there is little energy available to the jets in the final state, it has a low efficiency for passing the selection criteria. At the opposite extreme is a model with a gluino mass at 1300 GeV, and a 1000 GeV mass splitting. While such heavy gluinos

have a very small cross-section, these events have a total efficiency of 65% before the tighter b-tag requirements are made. The table also motivates why a b-tag multiplicity of 2 is kept as a signal region. At the bottom of Table 4.7, three different b-tag multiplicity selections are compared with the rest of the cutflow. The signal scenario with small mass splitting has about one third as many events with three b-tags as it does with two b-tags. The goal of this analysis is to cover as much of the T1bbbb parameter space as possible, so the lower b-tag selection is important as well. To include these events but keep the higher b-tag multiplicity region more pure, the signal region is separated into two independent samples, an $=2$ b-tags region and a ≥ 3 b-tags region.

A useful way of examining the selection criteria in an analysis is to construct a measure of how well any individual cut removes background and keeps signal events. Table 4.8 lists the signal yield for three T1bbbb scenarios divided by the square root of the expected background yield from simulation for several important stages in the cutflow. In a way, this quantity normalizes the signal to the amount of statistical fluctuation expected by the background. If the quantity is greater than unity, the amount of signal is more than one standard deviation away from the expected (poisson-distributed) background. In the first row, the table shows that an increase in the $E_{\mathrm{T}}^{\mathrm{miss}}$ requirement to 250 GeV does a very good job of suppressing the background while keeping the signal efficiency relatively high. By the end of the cutflow, where ≥ 2 b-tags are necessary, there is slightly more signal than the expected background fluctuations. The final two lines show the power of separating the two b-tag regions. The $=2$ b-tag region has a strong amount of signal with moderate cross-

Table 4.7: Yields and relative efficiencies of three T1bbbb scenarios with increasing event selection requirements.

	$M_{\tilde{g}}$=800 GeV		$M_{\tilde{g}}$=1100 GeV		$M_{\tilde{g}}$=1300 GeV	
	M_{LSP}=600 GeV		M_{LSP}=700 GeV		M_{LSP}=300 GeV	
Requirement	Yield	Rel. Eff.	Yield	Rel. Eff.	Yield	Rel. Eff.
$E_T^{miss} > 150$ GeV $H_T > 400$ GeV	503	0.22	110	0.73	27.2	0.93
$\geq$1 CSVM b-tag	462	0.92	106	0.96	26.4	0.97
2 jets p_T >70 GeV, third jet p_T >50 GeV	434	0.94	99.1	0.93	26.2	0.99
E_T^{miss} >250 GeV	235	0.54	67.5	0.68	23.0	0.88
$\Delta\phi_N$ >4.0	221	0.94	63.3	0.94	19.9	0.87
Lepton and track veto	209	0.95	60.2	0.96	19.0	0.96
Total efficiency	0.09		0.40		0.65	
Efficiency with respect to the end of cutflow for each b-tag multiplicity:						
=2 CSVM b-tags	91.4	0.44	24.0	0.40	6.8	0.36
=3 CSVM b-tags	38.2	0.18	19.3	0.32	6.6	0.34
$\geq$4 CSVM b-tags	5.3	0.03	5.0	0.08	2.6	0.13

Table 4.8: Effect of important event selection requirements within the analysis cutflow, expressed as the signal yield (Sig) for each of three T1bbbb scenarios divided by the square root of the expected background yield from simulated events (Bkg). Bottom two rows show distinct analysis regions. Intermediate requirements within the cutflow are implied.

	$M_{\tilde{g}}$=800 GeV	$M_{\tilde{g}}$=1100 GeV	$M_{\tilde{g}}$=1300 GeV
	M_{LSP}=600 GeV	M_{LSP}=700 GeV	M_{LSP}=300 GeV
Requirement	Sig/$\sqrt{Bkg}$	Sig/$\sqrt{Bkg}$	Sig/$\sqrt{Bkg}$
$E_{\mathrm{T}}^{\mathrm{miss}}$ >250 GeV	1.6	2.0	2.6
$\Delta\phi_N^{\mathrm{min}}$ >4.0	1.2	1.2	1.1
Lepton and track veto	1.4	1.4	1.4
≥2 CSVM b-tags	1.2	1.5	1.6
=2 CSVM b-tags	3.3	0.8	0.2
≥3 CSVM b-tags	1.1	1.8	2.0

section and low mass splitting. However, to probe scenarios with very small cross-section, ≥3 b-tags are needed to have a good relative amount of signal.

An important feature of this analysis is the use of the $E_{\mathrm{T}}^{\mathrm{miss}}$ shape to distinguish signal from background. Signal is expected at the tails of the $E_{\mathrm{T}}^{\mathrm{miss}}$ distribution, therefore, we use data-driven methods of predicting the size and shape of the full $E_{\mathrm{T}}^{\mathrm{miss}}$ distributions for each of the Standard Model background processes. The data is examined down to the start of the trigger plateau, $E_{\mathrm{T}}^{\mathrm{miss}}$ >150 GeV, which affords sufficient range to validate the predicted background spectra where they are expected to vastly dominate any signal. The topology of an event, including the magnitude of $E_{\mathrm{T}}^{\mathrm{miss}}$, is correlated with the overall

energy scale of the event, so the search regions are divided into two once more, for 400<H_{T} <800 GeV and H_{T} >800 GeV. Binning in this way provides a probe of models with lower values of H_{T}, while not diluting the particularly sensitive high-H_{T} region, in a statistically independent way. Figure 4.18 and Fig. 4.19 show the event yields of the T1bbbb process in each signal region across a wide range in gluino and neutralino masses. Each subfigure is a different signal region defined by H_{T}, $E_{\mathrm{T}}^{\mathrm{miss}}$, and b-tag multiplicity. The yields at moderate (250–350 GeV) and high (>350 GeV) are shown separately, for a total of eight signal regions. The following chapter describes the data-driven predictions of the $E_{\mathrm{T}}^{\mathrm{miss}}$ spectra of Standard Model backgrounds in the four regions of H_{T} and b-tag multiplicity, as well as in the low b-tag multiplicity validation region.

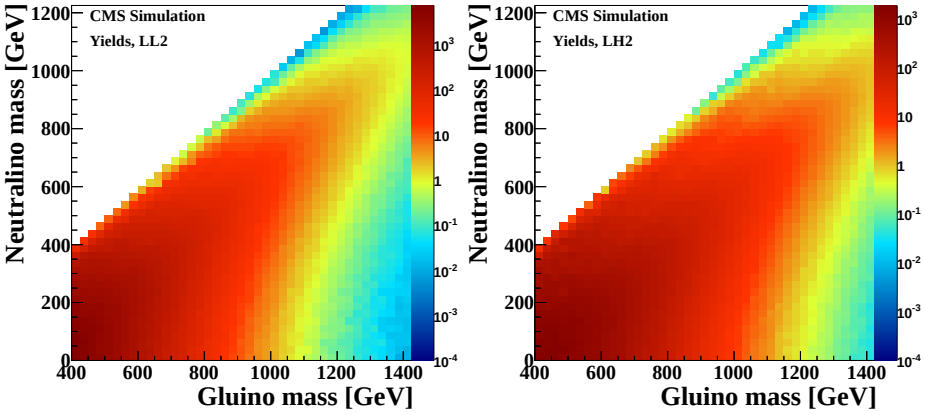

(a) 400<H_{T} <800 GeV, 250<$E_{\mathrm{T}}^{\mathrm{miss}}$ <350 GeV (b) 400<H_{T} <800 GeV, $E_{\mathrm{T}}^{\mathrm{miss}}$ >350 GeV

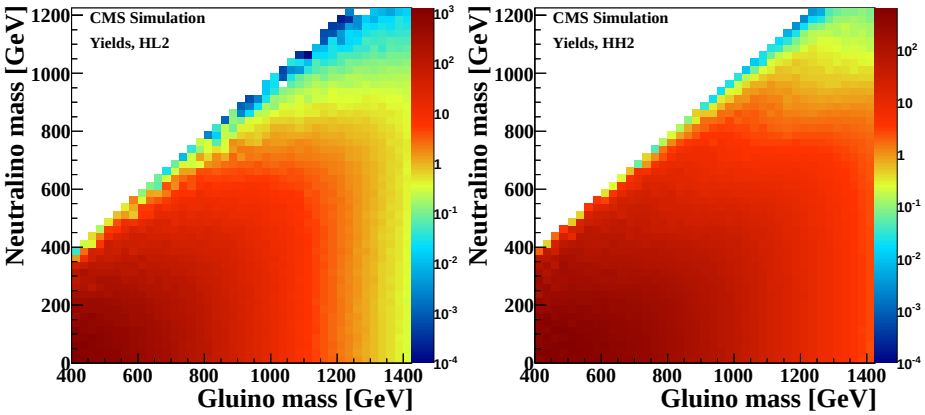

(c) H_{T} >800 GeV, 250<$E_{\mathrm{T}}^{\mathrm{miss}}$ <350 GeV (d) H_{T} >800 GeV, $E_{\mathrm{T}}^{\mathrm{miss}}$ >350 GeV

Figure 4.18: Signal yields for the T1bbbb simplified model, in the gluino–neutralino mass plane. Each subfigure presents a signal region with =2 b-tags. The z-axis indicates the number of events from simulation expected in the signal region based on the gluino pair production cross-section and signal efficiency for the mass point passing the event selection criteria.

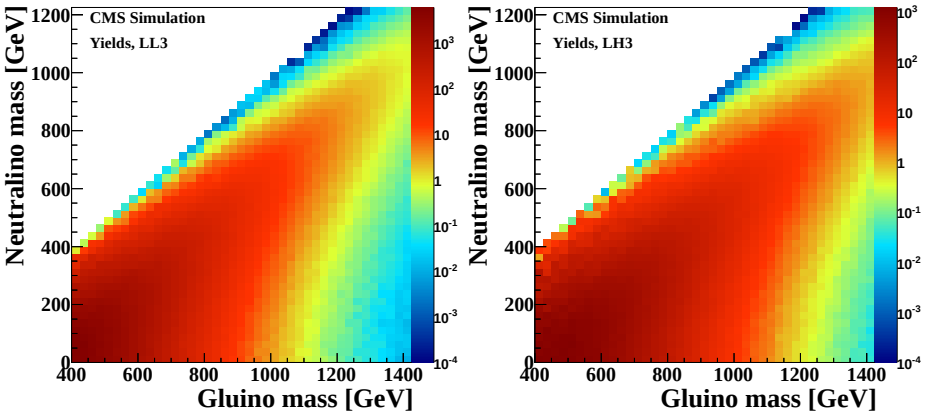

(a) 400<H_{T} <800 GeV, 250<$E_{\mathrm{T}}^{\mathrm{miss}}$ <350 GeV (b) 400<H_{T} <800 GeV, $E_{\mathrm{T}}^{\mathrm{miss}}$ >350 GeV

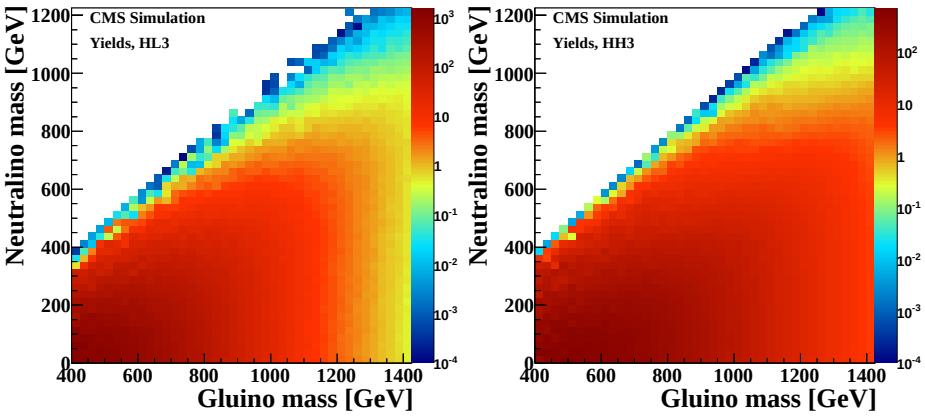

(c) H_{T} >800 GeV, 250<$E_{\mathrm{T}}^{\mathrm{miss}}$ <350 GeV (d) H_{T} >800 GeV, $E_{\mathrm{T}}^{\mathrm{miss}}$ >350 GeV

Figure 4.19: Signal yields for the T1bbbb simplified model, in the gluino–neutralino mass plane. Each subfigure presents a signal region with $\geq$3 b-tags. The z-axis indicates the number of events from simulation expected in the signal region based on the gluino pair production cross-section and signal efficiency for the mass point passing the event selection criteria.

Chapter 5

Background Predictions

As described in Sec. 4.5, the primary background processes for this analysis are $t\bar{t}$, multi-jet, and $Z \to \nu\bar{\nu}$ production. Respectively, they comprise 72%, 13%, and 7% of the Standard Model events in the analysis sample with two b-tagged jets. This chapter address each component of the background prediction individually, using predominantly data-driven methods. Since the sources of $E_{\mathrm{T}}^{\mathrm{miss}}$ differ between these main backgrounds, different techniques are used to model the size and shape of the $E_{\mathrm{T}}^{\mathrm{miss}}$ distribution for each. The sources of $E_{\mathrm{T}}^{\mathrm{miss}}$ comprise three scenarios: events with one neutrino from a W boson (semi-leptonic $t\bar{t}$, W+jets, and single-top), events with two neutrinos (dilepton $t\bar{t}$, $Z \to \nu\bar{\nu}$), and events with mismeasured jets (multi-jet QCD).

The majority of events entering the analysis sample are semi-leptonic $t\bar{t}$ events, in which one W boson decays to leptons and the second W boson decays to hadrons. Figure 5.1 shows the leptonic and hadronic decay modes of the W boson. Roughly two thirds of the

Figure 5.1: The CKM-preferred decay options for a W^+ boson. There are three possibilities for leptonic decay, and six possibilities for hadronic decay. Since the mass of the on-shell W is much larger than the decay products, the branching fractions of each is roughly equal.

time, the W will decay hadronically. About one third of the time, it produces a charged lepton and a neutrino. Production of $t\bar{t}$ in which both W bosons decay hadronically is not significant because there is not enough $E_{\mathrm{T}}^{\mathrm{miss}}$ for the events to enter the analysis sample. These events are considered a part of the multi-jet QCD background.

The background of $t\bar{t}$, W+jets, and single-top events include at least one leptonic W boson decay. To enter the analysis sample, which includes a rejection of reconstructed electrons and muons, the lepton is either not observed or does not pass the object selection outlined in Sec. 3.3. The two scenarios are presented in Fig. 5.2, in which an electron or muon in the final state is not reconstructed, or a τ-lepton is created which decays hadronically. These two categories represent different sources of $E_{\mathrm{T}}^{\mathrm{miss}}$, and therefore different techniques

Figure 5.2: Conditions leading to large $E_{\mathrm{T}}^{\mathrm{miss}}$ in $t\bar{t}$, W+jets, and single-top processes without a reconstructed lepton. The detector observation of the W decay products are shown in red.

are used to predict the distribution. Since the scenarios are common to $t\bar{t}$, W+jets, and single-top production, these processes are grouped together and called $t\bar{t}/W/t$. For the first category of events, we use a single lepton control sample and knowledge of the polarization of the W boson to obtain the $E_{\mathrm{T}}^{\mathrm{miss}}$ spectrum. This data-driven method is described in Sec. 5.1. The second category, described in Sec. 5.2, exploits the p_{T} of an observed muon to predict the amount of τ-lepton energy contributing to the $E_{\mathrm{T}}^{\mathrm{miss}}$.

A small portion of the $t\bar{t}$ and single-top (produced with a W boson) background is fully leptonic with electrons and/or muons in the final state. Since this background is small and unique, the method for predicting the $E_{\mathrm{T}}^{\mathrm{miss}}$ spectra from these events (Category 3 $t\bar{t}/W/t$) is described in Sec. 5.3.

Multi-jet production only enters the analysis sample by the presence of a greatly mismeasured jet, which causes an imbalance in transverse momentum of the event. The data-driven QCD prediction in Sec. 5.5 relies on the approximate independence of the $E_{\mathrm{T}}^{\mathrm{miss}}$ and $\Delta\phi_N$ quantities. It uses control samples at low $E_{\mathrm{T}}^{\mathrm{miss}}$ and low $\Delta\phi_N$, where multi-jet events are dominant.

When produced with multiple jets from the hard scatter and final state radiation, $Z \to \nu\bar{\nu}$ events are an irreducible background for this analysis. Fortunately, it is predicted by measuring dilepton Z boson decays, which are understood to a high precision. Dimuon and dielectron control samples with a loosened b-tag selection are used to study the characteristics of $Z \to l^+l^-$ events, and a low $E_{\mathrm{T}}^{\mathrm{miss}}$, multi-jet enriched sample is used to study the effect of tightening the b-tag selection. This procedure is detailed in Sec. 5.6.

5.1 Predicting the $t\bar{t}$, W+jets, and single top background with one $W \to e/\mu/(\tau \to e/\mu)$ decay

At the LHC, pairs of top and anti-top quarks are produced via the strong interaction, and decay via the weak interaction. As seen in the CKM matrix discussed in Sec. 2, nearly 100% of top quark decays are to a b-quark and W boson. In semi-leptonic $t\bar{t}$ decay, shown in Fig. 5.3, one top-quark decay results in a b-jet and two light-quark jets, and the other top-quark final state is a b-jet, a charged lepton, and neutrino. When the charged lepton is a muon or electron, either prompt or through the decay of a τ-lepton, we expect to observe it in the detector with high efficiency. Under certain conditions, this is not the case, and these events may enter the analysis sample, which requires zero reconstructed leptons. This section describes the conditions under which the charged lepton is not observed, and how understanding this behavior leads to an interesting method for predicting the $E_{\mathrm{T}}^{\mathrm{miss}}$ spectrum of these events.

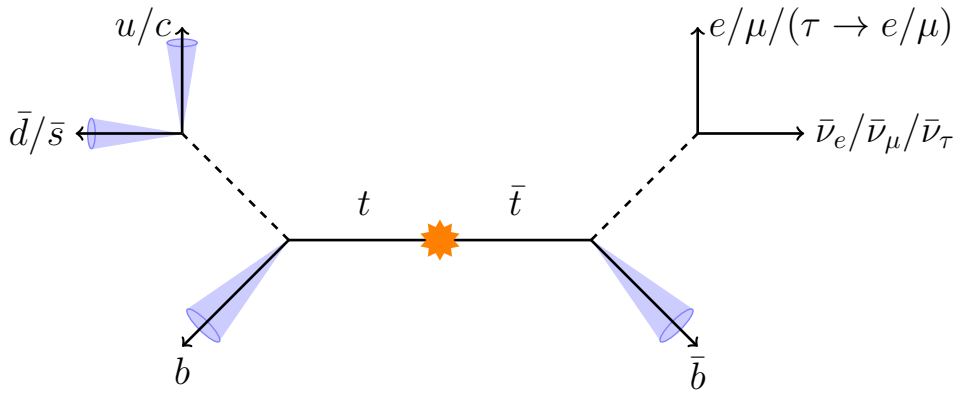

Figure 5.3: Sketch of a Category 1 semi-leptonic $t\bar{t}$ event, showing the neutrinos ($E_{\mathrm{T}}^{\mathrm{miss}}$), jets, and b-jets in the final state, and a charged lepton which is not observed in the lepton-vetoed analysis sample.

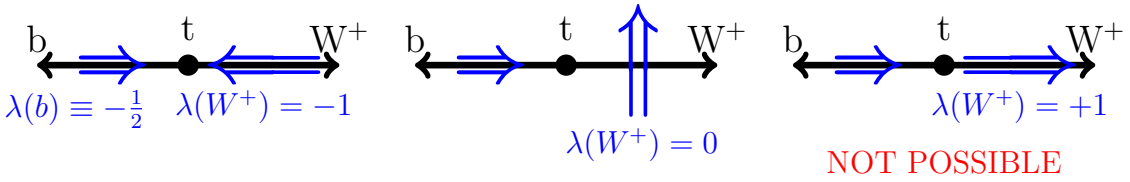

Figure 5.4: Orientation of possible W boson and b-quark momenta (black arrows) and spins (blue double arrows) from top quark decay, for a relativistic b-quark.

5.1.1 Characteristics of semi-leptonic $t\bar{t}$ decay

The decay of a top-quark imposes interesting conditions on the helicity of its decay products. Figure 5.4 illustrates the directions of the momenta and spins of the daughter particles, in the rest frame of the top. Since the b-quark is very light with respect to the top, it is relativistic when it is produced. In the relativistic limit, the b-quark helicity is equal to its chirality. The values are set (for helicities $\lambda(b) = -1/2$, $\lambda(\bar{b}) = +1/2$) by the V–A interaction described in Sec. 2, which only couples to the left-handed components of particles and the right-handed components of anti-particles. As a spin-1 particle, the W boson has three possibilities for the projection of its spin onto the direction of its momentum. Figure 5.4 shows each of the three possibilities (left to right), left-handed, longitudinal, and right-handed. Conservation of angular momentum requires that the sum of the W and b-quark add to the spin projection of the top ($\pm 1/2$) along its decay axis. With these two restrictions, the W boson is left with two possible helicities, one longitudinal and one transverse.

It is important to note here that the choice of drawing the longitudinal spin of the W upward is arbitrary. The direction of this polarization is simply perpendicular to the W

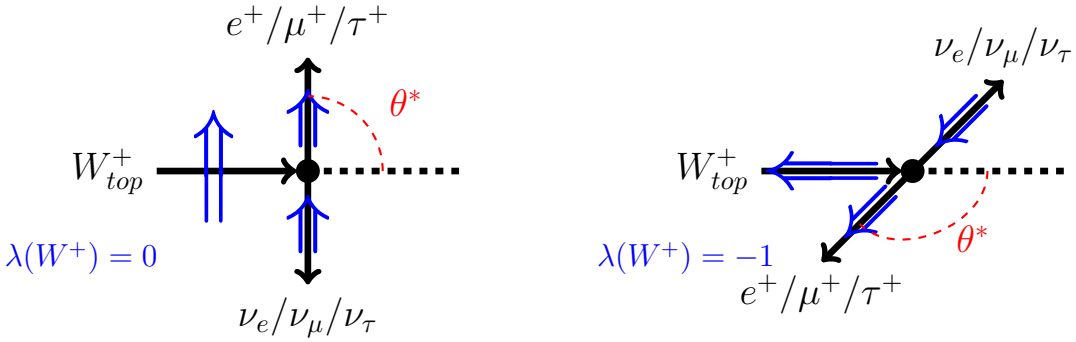

Figure 5.5: Probable orientations of momenta (black arrows) and spins (blue double arrows) for the W boson in the top quark rest frame and the leptons in the W boson rest frame.

momentum, and is in fact a superposition of all directions outgoing from the momentum axis. The three possible directions of angular momentum for a spin 1 (J=1) object can be expressed as:

$$\begin{aligned} |J, M\rangle &= \sum_{M'=-J}^{J} d^J_{M,M'} |J, M'\rangle \\ |1, 1\rangle &= \sum_{M'=-1}^{1} d^1_{1,M'} |1, M'\rangle. \end{aligned} \tag{5.1}$$

Eq. 5.1 shows that the rate of each helicity state includes *d-functions*, which are related to the particle's decay products.

The spin states of the W boson are reflected in the angular distribution of decay products. This is demonstrated in Fig. 5.5, where the momentum and spin projections of the W boson are shown in the top-quark rest frame, and those of its daughters in the W rest frame. The neutrino is relativistic, therefore it must be have λ=–1/2 in this frame, and by conservation of angular momentum, the electron helicity is +1/2. In the case of anti-top decay, the transversely polarized W^- has λ=+1, and the anti-neutrino is forced to

have λ=+1/2. For these events, the W^- decays like the drawing on the right in Fig. 5.5, but with all the blue arrows flipped. Recall that the drawing on the left is rotated about the direction of the W boson momentum. Both drawings show that the polarization of the W boson affects the angular distributions of its decay products. The *d-functions* associated with each helicity state are defined as

$$\begin{aligned} d^1_{1,1}(\cos\theta^*) &= \frac{1}{2}(1+\cos\theta^*) \\ d^1_{1,0}(\cos\theta^*) &= \frac{1}{\sqrt{2}}(\sin\theta^*) \\ d^1_{1,-1}(\cos\theta^*) &= \frac{1}{2}(1-\cos\theta^*)\,. \end{aligned} \tag{5.2}$$

Therefore, the angular distribution of the lepton from Eq. 5.1 is given by

$$\frac{dN}{dcos\theta} \propto (1-\cos\theta^*)^2 f_- + 2sin^2\theta^* f_0 + (1+\cos\theta^*)^2 f_+, \tag{5.3}$$

where

$$f_+ + f_0 + f_- = 1. \tag{5.4}$$

The relative magnitudes of the different polarizations, the coefficients f, are determined experimentally. The fraction of W^+ bosons with λ=+1 is labeled f_+, λ=–1 is labeled f_-, and longitudinal polarization is denoted f_0. In the case of W^-, the f_+ term is non-negligible, analogous to the f_- piece for W^+, however, the sign in front of each $\cos\theta^*$ is flipped. Therefore, the angular distribution of charged leptons is the same for both W bosons.

The quantity $\cos\theta^*$ directly describes the angle between the outgoing charged lepton momenta in the W rest frame with respect to the W boson momentum in the top rest

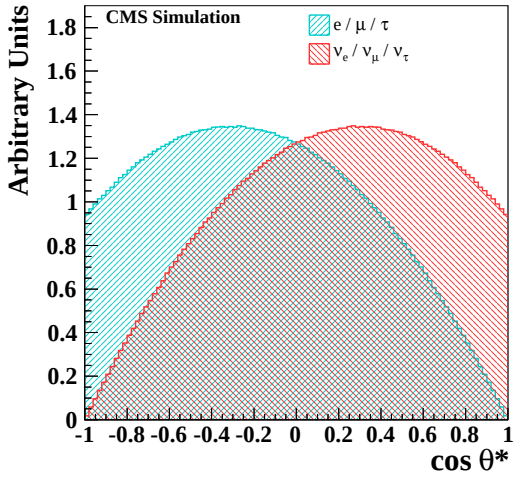

Figure 5.6: Angular distributions for all simulated semi-leptonic $t\bar{t}$ events. Blue hatched histogram is $\cos\theta^*$, while its reflection (the angle with respect to the neutrino) is shown in hatched red.

frame. It is shown for both the charged and uncharged leptons (by definition, the reflection of the charged lepton distribution about the y-axis) in Fig. 5.6. In simulated events, both leptons are boosted to the W boson center of mass frame (through the top center of mass frame), then the angle of either object is calculated with respect to the W boson momentum in the top center of mass frame. As described above, the right-handed component is very close to zero. Theoretical calculations predict f_-=0.311±0.005, f_0=0.687±0.005, and f_+=0.0017±0.0001 for W^+ decays [28], which is consistent with experimental measurements [29]. The simulated events very clearly show this simple angular distribution, well-understood by both theoretical and experimental results.

This quantity reveals important information about the relationship between $E_{\mathrm{T}}^{\mathrm{miss}}$ and reconstructed leptons observed in $t\bar{t}$ events at the CMS experiment. When a lepton is produced with high $\cos\theta^*$, the direction of its momentum aligns with the direction of the

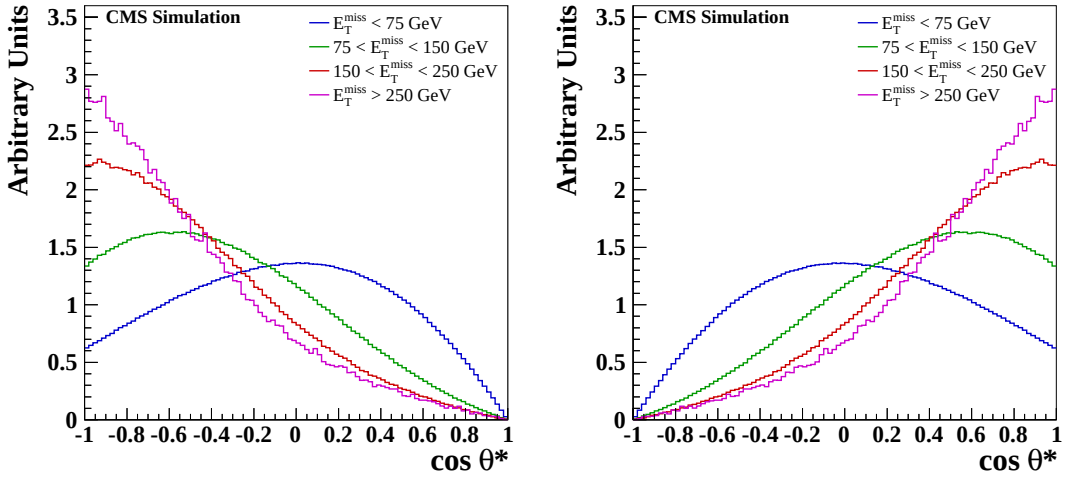

(a) Angle with respect to charged lepton.

(b) Angle with respect to neutrino.

Figure 5.7: Angular distributions for all simulated semi-leptonic $t\bar{t}$ events, using generator-level event information. Events are separated according to $E_{\mathrm{T}}^{\mathrm{miss}}$, starting from less than 70 GeV (blue), to greater than 250 GeV (magenta). Histograms are normalized to each other.

boost of the W boson parent. Therefore, it has a higher momentum in the top quark (or lab) frame than the other decay product. In the CMS experiment, the transverse momentum of a single neutrino can be approximated by the $E_{\mathrm{T}}^{\mathrm{miss}}$. Figure 5.7 shows the angular distribution of the leptons in slices of $E_{\mathrm{T}}^{\mathrm{miss}}$. At higher $E_{\mathrm{T}}^{\mathrm{miss}}$, the neutrino is produced along the direction of the W boson momentum, achieving higher p_{T} which is responsible for the high $E_{\mathrm{T}}^{\mathrm{miss}}$. Knowledge of the polarization of the W boson is very useful for this analysis because it connects a very well understood quantity in $t\bar{t}$ events, the angular distribution of charged leptons, with the quantity we are interested in modeling, $E_{\mathrm{T}}^{\mathrm{miss}}$.

Unfortunately, it is not possible to measure the quantity $\cos\theta^*$ in data, since we do not measure the top quark momenta nor do we have three-dimensional information about the neutrino. Therefore, we calculate this angle projected onto the transverse plane, where

$E_{\mathrm{T}}^{\mathrm{miss}}$ is taken as the transverse momentum of the neutrino. We only consider events with an electron or muon for this procedure, since tau leptons cannot be reliably reconstructed with high efficiency and low fake rate. Furthermore, we neglect the momenta of the top quarks in boosting to the W boson center of mass frame. This quantity is called $\Delta\theta_T$. The *generator-level* $\Delta\theta_T$ quantity is calculated in simulated events using the reconstructed $E_{\mathrm{T}}^{\mathrm{miss}}$ in the event, but the generator-level information about the charged lepton p_{T}, regardless of whether the lepton was reconstructed or not.

A comparison of generator-level $\Delta\theta_T$ with $\cos\theta^*$ in simulated events is plotted in Fig. 5.8. The plots show how the size and shape of the angular distribution changes as the selection criteria described in Sec. 4.4 are applied to create the analysis sample. Cuts on $E_{\mathrm{T}}^{\mathrm{miss}}$ and lepton reconstruction dramatically sculpt this shape, whereas the $\Delta\phi_N^{\mathrm{min}}$ and number of b-tagged jets only modify the size of the yield. The $E_{\mathrm{T}}^{\mathrm{miss}}$ cut eliminates events where the neutrino is produced with momentum opposite of the direction of the W boson. In this scenario, the neutrino does not benefit from the boost of the parent particle, and is less likely to achieve a high enough momentum. The lepton and track veto eliminates events with electrons or muons having p_{T} greater than 20 GeV. This further pushes the angular distributions against the direction of the W boson, because charged leptons produced backwards with respect to the W would be more likely to have low p_{T} and escape reconstruction.

The effect of the angular distribution of the leptons and their momenta is further explored in Fig. 5.10. Here, the generator-level $\Delta\theta_T$ distribution from simulated events

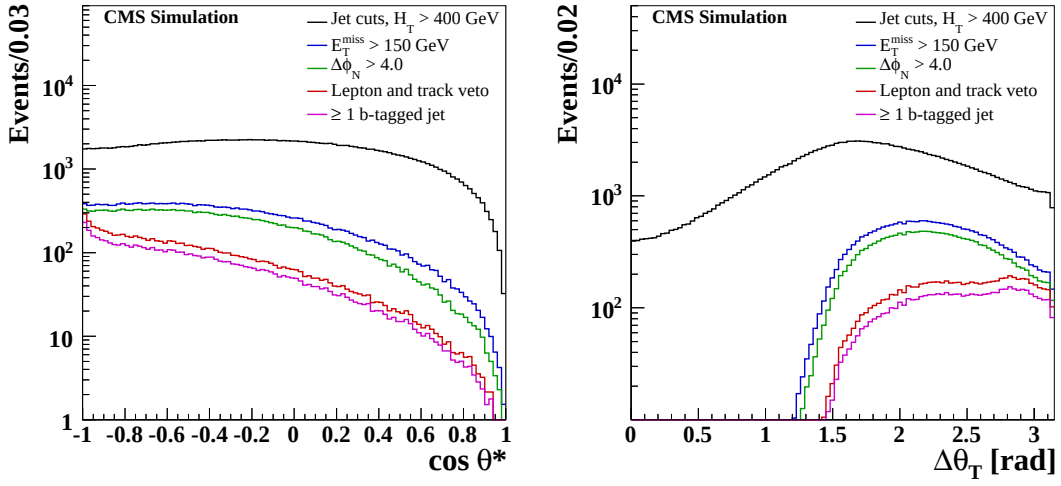

(a) The $\cos\theta^*$ shape with increasing cuts.

(b) Generator-level $\Delta\theta_T$ with increasing cuts.

Figure 5.8: The changing shape of generator-level angles between the charged lepton and the W boson. The histogram with the loosest selection is drawn in black, requiring H_{T} >400 GeV, 2 jets with p_{T} >70 GeV, and a third jet with p_{T} >50 GeV. A cut on $E_{\mathrm{T}}^{\mathrm{miss}}$ >150 GeV is added to produce the histogram in blue. Additional cuts on $\Delta\phi_N^{\mathrm{min}}$, the presence of a reconstructed charged lepton or track, and at least one b-tagged jet produce the green, red, and magenta histograms, respectively.

passing the lepton veto is shown. Events are separated according to the reason that the electron or muon was not successfully reconstructed. The most common situations are when the lepton p_{T} is too low, or it is too close to a jet in the event (causing it to fail the isolation requirement). If the electron or muon is directly from the decay of the W boson, it is called *prompt*, and if it is from the intermediate decay of the W boson to a tau, it is referred to as *secondary*. Simulated semi-leptonic $t\bar{t}$ events from the analysis sample, with all the cuts described above, are plotted, using the generator-level p_{T} of the charged lepton to reconstruct the W boson p_{T}. In events with a prompt electron or muon, the majority of the events fail the p_{T} or isolation requirement for reconstructing leptons. As expected, the events having a charged lepton with p_{T} less than 20 GeV are at the extreme end of the $\Delta\theta_T$

Figure 5.9: Diagram of the angle $\Delta\theta_T$ (in blue) from reconstructed transverse quantities. When the angle is small (left), the charged lepton tends to have large momentum due to the boost from the W boson. When the angle is large (right), the charged lepton is directed against the momentum of the W boson, and tends to have lower momentum.

distribution. These are events where the charged lepton is produced against the direction of the W boson, and therefore the forward-produced neutrino is more likely to result in higher $E_{\mathrm{T}}^{\mathrm{miss}}$ in them. Events with secondary leptons demonstrate a similar effect. The yield of these events is smaller than for prompt electrons and muons, due to the branching fractions of the tau, and the majority of events fail the p_{T} requirement. This is because two additional neutrinos in the final state are taking away some of the tau momentum. The distribution of these events is broader than for prompt leptons, but as expected, events at the highest angles are almost exclusively low p_{T}, since the neutrino is produced in the forward direction with high momentum.

Figure 5.12 shows the $E_{\mathrm{T}}^{\mathrm{miss}}$ distributions separately for simulated events where the lepton passes or fails to be reconstructed according to the definition of the lepton veto. Events with prompt or secondary leptons are combined, since in data they are indistinguishable, and they are treated identically by this method. The samples are divided according to the value of $\Delta\theta_T$ calculated from the generator-level charged lepton. The figure shows a striking difference between the shapes of the $E_{\mathrm{T}}^{\mathrm{miss}}$ spectra at different values of $\Delta\theta_T$.

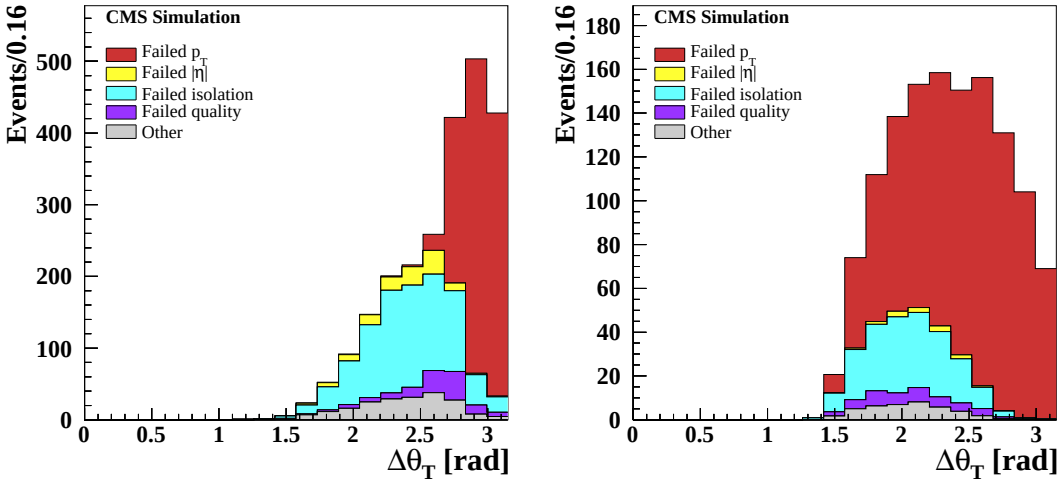

(a) Prompt electrons and muons.

(b) Secondary electrons and muons from tau decay.

Figure 5.10: Stacked histograms from simulated events representing the reason for not reconstructing electrons and muons in semi-leptonic $t\bar{t}$ events, as a function of the generator-level angle of the charged lepton with the W boson. All analysis cuts are applied. Plotted separately for prompt electrons and muons (left), and secondary electrons and muons from tau decay (right). Events in the red histograms have an electron or muon with p_{T} less than 20 GeV. In yellow, the lepton has $|\eta|$ >2.4, or has an electron that goes through a crack in the calorimeter. In cyan, the lepton is close to a jet in the event, causing it to fail the isolation requirement on reconstructed leptons. In violet, the lepton fails any other of the requirements on reconstructed leptons.

Meanwhile, these shapes are unaffected by the reconstruction status of the lepton. This observation is the result of the relationships between the angle of the charged lepton and the magnitude of the $E_{\mathrm{T}}^{\mathrm{miss}}$ described above. It tells us that regardless of whether the electron or muon was reconstructed, the $E_{\mathrm{T}}^{\mathrm{miss}}$ distributions for these $t\bar{t}$ events are determined by its value of $\Delta\theta_T$. Since $\Delta\theta_T$ has a strong theoretical and experimental foundation, we rely on the expected shape of this quantity for events where the lepton is not reconstructed and therefore enters the analysis sample. The $E_{\mathrm{T}}^{\mathrm{miss}}$ spectrum for these events can be taken from a single lepton control sample in data, reweighted to reflect the angular distribution of

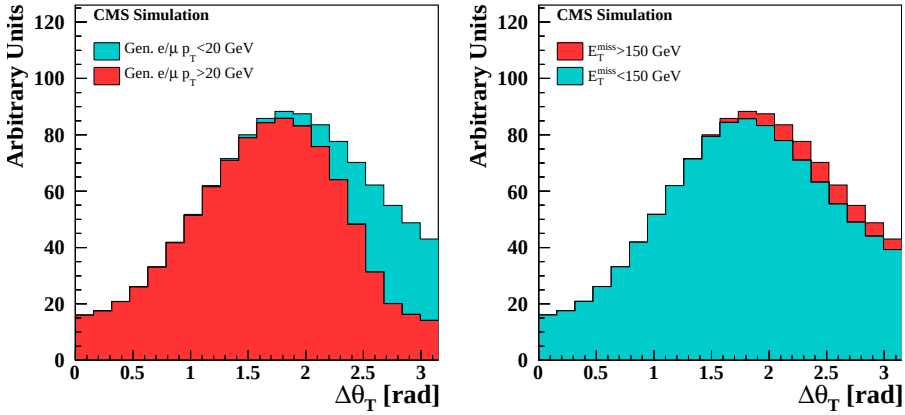

(a) Primary e/μ from W decay.

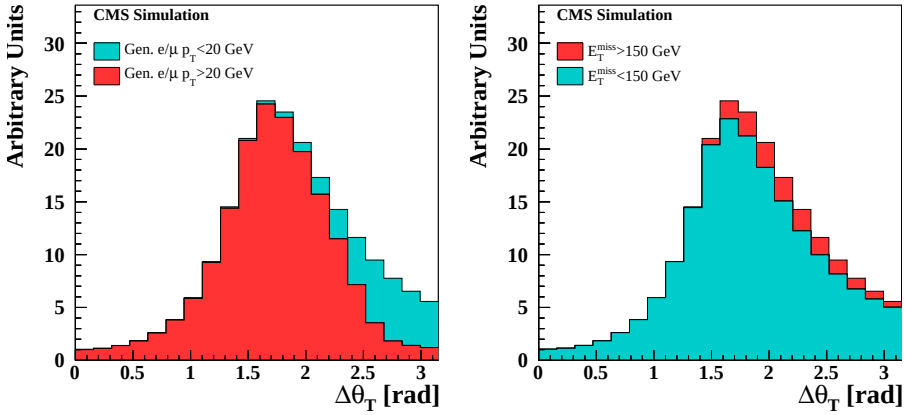

(b) Secondary e/μ from W$\rightarrow \tau$.

Figure 5.11: Distribution of $\Delta\theta_T$ from simulated events using the generator-level electron and muon p_{T}, regardless of lepton reconstruction. Stacked histograms separate events by lepton p_{T} and $E_{\mathrm{T}}^{\mathrm{miss}}$, shown for events with prompt and secondary leptons from τ-lepton decay.

unreconstructed leptons. This weighting procedure will give higher weights to single lepton events at high $\Delta\theta_T$ (and $E_{\mathrm{T}}^{\mathrm{miss}}$), and lower weights to events with lower $\Delta\theta_T$. The result is a distribution with values of $E_{\mathrm{T}}^{\mathrm{miss}}$ taking directly from data, scaled according to the expected yield of unreconstructed leptons with similar $\Delta\theta_T$.

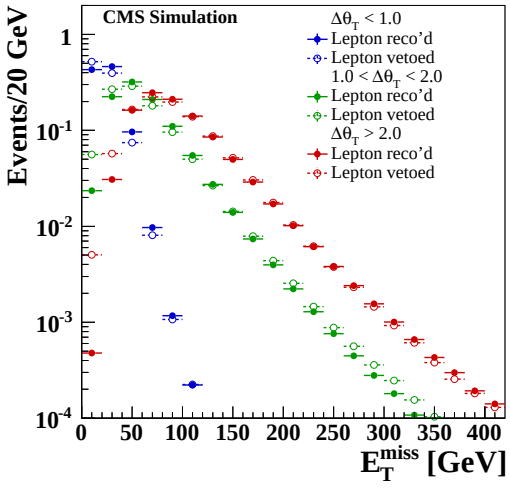

Figure 5.12: $E_{\mathrm{T}}^{\mathrm{miss}}$ spectrum of simulated semi-leptonic $t\bar{t}$ events, plotted separately for events where the electron or muon was reconstructed (solid circle), or passed the veto selection (open circle). Events are further divided according to their range of $\Delta\theta_T$, from low (blue) to high (red). Distributions are normalized to each other.

The principles of this strategy are demonstrated in data in a high H_{T} single lepton sample with low $E_{\mathrm{T}}^{\mathrm{miss}}$ threshold and $\geq$2 b-tags. First, Fig. 5.13(a) shows $\Delta\theta_T$ with respect to H_{T} and $E_{\mathrm{T}}^{\mathrm{miss}}$. It is uncorrelated with H_{T}, but related to $E_{\mathrm{T}}^{\mathrm{miss}}$ as expected, with a distinct hole at high $\Delta\theta_T$ where $E_{\mathrm{T}}^{\mathrm{miss}}$ >100 GeV, in which leptons directed backwards with respect to the W boson are lost. Figure 5.13(b) and (c) are the same two dimensional histograms in simulated $t\bar{t}$ events. For the most part, they are similar, except the lepton-vetoed events in simulation fill in the gap at high $\Delta\theta_T$. Importantly, Fig. 5.14 compares the distributions of $\Delta\theta_T$ and $E_{\mathrm{T}}^{\mathrm{miss}}$ between data and simulated $t\bar{t}$, in slices of the other quantity. The agreement between simulation and data in Fig. 5.14(a) shows that $\Delta\theta_T$ is a well-modeled quantity in simulated events. Furthermore, the angular distribution of high $E_{\mathrm{T}}^{\mathrm{miss}}$ events is peaked at higher $\Delta\theta_T$, as expected, which then sharply falls at the highest

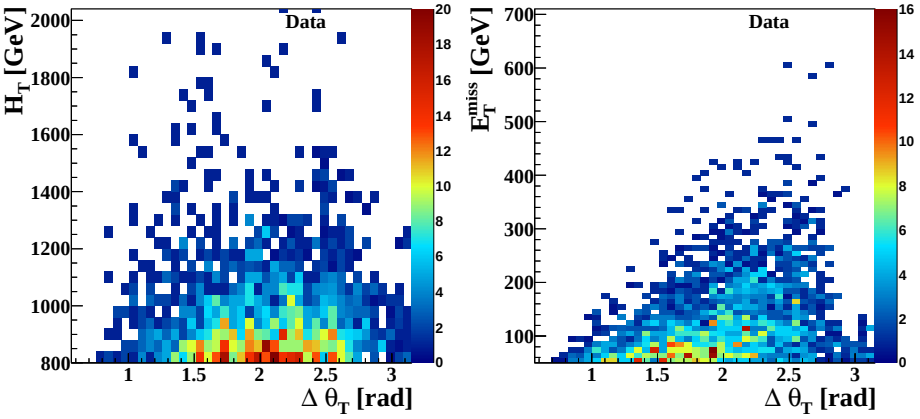

(a) Single lepton data control sample.

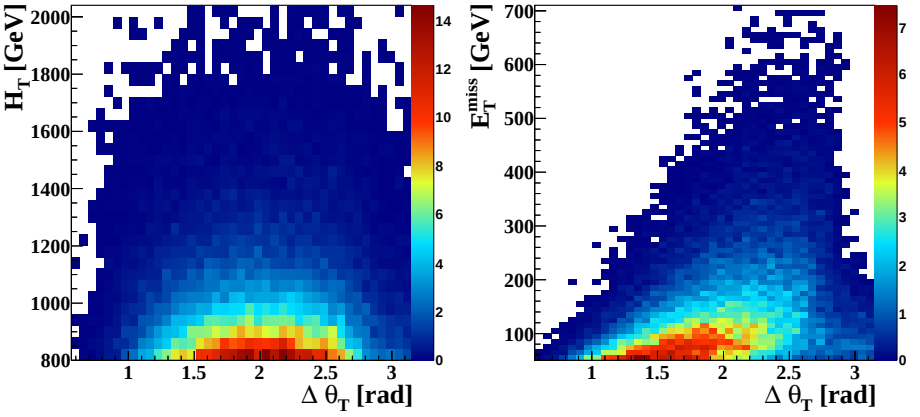

(b) Single lepton control sample $t\bar{t}$ simulated events.

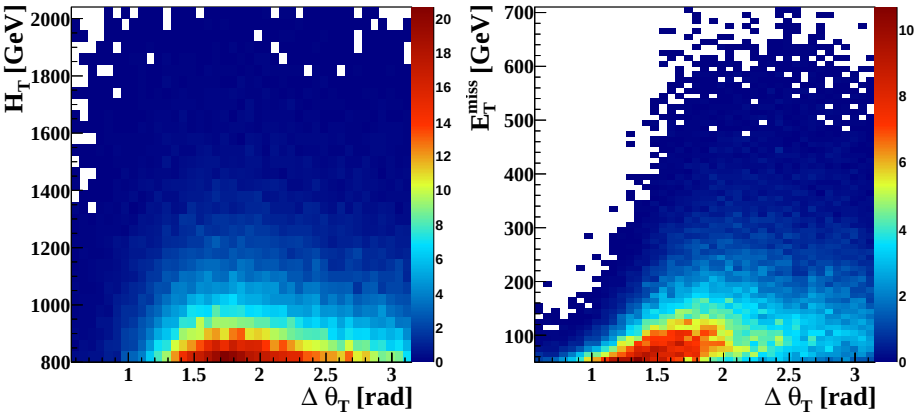

(c) Lepton-vetoed sample $t\bar{t}$ simulated events.

Figure 5.13: Distribution of $\Delta\theta_T$ with respect to H_{T} (left) and $E_{\mathrm{T}}^{\mathrm{miss}}$ (right), for events in a single lepton control sample or lepton-vetoed sample, with a loosened $E_{\mathrm{T}}^{\mathrm{miss}}$ requirement, H_{T} >800 GeV, and ≥2 b-tags.

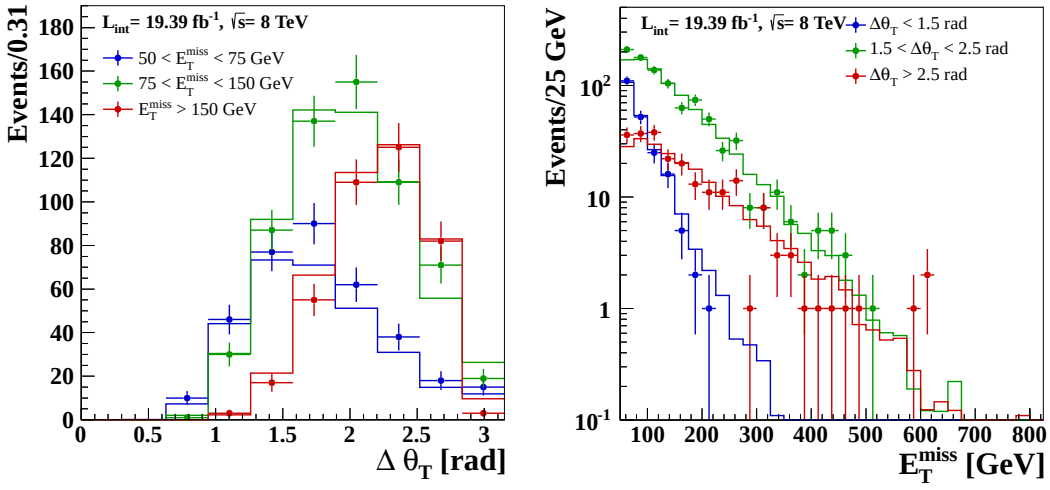

Figure 5.14: Comparison of data (points with error bars) and simulated events (solid lines) in a single lepton sample with a loosened $E_{\mathrm{T}}^{\mathrm{miss}}$ requirement, H_{T} >800 GeV, and ≥2 b-tags.

values due to the loss of leptons at low p_{T}, as shown in Fig. 5.10. Figure 5.14(b) shows the $E_{\mathrm{T}}^{\mathrm{miss}}$ spectrum of the same events for three regions of $\Delta\theta_T$. The Category 1 background prediction directly takes values of $E_{\mathrm{T}}^{\mathrm{miss}}$ in the tail of the distribution from single lepton data, knowing that the lepton-vetoed sample has the same $E_{\mathrm{T}}^{\mathrm{miss}}$ distribution when the lost lepton has the same angle with respect to the W boson.

5.1.2 Definition of control samples

A sample enriched with top quark and W boson events is created from the analysis dataset and selection criteria described in Sec. 4.4, with a few changes. Instead of a veto on reconstructed leptons, we require exactly one electron or muon satisfying the criteria used for the veto. The goal of this control sample is to obtain the behavior of events where exactly one W boson decays leptonically. To achieve this, an additional cut on the transverse mass

(M_T) of the lepton and $E_{\mathrm{T}}^{\mathrm{miss}}$ is asserted. If both are the product of a W boson decay, the transverse mass will be at or below the W mass, about 81 GeV. The transverse mass will be higher if there are two leptonic W decays. To supress these events, only those with M_T <100 GeV are included in the single lepton control sample. The distribution of this quantity in bins of H_{T} and number of b-tagged jets is shown in Fig. 5.15. There, the steep fall in events just above the W mass is clear in each bin, and the shape of distributions from simulation is consistent with the observation in data. Even though the regions with a single b-tagged jet are not sensitive to signal, they provide samples with high yields in the two H_{T} bins with a similar composition of processes to the =2 b-tag and $\geq$3 b-tag samples used in the prediction of the $t\bar{t}/W/t$ background. Comparing the behavior of data and simulated events in this sample is a good test of how well simulated events can provide an understanding of the observations in data.

While very similar to the quantity M_T, the transverse momentum of a reconstructed W boson in the single lepton control sample is important because it feeds directly into the calculation of $\Delta\theta_T$. The momentum of the W boson and the angle at which its daughters are produced with respect to it are the ingredients which determine the $E_{\mathrm{T}}^{\mathrm{miss}}$ (neutrino) and charged lepton momenta. Despite the low yields at a high number of b-tagged jets, the shape of the W p_{T} is well modeled in simulated events, shown in Fig. 5.16, which provides confidence that the sample in data is well understood. In these plots and all following plots from the single lepton control sample, the M_T cut at 100 GeV is applied.

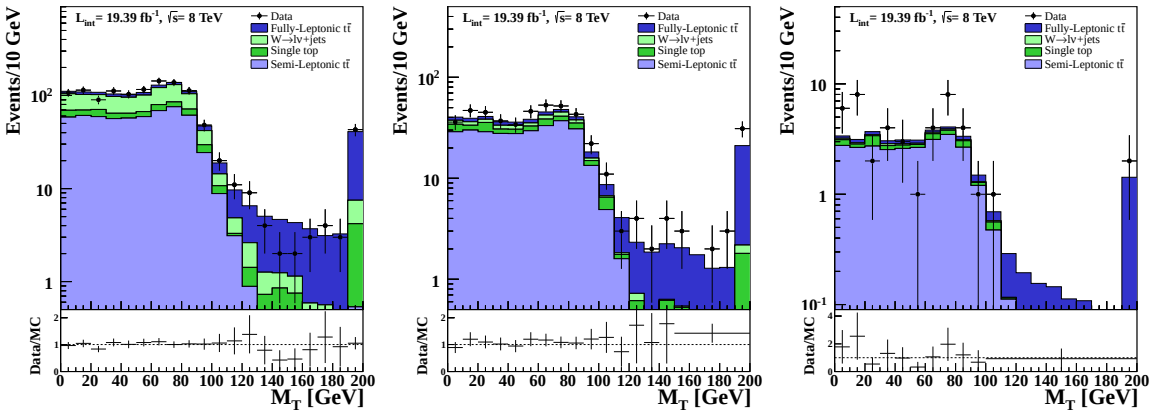

(a) 400<H_{T} <800 GeV, =1 b-tag (b) 400<H_{T} <800 GeV, =2 b-tags (c) 400<H_{T} <800 GeV, ≥3 b-tags

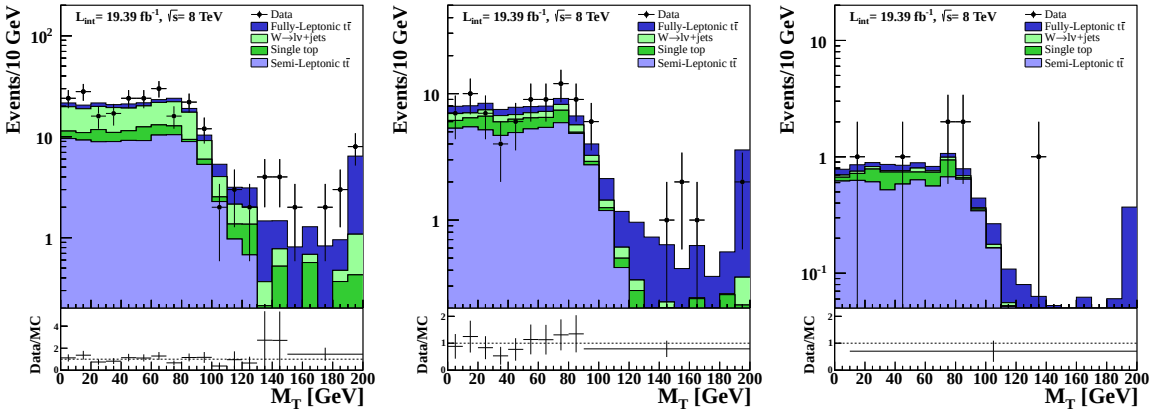

(d) H_{T} >800 GeV, =1 b-tag (e) H_{T} >800 GeV, =2 b-tags (f) H_{T} >800 GeV, ≥3 b-tags

Figure 5.15: The transverse mass of the $E_{\mathrm{T}}^{\mathrm{miss}}$ and reconstructed muon or electron, divided by H_{T} and number of b-tagged jets. Black points with error bars are data from the control sample with the cut on M_T removed. Stacked, colored histograms are yields from simulated events.

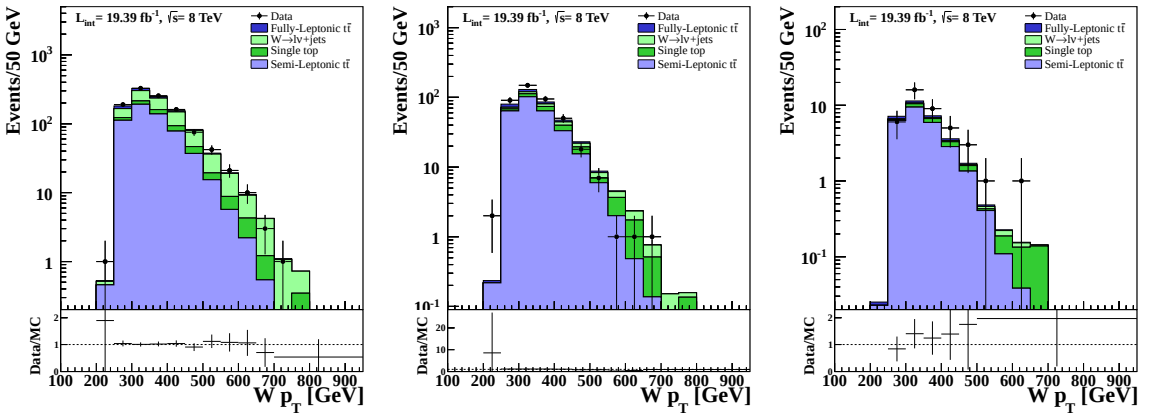

(a) 400<H_{T} <800 GeV, =1 b-tag (b) 400<H_{T} <800 GeV, =2 b-tags (c) 400<H_{T} <800 GeV, ≥3 b-tags

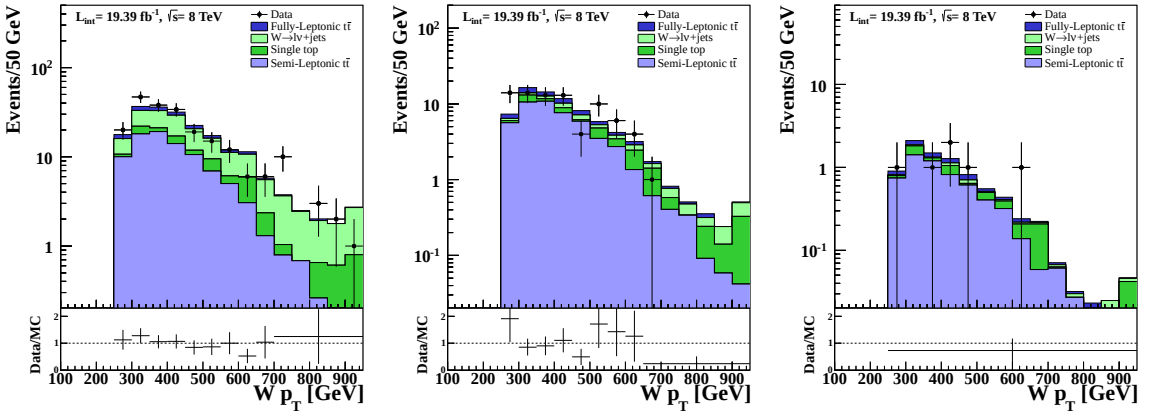

(d) H_{T} >800 GeV, =1 b-tag (e) H_{T} >800 GeV, =2 b-tags (f) H_{T} >800 GeV, ≥3 b-tags

Figure 5.16: The transverse momentum of the reconstructed W boson, using $E_{\mathrm{T}}^{\mathrm{miss}}$ and the transverse momentum of the electron or muon. Events are divided by H_{T} and number of b-tagged jets. Black points with error bars are data from the control sample. Stacked, colored histograms are yields from simulated events.

Figure 5.17 shows the important $E_{\mathrm{T}}^{\mathrm{miss}}$ distributions of the single lepton control sample, in bins of H_{T} and number of b-tagged jets. It is crucial because the events in data provide the values of $E_{\mathrm{T}}^{\mathrm{miss}}$ used in the prediction of the tt/W/t background. As described above, the $E_{\mathrm{T}}^{\mathrm{miss}}$ in $t\bar{t}/W/t$ events failing the veto (entering the single lepton control sample) or entering the analysis sample come from the same source, and therefore should have very similar distributions. However, the cuts on the leptons create a bias in the angle at which the neutrino momentum points with respect to the W boson, causing a broadening of the $E_{\mathrm{T}}^{\mathrm{miss}}$ spectrum in a way which this analysis accounts for.

The final crucial check of the single lepton control sample is the distribution of $\Delta\theta_T$ itself, shown in Fig. 5.18. The method of predicting the tt/W/t background relies on this angle being very well understood theoretically and experimentally, unlike the $E_{\mathrm{T}}^{\mathrm{miss}}$ distribution. These plots show very good agreement between data and simulated events. This is most clearly shown in the high-statistics =1 b-tag samples, at both low and high H_{T}. Individual events in data will be reweighted according to their value of $\Delta\theta_T$, explained in the next subsection.

5.1.3 Method for predicting $E_{\mathrm{T}}^{\mathrm{miss}}$ spectrum

As explained in this section, the angle between the W boson and its daughter particle is well known and shown to be accurately generated in simulated events when compared to events in the single lepton control sample. The distribution in the control sample is sculpted because events at high $\Delta\theta_T$ often fail to pass the electron and muon selection criteria and enter the lepton-vetoed analysis sample instead. These events tend to

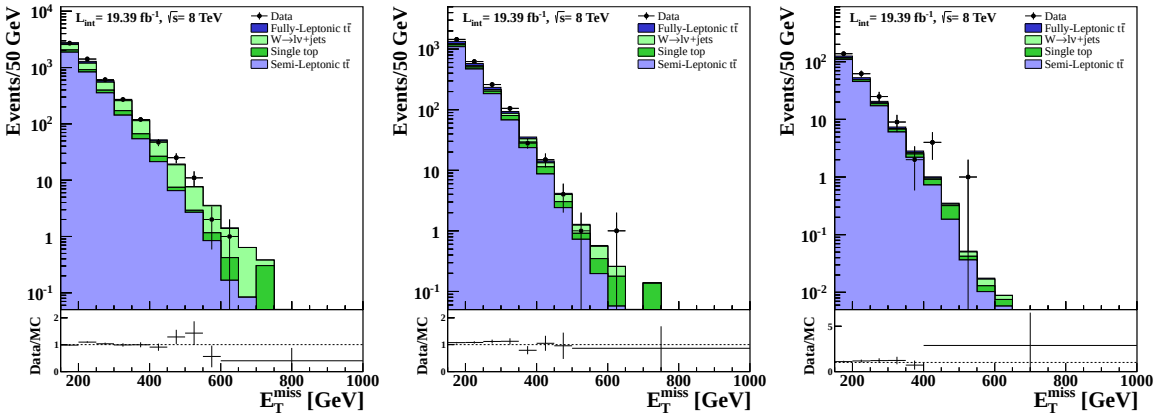

(a) 400<H_{T} <800 GeV, =1 b-tag (b) 400<H_{T} <800 GeV, =2 b-tags (c) 400<H_{T} <800 GeV, ≥3 b-tags

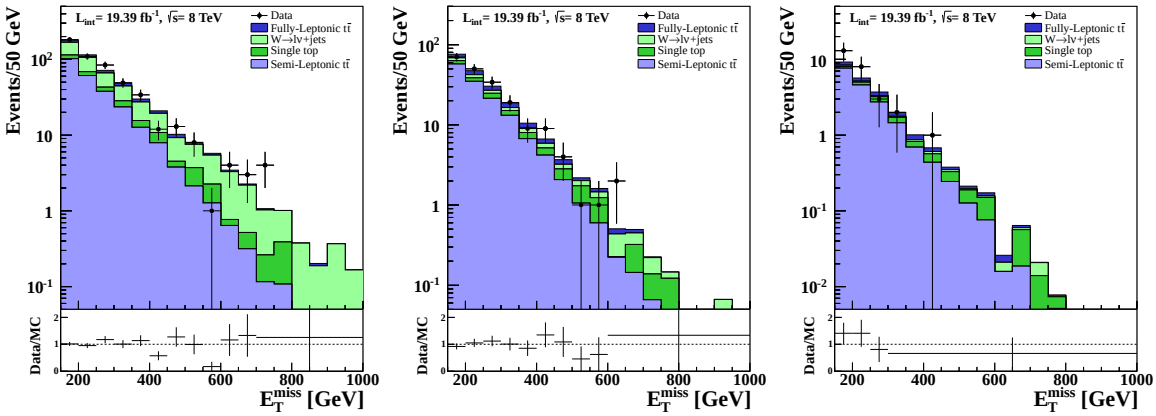

(d) H_{T} >800 GeV, =1 b-tag (e) H_{T} >800 GeV, =2 b-tags (f) H_{T} >800 GeV, ≥3 b-tags

Figure 5.17: $E_{\mathrm{T}}^{\mathrm{miss}}$ of events in the single lepton control sample, divided by H_{T} and number of b-tagged jets. Black points with error bars are data. Stacked, colored histograms are yields from simulated events.

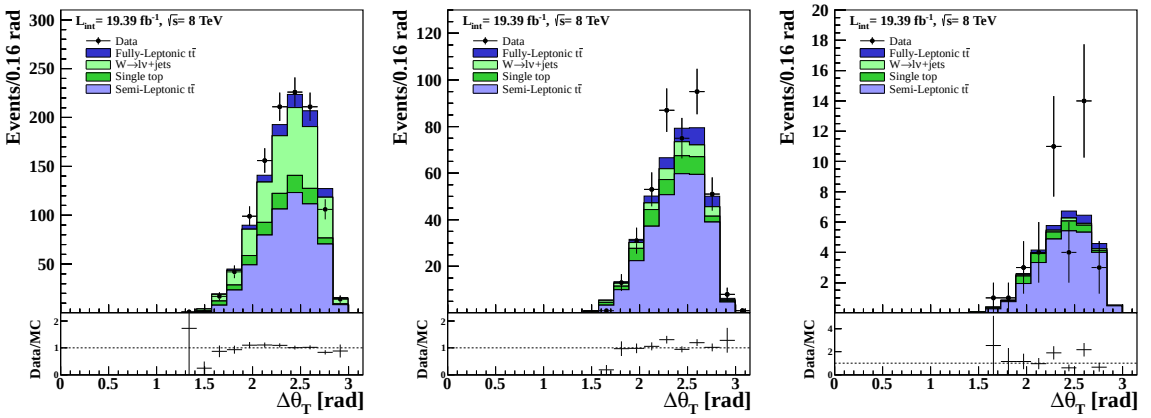

(a) 400<H_{T} <800 GeV, =1 b-tag (b) 400<H_{T} <800 GeV, =2 b-tags (c) 400<H_{T} <800 GeV, ≥3 b-tags

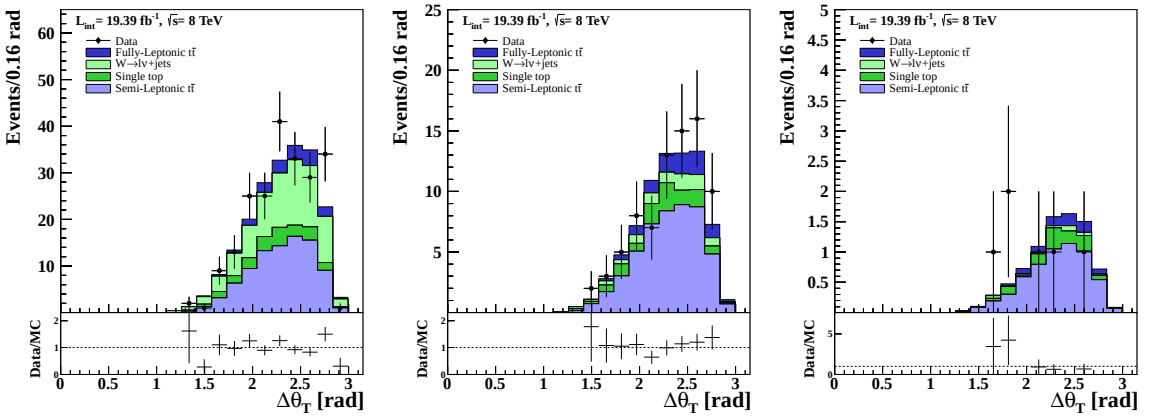

(d) H_{T} >800 GeV, =1 b-tag (e) H_{T} >800 GeV, =2 b-tags (f) H_{T} >800 GeV, ≥3 b-tags

Figure 5.18: Angle between the reconstructed charged lepton transverse momentum in the W rest frame and the W transverse momentum in the lab frame. Events are divided by H_{T} and number of b-tagged jets. Black points with error bars are data from the control sample. Stacked, colored histograms are yields from simulated events.

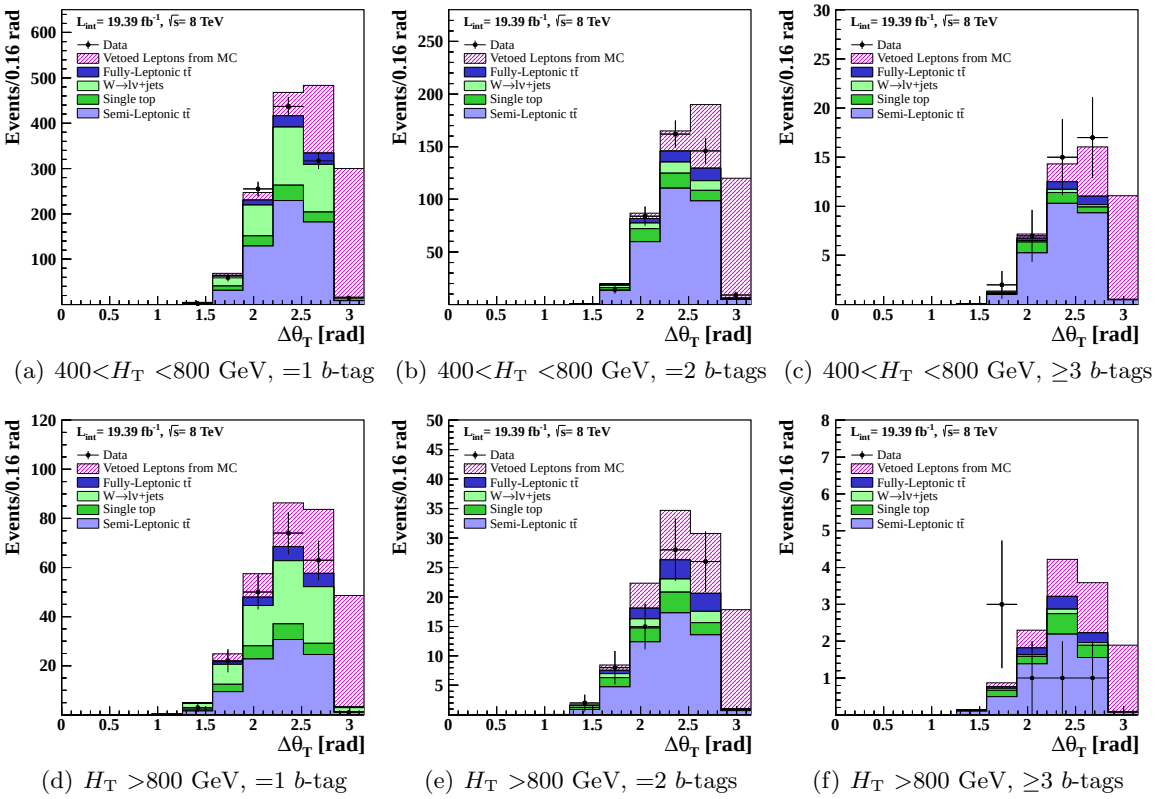

(a) 400<H_{T} <800 GeV, =1 b-tag (b) 400<H_{T} <800 GeV, =2 b-tags (c) 400<H_{T} <800 GeV, ≥3 b-tags

(d) H_{T} >800 GeV, =1 b-tag (e) H_{T} >800 GeV, =2 b-tags (f) H_{T} >800 GeV, ≥3 b-tags

Figure 5.19: Angle between the electron or muon transverse momentum in the W rest frame and the W transverse momentum in the lab frame. Events are binned according to the regions of the scale factors, except for the last two bins, which are combined to obtain the scale factor for that region. The distributions are shown separately according to H_{T} and the number of b-tagged jets. Black points with error bars are data from the control sample. Stacked, colored histograms are yields from simulated events that are expected to enter the single lepton control sample. The stacked, hatched, magenta histograms represent the distribution from events from simulation where exactly one W boson decayed leptonically (possibly through a tau) to a muon or electron, which fails the veto criteria and causes the event to enter the analysis sample. Here, the generator-level electron or muon momentum is used to calculate $\Delta\theta_T$.

have low lepton p_{T} and high $E_{\mathrm{T}}^{\mathrm{miss}}$, directly due to the effects of the W boson p_{T} and angle of the lepton p_{T} with respect to it.

Figure 5.19 shows the $\Delta\theta_T$ distribution of all events with exactly one W boson decaying leptonically to an electron or muon, regardless of whether the charged lepton

passes the veto selection criteria. As in Fig. 5.18, the black points and colored histograms represent the yields in the single lepton control sample in data and simulation, respectively. The hatched magenta distribution stacked on top of the simulated events represents the Category 1 events in which the electron or muon was either not observed or did not pass the selection criteria. The $E_{\mathrm{T}}^{\mathrm{miss}}$ spectrum of these events needs to be modeled to predict the amount of background present in the signal sample. As shown in Fig. 5.12, Category 1 events with the same value of $\Delta\theta_T$ generally have the same distribution of $E_{\mathrm{T}}^{\mathrm{miss}}$. For each bin of $\Delta\theta_T$, approximately 0.16 radians, the ratio of simulated events in the signal sample (hatched magenta area) with respect to simulated events in the control sample (solid colored histogram) is calculated. This ratio is used to scale the weight of events in the control sample in data for that $\Delta\theta_T$ bin, replicating the $\Delta\theta_T$ shape expected of events in the signal region. This simulation-based ratio is the only quantity in this method taken from simulation. It was chosen because the polarization of W bosons and reconstructed lepton efficiencies are known to high precision, therefore the $\Delta\theta_T$ distribution is well understood. Using a ratio eliminates many sources of systematic uncertainty that would otherwise arise from using yields from simulation because these effects cancel.

The values of scale factors are calculated separately for each b-tag multiplicity and H_{T} bin. They are shown in Table 5.1 for H_{T} 400-800 GeV, and Table 5.2 for H_{T} greater than 800 GeV. Since the $\Delta\theta_T$ distribution is compressed to high values, five scale factors for different $\Delta\theta_T$ ranges are used. The highest $\Delta\theta_T$ range is double the size of the others, covering the last two histogram bins in Fig. 5.19. The last bin in this figure always has a

Table 5.1: $\Delta\theta_T$-based scale factors from simulation, for the H_{T} range from 400 to 800 GeV. These scale factors are applied to the yields in the single-lepton data control sample.

$400 < H_{\mathrm{T}} < 800$ GeV	$= 1$ b-tagged jet	$= 2$ b-tagged jets	≥ 3 b-tagged jets
$1.26 < \Delta\theta_T < 1.575$	0.022 ± 0.011	0.024 ± 0.022	0.052 ± 0.057
$1.575 < \Delta\theta_T < 1.89$	0.069 ± 0.007	0.058 ± 0.014	0.089 ± 0.041
$1.89 < \Delta\theta_T < 2.205$	0.071 ± 0.004	0.061 ± 0.006	0.063 ± 0.010
$2.205 < \Delta\theta_T < 2.52$	0.123 ± 0.004	0.131 ± 0.006	0.145 ± 0.011
$\Delta\theta_T > 2.52$	1.238 ± 0.019	1.283 ± 0.028	1.345 ± 0.046

Table 5.2: $\Delta\theta_T$-based scale factors from simulation, when H_{T} is greater than 800 GeV. These scale factors are applied to the yields in the single-lepton data control sample.

$H_{\mathrm{T}} > 800$ GeV	$= 1$ b-tagged jet	$= 2$ b-tagged jets	≥ 3 b-tagged jets
$1.26 < \Delta\theta_T < 1.575$	0.035 ± 0.012	0.036 ± 0.0169	0.017 ± 0.008
$1.575 < \Delta\theta_T < 1.89$	0.152 ± 0.017	0.118 ± 0.0175	0.137 ± 0.042
$1.89 < \Delta\theta_T < 2.205$	0.200 ± 0.017	0.235 ± 0.0207	0.261 ± 0.041
$2.205 < \Delta\theta_T < 2.52$	0.256 ± 0.015	0.319 ± 0.0242	0.312 ± 0.036
$\Delta\theta_T > 2.52$	1.172 ± 0.044	1.243 ± 0.0673	1.368 ± 0.140

very low number of events in the control sample, while this is where the distribution for signal region events peaks. It is possible for some regions to have no control sample events in this important bin, so for the purposes of calculating and applying the scale factor, combining the two ensures that the high $\Delta\theta_T$ signal region is accounted for. Due to the peaking of simulated signal events at high $\Delta\theta_T$, control sample events with $\Delta\theta_T$ less than 2.205 radians have a small weight, and little effect on the final $E_{\mathrm{T}}^{\mathrm{miss}}$ distribution. Scaling events having $\Delta\theta_T$ greater than 2.52 results in the greatest effect, increasing the yield by 20-30%.

Figure 5.20 shows the result of scaling the data control sample by the ratios described above. The colored histograms are the yields from Category 1 simulated events where the electron or muon is either not observed or does not pass all selection criteria, and enters the signal region. The black points are events from data in the single lepton control sample, which have been scaled by the $\Delta\theta_T$-based scale factors. For most regions, the resulting distribution is quite similar to what is expected from simulation. However, the sample with high H_{T} and $\geq$3 b-tagged jets has low statistics, and the effect is most pronounced in the final two $\Delta\theta_T$ bins where the yield fluctuates down. As a result, we expect the predicted $E_{\mathrm{T}}^{\mathrm{miss}}$ spectrum for this region to be less than what the distribution from simulated events would show.

5.1.4 Evaluation of systematic uncertainties

Table 5.4 and Table 5.5 list the effects of important sources of systematic uncertainty on the prediction of Category 1 events. In using the ratios of simulation-based

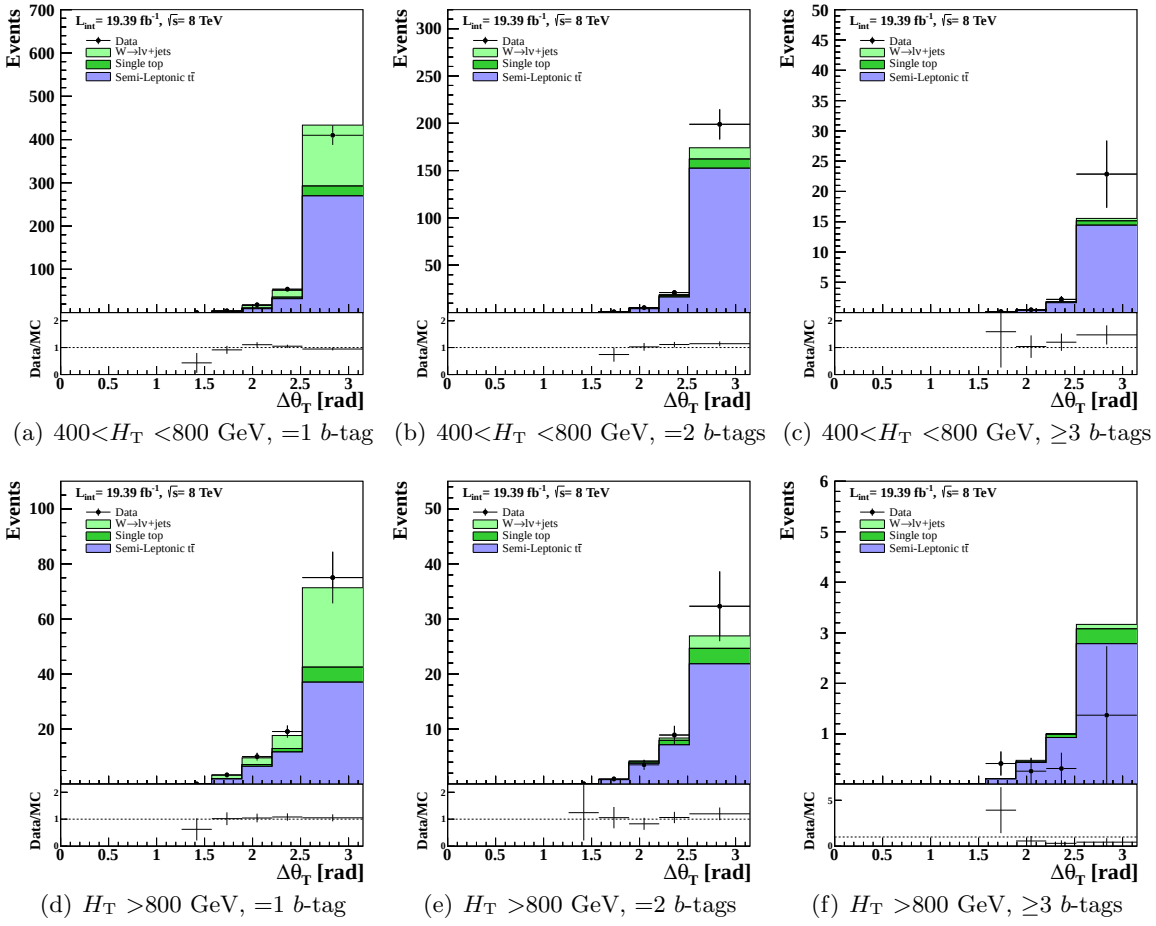

(a) 400<H_{T} <800 GeV, =1 b-tag (b) 400<H_{T} <800 GeV, =2 b-tags (c) 400<H_{T} <800 GeV, ≥3 b-tags

(d) H_{T} >800 GeV, =1 b-tag (e) H_{T} >800 GeV, =2 b-tags (f) H_{T} >800 GeV, ≥3 b-tags

Figure 5.20: Angle between the electron or muon transverse momentum in the W rest frame and the W transverse momentum in the lab frame. Events are binned according to the regions of the scale factors, and shown separately for different H_{T} and number of b-tagged jets. Black points with error bars are data from the control sample, with weights modified by the scale factors obtained from simulated events. Stacked, colored histograms are yields from simulated events where exactly one W boson decayed leptonically (possibly through a tau) to a muon or electron, which fails the veto criteria and causes the event to enter the analysis sample. Here, the generator-level electron or muon momentum is used to calculate $\Delta\theta_T$.

Table 5.3: Observed and predicted yields of Category 1 $t\bar{t}/W/t$ events from data and MC. Events are binned in H_{T} and $E_{\mathrm{T}}^{\mathrm{miss}}$. Uncertainties are statistical, and include the statistical uncertainty on the scale factor from simulation.

H_{T} [GeV]		400 – 800			> 800	
$E_{\mathrm{T}}^{\mathrm{miss}}$ [GeV]	150 – 250	250 – 350	> 350	150 – 250	250 – 350	> 350
Prediction						
=1 b-tag	2067 ± 54	370.6 ± 19	91.3 ± 9.0	167 ± 14	61.1 ± 7.4	38.8 ± 5.6
=2 b-tags	1042 ± 38	187.1 ± 15	30.8 ± 7.0	67.5 ± 8.6	30.9 ± 5.5	14.8 ± 3.7
≥3 b-tags	110.7 ± 13	18.7 ± 4.7	4.9 ± 3.0	9.8 ± 3.0	2.2 ± 1.4	0.14 ± 0.14
$t\bar{t}/W/t$ MC						
=1 b-tag	2093 ± 11	404.1 ± 5.0	96.2 ± 2.8	172.9 ± 3.3	63.94 ± 2.0	38.0 ± 1.8
=2 b-tags	983.1 ± 6.2	169.4 ± 2.6	28.3 ± 1.0	75.0 ± 1.6	27.2 ± 1.0	13.42 ± 0.70
≥3 b-tags	96.27 ± 0.98	15.74 ± 0.38	2.08 ± 0.10	9.51 ± 0.31	3.26 ± 0.17	1.49 ± 0.15

Table 5.4: Percent effect of systematic uncertainties on the prediction of estimated event yields, 400<H_{T} <800 GeV.

		Jet energy scale	Jet energy resolution	b-tag efficiency	W frac.
$E_{\mathrm{T}}^{\mathrm{miss}}$ 150-250	=1 b-tag	±2.8	+0.23 -0.39	±0.38	±2.1
	=2 b-tags	±3.3	+0.35 -0.08	±0.06	±0.43
	≥3 b-tags	+1.8 -5.5	+0.06 -0.22	±0.05	±0.10
$E_{\mathrm{T}}^{\mathrm{miss}}$ 250-350	=1 b-tag	+1.5 -4.6	± 0.12	±0.08	±0.52
	=2 b-tags	+2.3 -4.2	± 0.22	±0.08	±0.04
	≥3 b-tags	+5.1 -1.5	± 0.48	±0.15	±0.12
$E_{\mathrm{T}}^{\mathrm{miss}}$ >350	=1 b-tag	+2.8 -1.2	±0.37	±0.22	+0.83 -1.18
	=2 b-tags	+1.6 -3.4	±0.23	±0.09	±0.02
	≥3 b-tags	+4.7 -0.5	±0.52	±0.13	±0.17

Table 5.5: Percent effect of systematic uncertainties on the prediction of estimated event yields, H_{T} >800 GeV.

		Jet energy scale	Jet energy resolution	b-tag efficiency	W frac.
$E_{\mathrm{T}}^{\mathrm{miss}}$ 150-250	=1 b-tag	+0.7 -5.3	+0.06 -0.17	±0.11	±0.11
	=2 b-tags	+1.1 -6.0	± 0.14	±0.05	±0.18
	≥3 b-tags	+4.4 -7.4	+0.84 -0.38	±0.18	±0.55
$E_{\mathrm{T}}^{\mathrm{miss}}$ 250-350	=1 b-tag	+5.6 -8.3	±0.24	±0.23	±0.75
	=2 b-tags	+7.0 -8.2	±0.39	±0.04	±0.78
	≥3 b-tags	+8.9 -11.1	±0.91	±0.42	±1.5
$E_{\mathrm{T}}^{\mathrm{miss}}$ >350	=1 b-tag	+4.0 -7.2	±0.07	±0.53	±1.5
	=2 b-tags	±7.4	±0.36	±0.01	±0.83
	≥3 b-tags	±25	±1.5	±0.87	±2.2

quantities to correct the Category 1 prediction, we measure the effect of the potential difference between simulation and data.

In particular, the jet-based uncertainties (arising from the calorimeter performance) are important in all background predictions for a search with a large amount of hadronic activity. First, we vary the jet energy scale, for which we measure the $\Delta\theta_T$ scale factor in simulated events if all the jets in each event had 5% more transverse momentum. This also requires an adjustment of the $E_{\mathrm{T}}^{\mathrm{miss}}$, which calculated from particle flow objects, including jets. This is repeated for all jets assigning 5% less transverse momentum. The resulting range about the central prediction represents the systematic uncertainty on the data-driven prediction given an incorrect assesment of the jet energy scale effecting the $\Delta\theta_T$ scale factor. As seen in the table, this provides the largest variation in the final prediction. The extent to which any systematic uncertainty can effect the final result is reduced by only using ratios of quantities from simulation, which tends to cancel out the larger effects. Next, the simulated jet energy resolution may not accurately model the data. To test this effect, we modify the jet p_{T} according to the difference between the reconstructed value and *true* generator-level value. Similarly, we adjust the $E_{\mathrm{T}}^{\mathrm{miss}}$ and record the small effect of this variation on the final result.

Another very important systematic uncertainty is the uncertainty on the b-tag efficiency. All simulated events are weighted such that the b-tag efficiency for those events are the same as in data. However, there is an uncertainty in the measured value of the b-tag efficiency in data, which depends on the p_{T} and of the jet. All simulated events are each

given a probability to be identified as having zero, one, two, three, or more b-tagged jets. The events used for computing the $\Delta\theta_T$ scale factor have these probabilities adjusted to reflect a reduction or enhancement in b-tag efficiency according to the appropriate measured uncertainty. This effect is limited to less than 1%.

A final uncertainty of particular importance in the $\Delta\theta_T$ method is the relative contamination of W+jets events in what is largely a $t\bar{t}$ dominated sample. As seen above, there is a small shape difference in $\Delta\theta_T$ between the two backgrounds, and if the relative fraction of W+jets is very large (or very small) the method must be robust. To measure this systematic uncertainty, we vary the yield of W+jets by $\pm 50\%$ in calculating the $\Delta\theta_T$ scalefactors, and check the effect on the final result. This variation has a larger effect in the $=1$ b-tag validation region, where the W+jets component of the background is larger, but it is still much smaller than any statistical uncertainties. Knowing that the uncertainty of a prediction is dominated by the size of control samples, and not unknowns within the methodology itself, is one of the main benefits of using data-driven predictions.

Another systematic uncertainty that was important in previous applications of this method has been the uncertainty on the top-quark p_{T} spectrum. Like the $E_{\mathrm{T}}^{\mathrm{miss}}$ spectrum, the tails of this distribution are being probed where the validity of simulation was not rigorously studied. Before the completion of this analysis, the collaboration endorsed a correction factor to the p_{T} spectrum of top-quarks such that reconstructed quantities that rely on this distribution are closer to observations in data [30]. Since this correction is applied here, the p_{T} spectrum is not varied to obtain an additional uncertainty. As a check,

the effect of removing this correction is tested. The effect on yields at low H_{T} (400–800 GeV) is a slight decrease, with up to a –1.1% change in the prediction from data. At high H_{T}, the yields in most analysis regions increased by less than +5%. However, the $\geq$3 b-tag selection increased by the greatest amount, +7.0% at moderate $E_{\mathrm{T}}^{\mathrm{miss}}$ (250–350 GeV) and +22% at high $E_{\mathrm{T}}^{\mathrm{miss}}$.

The systematic uncertainties on the scale factor associated with the size of the simulated samples are included in all tables as part of the statistical uncertainty on the method. Therefore, the statistical uncertainties listed in the next section include the effects of both the data control sample size and the size of simulated samples.

5.1.5 $E_{\mathrm{T}}^{\mathrm{miss}}$ spectrum results

The resulting $E_{\mathrm{T}}^{\mathrm{miss}}$ spectra from the $\Delta\theta_T$ method in each analysis region are shown in Fig. 5.21. Figures 5.21(a) and (b) are the predictions for the two H_{T} regions in the =1 b-tag validation sample, where the potential amount of signal would be negligible with respect to the Standard Model background. Since the prediction represents only a portion of the events in the analysis sample, the data is not shown. Instead, the prediction is compared with the expected $t\bar{t}/W/t$ spectrum from simulated events. While the data-driven prediction is important for reducing systematic uncertainty and using the most accurate picture of event kinematics from data, years of experience producing accurate simulation has yielded a very good description of most Standard Model processes in the bulk of kinematic space. In the high-statistics validation regions, the $\Delta\theta_T$ method is very close to simulation for the full range of $E_{\mathrm{T}}^{\mathrm{miss}}$ across three orders of magnitude, which is very reassuring. In the important

Table 5.6: Predicted yields of Category 1 events in each analysis region. The first uncertainty is statistical, and the second is from systematic sources.

	150<$E_{\mathrm{T}}^{\mathrm{miss}}$ <250 GeV	250<$E_{\mathrm{T}}^{\mathrm{miss}}$ <350 GeV	$E_{\mathrm{T}}^{\mathrm{miss}}$ >350 GeV
400<H_{T} <800 GeV			
=1 b-tag	2067 ± 58 ± 72	371 ± 20 ± 12	91 ± 11 ± 2
=2 b-tags	1042 ± 43 ± 34	187 ± 15 ± 6	30.8 ± 7.0 ± 0.8
≥3 b-tags	111 ± 13 ± 4	18.7 ± 4.5 ± 0.6	4.9 ± 3.0 ± 0.1
H_{T} >800 GeV			
=1 b-tag	167 ± 15 ± 5	61.1 ± 7.5 ± 4.3	38.8 ± 7.0 ± 2.3
=2 b-tags	67.5 ± 9.0 ± 2	30.9 ± 5.5 ± 2.4	14.8 ± 3.8 ± 0.9
≥3 b-tags	9.8 ± 3.1 ± 0.6	2.2 ± 1.4 ± 0.2	0.137 ± 0.144 ± 0.03

=2 b-tag and ≥3 b-tag regions, we observe similar agreement. Using smaller control samples with ≥3 b-tags, statistical fluctuations become more important. In Fig. 5.21(f), the $\Delta\theta_T$ prediction performs well up to about 300 GeV. However, a downward fluctuation in the number of single lepton events in the high $\Delta\theta_T$ region, as observed above, depletes the high $E_{\mathrm{T}}^{\mathrm{miss}}$ region.

Table 5.6 lists the predicted yields of Category 1 events in each analysis region. For the most part, statistical uncertainties are much larger than the systematic ones. This is a good feature of the analysis, since in principle the uncertainty can be reduced by obtaining a larger data sample, and is not strictly limited by assumptions made in the method. These

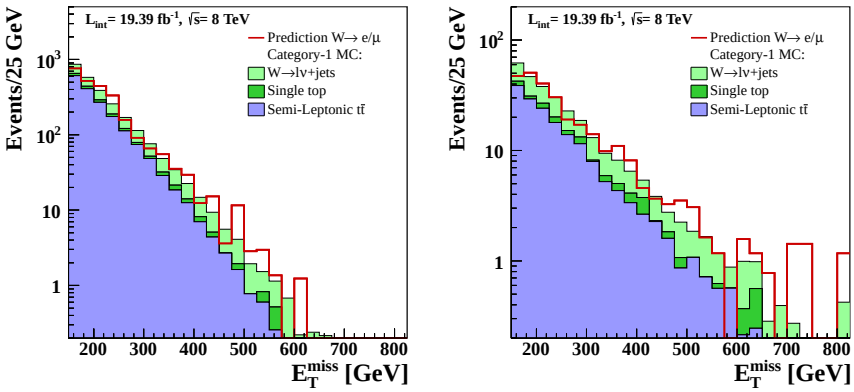

(a) 400<H_{T} <800 GeV, =1 b-tag

(b) H_{T} >800 GeV, =1 b-tag

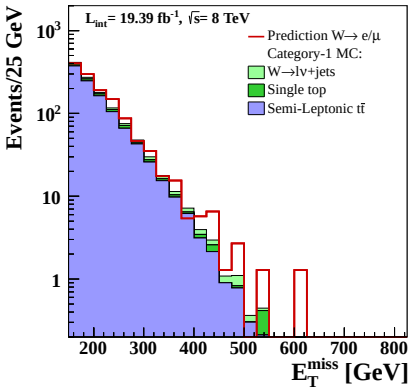

(c) 400<H_{T} <800 GeV, =2 b-tags

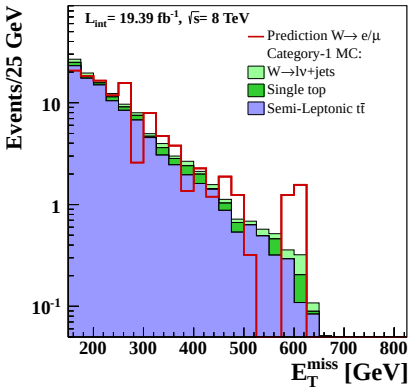

(d) H_{T} >800 GeV, =2 b-tags

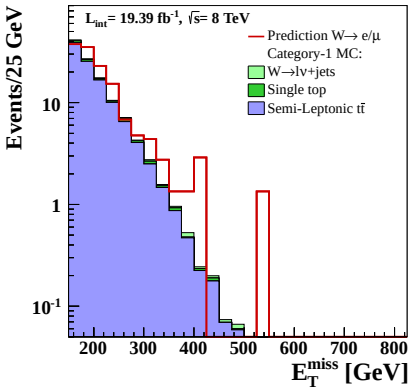

(e) 400<H_{T} <800 GeV, ≥3 b-tags

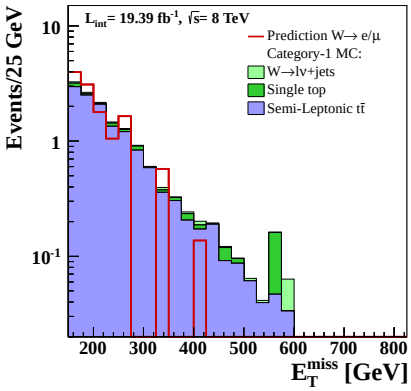

(f) H_{T} >800 GeV, ≥3 b-tags

Figure 5.21: Predicted $E_{\mathrm{T}}^{\mathrm{miss}}$ distributions of Category 1 events in each region of H_{T} and b-tag multiplicity. The solid red line is the predicted $E_{\mathrm{T}}^{\mathrm{miss}}$ spectrum taken from data in the single lepton control sample and weighted according to the $\Delta\theta_T$-based scale factor. The stacked, colored histograms represent the distribution of simulated Category 1 $t\bar{t}$, W+jets, and single top events.

yields are combined with the predictions of Category 2 and Category 3 yields to create a complete picture of the $t\bar{t}$, W+jets, and single-top content in each signal region.

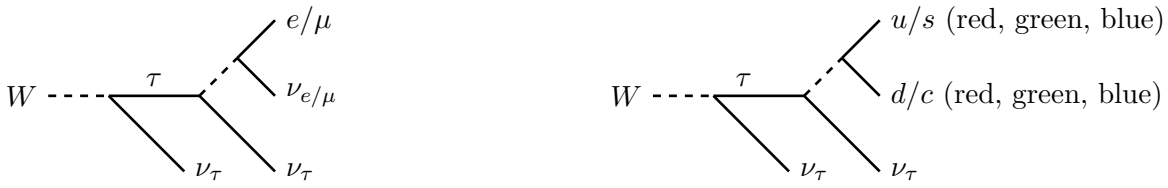

Figure 5.22: A W boson decay to a τ-lepton. The diagram on the left shows the possibilities of decays to the lighter leptons, which may be observed in the detector. The diagram on the right shows the possibilities of decays to quarks, which are observed as jets.

5.2 Predicting the $t\bar{t}$, W+jets, and single top background where at least one $W \to \tau \to$hadrons

A leptonic W decay, within a $t\bar{t}$, W+jets, or single top process, can produce a final state with no charged leptons. As demonstrated earlier in this chapter (Fig. 5.1), almost 10% of W boson decays result in a τ-lepton. Figure 5.22 shows the possible final states for this scenario. Approximately 33% of τ-decays result in an electron or muon, while the remaining 66% result in jets and missing energy in the final state. Since there is an observed or lost electron or muon, the former scenario is addressed in Sec. 5.1, and the latter is case addressed here. Events involving $t\bar{t}$, W+jets, or single-top production that include exactly one W boson decaying to a hadronic τ-lepton are considered to be in the Category 2 sample. Since this channel has unique properties, a specially designed technique is used to recover the $E_{\mathrm{T}}^{\mathrm{miss}}$ spectrum of this sample. The Category 3 cases where one or both W bosons result in a hadronic τ-lepton will also be discussed in this section.

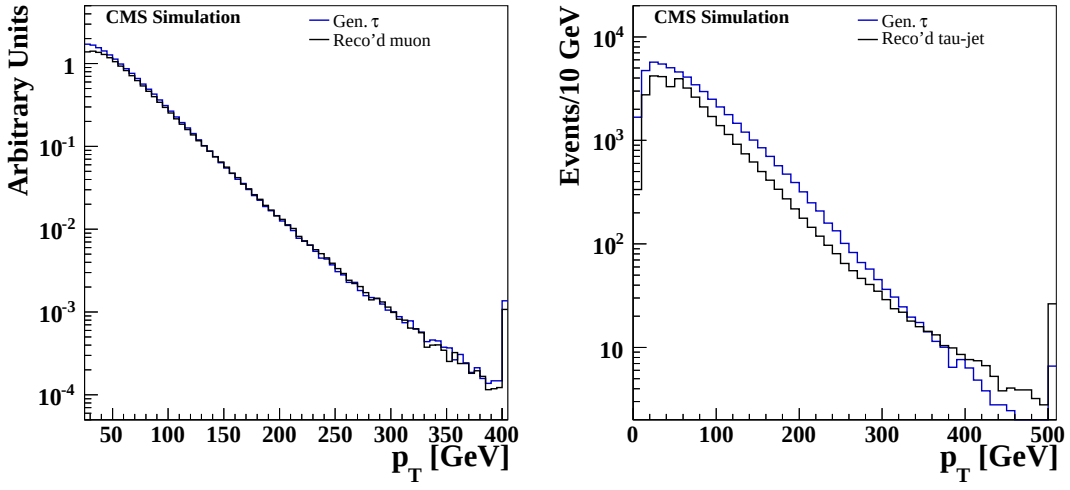

(a) Reco'd muon and generator-level τ-lepton. (b) Reco'd τ-jet and generator-level τ-lepton.

Figure 5.23: Transverse momentum spectra related to τ-leptons in Category 2 events from $t\bar{t}$ simulation. The solid blue line is the τ-lepton p_{T} determined from simulation without including detector reconstruction. The solid black line is muon or jet p_{T} with full detector reconstruction and object selection criteria applied. The jet must be within ΔR <0.2 of a generator-level τ-lepton.

5.2.1 Characteristics of hadronically decaying tau leptons

Since all charged leptons are very light with respect to the W boson, the p_{T} spectra of lepton decay products from a W should be identical for a given process, apart from polarization effects. However, the methods for measuring the different charged lepton p_{T} are very different. A hadronically decaying τ-lepton produces a small number of tracks in the tracker and an energy deposit in the calorimeter, as well as an additional neutrino. Therefore, the reconstructed p_{T} of the τ-lepton is affected by the loss of energy to the neutrino as well as the jet energy resolution of the calorimeter. Both of these effects contribute to the reconstructed $E_{\mathrm{T}}^{\mathrm{miss}}$ in the event, which must be accurately modeled in the prediction of the $E_{\mathrm{T}}^{\mathrm{miss}}$ spectrum of Category 2 events.

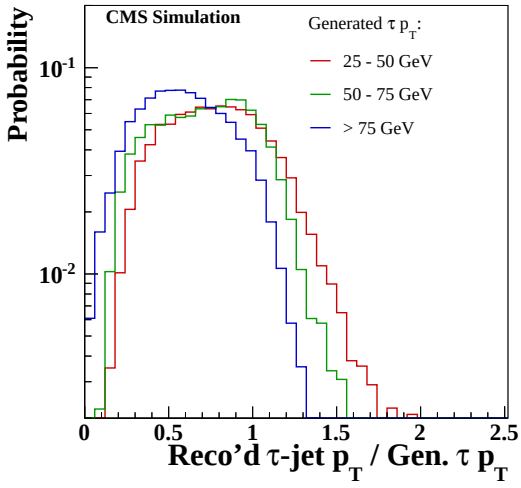

Figure 5.24: The ratio of energy deposited in the calorimeter for τ-leptons with respect to the total τ-lepton energy, plotted separately for three different p_{T} ranges.

The p_{T} spectrum of reconstructed muons in data should be very similar to the p_{T} spectrum of τ-leptons, which cannot be reconstructed in data. Figure 5.23(a) compares the p_{T} spectrum of muons (using selection criteria described later in Table 5.8) with simulated τ-leptons (as determined from generator-level information), both from the decay of a W boson. As expected, they are nearly identical. We focus on the muon because its reconstruction efficiency and momentum resolution are excellent, and they do not leave jet-like clutter in the calorimeter as electrons do.

Figure 5.23(b) compares the p_{T} spectra of τ-leptons and reconstructed τ-jets. The reconstructed τ-jet is from a sample of simulated Category 2 $t\bar{t}$ events, and is within ΔR <0.2 of a simulated τ-lepton. Clearly, the loss of τ-lepton energy is reflected in the measured p_{T} distribution of the reconstructed jets associated with its decay.

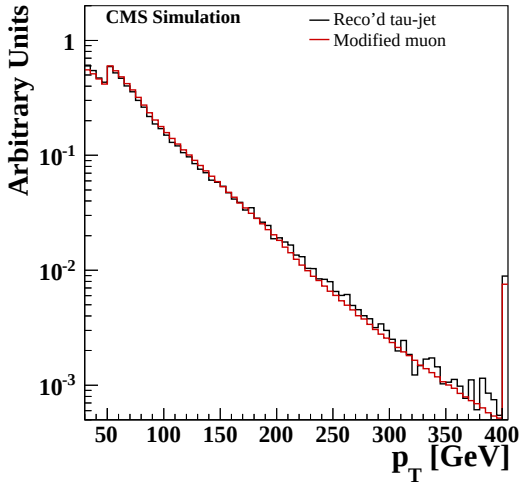

Figure 5.25: Transverse momentum spectra related to τ-leptons in Category 2 events from $t\bar{t}$ simulation. Black line represents good reconstructed jets within ΔR <0.2 of a τ-lepton. Red line represents good reconstructed muons whose momentum has been modified by the jet energy response function. Baseline analysis selection is applied, including the requirement of $\geq$3 jets with p_{T} >50 GeV, where the modified muon is considered a jet.

The relationship between generator-level τ-lepton p_{T} and reconstructed τ-jet p_{T} is shown using simulated events in Fig. 5.24. Category 2 events with a good reconstructed jet within ΔR <0.2 of the hadronically-decaying τ-lepton are plotted according to the magnitude of the τ-jet p_{T} divided by the generator-level τ-lepton p_{T}. This is called the *jet energy response function*, and it shows the amount of *visible* energy deposited in the calorimeter for a particular τ-lepton momentum. At lower τ-lepton p_{T}, a higher fraction of the τ-lepton momentum tends to be observed in the calorimeter. The remaining portion of the τ-lepton momentum is lost, and contributes to $E_{\mathrm{T}}^{\mathrm{miss}}$. The visible energy fraction can be higher than one due to the jet energy resolution of the calorimeters, which can cause the p_{T} to be mismeasured.

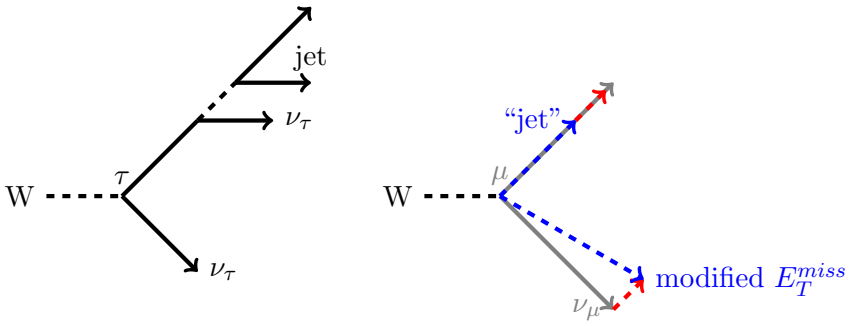

Figure 5.26: Adjusting a single muon event to emulate a hadronic τ-lepton decay. A fraction of the τ-lepton p_{T} is assigned to a "jet" (blue), according to Fig. 5.24. The remaining τ-lepton energy (red) is added to the $E_{\mathrm{T}}^{\mathrm{miss}}$.

The jet energy response function is used to determine the relative amount of τ-lepton energy that is reconstructed as a jet. This is applied to the reconstructed muons in data according to a procedure described later in this section. Figure 5.25 shows the p_{T} of jets matched to a hadronically-decaying τ-lepton in Category 2 events, as seen in Fig. 5.23. In red is the p_{T} spectrum of muons which have been scaled by the jet energy response function on an event-by-event basis. It now very closely agrees with the shape of the τ-jets across several orders of magnitude. Now that the modified muon represents a jet, many other event variables must be recalculated. In particular, an event with H_{T} below the threshold of this analysis may be increased by the mock jet, and pass the H_{T} selection.

The next subsection will describe the muon control sample used for the prediction of Category 2 events, followed by a more detailed description of the procedure used to obtain a good prediction of the size and shape of the $E_{\mathrm{T}}^{\mathrm{miss}}$ distribution of Category 2 events.

Table 5.7: Triggers available at each run and the subsample luminosities .

Runs A, B	5.228 fb^{-1}	HLT_IsoMu24 HLT_IsoMu24_eta2p1
Run C	6.897 fb^{-1}	HLT_IsoMu24 HLT_IsoMu24_eta2p1
Run D	7.273 fb^{-1}	HLT_IsoMu24_eta2p1

Table 5.8: Selection criteria for the single tight muon control sample. The quality criteria for jets, electrons, and muons are the same as Sec. 3.3.3, unless otherwise specified.

Quantity	Requirement
H_{T}	none
Jets	≥ 2 w/ p_{T} >50 GeV ≥ 1 w/ p_{T} >70 GeV
$\Delta\phi_N^{\mathrm{min}}$	none
Electrons	= 0 passing inverted electron veto
Muons	= 1 passing inverted muon veto = 1 w/ p_{T} >25 GeV, $\lvert\eta\rvert$ <2.1, rel. iso.<0.1
$E_{\mathrm{T}}^{\mathrm{miss}}$	none
b-tags	≥ 1 CSVM jets

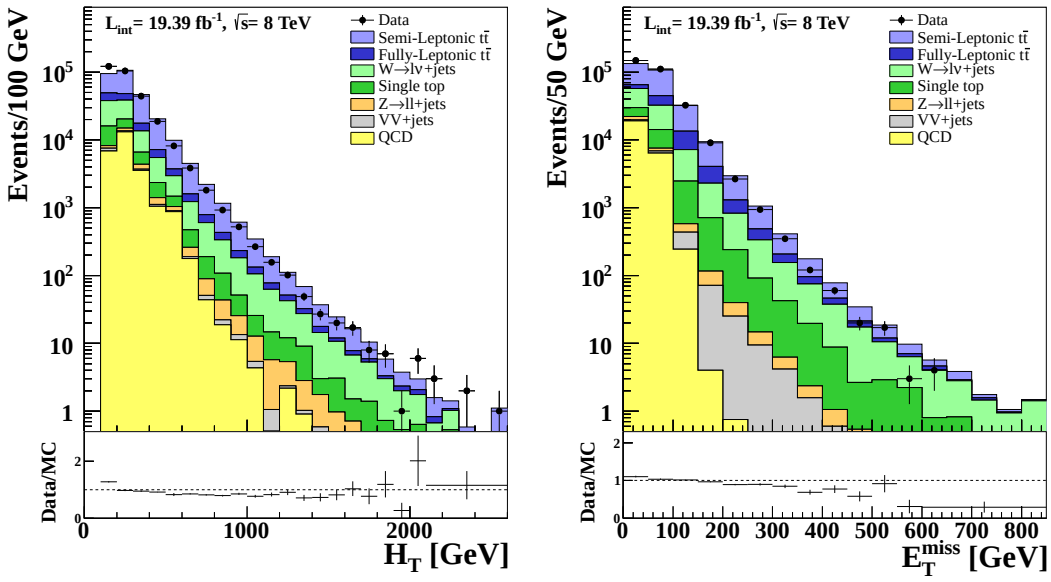

Figure 5.27: Basic kinematic distributions in the single tight muon control sample. Black points with error bars are data. Stacked colored histograms are from simulated events.

5.2.2 Definition of control sample

To predict the $E_{\mathrm{T}}^{\mathrm{miss}}$ spectrum of the Category 2 background, we require a control sample of single muon events which can be made to mock-up a hadronic τ-lepton event. Since a mock jet may be added to an event, the sample must have reduced jet multiplicity requirements, and no restriction on the minimum H_{T} or $E_{\mathrm{T}}^{\mathrm{miss}}$. Therefore, we choose the sample of events passing triggers from the *SingleMu* dataset, listed in Table 5.7. The selection criteria for this sample are listed in Table 5.8. To keep the trigger rates acceptably low, only events with isolated muons with p_{T} >24 GeV and within an $|\eta|$ <2.1 are stored. To ensure our sample lies on the plateau of the trigger efficiency, we place the p_{T} cut on muons in the control sample at 25 GeV. Since the selection criteria for muons in this sample are stricter than the inverted lepton veto, this is called the *single tight muon* control sample.

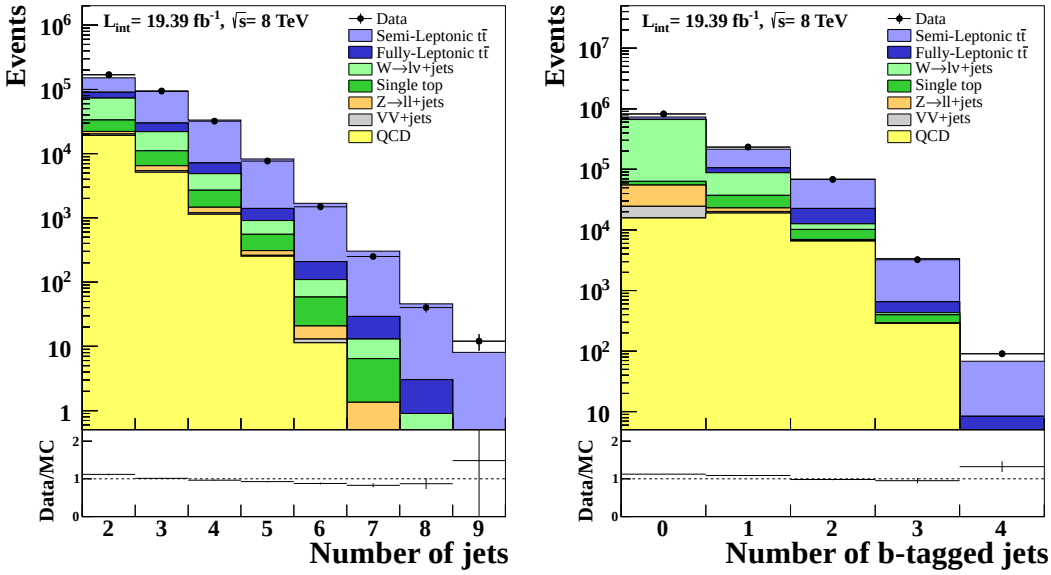

Figure 5.28: Distributions of the number of jets in the single tight muon control sample. Jets in the left plot have p_{T} >50 GeV. A jet is b-tagged if it has p_{T} >30 GeV and passes CSVM. Black points with error bars are data. Stacked colored histograms are from simulated events.

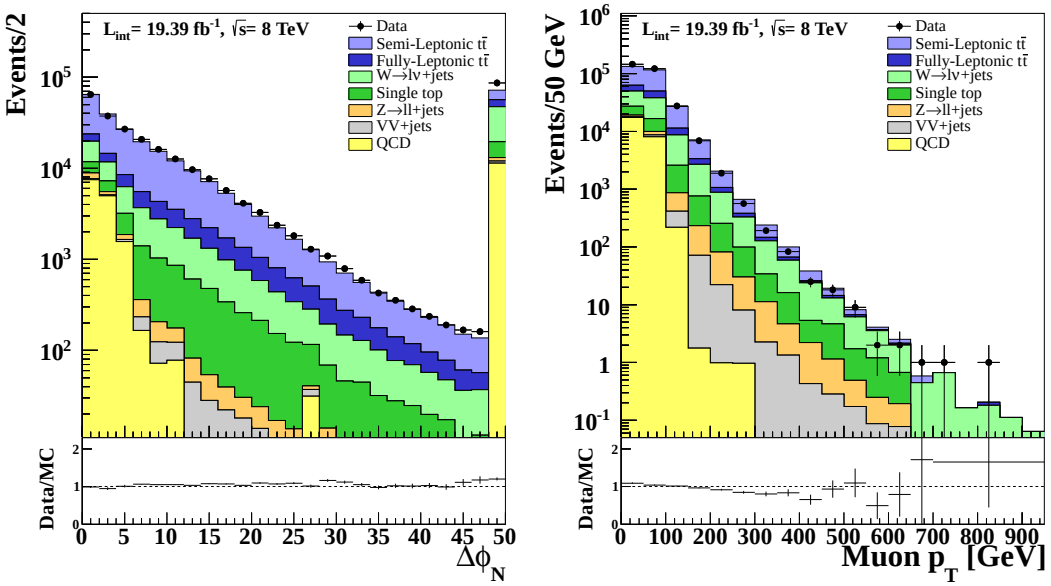

Figure 5.29: Distributions of $\Delta\phi_N^{\mathrm{min}}$ and muon p_{T} in the single tight muon control sample. Black points with error bars are data. Stacked colored histograms are from simulated events.

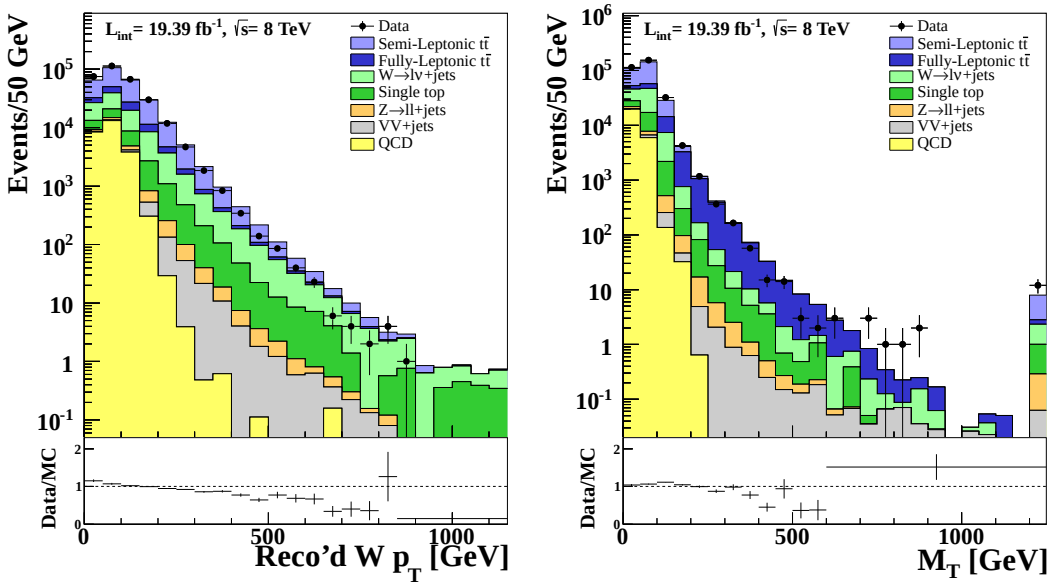

Figure 5.30: Distributions of W p_{T} and M_T in the single tight muon control sample. Both of these quantities are calculated from the reconstructed muon and $E_{\mathrm{T}}^{\mathrm{miss}}$ in the event. Black points with error bars are data. Stacked colored histograms are from simulated events.

To validate this control sample, several important kinematic distributions are shown in Fig. 5.27, Fig 5.28, Fig 5.29, Fig 5.30. They are important in demonstrating that the composition and behavior of the control sample is well understood, and therefore can be reliably implemented in the background prediction procedure. All figures have the control sample criteria listed in Table 5.8 applied. The weights of events from simulation are determined by the cross-section of the process and modified as discussed Ch. 4. Events from $t\bar{t}$ and $Z \to \nu\bar{\nu}$ processes are scaled down to 90%, and purely QCD events have their weights increased by 35%. The first of these figures shows the most basic event quantities, H_{T} and $E_{\mathrm{T}}^{\mathrm{miss}}$. The simulated events are a good description of the shape observed in data, except at the lowest end of H_{T}. This is because the QCD and Drell-Yan yields are not fully represented the lowest values of H_{T}, which effects the low energy end of a few kine-

matic distributions. Unlike in other control samples, no requirements are made on these quantities, since we expect them to change once we introduce the mock τ-jet. Next, the number of jets and b-tagged jets in data are compared with simulated events. The data and simulation are in very close agreement except in the lowest bins, as expected. Figure 5.29 shows two more important event quantities. Interestingly, the shape of $\Delta\phi_N^{\min}$ is modeled remarkably well in simulation. The simulated muon p_{T} is slightly low between 200 and 450 GeV. Since the background prediction uses the muon p_{T} as a measure for how much energy a τ-lepton has, we only use the distribution provided by data, and do not need to worry about the simulation matching perfectly. The final validation plots, in Fig. 5.30, show event quantities derived from both the muon p_{T} and $E_{\mathrm{T}}^{\mathrm{miss}}$. The W boson p_{T} is the vector sum of the muon p_{T} and $E_{\mathrm{T}}^{\mathrm{miss}}$. The distribution from data is slightly softer than expected from simulated events. However, the M_T appears to be well modeled.

5.2.3 Method for predicting $E_{\mathrm{T}}^{\mathrm{miss}}$ spectrum

As described above, a tight muon is used to model the behavior of a τ-jet in order to predict the $E_{\mathrm{T}}^{\mathrm{miss}}$ spectrum in Category 2 events. The probability of a τ-lepton to create a jet of a particular energy is defined by the distributions shown in Fig. 5.24. Since this shape varies slightly with lepton p_{T}, it is separated by three different momentum ranges. In order to take full advantage of this information in the kinematic tails of the control sample, each single muon event samples the full energy fraction distribution. That is, for each bin in Fig. 5.24, the muon p_{T} is multiplied by the value on the x-axis, and given a weight which is the height of that bin.

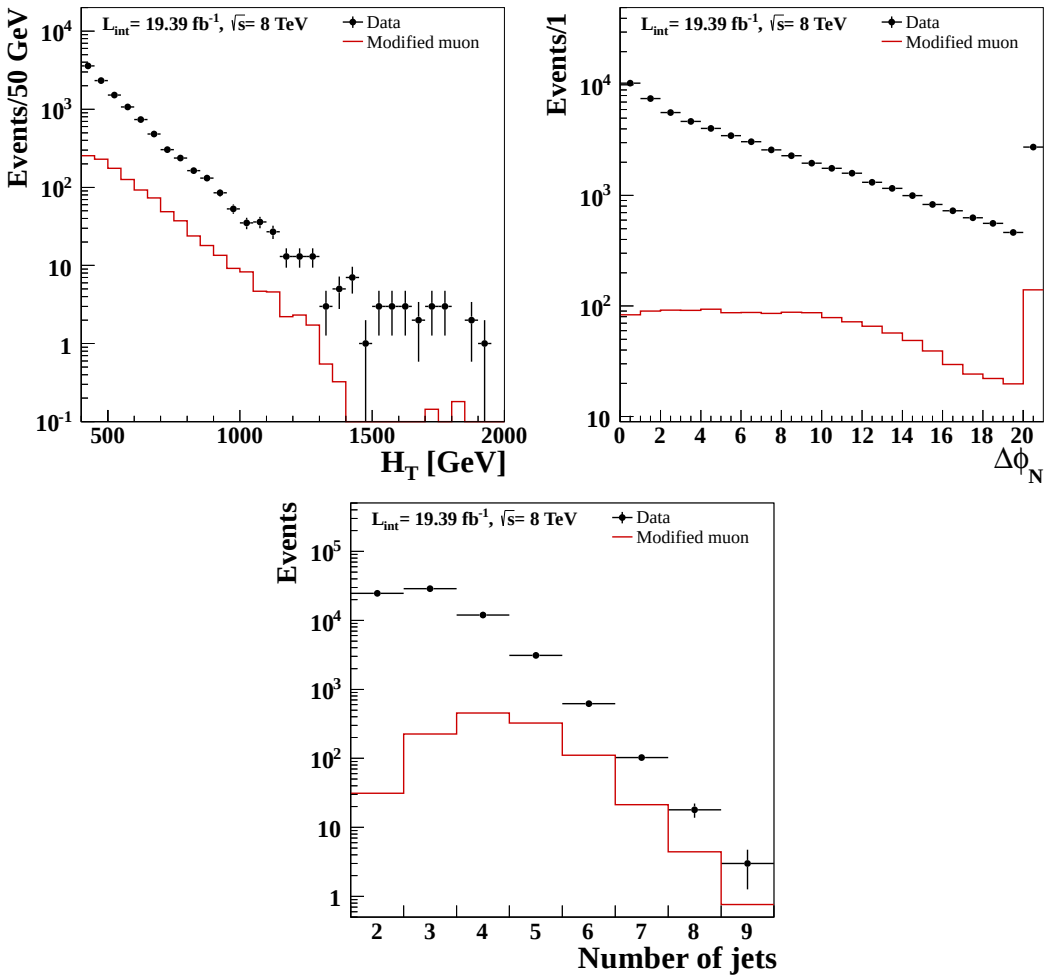

Figure 5.31: Modification of the distributions of jet-based quantities in the single tight muon control sample (defined in Table 5.8). Black points with error bars are the distribution of data in the control sample. Solid red line is the modified distribution of data with the muon emulating a mock τ-jet, and full analysis selection applied.

For each energy fraction assigned to the muon, the event quantities are recalculated considering a jet with that momentum. Most importantly, the remainder of the momentum of the muon is added vectorially to the $E_{\mathrm{T}}^{\mathrm{miss}}$ in the event. In addition, the H_{T}, number of jets, and $\Delta\phi_N^{\mathrm{min}}$ of the event are recalculated. Figure 5.31 shows the distributions of these three quantities before and after adjustment due to the presence of a mock jet. The black points with error bars are events in data passing the baseline control sample selection defined in Table 5.8. After the values for each event are modified, the selection criteria detailed in Sec. 4.4 are applied to the modified quantities. As expected, the distributions of H_{T} and number of jets become harder. The additional jet causes the value of $\Delta\phi_N^{\mathrm{min}}$ to be less peaked at zero, and appear more like semileptonic $t\bar{t}$ distribution in the lepton-vetoed analysis sample.

The most important modification to the event from this procedure is the change in the $E_{\mathrm{T}}^{\mathrm{miss}}$ spectrum. Figure 5.32 provides the distributions of $E_{\mathrm{T}}^{\mathrm{miss}}$ before and after the modifications due to the mock jet, binned according to the number of b-tagged jets. The data points are from the loosest selection criteria for the control sample, shown alongside the distribution after modification and additional cuts. The modified $E_{\mathrm{T}}^{\mathrm{miss}}$ shape is broader. Since each event may enter the histogram many times, a single event in data is spread over multiple bins, causing low bumps in the high $E_{\mathrm{T}}^{\mathrm{miss}}$ tails.

The modified $E_{\mathrm{T}}^{\mathrm{miss}}$ shape is validated in Fig. 5.33. This figure compares the *true* $E_{\mathrm{T}}^{\mathrm{miss}}$ shape of Category 2 events in simulation with the distribution of modified simulated events with a reconstructed tight muon, and provides two important pieces of information.

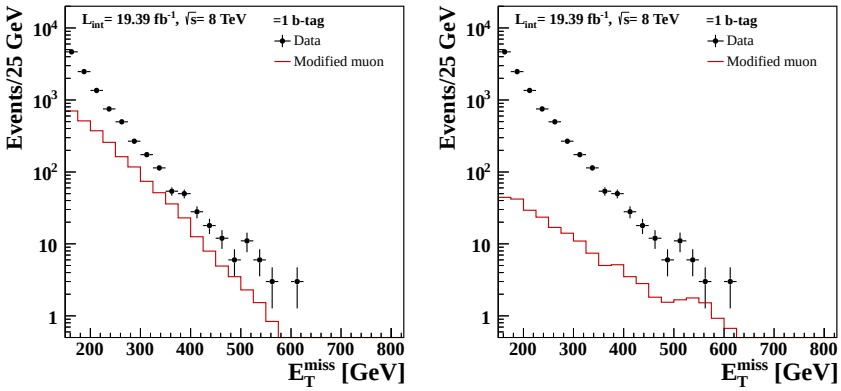

(a) 400<H_{T} <800 GeV, =1 b-tag (b) H_{T} >800 GeV, =1 b-tag

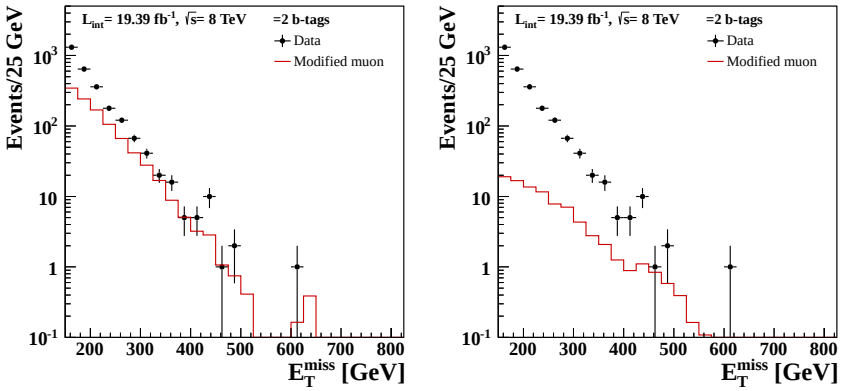

(c) 400<H_{T} <800 GeV, =2 b-tags (d) H_{T} >800 GeV, =2 b-tags

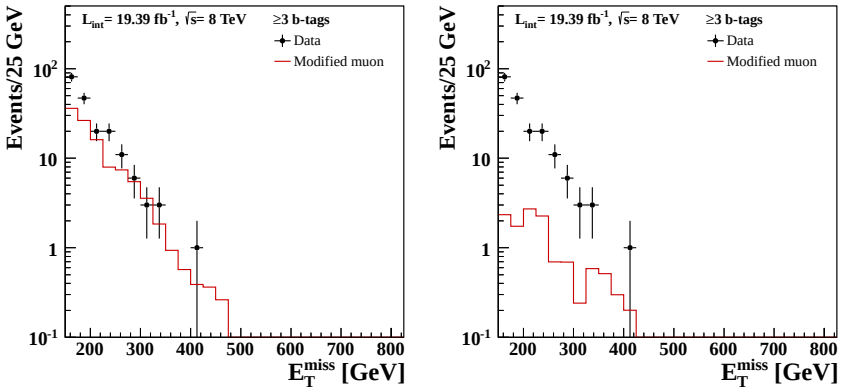

(e) 400<H_{T} <800 GeV, ≥3 b-tags (f) H_{T} >800 GeV, ≥3 b-tags

Figure 5.32: Modification of $E_{\mathrm{T}}^{\mathrm{miss}}$ to predict the shape in Category 2 events. Black points with error bars are the distribution of $E_{\mathrm{T}}^{\mathrm{miss}}$ in the control sample. Solid red line is the modified distribution of data with the muon emulating a mock τ-jet, and full analysis selection applied.

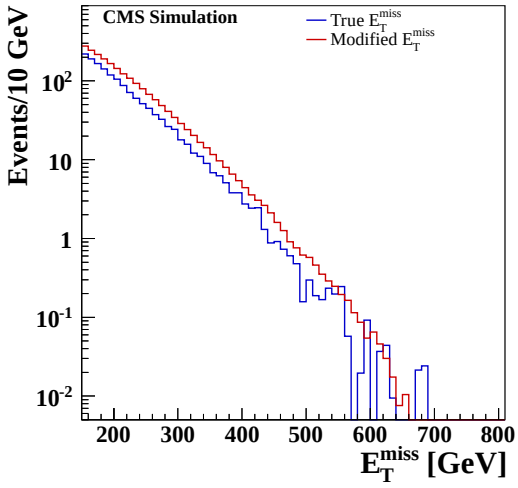

Figure 5.33: Distribution of $E_{\mathrm{T}}^{\mathrm{miss}}$ from simulated events, comparing the τ-jet emulation method with the target spectrum. The solid blue line is the $E_{\mathrm{T}}^{\mathrm{miss}}$ spectrum of Category 2 events which are expected to be in the analysis sample and which must be predicted from events in data. The solid red line is the $E_{\mathrm{T}}^{\mathrm{miss}}$ spectrum of single tight muon events with the τ-jet emulation and all selection criteria applied. This is the expected result from applying the procedure to data.

First, using the knowledge of the energy fraction of τ-jets reproduces the desired $E_{\mathrm{T}}^{\mathrm{miss}}$ shape remarkably well. Shape differences appear in the low $E_{\mathrm{T}}^{\mathrm{miss}}$ validation region, <200 GeV, where an additional correction factor will be needed. Secondly, the size of the desired $E_{\mathrm{T}}^{\mathrm{miss}}$ distribution is approximately two thirds of the result obtained from modified single muon events. This is preferred, because it means that the statistical power of the control sample is greater than the size of background to be predicted. Therefore, it is less likely to have too few events in the tails of the control sample where background is present. The difference in the sizes of the two distributions are determined by the hadronic tau branching fraction and tight muon reconstruction effiency. Both of these aspects are very well-understood by experimentalists and therefore well-modeled in simulations. We take the scale factor to

reduce the modified $E_{\mathrm{T}}^{\mathrm{miss}}$ shape by the appropriate size from dividing the simulated events in blue by the events in red in Fig. 5.33, calculated for each signal region.

Table 5.9 lists the scale factors applied to modified $E_{\mathrm{T}}^{\mathrm{miss}}$ spectra for each signal region, binned by H_{T} and number of b-tagged jets. An hadronic τ-lepton does have a chance of being mistagged as a b-jet. This effect is taken into account as the scale factor increases with the number of b-tagged jets, but it does not affect the shape of the $E_{\mathrm{T}}^{\mathrm{miss}}$ distribution.

Three additional columns are provided in Table 5.9 for Category 3 events which include a hadronic τ-lepton. The second W boson decay can be to a prompt or secondary muon, a prompt or secondary electron, or to another hadronic τ-lepton. In the first two cases, the basic single tight muon criteria described in Table 5.8 are used, but the electron or second muon veto is inverted to require the additional lepton. As in the case of the single muon sample, first tight muon undergoes the procedure to create a mock τ-jet, and event quantities are modified. The scale factors for μ+τ-jet and e+τ-jet events are similar, as expected. The case of two hadronic τ-jets is more complicated, since for each selected energy fraction of the first muon, all possible energy fractions of the second muon must be sampled. Considering the reconstruction efficiency of two tight muons and the branching fraction of two hadronic τ-leptons, a set of scale factors for these Category 3 events are also calculated and included in Table 5.9.

As seen in Fig. 5.33, a small shape difference is observed between the desired and predicted $E_{\mathrm{T}}^{\mathrm{miss}}$ spectrum at low values. Simulation-based correction factors, κ, are applied to adjust for small differences in the shape. For the purpose of plotting these shapes,

Table 5.9: Scale factors to convert yields from single tight muon events (or with an additional lepton) to hadronic tau events, taken from simulation.

	1 τ-jet	μ + τ-jet	e + τ-jet	2 τ-jets
$400 < H_{\mathrm{T}} < 800$ GeV				
=1 b-tag	0.573 ± 0.013	0.399 ± 0.030	0.341 ± 0.019	0.518 ± 0.040
=2 btags	0.656 ± 0.013	0.460 ± 0.034	0.395 ± 0.028	0.633 ± 0.051
≥3 b-tags	0.723 ± 0.022	0.555 ± 0.079	0.448 ± 0.077	0.859 ± 0.14
$H_{\mathrm{T}} > 800$ GeV				
=1 b-tag	0.571 ± 0.032	0.383 ± 0.074	0.521 ± 0.078	0.438 ± 0.071
=2 b-tags	0.588 ± 0.028	0.502 ± 0.060	0.514 ± 0.051	0.561 ± 0.097
≥3 b-tags	0.585 ± 0.038	0.511 ± 0.097	0.550 ± 0.093	0.559 ± 0.16

κ factors are calculated for and applied to the low $E_{\mathrm{T}}^{\mathrm{miss}}$ region from 150 to 250 GeV, for the single τ-jet prediction and collectively for the Category 3 events. The values are listed in Table 5.10. These corrections do not effect the predicted background in the signal regions. However, a non-negligible shape difference is observed in the high H_{T} sample at the highest range of $E_{\mathrm{T}}^{\mathrm{miss}}$, >350 GeV. Therefore, κ factors are applied to events in this $E_{\mathrm{T}}^{\mathrm{miss}}$ range from the single τ-jet sample. There are too few dilepton events in the high $E_{\mathrm{T}}^{\mathrm{miss}}$ regions to make κ factors necessary for Category 3 predictions.

The evaluation of the statistical uncertainty for the modified muon procedure is complicated by the fact that any one event in the control sample can contribute to the prediction in multiple analysis regions. Therefore, we use a procedure that separately

Table 5.10: Correction factors, κ, to convert yields from single tight muon events (or with an additional lepton) to hadronic tau events in two $E_{\mathrm{T}}^{\mathrm{miss}}$ regions, taken from simulation.

	$150 < E_{\mathrm{T}}^{\mathrm{miss}} < 250$ GeV		$E_{\mathrm{T}}^{\mathrm{miss}} > 350$ GeV
	1 τ-jet	$\mu\tau$, $e\tau$, $\tau\tau$	1 τ-jet
$400 < H_{\mathrm{T}} < 800$ GeV			
=1 b-tag	1.15 ± 0.01	1.10 ± 0.02	1.00 ± 0.04
=2 b-tags	1.05 ± 0.01	1.12 ± 0.03	0.95 ± 0.04
≥3 b-tags	1.07 ± 0.01	1.16 ± 0.04	0.93 ± 0.06
$H_{\mathrm{T}} > 800$ GeV			
=1 b-tag	1.30 ± 0.03	1.21 ± 0.08	0.84 ± 0.05
=2 b-tags	1.27 ± 0.03	1.14 ± 0.08	0.83 ± 0.05
≥3 b-tags	1.36 ± 0.04	1.16 ± 0.11	0.81 ± 0.06

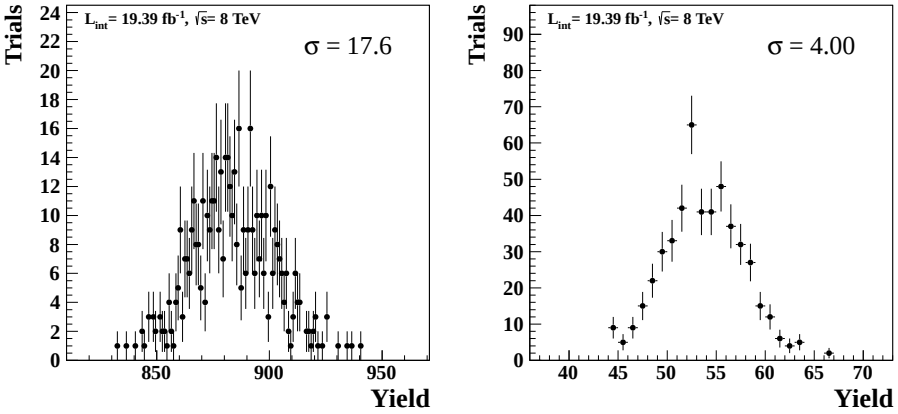

(a) 400<H_{T} <800 GeV, 250<$E_{\mathrm{T}}^{\mathrm{miss}}$ <350 GeV, =1 b-tag

(b) H_{T} >800 GeV, 250<$E_{\mathrm{T}}^{\mathrm{miss}}$ <350 GeV, =2 b-tags

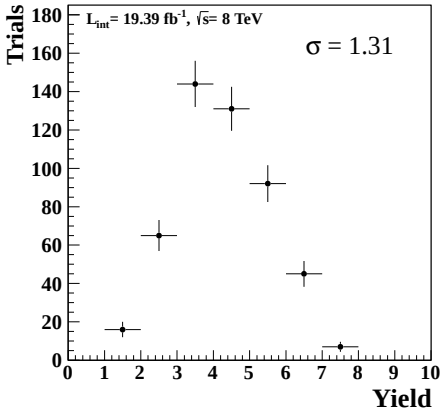

(c) 400<H_{T} <800 GeV, $E_{\mathrm{T}}^{\mathrm{miss}}$ >350 GeV, $\geq$3 b-tags

Figure 5.34: Distribution of predicted yields of Category 2 events from data. For each measurement of the predicted yield, every event in the tight muon control sample randomly samples the τ-jet energy fraction distribution. This is repeated 500 times to find the variance of this sample. Note that no scale factor (Table 5.9) has been applied.

calculates the uncertainty in each H_{T}, $E_{\mathrm{T}}^{\mathrm{miss}}$, and b-tag multiplicity region. Using the data control sample, for each event we randomly sample the τ-jet energy fraction distribution once. This is repeated for the full dataset 500 times, generating 500 predictions for each kinematic region, based on the mobility of the data across the different bins given the distribution of possible τ-jet energies. Figure 5.34 shows the distribution of yields for three representative regions. Plotted is the yield predicted by each test. Also shown is the variance observed for each region.

The variance of these distributions is the stastical uncertainty on the control sample for that region. The same procedure is repeated on simulated events to obtain the appropriate statistical uncertainty on the scale factors and κ factors in Table 5.9 and Table 5.10. These size of these uncertainties are consistent with expected values in which the control sample is twice the size of the predicted yields.

5.2.4 Evaluation of systematic uncertainties

For the most part, potential sources of systematic uncertainty in the hadronic tau prediction are the same as those described in Sec. 5.1 for the lost μ/e case. An additional uncertainty arises from the energy in the jet fraction of a tau decay, which we take to be 5%, based on studies made by other analyses [31]. We observe the effects on the simulation-based scale factor by modifying certain quantities in simulated events by a reasonable amount to cover each source of uncertainty and then applying the muon substitution method.

Table 5.12 and Table 5.13 list the effects of important sources of systematic uncertainty on the prediction of Category 2 events. The most significant effect comes from

Table 5.11: Observed and predicted yields of Category 2 $t\bar{t}/W/t$ events from data and MC. Events are binned in H_{T} and $E_{\mathrm{T}}^{\mathrm{miss}}$. Uncertainties are statistical, and include the statistical uncertainty on the scale factor from simulation.

H_{T}	400 – 800 GeV			$>$ 800 GeV		
$E_{\mathrm{T}}^{\mathrm{miss}}$	150 – 250 GeV	250 – 350 GeV	$>$ 350 GeV	150 – 250 GeV	250 – 350 GeV	$>$ 350 GeV
Prediction						
=1 b-tag	1844 ± 47	406 ± 12	93.8 ± 5.8	139 ± 11	49.4 ± 3.8	27.6 ± 3.1
=2 b-tags	860 ± 37	152.8 ± 7.9	22.9 ± 2.7	61.0 ± 7.1	21.9 ± 2.5	7.5 ± 1.6
≥3 b-tags	86.6 ± 7.4	18.3 ± 1.9	2.57 ± 0.85	9.07 ± 2.7	2.21 ± 0.71	1.10 ± 0.66
$t\bar{t}/W/t$ MC						
=1 b-tag	1729 ± 10	369 ± 5	91 ± 3	129 ± 3	54 ± 2	32 ± 1
=2 b-tags	777 ± 6	141 ± 2	23 ± 1	56 ± 2	21.6 ± 0.9	10.3 ± 0.6
≥3 b-tags	75.3 ± 0.8	12.3 ± 0.3	1.7 ± 0.1	7.0 ± 0.3	2.4 ± 0.1	0.94 ± 0.07

Table 5.12: Percent effect of systematic uncertainties on the single tau method predictions, $400 < H_T < 800$ GeV, calculated from simulated events.

		Jet energy scale	Jet energy resolution	b-tag efficiency	τ-jet energy fraction
E_T^{miss} 150–250	=1 b-tag	±1.5	±0.02	±0.08	±0.28
	=2 b-tags	±1.3	±0.04	–	±0.28
	≥3 b-tags	±2.4	±0.04	±0.02	±0.28
E_T^{miss} 250–350	=1 b-tag	±1.5	±0.2	±0.04	±0.29
	=2 b-tags	±2.8	±0.4	±0.1	±0.28
	≥3 b-tags	±1.7	±0.3	±0.1	±0.28
E_T^{miss} >350	=1 b-tag	±2.7	±0.6	±0.1	±0.28
	=2 b-tags	±2.7	±0.6	±0.1	±0.27
	≥3 b-tags	±3.0	±0.4	±0.2	±0.27

Table 5.13: Percent effect of systematic uncertainties on the single tau method predictions, H_{T} >800 GeV, calculated from simulated events.

		Jet energy scale	Jet energy resolution	b-tag efficiency	τ-jet energy fraction
$E_{\mathrm{T}}^{\mathrm{miss}}$ 150–250	=1 b-tag	±2.7	±0.7	±0.1	±0.28
	=2 b-tags	±1.6	±0.4	±0.1	±0.28
	≥3 b-tags	±3.6	±0.5	±0.1	±0.29
$E_{\mathrm{T}}^{\mathrm{miss}}$ 250 – 350	=1 b-tag	±1.1	±0.4	±0.2	±0.29
	=2 b-tags	±3.0	±0.4	±0.1	±0.29
	≥3 b-tags	±7.2	±0.8	±0.4	±0.29
$E_{\mathrm{T}}^{\mathrm{miss}}$ >350	=1 b-tag	±1.4	±0.9	±0.5	±0.29
	=2 b-tags	±3.5	±0.9	±0.1	±0.29
	≥3 b-tags	±5.3	±0.8	±0.3	±0.29

varying the jet energy scale, which imposes a change in the momentum of all jets by increasing (and then decreasing) the momenta by 5%. In the hadronic tau method, this results in changes around a few percent, and over 5% in a few regions. This is unsurprising because the magnitude of the momentum of the jets play a significant role in whether the event will subsequently be modified by the muon momentum. However, the effect is mostly below 5% due to the canceling effects imposed by dividing the modified muon $E_{\mathrm{T}}^{\mathrm{miss}}$ spectrum by the $E_{\mathrm{T}}^{\mathrm{miss}}$ spectrum of Category 2 events passing the analysis selection in order to calculate the simulation-based scale factor. Similarly, the effect of the jet energy resolution and b-tag efficiency uncertainties have an insignificant effect, less than 1%. Lastly, it is important to consider the effect of slightly different jet energies entering into the calculation for the modified muon $E_{\mathrm{T}}^{\mathrm{miss}}$ spectrum. The result is consistently a change of about 0.3%, regardless of the region. This is because this modification only effects the relative amount of energy extracted from the muon, and there is no migration of events between regions. Events with high H_{T} tend to have muons with higher p_{T}, resulting in a larger absolute change to the yield, but this effect is small.

As above, Table 5.14 and Table 5.15 list the effects of important sources of systematic uncertainty in the case where at least one high p_{T} muon emulates a τ-jet in a fully leptonic $t\bar{t}$ decay. The results are similar to the single lepton uncertainties, including the fact that the jet energy scale is the dominant source of uncertainty. However, the jet-based uncertainties have a larger effect on the result, likely because there are only two jets from the hard scatter, and the third is more likely to be the modified muon.

Table 5.14: Percent effect of systematic uncertainties on the di-tau method predictions, $400 < H_{\mathrm{T}} < 800$ GeV, calculated from simulated events.

		Jet energy scale	Jet energy resolution	b-tag efficiency	τ-jet energy fraction
$E_{\mathrm{T}}^{\mathrm{miss}}$ 150–250	=1 b-tag	±2.7	±0.3	±0.4	±0.27
	=2 b-tags	±1.7	±0.2	±0.1	±0.27
	≥3 b-tags	±1.1	±0.5	±0.6	±0.27
$E_{\mathrm{T}}^{\mathrm{miss}}$ 250–350	=1 b-tag	±3.8	±1.1	±0.4	±0.27
	=2 b-tags	±5.9	±1.7	±0.03	±0.26
	≥3 b-tags	±7.6	±0.4	±1.2	±0.27
$E_{\mathrm{T}}^{\mathrm{miss}}$ >350	=1 b-tag	±3.8	±1.1	±0.4	±0.27
	=2 b-tags	±6.0	±1.7	±0.03	±0.26
	≥3 b-tags	±7.0	±0.3	±1.2	±0.27

Table 5.15: Percent effect of systematic uncertainties on the di-tau method predictions, H_{T} >800 GeV, calculated from simulated events.

		Jet energy scale	Jet energy resolution	b-tag efficiency	τ-jet energy fraction
$E_{\mathrm{T}}^{\mathrm{miss}}$ 150–250	=1 b-tag	±7.6	±0.4	±0.2	±0.28
	=2 b-tags	±8.3	±0.9	±0.2	±0.28
	≥3 b-tags	±6.8	±1.8	±0.7	±0.29
$E_{\mathrm{T}}^{\mathrm{miss}}$ 250–350	=1 b-tag	±6.8	±0.3	±0.3	±0.29
	=2 b-tags	±2.1	±0.7	±0.1	±0.28
	≥3 b-tags	±7.4	±1.3	±1.4	±0.28
$E_{\mathrm{T}}^{\mathrm{miss}}$ >350	=1 b-tag	±5.7	±0.3	±0.3	±0.29
	=2 b-tags	±1.6	±0.7	±0.1	±0.29
	≥3 b-tags	±6.9	±1.6	±1.4	±0.29

Table 5.16: Predicted yields of Category 2 events in three ranges of $E_{\mathrm{T}}^{\mathrm{miss}}$. The first uncertainty is statistical and the second is from systematic sources.

	$150<E_{\mathrm{T}}^{\mathrm{miss}}<250$ GeV	$250<E_{\mathrm{T}}^{\mathrm{miss}}<350$ GeV	$E_{\mathrm{T}}^{\mathrm{miss}}>350$ GeV
$400<H_{\mathrm{T}}<800$ GeV			
=1 b-tag	$1844 \pm 47 \pm 28$	$406 \pm 12 \pm 6$	$93.8 \pm 5.8 \pm 2.6$
=2 b-tags	$860 \pm 37 \pm 11$	$152.8 \pm 7.9 \pm 4.3$	$22.9 \pm 2.7 \pm 0.6$
$\geq$3 b-tags	$86.6 \pm 7.4 \pm 2$	$18.3 \pm 1.9 \pm 0.3$	$2.57 \pm 0.85 \pm 0.08$
$H_{\mathrm{T}}>800$ GeV			
=1 b-tag	$139 \pm 11 \pm 4$	$49.4 \pm 3.8 \pm 0.6$	$27.6 \pm 3.1 \pm 0.5$
=2 b-tags	$61.0 \pm 7.1 \pm 1$	$21.9 \pm 2.5 \pm 0.7$	$7.5 \pm 1.6 \pm 0.3$
$\geq$3 b-tags	$9.1 \pm 2.7 \pm 0.3$	$2.21 \pm 0.71 \pm 0.2$	$1.10 \pm 0.66 \pm 0.06$

5.2.5 $E_{\mathrm{T}}^{\mathrm{miss}}$ spectrum results

Figure 5.35 compares the predicted $E_{\mathrm{T}}^{\mathrm{miss}}$ spectra of Category 2 events with simulation. Since no large discrepancies between data and simulation in the control sample have been observed, we expect the predicted $E_{\mathrm{T}}^{\mathrm{miss}}$ spectrum to be very similar to simulation. The data-driven prediction is shown in three bins of $E_{\mathrm{T}}^{\mathrm{miss}}$ in order to accurately show the uncertainty in its shape. The prediction is close to $E_{\mathrm{T}}^{\mathrm{miss}}$ distribution in data in every analysis region. The predicted yields are listed in Table 5.16. In every region, the statistical uncertainty dominates sources of systematic uncertainties.

As shown above for Category 2 events, Fig. 5.36 provides the predicted $E_{\mathrm{T}}^{\mathrm{miss}}$ spectra of Category 3 events with at least one hadronic τ-lepton decay. The effect of

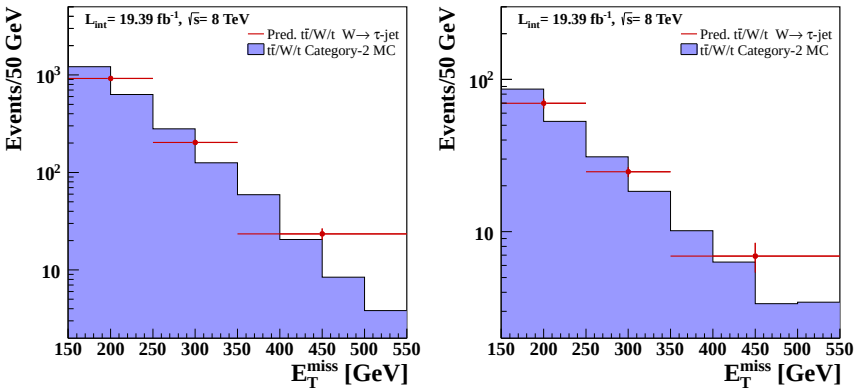

(a) 400<H_{T} <800 GeV, =1 b-tag (b) H_{T} >800 GeV, =1 b-tag

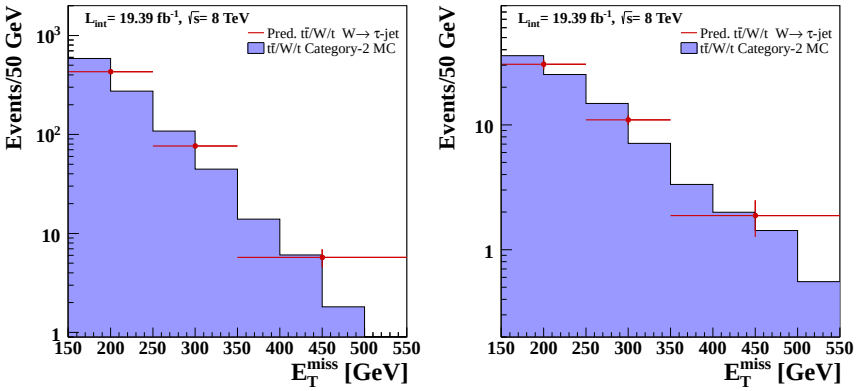

(c) 400<H_{T} <800 GeV, =2 b-tags (d) H_{T} >800 GeV, =2 b-tags

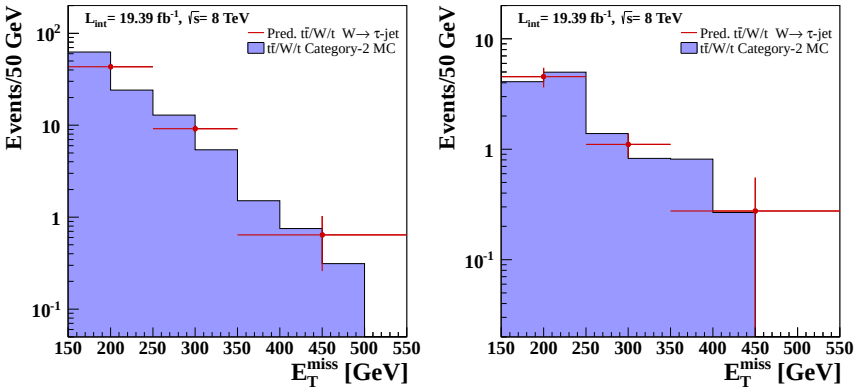

(e) 400<H_{T} <800 GeV, ≥3 b-tags (f) H_{T} >800 GeV, ≥3 b-tags

Figure 5.35: Predicted $E_{\mathrm{T}}^{\mathrm{miss}}$ distributions of Category 2 events in each region of H_{T} and b-tag multiplicity. Red points with error bars are the predicted $E_{\mathrm{T}}^{\mathrm{miss}}$ spectrum taken from data in the single tight muon control sample and modified by the τ-jet emulation procedure. The uncertainty shown is statistical only. The blue histogram represents the distribution of simulated Category 2 $t\bar{t}$, W+jets, and single top events.

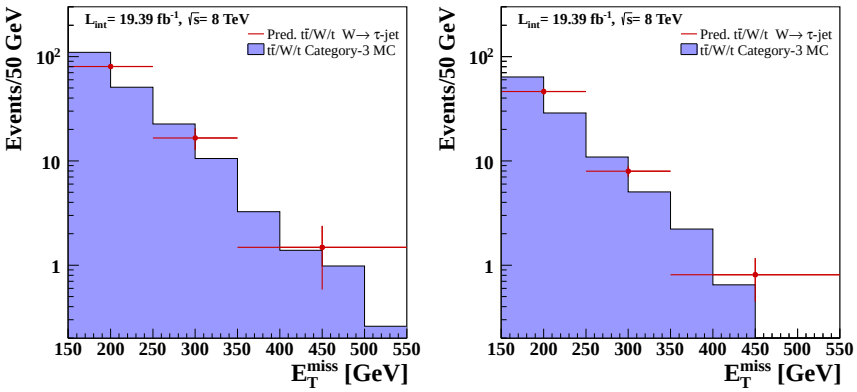

(a) 400<H_{T} <800 GeV, =1 b-tag (b) H_{T} >800 GeV, =1 b-tag

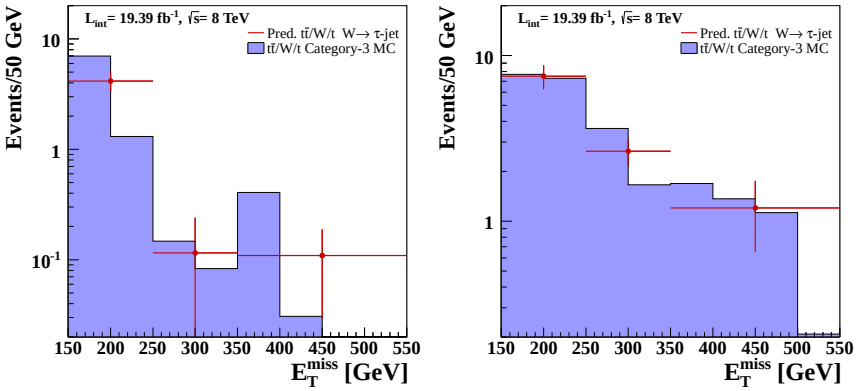

(c) 400<H_{T} <800 GeV, =2 b-tags (d) H_{T} >800 GeV, =2 b-tags

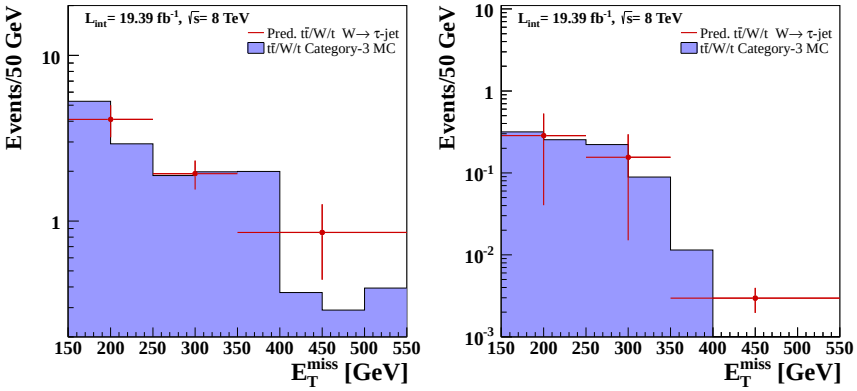

(e) 400<H_{T} <800 GeV, ≥3 b-tags (f) H_{T} >800 GeV, ≥3 b-tags

Figure 5.36: Predicted $E_{\mathrm{T}}^{\mathrm{miss}}$ distributions of Category 2 events with an additional lepton in each region of H_{T} and b-tag multiplicity. Red points with error bars are the predicted $E_{\mathrm{T}}^{\mathrm{miss}}$ spectrum taken from data in the single tight muon control sample and modified by the τ-jet emulation procedure. The uncertainty shown is statistical only. The blue histogram represents the distribution of simulated Category 2 $t\bar{t}$, W+jets, and single top events.

Table 5.17: Prediction of dilepton hadronic τ component of Category 3 events in three ranges of $E_{\mathrm{T}}^{\mathrm{miss}}$. The first uncertainty is statistical and the second is from systematic sources.

	$150<E_{\mathrm{T}}^{\mathrm{miss}}<250$ GeV	$250<E_{\mathrm{T}}^{\mathrm{miss}}<350$ GeV	$E_{\mathrm{T}}^{\mathrm{miss}}>350$ GeV
$400<H_{\mathrm{T}}<800$ GeV			
$=1$ b-tag	$160.6 \pm 9.3 \pm 4.4$	$33.1 \pm 7.7 \pm 1.3$	$5.9 \pm 1.8 \pm 0.2$
$=2$ b-tags	$92.5 \pm 6.5 \pm 1.6$	$15.9 \pm 1.8 \pm 0.4$	$3.2 \pm 0.87 \pm 0.2$
≥ 3 b-tags	$8.3 \pm 1.6 \pm 0.1$	$0.23 \pm 0.09 \pm 0.02$	$0.44 \pm 0.16 \pm 0.03$
$H_{\mathrm{T}}>800$ GeV			
$=1$ b-tag	$15.0 \pm 2.4 \pm 1.1$	$5.3 \pm 0.99 \pm 0.36$	$4.8 \pm 1.1 \pm 0.3$
$=2$ b-tags	$8.2 \pm 1.8 \pm 0.7$	$3.87 \pm 0.77 \pm 0.09$	$3.41 \pm 0.82 \pm 0.06$
≥ 3 b-tags	$0.57 \pm 0.49 \pm 0.04$	$0.31 \pm 0.28 \pm 0.02$	0.012 ± 0.002

the small size of the tight muon dilepton control sample is reflected in the sizes of the uncertainties on the predicted distribution. There are also relatively few simulated events, as evidenced by the bin-to-bin fluctuations at higher b-tag multiplicities. However, the shapes are very similar in the well-populated $=1$ b-tag validation regions, suggesting an acceptable result for the prediction of this relatively small background. The predicted yields are listed in Table 5.17. In every region, the statistical uncertainty dominates sources of systematic uncertainties.

With predictions of yields in Category 1 and Category 2, the majority of the $t\bar{t}$, W+jets, and single top background is determined. These cover the scenarios in which exactly one W boson decays leptonically, either to a prompt or secondary electron or muon

which is not identified, or to a τ-lepton which decays hadronically. Also covered is the scenario in which one W boson decays to a hadronically decaying τ-lepton and a second W boson also decays leptonically. The final case to complete the $t\bar{t}/W/t$ prediction is the smallest component, in which two W bosons decay to prompt or secondary electrons or muons, neither of which are identified as such.

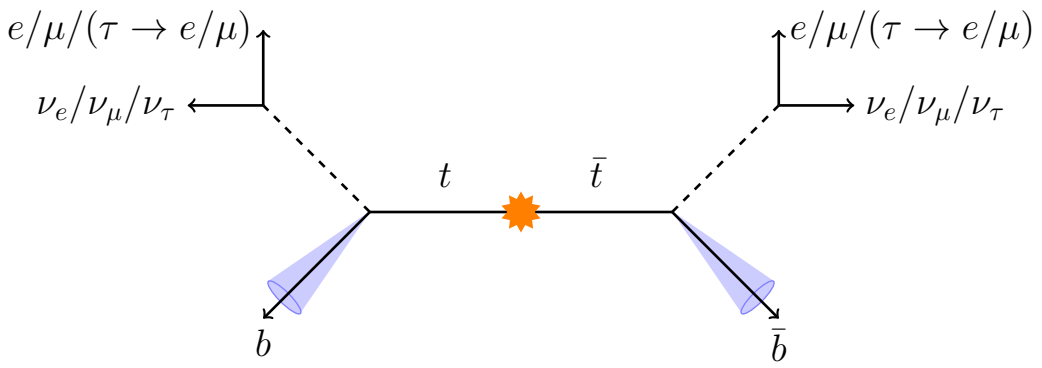

Figure 5.37: Sketch of a Category 3 dilepton $t\bar{t}$ event, showing the neutrinos ($E_{\mathrm{T}}^{\mathrm{miss}}$) and b-jets in the final state, and charged leptons which are not observed in the lepton-vetoed analysis sample.

5.3 Predicting the $t\bar{t}$ and single top background with two $W \to e/\mu/(\tau \to e/\mu)$ decays

Category 3 events involve the decay of two W bosons into an electron or muon, including secondary leptons from a tau. These events provide the smallest contribution to the signal region of all three final state categories involving electroweak production. Since the yields in the signal regions are so small, our prediction of this background takes the shape of $E_{\mathrm{T}}^{\mathrm{miss}}$ from simulation, rescaled according to the observed yields in a dilepton control sample.

A control sample of ee, $e\mu$, and $\mu\mu$ events is constructed from the same main dataset described in Sec. 4.4. The same selection criteria are applied, with the exception of the isolated track and lepton vetoes. The lepton veto criteria (Sec. 3.3.3) are inverted to select for events with two reconstructed leptons, either muons, electrons, or one of each.

Since the yields of this sample are small, the $E_{\mathrm{T}}^{\mathrm{miss}}$ cut is placed at the lowest value possible on the trigger efficiency plateau, at 150 GeV.

To support the validity of this method, a comparison of the simulated $E_{\mathrm{T}}^{\mathrm{miss}}$ spectra in the dilepton control sample and lepton-vetoed analysis sample is shown in Fig. 5.38. As with the methods used to estimate the yields from other Standard Model sources, this prediction is performed separately for each H_{T} and b-tag multiplicity region. The red histograms represent the $E_{\mathrm{T}}^{\mathrm{miss}}$ spectra of Category 3 events we are interested in estimating. This figure shows that the number of observed dilepton events is expected to be 3-5 times larger than the number of background events that are in the analysis sample (where two leptons are produced but not reconstructed). It is desirable to have a large statistical advantage in a control sample to estimate very small amounts of background.

The $E_{\mathrm{T}}^{\mathrm{miss}}$ spectra of events in the dilepton control sample are shown in Fig. 5.39, comparing the distributions of events from data and simulation. The shape from simulation closely agrees with the observation in data in the lowest H_{T} and b-tag multiplicity region, where there is a high number of events. While the number of events decreases with tightening selection criteria, a good level of agreement appears to continue. The yields from these samples are used to rescale the $E_{\mathrm{T}}^{\mathrm{miss}}$ shapes of simulated lepton-vetoed events, which are shown in Fig. 5.38. Applying a correction factor from data accounts for any mismodeling of the dilepton production in simulation.

Since the simulated $E_{\mathrm{T}}^{\mathrm{miss}}$ distribution agrees well with the observed $t\bar{t}/W/t$ dilepton events in data, the data-based corrections to the lepton-vetoed yields from simulation

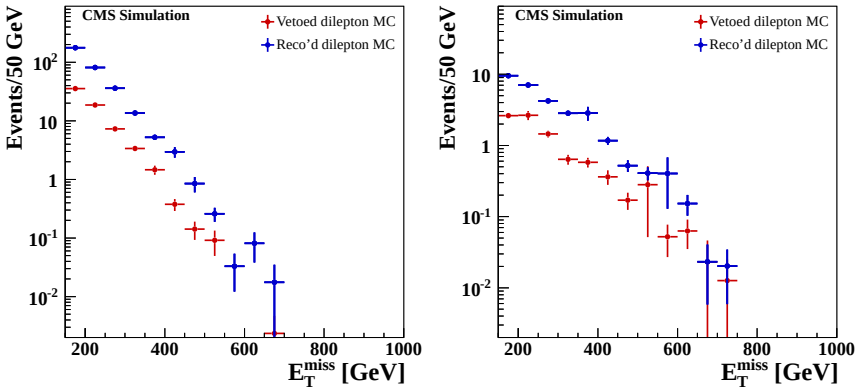

(a) 400<H_T <800 GeV, =1 b-tag (b) H_T >800 GeV, =1 b-tag

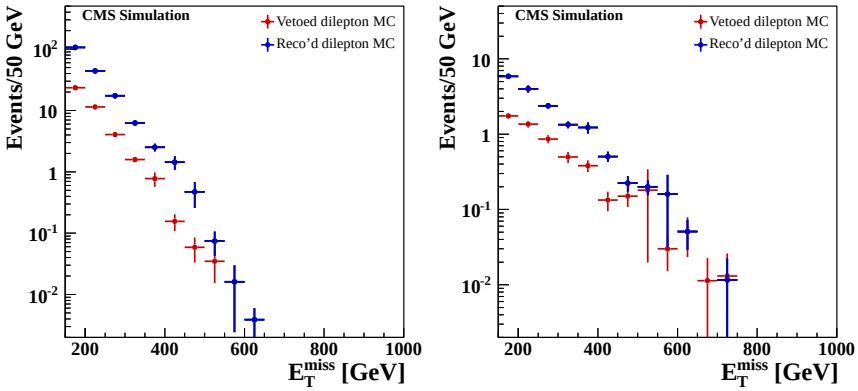

(c) 400<H_T <800 GeV, =2 b-tags (d) H_T >800 GeV, =2 b-tags

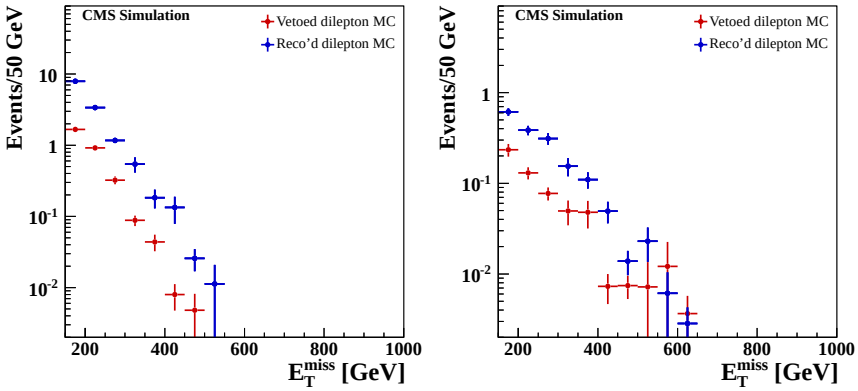

(e) 400<H_T <800 GeV, ≥3 b-tags (f) H_T >800 GeV, ≥3 b-tags

Figure 5.38: Distribution of E_T^{miss} in simulated events with two reconstructed leptons having no generator-level requirements (blue) and no leptons passing the reconstruction requirements in events in which W bosons have produced two prompt or secondary electrons or muons (red).

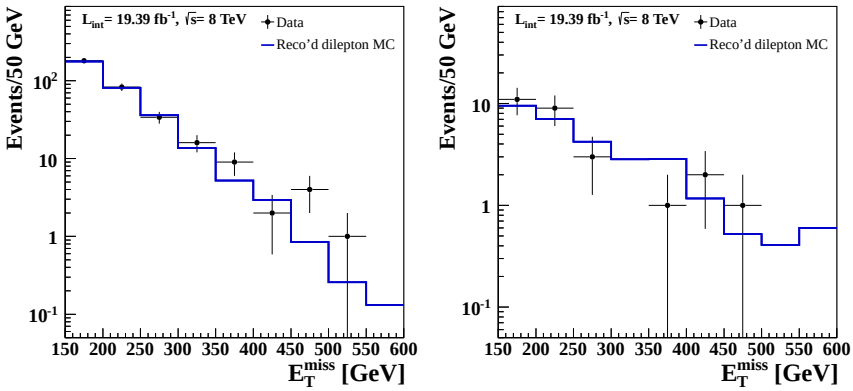

(a) 400<H_T <800 GeV, =1 b-tag (b) H_T >800 GeV, =1 b-tag

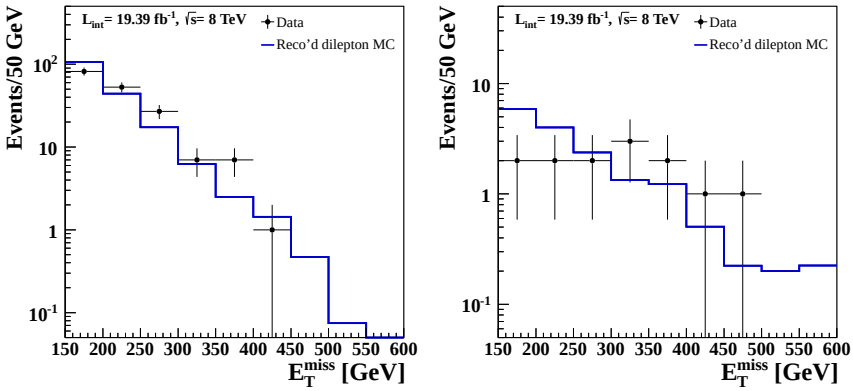

(c) 400<H_T <800 GeV, =2 b-tags (d) H_T >800 GeV, =2 b-tags

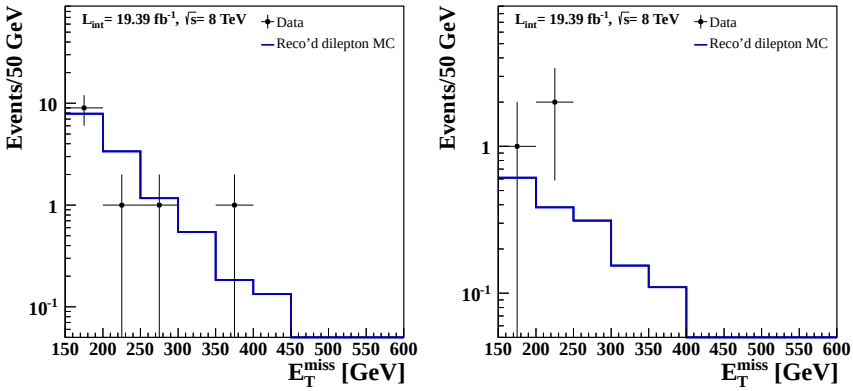

(e) 400<H_T <800 GeV, ≥3 b-tags (f) H_T >800 GeV, ≥3 b-tags

Figure 5.39: Distribution of E_T^{miss} from the dilepton control sample in data (black points with error bars) and simulated events (blue).

Table 5.18: Scale factors used to estimate the Category 3 yields in each H_{T} and b-tag multiplicity bin. They are obtained from dilepton control samples in data and simulation in which $E_{\mathrm{T}}^{\mathrm{miss}}$ >150 GeV.

		Data yield	MC yield	Scale factor
Low H_{T}	=1 b-tag	330 ± 18	316.9 ± 3.5	1.04 ± 0.06
	=2 b-tags	177 ± 13	178.7 ± 2.3	0.99 ± 0.08
	≥3 b-tags	12 ± 3.5	13.4 ± 0.4	0.90 ± 0.26
High H_{T}	=1 b-tag	27 ± 5.2	29.2 ± 1.2	0.93 ± 0.18
	=2 b-tags	13 ± 3.6	16.0 ± 0.7	0.81 ± 0.23
	≥3 b-tags	3 ± 1.7	1.67 ± 0.10	1.8 ± 1.0

are consistent with unity. Table 5.18 lists these corrections as well as the yields from which they are calculated for each H_{T} and b-tag multiplicity bin.

With the correction factor from the dilepton control sample applied, the shape of $E_{\mathrm{T}}^{\mathrm{miss}}$ from simulated Category 3 events represents the prediction of this background. The predicted distributions and data control sample distributions are shown in Fig. 5.40.

The predicted yields from this source of background for high $E_{\mathrm{T}}^{\mathrm{miss}}$ signal regions are shown in Table 5.20. As expected, they are small. In addition, the uncertainty from the jet energy scale is included in the table. The predicted $E_{\mathrm{T}}^{\mathrm{miss}}$ spectrum from Category 3 events is combined with the predictions from the other two categories to create a complete picture of the $E_{\mathrm{T}}^{\mathrm{miss}}$ spectrum for $t\bar{t}$, W+jets, and single-top events.

Table 5.19: Percent effect of jet energy scale uncertainty on the dilepton ($ee/\mu\mu/e\mu$) prediction, calculated from simulated events.

	$E_{\mathrm{T}}^{\mathrm{miss}}$ 150–250	$E_{\mathrm{T}}^{\mathrm{miss}}$ 250–350	$E_{\mathrm{T}}^{\mathrm{miss}}$ >350
400<H_{T} <800 GeV			
=1 b-tag	± 5.8%	± 3.4%	± 9.2%
=2 b-tags	± 4.5%	± 4.1%	± 6.6%
≥3 b-tags	± 1.2%	± 1.2%	± 18.6%
H_{T} >800 GeV			
=1 b-tag	± 18.2%	± 6.5%	± 15.9%
=2 b-tags	± 14.0%	± 8.1%	± 19.3%
≥3 b-tags	± 12.9%	± 5.2%	± 9.1%

Table 5.20: Prediction of Category 3 events in two ranges of $E_{\mathrm{T}}^{\mathrm{miss}}$.

	250<$E_{\mathrm{T}}^{\mathrm{miss}}$ <350 GeV	$E_{\mathrm{T}}^{\mathrm{miss}}$ >350 GeV
400<H_{T} <800 GeV		
=1 b-tag	11.09 ± 0.46 ± 0.38	2.15 ± 0.28 ± 0.20
=2 b-tags	5.58 ± 0.29 ± 0.23	1.01 ± 0.21 ± 0.07
≥3 b-tags	0.37 ± 0.04	0.05 ± 0.01
H_{T} >800 GeV		
=1 b-tag	1.93 ± 0.19 ± 0.13	0.93 ± 0.18 ± 0.15
=2 b-tags	1.11 ± 0.14 ± 0.09	0.77 ± 0.19 ± 0.15
≥3 b-tags	0.23 ± 0.02 ± 0.01	0.16 ± 0.02 ± 0.01

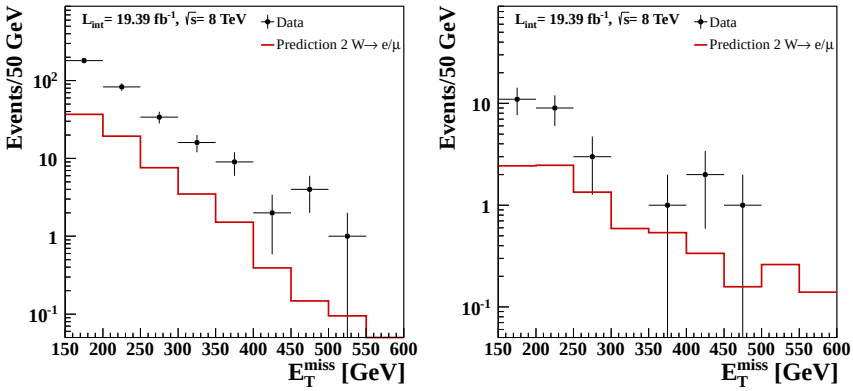

(a) 400<H_{T} <800 GeV, =1 b-tag (b) H_{T} >800 GeV, =1 b-tag

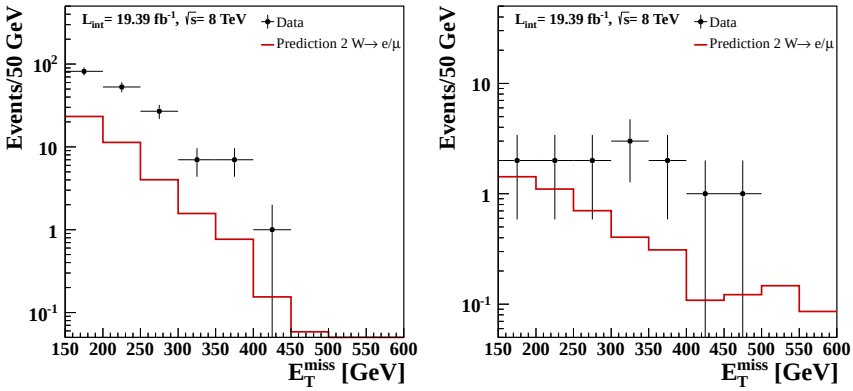

(c) 400<H_{T} <800 GeV, =2 b-tags (d) H_{T} >800 GeV, =2 b-tags

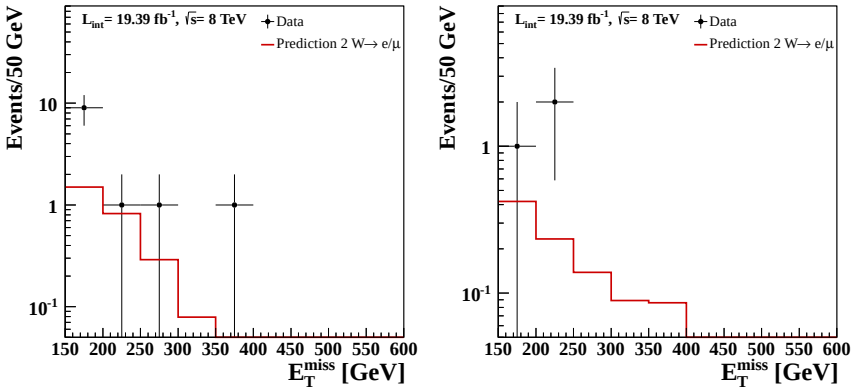

(e) 400<H_{T} <800 GeV, ≥3 b-tags (f) H_{T} >800 GeV, ≥3 b-tags

Figure 5.40: Predicted $E_{\mathrm{T}}^{\mathrm{miss}}$ spectrum of fully leptonic $t\bar{t}$ and single top events from data. Black points with error bars indicate the dilepton control sample in data, from which the predicted yield is calculated. Solid red line is the shape of $E_{\mathrm{T}}^{\mathrm{miss}}$ from Category 3 simulated events with prompt or secondary electrons and muons entering the analysis sample.

5.4 Combined $t\bar{t}$, W+jets, and single top prediction

The background from $t\bar{t}$ production represents the largest contribution of Standard Model events in this analysis. In particular, when a lepton is produced but is not observed or does not pass selection criteria, the event appears to be purely hadronic with potentially large $E_{\mathrm{T}}^{\mathrm{miss}}$ from the neutrino. In addition, there are two b-quarks which may be identified by the CSV b-tag algorithm, making this background very similar to the T1bbbb simplified model of supersymmetry. Since they have the same source of overlooked leptons and $E_{\mathrm{T}}^{\mathrm{miss}}$, W+jets and single-top backgrounds are grouped together with $t\bar{t}$ in determining the number of events with one neutrino (and sometimes two) in the signal regions.

The data-driven methods for predicting these yields are based on the type of charged lepton present. Electrons and muons from the decay of the W boson have an angular distribution determined by the polarization of the W, which can be exploited to accurately predict the size and shape of the $E_{\mathrm{T}}^{\mathrm{miss}}$ distribution from these events (Sec. 5.1). Alternatively, if the W boson decays to a τ-lepton which decays hadronically, these events also may enter the signal regions. Knowledge of how these leptons are observed by the detector and contribute to the $E_{\mathrm{T}}^{\mathrm{miss}}$ themselves is applied and described in Sec. 5.2. Lastly, a small portion of events may include more than one charged lepton. The case with two neutrinos is a small background, and described in Sec. 5.3. When two neutrinos are produced directly from the W boson, along with at least one hadronic τ-lepton, the predicted $E_{\mathrm{T}}^{\mathrm{miss}}$ spectrum must take into account the additional missing energy, therefore, this scenario is discussed in Sec. 5.2.

The results of each method of determining the $t\bar{t}/W/t$ background are shown together in Table 5.21 and Table 5.22. The first shows each signal region binned in $E_{\mathrm{T}}^{\mathrm{miss}}$ and H_{T} where the 2 CSVM b-jets are observed. As expected, the single lepton components (the first two rows) are the dominant fraction, with slightly more events from Category 1 (1 $e/\mu/(\tau \to e/\mu)$). However, the statistical uncertainty on the Category 2 events is half the size of the Category 1 result. This is because the control sample size for the Category 2 method is twice as large. There are consistently roughly three times more dilepton events with a τ-jet (row four) than without (row three) in Table 5.21. Once at least b-jets are required, the yields from events with a τ-jet and those without one become nearly equivalent, in both the single lepton and dilepton cases. In all cases, the statistical uncertainty is larger than the systematic uncertainty. However, the systematic uncertainty, driven by the uncertainty in the jet energy scale, is not negligible.

It is important to note here an unfortunate result at high H_{T}, $E_{\mathrm{T}}^{\mathrm{miss}}$, and b-tag multiplicity. The first row of Table 5.22 shows the Category 1 result, which we expect to be equivalent to the Category 2 result (second row), is nearly a factor of ten lower. This is most likely a direct result of a downward fluctuation of events in the most important kinematic region of the single lepton control sample shown in Fig. 5.19(f) and Fig. 5.20(f). Since this accounts for nearly half of the $t\bar{t}/W/t$ prediction in this region, we can expect that the data observed in this bin will exceed the data-driven prediction.

Figure 5.41 visually shows the results of the $t\bar{t}/W/t$ background prediction. Each of the four stacked, colored histograms represent the predicted $E_{\mathrm{T}}^{\mathrm{miss}}$ spectrum from each

Table 5.21: Estimated event yields from the production of $t\bar{t}$, W+jets, and single top in each of the $H_{\mathrm{T}}/E_{\mathrm{T}}^{\mathrm{miss}}$ signal regions, with =2 b-tagged jets.

Category	$400 < H_{\mathrm{T}} < 800$ GeV		$H_{\mathrm{T}} > 800$ GeV	
	$250 < E_{\mathrm{T}}^{\mathrm{miss}} < 350$ GeV	$E_{\mathrm{T}}^{\mathrm{miss}} > 350$ GeV	$250 < E_{\mathrm{T}}^{\mathrm{miss}} < 350$ GeV	$E_{\mathrm{T}}^{\mathrm{miss}} > 350$ GeV
1 e/μ	187 ± 15 ± 6	30.8 ± 7.0 ± 0.8	30.9 ± 5.5 ± 2.4	14.8 ± 3.8 ± 0.9
1 $\tau \to had$	153 ± 8 ± 4	22.9 ± 2.7 ± 0.6	21.9 ± 2.5 ± 0.7	7.5 ± 1.6 ± 0.3
2 e/μ	5.58 ± 0.29 ± 0.23	1.01 ± 0.21 ± 0.07	1.11 ± 0.14 ± 0.09	0.77 ± 0.19 ± 0.15
$\tau \to had + e/\mu/\tau$	15.9 ± 1.8 ± 0.4	3.2 ± 0.9 ± 0.2	3.9 ± 0.8 ± 0.1	3.4 ± 0.8 ± 0.1
Total $t\bar{t}/W/t$	362 ± 17 ± 7	57.9 ± 7.4 ± 1.0	57.8 ± 6.1 ± 2.5	26.5 ± 4.2 ± 1.0

Table 5.22: Estimated event yields from the production of $t\bar{t}$, W+jets, and single top in each of the $H_{\mathrm{T}}/E_{\mathrm{T}}^{\mathrm{miss}}$ signal regions, with $\geq$3 b-tagged jets.

Category	$400 < H_{\mathrm{T}} < 800$ GeV		$H_{\mathrm{T}} > 800$ GeV	
	$250 < E_{\mathrm{T}}^{\mathrm{miss}} < 350$ GeV	$E_{\mathrm{T}}^{\mathrm{miss}} > 350$ GeV	$250 < E_{\mathrm{T}}^{\mathrm{miss}} < 350$ GeV	$E_{\mathrm{T}}^{\mathrm{miss}} > 350$ GeV
1 e/μ	18.7 ± 4.5 ± 0.6	4.9 ± 3.0 ± 0.1	2.2 ± 1.4 ± 0.2	0.14 ± 0.14 ± 0.03
1 $\tau \to had$	18.3 ± 1.9 ± 0.3	2.57 ± 0.85 ± 0.08	2.2 ± 0.7 ± 0.2	1.10 ± 0.66 ± 0.06
2 e/μ	0.37 ± 0.04	0.05 ± 0.01	0.23 ± 0.02 ± 0.01	0.16 ± 0.02 ± 0.01
$\tau \to had + e/\mu/\tau$	0.23 ± 0.09 ± 0.02	0.44 ± 0.16 ± 0.03	0.31 ± 0.28 ± 0.02	0.012 ± 0.002
Total $tt/W/t$	37.6 ± 4.9 ± 0.7	8.0 ± 3.1 ± 0.1	4.9 ± 1.6 ± 1.2	1.40 ± 0.67 ± 0.07

of the four channels. Results are shown for each signal region in the tables above, along with the =1 b-tag validation region and $E_{\mathrm{T}}^{\mathrm{miss}}$ down to 150 GeV. The solid red line is the $t\bar{t}/W/t$ $E_{\mathrm{T}}^{\mathrm{miss}}$ determined from simulated events. Although we do not rely on simulation to provide the most accurate description of physics at the kinematic extremes, it is very encouraging to see near perfect agreement with the predicted $E_{\mathrm{T}}^{\mathrm{miss}}$ spectrum from data in the regions with relatively large yields. Both the shape and normalization of the two spectra are extremely similar for =1 and =2 b-tags. At highest b-tag multiplicity, we observe fewer events. Figure 5.41(f) shows the problem with the most extreme signal bin. Here, only one re-weighted control sample event contributes to the Category 1 prediction where $E_{\mathrm{T}}^{\mathrm{miss}}$ >350 GeV. This will effect the total result discussed later. Overall, the methods of predicting the $t\bar{t}$, W+jets, and single-top backgrounds are very successful and produce important results for this analysis.

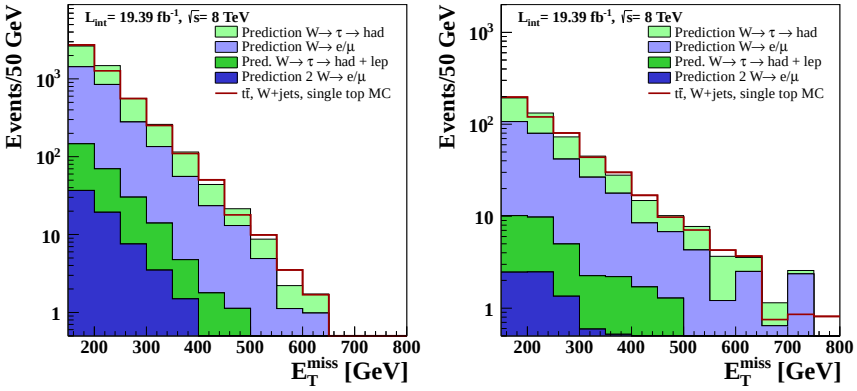

(a) 400<H_{T} <800 GeV, =1 b-tag

(b) H_{T} >800 GeV, =1 b-tag

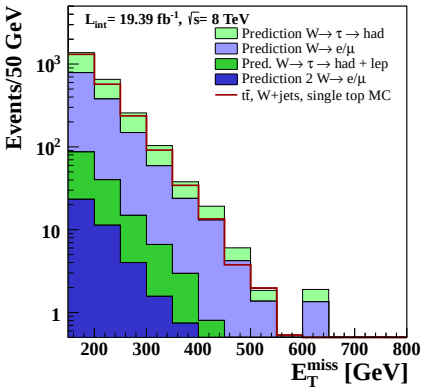

(c) 400<H_{T} <800 GeV, =2 b-tags

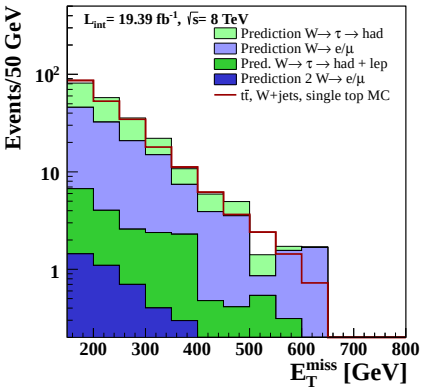

(d) H_{T} >800 GeV, =2 b-tags

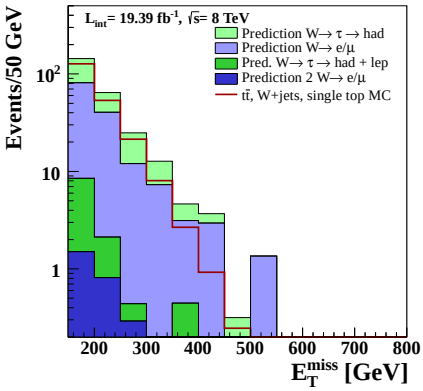

(e) 400<H_{T} <800 GeV, ≥3 b-tags

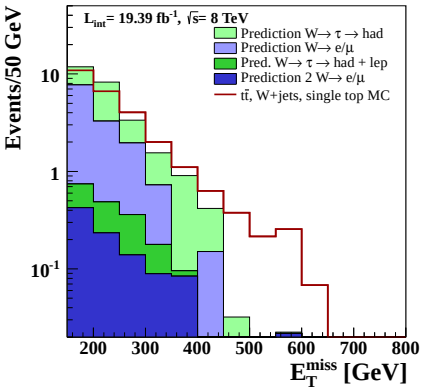

(f) H_{T} >800 GeV, ≥3 b-tags

Figure 5.41: Predicted $E_{\mathrm{T}}^{\mathrm{miss}}$ spectrum of $t\bar{t}$, W+jets, and single top events from data, compared with simulated events. Solid red line is the shape of $E_{\mathrm{T}}^{\mathrm{miss}}$ from simulated events. Stacked, colored histogram shows the predicted $E_{\mathrm{T}}^{\mathrm{miss}}$ spectra from each component of the $t\bar{t}/W/t$ prediction.

5.5 Predicting the QCD background

As described in Sec. 4.4, events with no genuine large $E_{\mathrm{T}}^{\mathrm{miss}}$, which are mainly from QCD multijet production, have a distinctive, sharply falling $\Delta\phi_N^{\mathrm{min}}$ distribution. Because $\Delta\phi_N^{\mathrm{min}}$ and $E_{\mathrm{T}}^{\mathrm{miss}}$ are nearly independent variables, the distributions of these quantities are used in a data-driven method for determining the multijet background. The shape of the $\Delta\phi_N^{\mathrm{min}}$ distribution in nearly pure data sample of QCD events is used to extrapolate the number of events in the high $E_{\mathrm{T}}^{\mathrm{miss}}$ signal regions. This method does not require a very elaborate treatment of the QCD background that other hadronic analyses use [31], because this background is small with respect other Standard Model processes. A comparison of data and simulated events supports this; however, the statistical power of the sample of simulated events is poor in certain kinematic regions. Therefore, simulation alone is not enough to provide a convincing prediction of the size of this background in the tails of the $E_{\mathrm{T}}^{\mathrm{miss}}$ distribution. The simple procedure described in this section allows us to predict the size of this small background using a large data sample. Careful cross-checks of both data control samples and ratios of simulated events help clarify our understanding of a fully hadronic kinematic region (with high $E_{\mathrm{T}}^{\mathrm{miss}}$ and b-tag multiplicity) where it is difficult to characterize purely QCD processes.

5.5.1 Characteristics of QCD events with missing transverse energy

A schematic diagram of the resolution-normalized angle between the $E_{\mathrm{T}}^{\mathrm{miss}}$ and a leading jet is shown in Fig. 5.42. For each of the three leading jets, j, we calculate

$$\Delta\phi_j = \frac{\Delta\phi(j, E_{\mathrm{T}}^{\mathrm{miss}})}{\sin^{-1}(\Delta_{Tj}/E_{\mathrm{T}}^{\mathrm{miss}})}, \tag{5.5}$$

where

$$\Delta_{Tj} = 0.1 \times \frac{\sqrt{\Sigma_{i\neq j}[p_x^j p_y^i - p_y^j p_x^i]^2}}{p_T^j}. \tag{5.6}$$

The numerator in Eq. 5.5, $\Delta\phi(j, E_{\mathrm{T}}^{\mathrm{miss}})$, is the angle between the p_{T} of jet j and $E_{\mathrm{T}}^{\mathrm{miss}}$. This alone is a good discriminator between events with real $E_{\mathrm{T}}^{\mathrm{miss}}$ from neutrinos or fake $E_{\mathrm{T}}^{\mathrm{miss}}$ from lost or poorly measured jets, since a mismeasured jet will be close in ϕ to the resulting missing transverse momentum. However, since we are predicting the shape of the $E_{\mathrm{T}}^{\mathrm{miss}}$ spectrum, we modify this quantity such that it is independent of the magnitude of $E_{\mathrm{T}}^{\mathrm{miss}}$. To achieve this, we apply the denominator $\sin^{-1}(\Delta_T/E_{\mathrm{T}}^{\mathrm{miss}})$, shown above. This divides out the possible contribution to the angle from the effect of the p_{T} resolution of all jets in the event. A resolution of 10% is assigned to each jet [32], and the component of each jet's uncertainty perpendicular to jet j is summed together as Δ_{Tj} (see Eq. 5.6).

The illustration in Fig. 5.42 shows jet labeled j as greatly mismeasured, possibly having some of its energy pass through a crack in the calorimeter. The magnitude of the momentum of the other two jets is smeared by the detector resolution, such that the reconstructed jet p_{T} (in black) is different than the true value (in gray). The total potential amount of smearing in the direction perpendicular to jet j is Δ_{Tj}. The way this figure is constructed, the angle $\sin^{-1}(\Delta_{Tj}/E_{\mathrm{T}}^{\mathrm{miss}})$ is very close to the angle $\Delta\phi(j, E_{\mathrm{T}}^{\mathrm{miss}})$, therefore

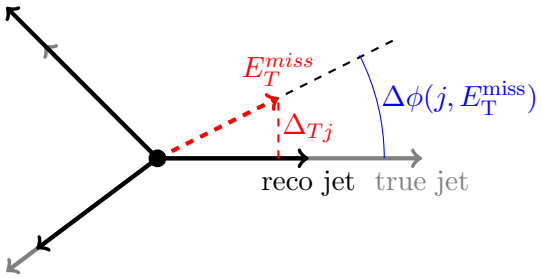

Figure 5.42: Calculating $\Delta\phi_N^{\mathrm{min}}$. The gray lines represent the true p_{T} of the three leading jets, and the black lines represent their reconstructed values, which vary according to the resolution of the calorimeter. The $E_{\mathrm{T}}^{\mathrm{miss}}$ is represented by a dashed red arrow. Its angle with respect to a greatly mismeasured jet, j, is in blue ($\Delta\phi(j, E_{\mathrm{T}}^{\mathrm{miss}})$). We approximate the differences between the gray and black arrows, and sum their components perpendicular to j, shown in dashed red (Δ_{Tj}).

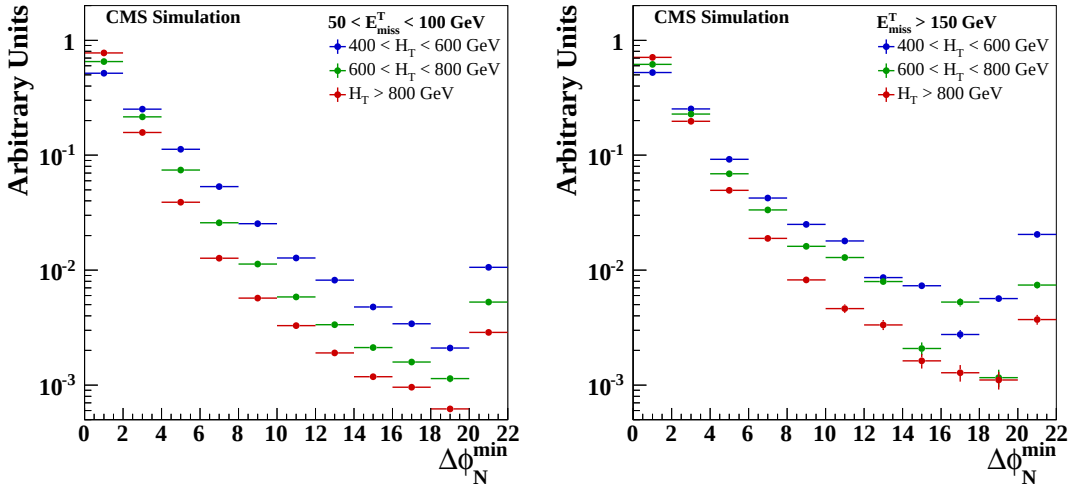

(a) $50 < E_{\mathrm{T}}^{\mathrm{miss}} < 100$ GeV (b) $E_{\mathrm{T}}^{\mathrm{miss}} > 150$ GeV

Figure 5.43: Distribution of the smallest resolution-normalized angle between $E_{\mathrm{T}}^{\mathrm{miss}}$ and any of the three leading jets ($\Delta\phi_N^{\mathrm{min}}$) from simulated QCD events. Baseline jet, lepton, track, and b-tag selection is applied (see Sec. 4.4). The sample is split into three H_{T} bins: 400–600 GeV (blue), 600–800 GeV (green), and >800 GeV (red). The distribution of events with low $E_{\mathrm{T}}^{\mathrm{miss}}$ is provided on the left, and that for the standard baseline analysis selection is on the right. All histograms are normalized to one.

$\Delta\phi_j$ is small. The procedure is repeated for each of the three leading jets in an event, and the smallest of $\Delta\phi_{(i,j,k)}$ is taken as $\Delta\phi_N^{\mathrm{min}}$ (in the case of Fig. 5.42, clearly jet j).

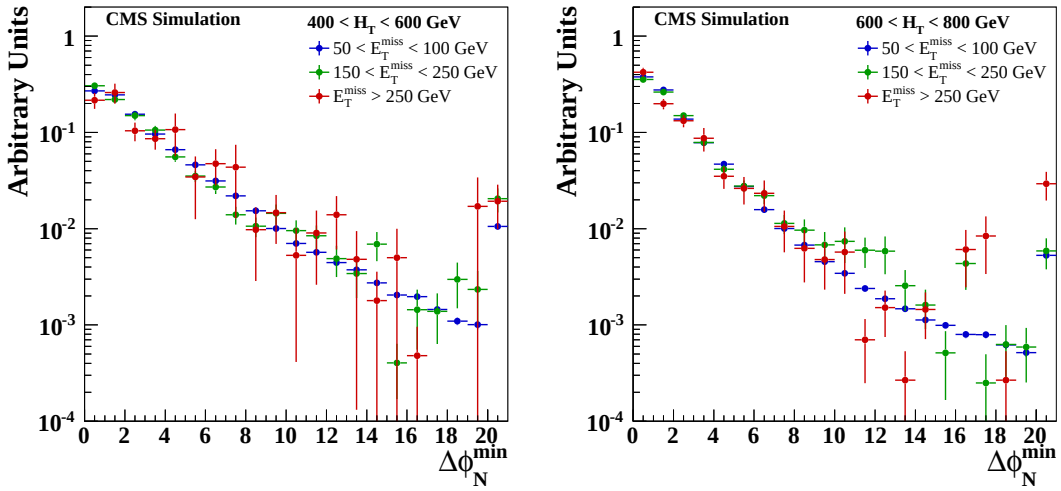

(a) $400 < H_{\mathrm{T}} < 600$ GeV

(b) $600 < H_{\mathrm{T}} < 800$ GeV

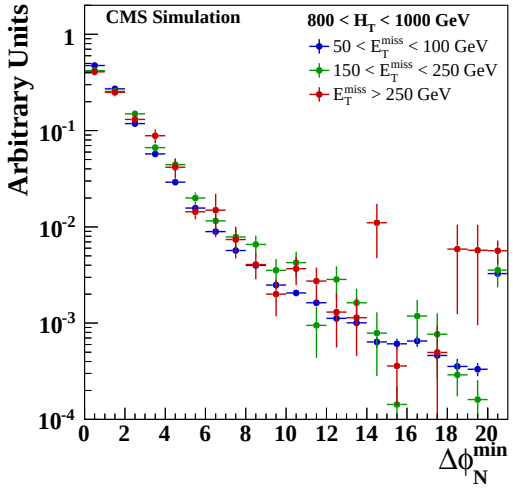

(c) $800 < H_{\mathrm{T}} < 1000$ GeV

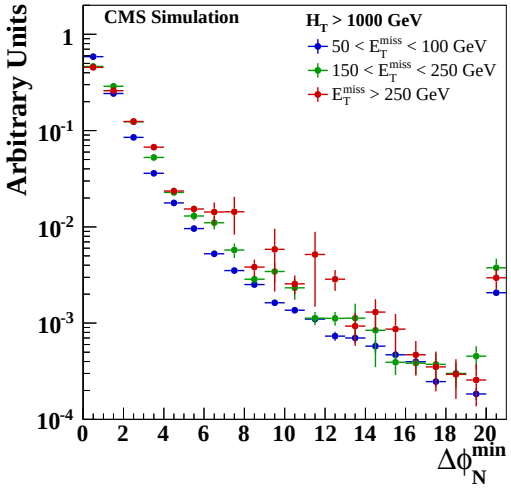

(d) $H_{\mathrm{T}} > 1000$ GeV

Figure 5.44: The smallest resolution-normalized angle between $E_{\mathrm{T}}^{\mathrm{miss}}$ and any of the three leading jets ($\Delta\phi_N^{\mathrm{min}}$) from simulated QCD events. Baseline jet, lepton, track, and b-tag selection is applied (see Sec. 4.4). The sample is split into three $E_{\mathrm{T}}^{\mathrm{miss}}$ bins: from 50 to 100 GeV (blue), from 150 to 250 GeV (green), and the high-$E_{\mathrm{T}}^{\mathrm{miss}}$ signal region with over 250 GeV (red). All histograms are normalized to one.

Since it is computed from the transverse momentum of jets, the $\Delta\phi_N^{\min}$ variable is sensitive to the H_{T} of an event. Figure 5.43 shows $\Delta\phi_N^{\min}$ distributions from simulated QCD events with baseline analysis cuts applied. The sample is split according to the H_{T} of an event, for both a very low $E_{\mathrm{T}}^{\mathrm{miss}}$ region (Fig. 5.43(a)) and the baseline analysis region (Fig. 5.43(b)). The value of H_{T} has a dramatic effect on the shape of the resulting $\Delta\phi_N^{\min}$ spectrum. As the number of jets in the event increases, the H_{T} of the event increases and the probability of a jet to be near the $E_{\mathrm{T}}^{\mathrm{miss}}$ increases. For this reason, a prediction for the QCD background is obtained separately for four different H_{T} bins. Within an H_{T} bin, the $\Delta\phi_N^{\min}$ distribution remains about the same despite the value of $E_{\mathrm{T}}^{\mathrm{miss}}$ in the event. This is illustrated by simulated events in Fig. 5.44. Four H_{T} bins are defined: 400–600 GeV, 600–800 GeV, 800–1000 GeV, and greater than 1000 GeV. For each H_{T} bin, the figure shows $\Delta\phi_N^{\min}$ in the three different slices of $E_{\mathrm{T}}^{\mathrm{miss}}$. In general, the shapes in different ranges of $E_{\mathrm{T}}^{\mathrm{miss}}$ are similar. Deviations at low $\Delta\phi_N^{\min}$ appear in the highest H_{T} range, where high $E_{\mathrm{T}}^{\mathrm{miss}}$ events have a broader distribution than those at lower $E_{\mathrm{T}}^{\mathrm{miss}}$. This effect is quantified from simulated events and applied as a correction to the QCD prediction, as described later in this section.

The shape of $\Delta\phi_N^{\min}$ in data with the baseline selection criteria applied (except for the requirement on $\Delta\phi_N^{\min}$ itself) is shown in Fig. 5.45. These plots show the long tail of multijet events entering the analysis regions where $\Delta\phi_N^{\min}$ >4.0. They also show that inverting the $\Delta\phi_N^{\min}$ cut creates a control sample that is dominated by QCD, but with a potentially non-negligible component from other sources. Small shape discrepancies between

data and simulated QCD are observed at low $\Delta\phi_N^{\min}$. However, the low $\Delta\phi_N^{\min}$ (<4.0) region is only used for the QCD background prediction described in this section, in which the shape of the $\Delta\phi_N^{\min}$ distribution is taken from the data. Therefore, the inconsistencies observed in these simulated QCD events are not important to this method.

Hadronic $t\bar{t}$ events have no weakly interacting particles in the final state, and for that reason may be considered a QCD process. The simulated distributions of these events are closely similar to simulated QCD events for key variables such as $E_{\mathrm{T}}^{\mathrm{miss}}$ and $\Delta\phi_N^{\min}$, as expected. Therefore, the prediction of QCD events described in this section naturally includes the small hadronic $t\bar{t}$ background.

5.5.2 Definition of control samples

To characterize the QCD background in this analysis, a QCD-rich control sample from data is required. Due to the independence of $\Delta\phi_N^{\min}$ and $E_{\mathrm{T}}^{\mathrm{miss}}$ for these events, we are interested in a low $E_{\mathrm{T}}^{\mathrm{miss}}$ sample where all other baseline selection criteria from the analysis may be kept the same. Such a low $E_{\mathrm{T}}^{\mathrm{miss}}$ sample is dominated by QCD, which has an exponentially falling $E_{\mathrm{T}}^{\mathrm{miss}}$ distribution and a very high cross section with respect to other standard model processes, as described in Sec. 4.4.

To obtain events with $E_{\mathrm{T}}^{\mathrm{miss}}$ down to 50 GeV, but without tightening any other analysis cuts, we rely on a prescaled data sample. The sample is composed of events that would pass the trigger threshold too often to be read out and stored every time. The JetHT dataset during Run C and Run D includes a prescaled *HLT_HT300* trigger, which allows the storage of 1 event for every 1000 satisfying the online H_{T} threshold at 300 GeV, for a

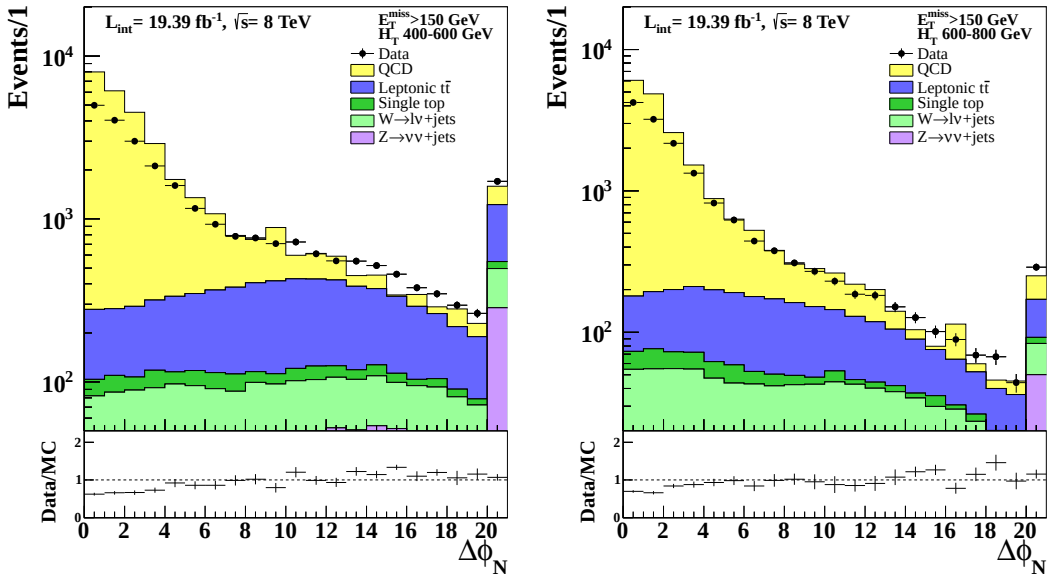

(a) $400 < H_{\mathrm{T}} < 600$ GeV

(b) $600 < H_{\mathrm{T}} < 800$ GeV

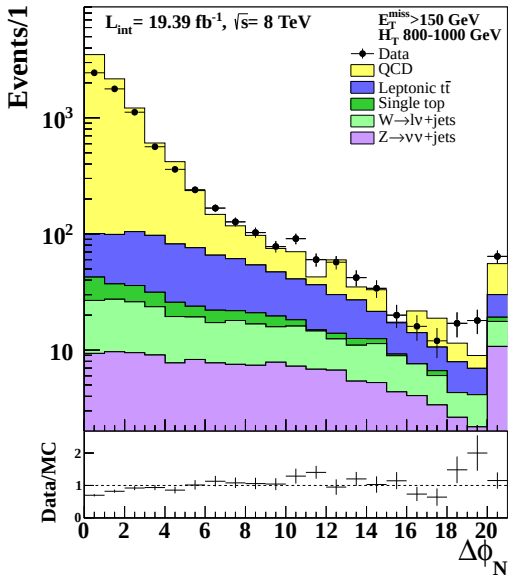

(c) $800 < H_{\mathrm{T}} < 1000$ GeV

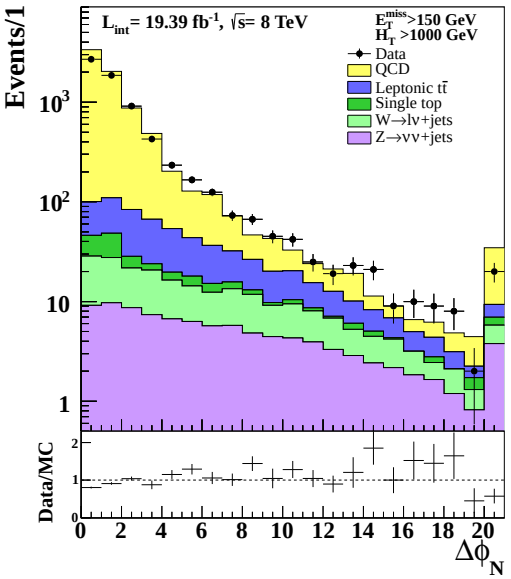

(d) $H_{\mathrm{T}} > 1000$ GeV

Figure 5.45: The smallest resolution-normalized angle between $E_{\mathrm{T}}^{\mathrm{miss}}$ and any of the three leading jets ($\Delta\phi_N^{\mathrm{min}}$) from data (black points with error bars) and simulated events (stacked, colored histograms). Baseline $E_{\mathrm{T}}^{\mathrm{miss}}$, jet, lepton, track, and b-tag selection is applied (see Sec. 4.4).

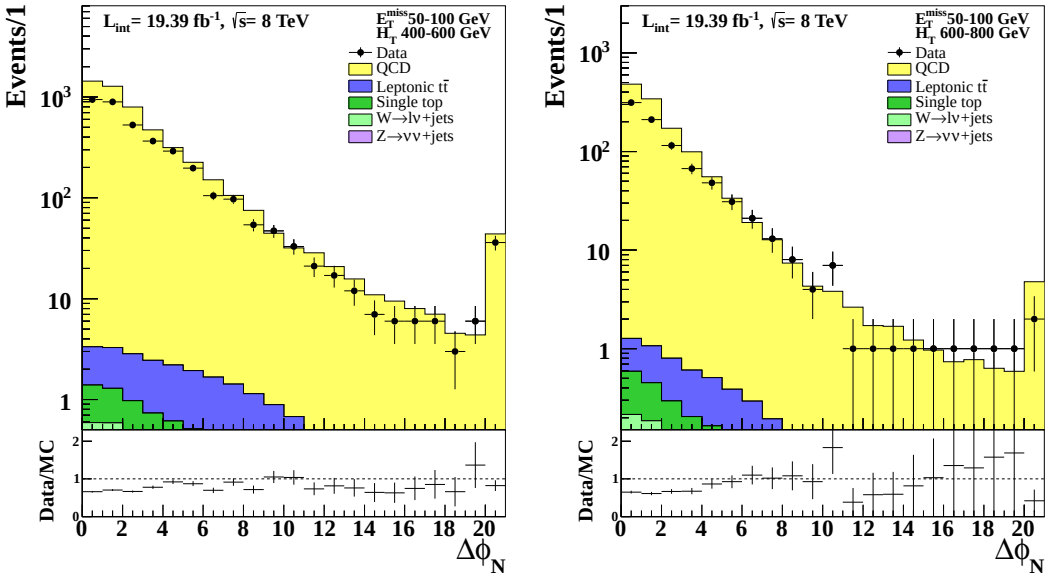

(a) $400 < H_{\mathrm{T}} < 600$ GeV

(b) $600 < H_{\mathrm{T}} < 800$ GeV

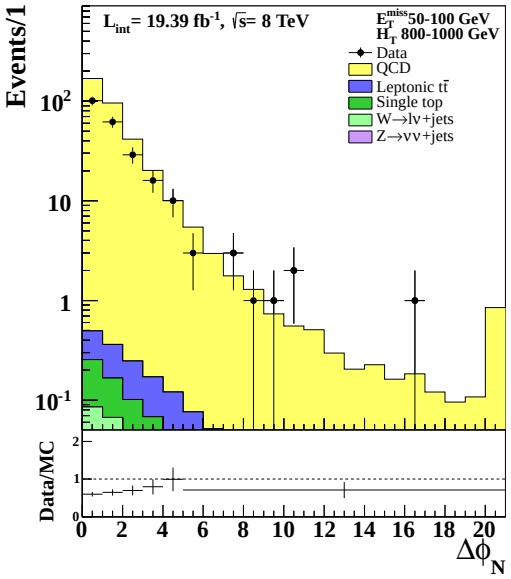

(c) $800 < H_{\mathrm{T}} < 1000$ GeV

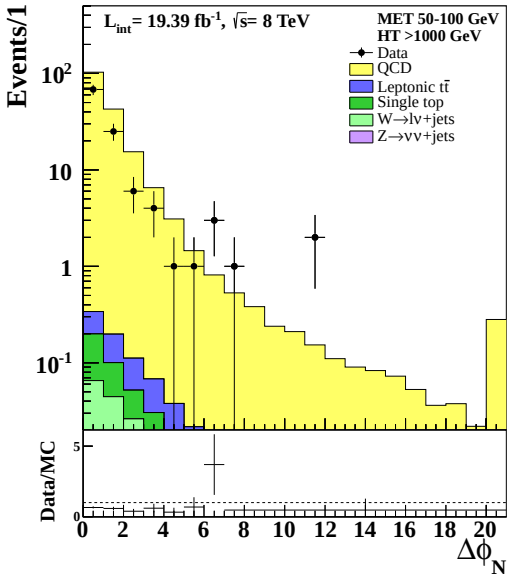

(d) $H_{\mathrm{T}} > 1000$ GeV

Figure 5.46: The smallest resolution-normalized angle between $E_{\mathrm{T}}^{\mathrm{miss}}$ and any of the three leading jets ($\Delta\phi_N^{\mathrm{min}}$) from prescaled data (black points with error bars) and simulated events (stacked, colored histograms) in the low $E_{\mathrm{T}}^{\mathrm{miss}}$ (50-100 GeV) control sample. Baseline jet, lepton, track, and b-tag selection is applied (see Sec. 4.4). Simulated events have been scaled by 1/1000 to account for the trigger rate of the data sample.

total of 6.4 fb^{-1} of data. The $E_{\text{T}}^{\text{miss}}$ range 50–100 GeV provided by this trigger is referred to as the E_{T}^{miss}-*sideband* (SB). The $\Delta\phi_N^{\text{min}}$ distribution for this sample is shown in Fig. 5.46, along with simulated events that have been scaled by 1/1000. The shape from simulated events is similar to the observations in data, but with a higher peak at zero. The important conclusion from this plot is that the expected yield from QCD is always at least two orders of magnitude greater than the combined yields from all other processes. This observation, along with the closeness of the MC yields (using the MC scale factors determined in Ch. 4) with data, demonstrates that this is a very pure sample. Since the background prediction only uses yields obtained from data, the small mis-modeling of the size and shape of the distribution from simulated events is not important.

5.5.3 Method for predicting yields

The method for predicting the QCD contribution to the signal region is straightforward. Knowing that the shape of $\Delta\phi_N^{\text{min}}$ does not change with $E_{\text{T}}^{\text{miss}}$ (within an H_{T} window) allows us to calculate the ratio of high $\Delta\phi_N^{\text{min}}$ events to low $\Delta\phi_N^{\text{min}}$ events in the QCD-enriched $E_{\text{T}}^{\text{miss}}$-sideband, and take advantage of this ratio at higher $E_{\text{T}}^{\text{miss}}$.

Without making any assumptions about the $E_{\text{T}}^{\text{miss}}$ shape of QCD events, we can use the control samples to predict the number of QCD events at high $E_{\text{T}}^{\text{miss}}$ passing the $\Delta\phi_N^{\text{min}}$ requirement. Figure 5.47 shows the analysis and control regions used for the QCD background prediction in the $E_{\text{T}}^{\text{miss}}$– $\Delta\phi_N^{\text{min}}$ plane. The boxes labeled A and B represent the prescaled $E_{\text{T}}^{\text{miss}}$-sideband, which is vastly dominated by QCD events. The ratio R_{SB} (calculated for each H_{T} bin) is the number of events in A divided by the number of events

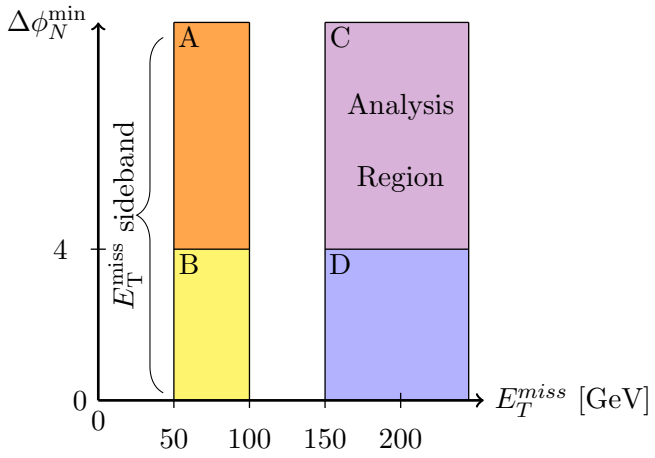

Figure 5.47: The areas of control samples for the QCD prediction, with respect to the analysis region, in the $E_{\mathrm{T}}^{\mathrm{miss}}$-$\Delta\phi_N^{\min}$ plane.

in B, which describes the shape of $\Delta\phi_N^{\min}$ for QCD events. Events in regions C and D are taken from the standard analysis dataset, and include a non-negligible amount of other backgrounds. Nonetheless, as will be discussed later in this section, R_{SB} describes the number of QCD events in C divided by the number of QCD events in D.

The predicted number of QCD events in the analysis region can be determined by a simple equation,

$$N_C^{QCD} = \frac{N_A}{N_B} \times N_D = R_{SB} \times N_D, \tag{5.7}$$

where N_X is the number of data events in one of the boxes defined above, and N_C^{QCD} is the predicted number of QCD events in the signal region (C) at high $E_{\mathrm{T}}^{\mathrm{miss}}$ and high $\Delta\phi_N^{\min}$. As seen in Fig. 5.45, region D has a small but non-negligible contribution of events from $t\bar{t}$, single-top, and W+jets sources. If we were to simply use the equation above, we would

overpredict the amount of QCD in the signal region. Instead, we can modify this equation,

$$N_C^{QCD} = R_{SB} \times (N_D - N_D^{ttWt}), \tag{5.8}$$

where N_D^{ttWt} is the expected yield of $t\bar{t}$, single-top, and W+jets events in region D.

While it is very difficult to directly probe the high $E_{\mathrm{T}}^{\mathrm{miss}}$ tail (region C) of QCD events in data, the characteristics of the $\Delta\phi_N^{\mathrm{min}}$ variable make it a useful tool for obtaining the total yield in that region. Since the signal region is separated according to b-tag multiplicity, we must study the the effect of the tagging on these quantities.

Figure 5.48 shows $\Delta\phi_N^{\mathrm{min}}$ distributions from data in the $E_{\mathrm{T}}^{\mathrm{miss}}$-sideband, separated according to H_{T} and the number of b-tagged jets. The shapes from simulated events are close to those observed in data, while being consistently slightly high in the first bin, as expected. The agreement (or lack thereof) between data and simulated QCD samples is clearly independent of b-tag multiplicity. Furthermore, since the number of b-tagged jets in an event does not affect the $\Delta\phi_N^{\mathrm{min}}$ calculation, and we observe that the shapes of $\Delta\phi_N^{\mathrm{min}}$ are consistent across b-tag multiplicities. This is shown for data in Fig. 5.49. Although the number of events at higher H_{T} is small, the shapes of $\Delta\phi_N^{\mathrm{min}}$ in each H_{T} region are identical.

Since the shape of $\Delta\phi_N^{\mathrm{min}}$ is not affected by the number of b-tagged jets, we use the prescaled data sample with $\geq$1 b-jet to calculate R_{SB}, to keep the statistical uncertainty on this quantity as low as possible. The ratio of events passing the $\Delta\phi_N^{\mathrm{min}}$ cut (>4.0) over the number of events failing it is shown in Table 5.23. Because the shape of $\Delta\phi_N^{\mathrm{min}}$ changes with H_{T}, the ratio is listed separately for each H_{T} bin. The first two rows are calculated from simulated QCD events for two $E_{\mathrm{T}}^{\mathrm{miss}}$ regions: the sideband from which the ratios are taken

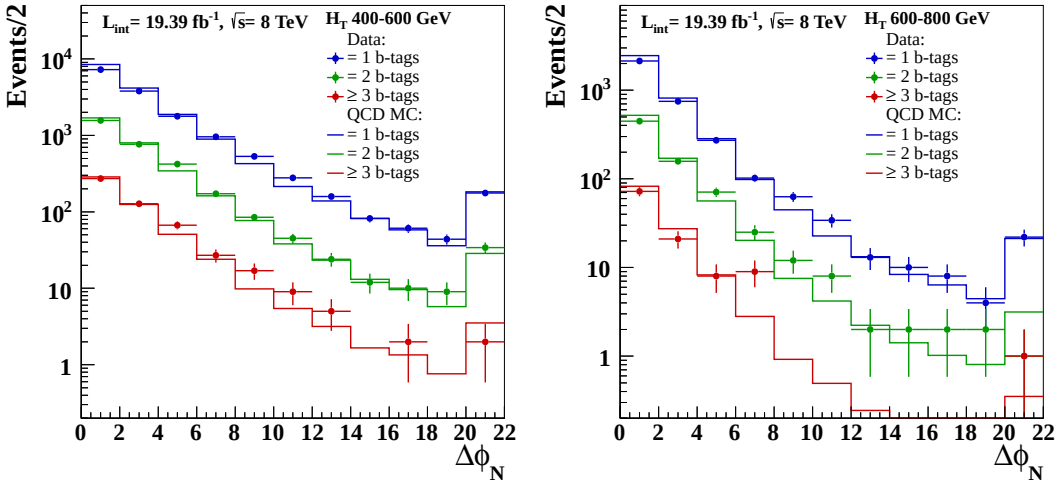

(a) $400 < H_{\mathrm{T}} < 600$ GeV

(b) $600 < H_{\mathrm{T}} < 800$ GeV

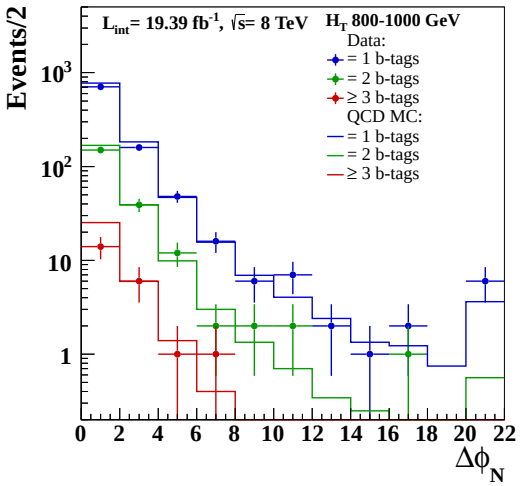

(c) $800 < H_{\mathrm{T}} < 1000$ GeV

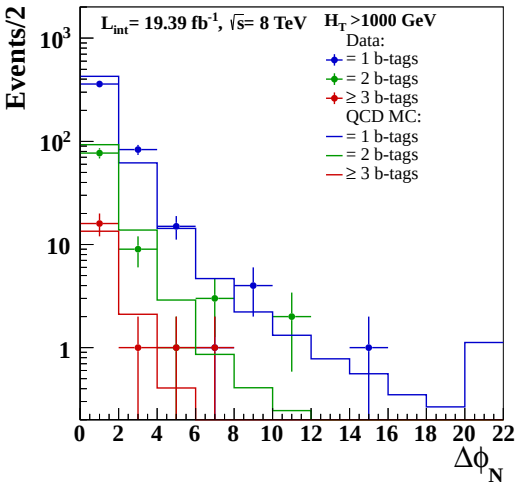

(d) H_{T} >1000 GeV

Figure 5.48: The smallest resolution-normalized angle between $E_{\mathrm{T}}^{\mathrm{miss}}$ and any of the three leading jets ($\Delta\phi_N^{\mathrm{min}}$) from data (colored points with error bars) and simulated QCD events (colored histograms) in the low $E_{\mathrm{T}}^{\mathrm{miss}}$ (50-100 GeV) control sample. Baseline jet, lepton, and track selection is applied (see Sec. 4.4). Both samples are split into three subsamples according to the number of b-tagged jets in the event, one (blue), two (green), or at least three (red). The distributions from simulation are normalized to the distributions from data.

and the analysis region where the ratios are applied. The table shows they are consistent, with some deviation occuring at the highest H_{T}, as expected. The bottom row shows the

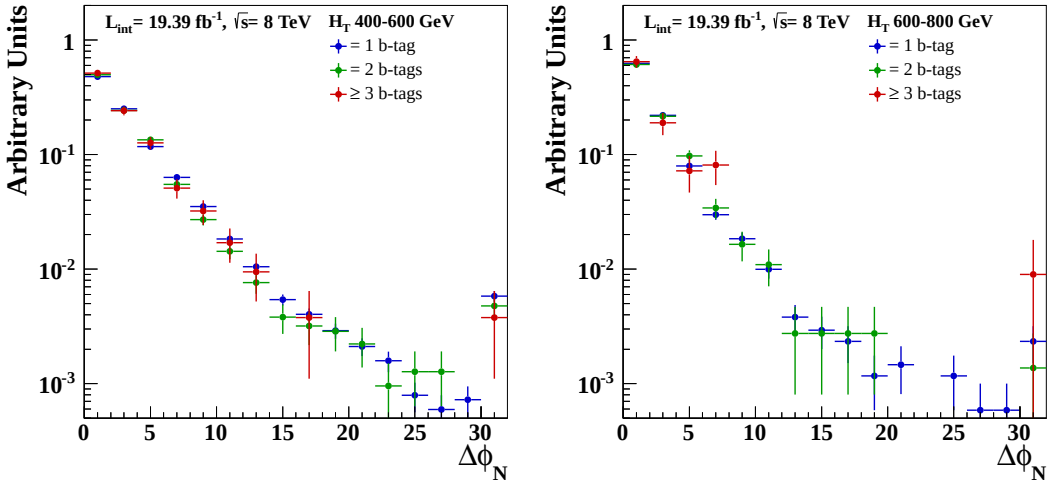

(a) $400 < H_{\mathrm{T}} < 600$ GeV

(b) $600 < H_{\mathrm{T}} < 800$ GeV

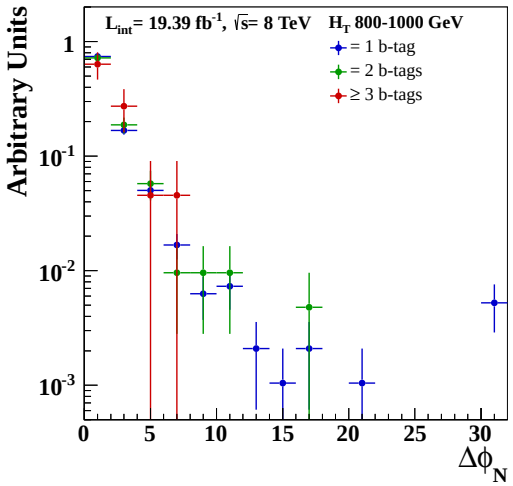

(c) $800 < H_{\mathrm{T}} < 1000$ GeV

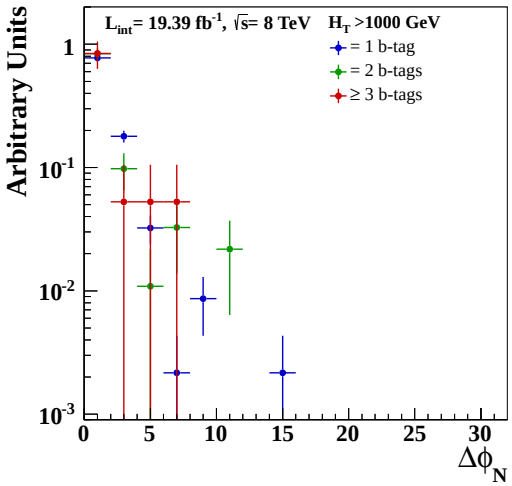

(d) H_{T} >1000 GeV

Figure 5.49: The smallest resolution-normalized angle between $E_{\mathrm{T}}^{\mathrm{miss}}$ and any of the three leading jets ($\Delta\phi_N^{\mathrm{min}}$) from data in the low $E_{\mathrm{T}}^{\mathrm{miss}}$ (50-100 GeV) control sample. Baseline jet, lepton, and track selection is applied (see Sec. 4.4). The sample is split according to the number of b-tagged jets in the event, one (blue), two (green), or at least three (red). The distributions are normalized to one.

ratios extracted from data in the $E_{\mathrm{T}}^{\mathrm{miss}}$-sideband, and can be compared to what is expected from simulated events. The purpose of using a control sample in data is to properly account for the true $\Delta\phi_N^{\mathrm{min}}$ shape if the simulation is not accurate. However, for the most part, the

Table 5.23: Ratios of events with $\Delta\phi_N^{\min}$ >4 to events with $\Delta\phi_N^{\min}$ <4, from simulated QCD events and data with at least 1 b-jet. Uncertainties are statistical only. The bottom row contains the values of R_{SB}, calculated from data.

Sample	$E_{\mathrm{T}}^{\mathrm{miss}}$ range	H_{T} range, in GeV			
		400 – 600	600 – 800	800 – 1000	>1000
MC	50–100 GeV	0.276 ± 0.004	0.137 ± 0.002	0.078 ± 0.001	0.053 ± 0.001
	>150 GeV	0.274 ± 0.022	0.172 ± 0.014	0.118 ± 0.010	0.083 ± 0.008
Data	50–100 GeV	0.35 ± 0.01	0.20 ± 0.02	0.10 ± 0.02	0.11 ± 0.05

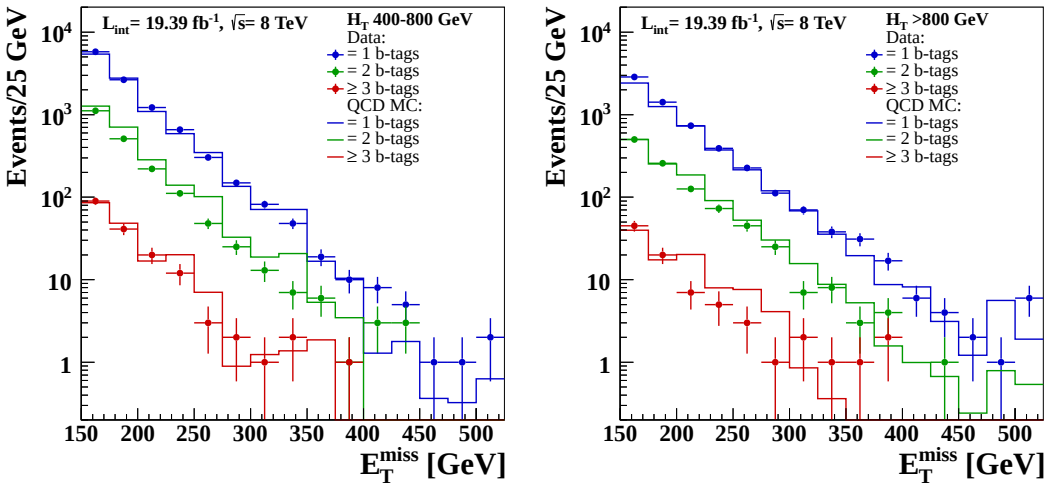

(a) 400 < H_{T} < 800 GeV (b) H_{T} > 800 GeV

Figure 5.50: Distribution of $E_{\mathrm{T}}^{\mathrm{miss}}$ from data (colored points with error bars) and simulated QCD events (colored histograms) in the low $\Delta\phi_N^{\min}$ (<4.0) control sample. Baseline jet, lepton, and track selection is applied (see Sec. 4.4). Both samples are split into three subsamples according to the number of b-jets in the event, one (blue), two (green), or at least three (red). The distributions from simulation are normalized to the distributions from data.

ratios from data happen to be close to what the simulated events predict, indicating that this quantity is mostly well modeled within statistical uncertainty.

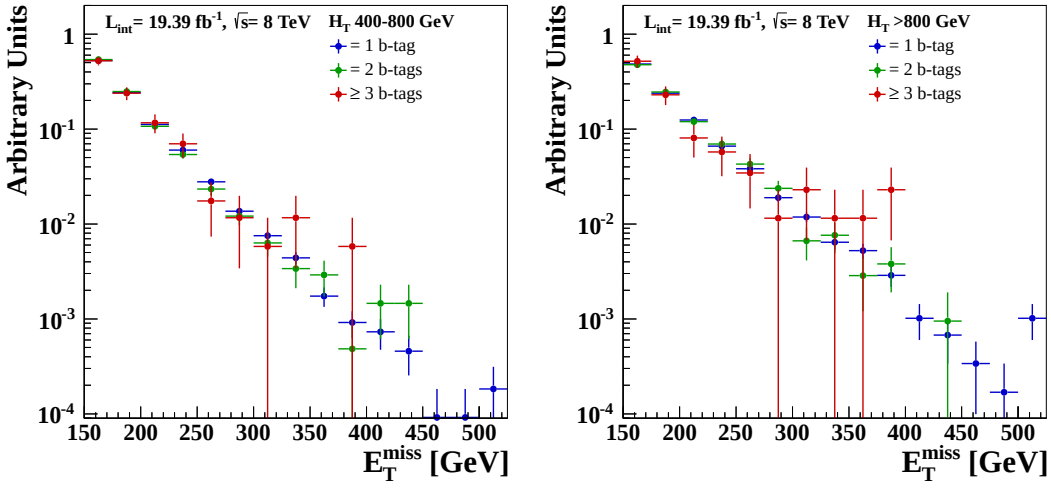

(a) $400 < H_T < 800$ (b) $H_T > 800$

Figure 5.51: Distribution of E_T^{miss} from data in the low $\Delta\phi_N^{min}$ (<4.0) control sample. Baseline jet, lepton, and track selection is applied (see Sec. 4.4). The sample is split according to the number of b-jets in the event, one (blue), two (green), or at least three (red). The distributions are normalized to one.

Before applying R_{SB} to the higher E_T^{miss} region, we must study certain properties of the multijets E_T^{miss} spectrum. Inverting the analysis cut on $\Delta\phi_N^{min}$ (at 4.0) creates a largely multijet control sample within the standard dataset. The E_T^{miss} spectrum of QCD events can be studied using this control sample (region D in Fig. 5.47), as an additional check on the behavior of multijets events in the E_T^{miss}–$\Delta\phi_N^{min}$ plane.

Figure 5.50 compares data with simulated QCD events, separated by H_T and b-tag multiplicity. As demonstrated in Fig. 5.45, there is some contamination from $t\bar{t}$ events in the very high tails of the E_T^{miss} distribution, and in regions of high b-tag multiplicity. Despite this, the shape of E_T^{miss} at low $\Delta\phi_N^{min}$ is well described by multijet simulation. Figure 5.51 compares the E_T^{miss} distributions with different b-tag multiplicities from data, all normalized to one. The level of agreement between the shapes indicates that the distribution of QCD

events is not affected by the presence of b-jets. Since the shape of $E_{\mathrm{T}}^{\mathrm{miss}}$ is independent of b-tag multiplicity, we can confidently use the value of R_{SB} taken from the $\geq$1 b-tag sample as applicable to the higher $E_{\mathrm{T}}^{\mathrm{miss}}$ region, regardless of b-tag multiplicity.

The presence of $t\bar{t}$ contamination in the low $\Delta\phi_N^{\mathrm{min}}$ region can effect the QCD prediction in certain signal regions. Figure 5.52 shows how large this effect can be in the problematic regions. There, the total yield of multijet events, even at low $\Delta\phi_N^{\mathrm{min}}$, is small. In the worst case, up to almost 33% of events at low $\Delta\phi_N^{\mathrm{min}}$ could have resulted from $t\bar{t}$ production. For this reason, we subtract the $t\bar{t}$, W+jets, and single-top yield as described in Eq. 5.8. Since the amount of contamination is small, the total prediction for QCD is also small, and the $\Delta\phi_N^{\mathrm{min}}$ distribution of $t\bar{t}$ events is well described by simulation, we take the value of this contamination from simulated events. This correction procedure contributes a negligible amount of additional statistical uncertainty.

5.5.4 Correction factors, κ

Even though the shape of $\Delta\phi_N^{\mathrm{min}}$ at low values is not simulated well, we can use ratios of simulated events to make corrections that account for small inconsistencies in the assumptions we make. The main assumption in this method is the lack of correlation between $E_{\mathrm{T}}^{\mathrm{miss}}$ and $\Delta\phi_N^{\mathrm{min}}$, given the construction of the angular quantity. This is related to the correlation between $\Delta\phi_N^{\mathrm{min}}$ and H_{T}, since events with high H_{T} have the potential for higher $E_{\mathrm{T}}^{\mathrm{miss}}$ that would be impossible for events with low H_{T}. A difference between the $\Delta\phi_N^{\mathrm{min}}$ shape at low $E_{\mathrm{T}}^{\mathrm{miss}}$ and the shape at high $E_{\mathrm{T}}^{\mathrm{miss}}$ appears as H_{T} increases, indicating a physical effect that should be corrected for. The differences in the shape of $\Delta\phi_N^{\mathrm{min}}$ at low

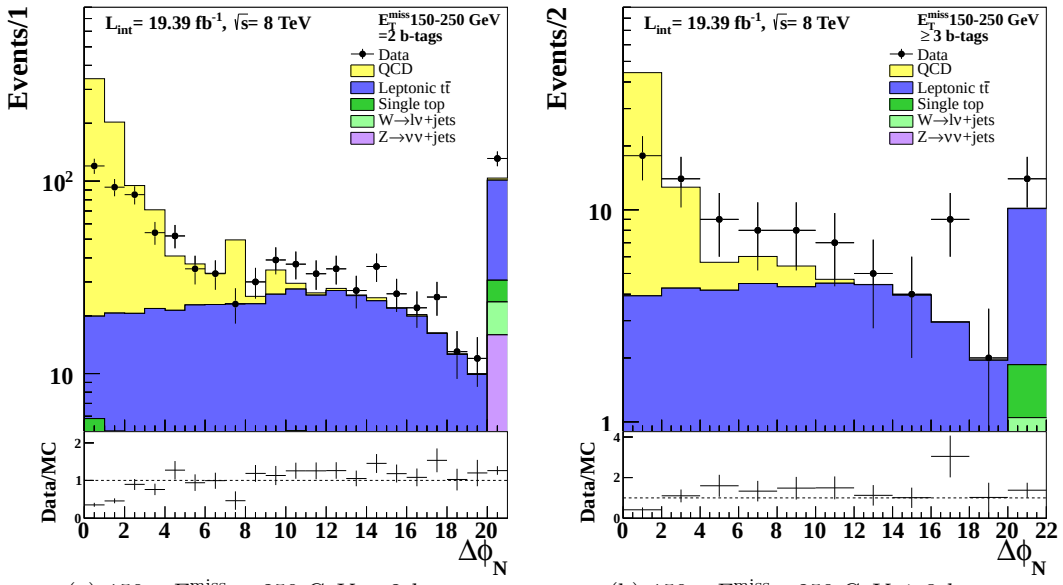

(a) 150< $E_{\mathrm{T}}^{\mathrm{miss}}$ < 250 GeV, =2 b-tags

(b) 150< $E_{\mathrm{T}}^{\mathrm{miss}}$ <250 GeV, ≥3 b-tags

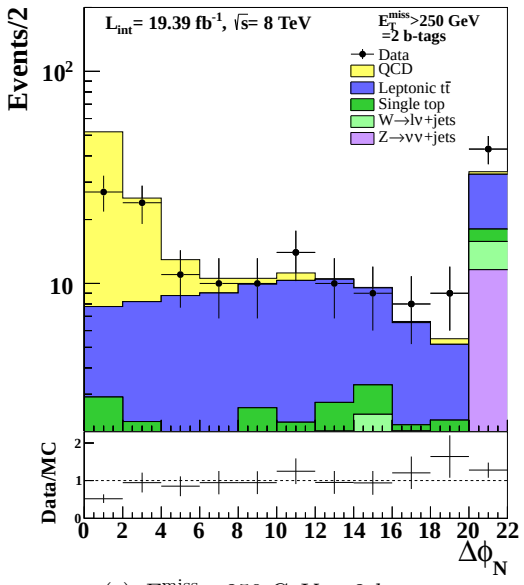

(c) $E_{\mathrm{T}}^{\mathrm{miss}}$ >250 GeV, =2 b-tags

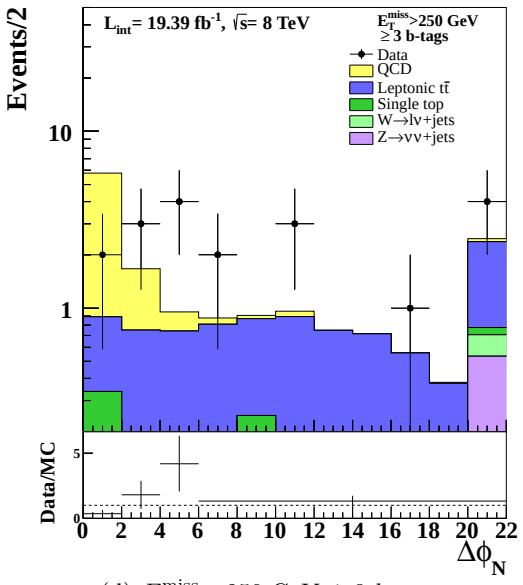

(d) $E_{\mathrm{T}}^{\mathrm{miss}}$ >250 GeV, ≥3 b-tags

Figure 5.52: The smallest resolution-normalized angle between $E_{\mathrm{T}}^{\mathrm{miss}}$ and any of the three leading jets ($\Delta\phi_N^{\mathrm{min}}$) from data (black points with error bars) and simulated events (stacked, colored histograms) for selected regions corresponding to the analysis sample. Baseline H_{T}, jet, lepton, and track selection is applied (see Sec. 4.4).

Table 5.24: Ratio of $R(E_{\mathrm{T}}^{\mathrm{miss}}$ >150 GeV) to R_{SB} from simulated QCD events, κ.

H_{T} range	400 – 600 GeV	600 – 800 GeV	800 – 1000 GeV	>1000 GeV
≥ 1 b-tag	1.00 ± 0.08	1.25 ± 0.11	1.52 ± 0.13	1.56 ± 0.15
$= 1$ b-tag	0.96 ± 0.08	1.31 ± 0.11	1.55 ± 0.13	1.54 ± 0.13
≥ 2 b-tags	1.16 ± 0.15	1.14 ± 0.17	1.51 ± 0.22	1.72 ± 0.34

Table 5.25: Effect of jet energy scale uncertainty on the QCD background predictions, calculated from simulated events.

H_{T} range	
400 – 800 GeV	±5.4%
> 800 GeV	±14.5%

and high $E_{\mathrm{T}}^{\mathrm{miss}}$ are quantified as ratios of the ratios from simulation listed in Table 5.23. The results are provided in Table 5.24, and clearly increase with H_{T}. These correction factors, κ, are calculated for the inclusive sample and for separating the sample according to b-tag multiplicity. It is not possible to include κ from the $\geq$3 b-tags region, because the raw yields in simulation are too small to provide meaningful results. Since the values of κ are so similar in the =1 and $\geq$2 b-tags regions, we use the correction factor calculated from the full $\geq$1 b-tag range. This factor provides a small correction to our prediction due to the $E_{\mathrm{T}}^{\mathrm{miss}}$ shape, while keeping the statistical uncertainty on the prediction as low as possible.

5.5.5 Evaluation of systematic uncertainty

While the major source of uncertainty in this method arises from the small sample sizes, we also examine the effect of the jet energy scale uncertainty on the κ correction factor. Using simulated events, we calculate the resulting change in κ when the p_{T} of all jets are varied by $\pm 5\%$. Like the R_{SB} and κ scale factors, these uncertainties only depend on H_{T}. They are listed in Table 5.25.

5.5.6 Results

Predicted yields of QCD events are obtained by subtracting the $t\bar{t}/W/t$ background from the low $\Delta\phi_N^{\mathrm{min}}$ data sample, applying R_{SB}, and finally the simulation-based κ-factor. The predicted yield and statistical uncertainty for each of the four H_{T} bins is shown in Table 5.26. The H_{T} regions are combined to reflect the bins of the complete analysis in Table 5.27 and Table 5.28, along with the expected yields from simulation (with the factor of 1.35 established in Ch. 4 applied). Each signal region is shown, as well as the validation regions at low $E_{\mathrm{T}}^{\mathrm{miss}}$ (150–250 GeV) and b-tag multiplicity (=1 b-tagged jet). The expected yields of QCD from the largely data-driven method is small, with reasonably-sized uncertainties. Overall, the yields obtained from simulation are close. Somewhat large discrepancies are observed at in the =1 b-tagged jet sample. However, the statistical uncertainties on both the predicted and simulated yields are large enough that they are not separated by more than two standard deviations.

Table 5.26: Predicted yields of QCD events for each H_{T} sub-range. Uncertainties are statistical, and include the statistical uncertainty of simulated events for the κ scale factor and the $t\bar{t}/W/t$ yield in the low $\Delta\phi_N^{\mathrm{min}}$ region.

H_{T} range	400 - 600 GeV	600 - 800 GeV	800 - 1000 GeV	>1000 GeV
$E_{\mathrm{T}}^{\mathrm{miss}}$ 150-250 GeV				
=1 b-tag	3553 ± 324	1970 ± 250	640 ± 160	740 ± 300
=2 b-tags	793 ± 74	450 ± 58	133 ± 32	120 ± 49
≥3 b-tags	53.5 ± 6.7	36.3 ± 5.6	10.1 ± 2.8	12.8 ± 5.5
$E_{\mathrm{T}}^{\mathrm{miss}}$ 250-350 GeV				
=1 b-tag	86.6 ± 9.9	107 ± 15	49 ± 12	75 ± 31
=2 b-tags	14.1 ± 2.9	17.6 ± 3.3	10.5 ± 2.9	14.7 ± 6.3
≥3 b-tags	1.98 ± 0.93	1.43 ± 0.74	0.80 ± 0.45	1.03 ± 0.65
$E_{\mathrm{T}}^{\mathrm{miss}}$ >350 GeV				
=1 b-tag	1.6 ± 1.0	5.6 ± 1.6	6.8 ± 2.0	16.2 ± 6.9
=2 b-tags	0	2.65 ± 0.98	0.54 ± 0.46	3.7 ± 1.8
≥3 b-tags	0	0.21 ± 0.26	0.38 ± 0.28	0.03 ± 0.18

Table 5.27: Predicted yields of QCD events from the data-driven method and simulation, $400<H_{\mathrm{T}}<800$ GeV. Statistical and systematic uncertainties are shown. The statistical uncertainty includes the statistical uncertainty of simulated events for the κ scale factor and the $t\bar{t}/W/t$ yield in the low $\Delta\phi_N^{\mathrm{min}}$ region.

$E_{\mathrm{T}}^{\mathrm{miss}}$ range	150 – 250 GeV	250 – 350 GeV	$>$ 350 GeV
Prediction from data			
=1 b-tag	5522 $\pm$ 410 $\pm$ 300	194 $\pm$ 18 $\pm$ 10	7.2 $\pm$ 1.9 $\pm$ 0.4
=2 b-tags	1243 $\pm$ 94 $\pm$ 67	31.7 $\pm$ 4.4 $\pm$ 1.7	2.65 $\pm$ 0.98 $\pm$ 0.14
$\geq$3 b-tags	89.7 $\pm$ 8.7 $\pm$ 4.8	3.4 $\pm$ 1.2 $\pm$ 0.2	0.21 $\pm$ 0.26 $\pm$ 0.01
QCD simulation			
=1 b-tag	4300 $\pm$ 240	173 $\pm$ 29	28 $\pm$ 16
=2 b-tags	1320 $\pm$ 120	43 $\pm$ 19	1.99 $\pm$ 0.77
$\geq$3 b-tags	71 $\pm$ 14	1.76 $\pm$ 0.78	0.09 $\pm$ 0.05

Table 5.28: Predicted yields of QCD events from the data-driven method and simulation, H_{T} >800 GeV. Statistical and systematic uncertainties are shown. The statistical uncertainty includes the statistical uncertainty of simulated events for the κ scale factor and the $t\bar{t}/W/t$ yield in the low $\Delta\phi_N^{\mathrm{min}}$ region.

$E_{\mathrm{T}}^{\mathrm{miss}}$	150 – 250 GeV	250 – 350 GeV	$>$ 350 GeV
Prediction from data			
=1 b-tag	1380 ± 340 ± 200	124 ± 33 ± 18	23.0 ± 7.2 ± 3.3
=2 b-tags	253 ± 59 ± 36	25.3 ± 6.9 ± 3.7	4.3 ± 1.9 ± 0.6
≥3 b-tags	22.9 ± 6.1 ± 3.3	1.82 ± 0.79 ± 0.26	0.41 ± 0.33 ± 0.06
QCD simulation			
=1 b-tag	680 ± 40	67.3 ± 6.2	17.7 ± 1.5
=2 b-tag	166 ± 17	20.2 ± 4.1	4.48 ± 0.63
≥3 b-tags	15.0 ± 4.4	1.38 ± 0.40	0.27 ± 0.06

5.6 Predicting the $Z \to \nu\bar{\nu}$ background

Background from Z+jets with $Z \to \nu\bar{\nu}$ is expected to comprise less than 10% of the Standard Model yield in the signal regions of this analysis. While these events are kinematically similar to $Z \to l^+l^-$ events, the neutrinos, unlike charged leptons, appear through $E_{\mathrm{T}}^{\mathrm{miss}}$. Since it is impossible to obtain a well-understood control sample dominated by $Z \to \nu\bar{\nu}$ events, we use a Z+jets sample with $Z \to l^+l^-$. Because the lighter charged leptons have high reconstruction efficiencies and good resolution, we restrict the definition of $Z \to l^+l^-$ to dimuon and dielectron events. The yield of $Z \to \nu\bar{\nu}$ is related to the observed $Z \to l^+l^-$ yield according to the ratio of their branching fractions and the lepton reconstruction efficiency. Furthermore, the observed dimuon and dielectron p_{T} spectra are similar in shape to the neutrinos. This method takes important kinematic quantities such as H_{T}, $E_{\mathrm{T}}^{\mathrm{miss}}$, and b-tag multiplicity directly from the data, and is simple to implement with few sources of systematic uncertainty.

5.6.1 Definition of the control sample

To obtain a control sample dominated by $Z \to l^+l^-$ events, we start with a dataset based on dimuon and dielectron triggers. The datasets and their corresponding integrated luminosities are listed in Table 5.29. From these, we select events passing the dilepton triggers listed in Table 5.30.

Selection criteria are imposed to ensure that the control sample is almost completely $Z \to l^+l^-$ and has the same hadronic features as the analysis sample. Differences

Table 5.29: Data samples used for the dilepton $Z \to l^+l^-$ control sample.

Name	$\mathcal{L}$ [pb^{-1}]
DoubleMu, DoubleElectron_Run2012A-13Jul2012-v1_AOD DoubleMu, DoubleElectron_Run2012A-recover-06Aug2012-v1_AOD	807
DoubleMu, DoubleElectron_Run2012B-13Jul2012-v4_AOD	4421
DoubleMu, DoubleElectron_Run2012C-24Aug2012-v1_AOD	495
DoubleMu, DoubleElectron_Run2012C-EcalRecover_11Dec2012-v1_AOD DoubleMu, DoubleElectron_Run2012C-PromptReco-v2_AOD	6311
DoubleMu, DoubleElectron_Run2012D-PromptReco-v1_AOD	7273

Table 5.30: Triggers used for the dilepton $Z \to l^+l^-$ control sample.

HLT_Ele17_CaloIdT_CaloIsoVL_TrkIdVL_TrkIsoVL
_Ele8_CaloIdT_CaloIsoVL_TrkIdVL_TrkIsoVL
HLT_Mu17_Mu8
HLT_Mu13_Mu8

Table 5.31: Selection criteria for the dilepton $Z \to l^+l^-$ control sample. The quality criteria for jets, electrons, and muons are the same as for the analysis sample. Differences from the analysis sample are listed here.

Quantity	Requirement
Leptons	=2 passing inverted veto criteria, p_{T} >17 GeV same flavor, opposite sign, 76.2< M_{ll} <106.2 GeV
$\Delta\phi_N^{\mathrm{min}}$	none
$E_{\mathrm{T}}^{\mathrm{miss}}$	none
Isolated tracks	none
b-tagged jets	$\geq$ 1 jet with CSV>0.244

from the criteria in Sec. 4.4 are listed in Table 5.31. The leptons must be the same flavor and have opposite charge. The quality, isolation, and pseudo-rapidity requirements used to veto leptons in the analysis sample are inverted for the dilepton selection. Furthermore, only events in which the leptons are consistent with the Z boson mass are included. The mass spectra for events in the control sample (without a cut on $M_{l^+l^-}$) are shown in Fig. 5.53. As expected, the spectrum peaks sharply at the Z boson mass, where the sample is dominated by $Z \to l^+l^-$ events. Since the sources of jet production in Z+jets events are independent of the Z decay mode, the usual H_{T} and jet requirements are the same as the analysis sample, with the exception of $\Delta\phi_N^{\mathrm{min}}$. The value of $\Delta\phi_N^{\mathrm{min}}$ relies on $E_{\mathrm{T}}^{\mathrm{miss}}$, which must be modified to emulate the shape from $Z \to \nu\bar{\nu}$ decay. For this reason, no cuts are placed on $E_{\mathrm{T}}^{\mathrm{miss}}$ or $\Delta\phi_N^{\mathrm{min}}$. The distribution of H_{T} (with the cut on H_{T} removed) and $\Delta\phi_N^{\mathrm{min}}$ are provided in Fig. 5.55.

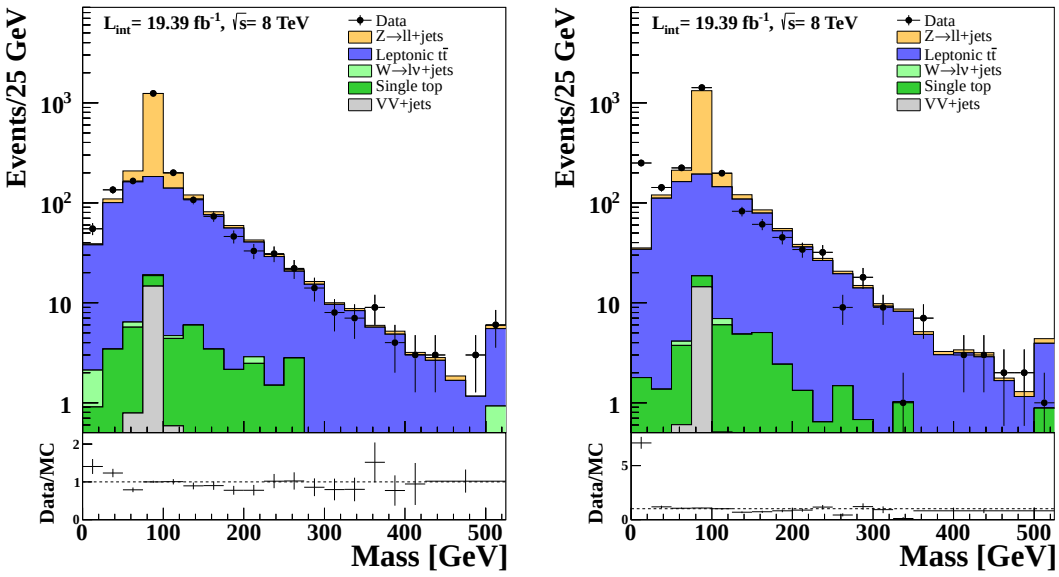

(a) Mass of electron pairs.

(b) Mass of muon pairs.

Figure 5.53: Mass of lepton pairs in the dilepton control sample. The black points are data, and the stacked histograms are from simulated events.

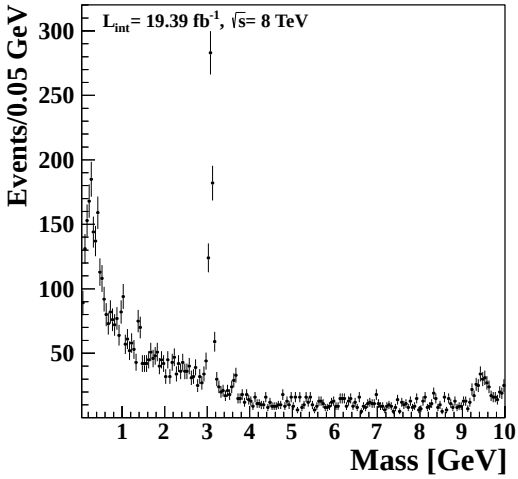

Figure 5.54: Mass of lepton pairs at very low values. All jet-related requirements have been removed. These events are not modeled in the $Z \to l^+l^-$ simulation samples.

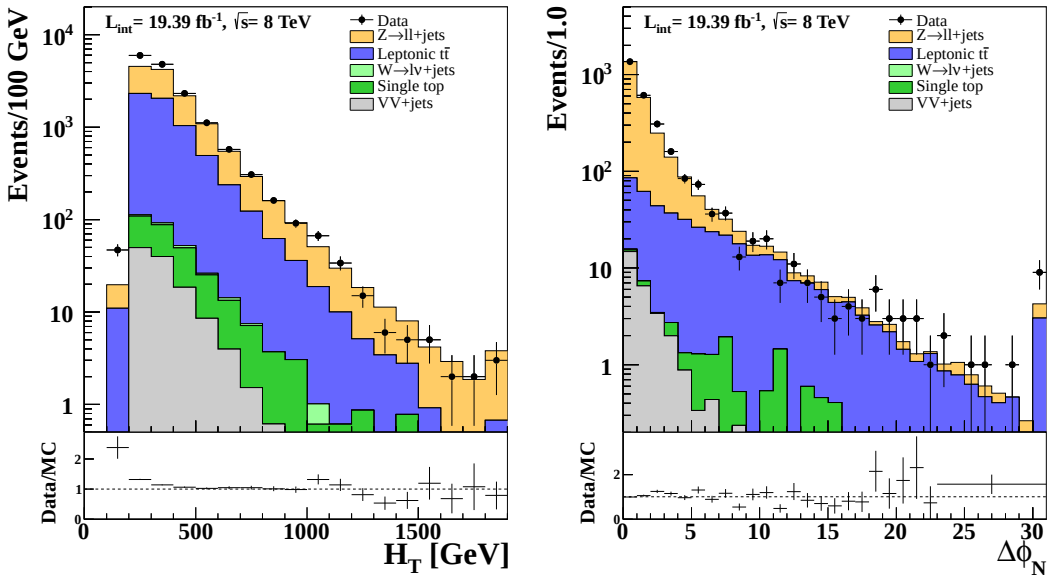

Figure 5.55: Distribution of jet-based quantities in the dilepton control sample, H_{T} (left) and $\Delta\phi_N^{\mathrm{min}}$ (right). The black points are data, and the stacked histograms are from simulated events.

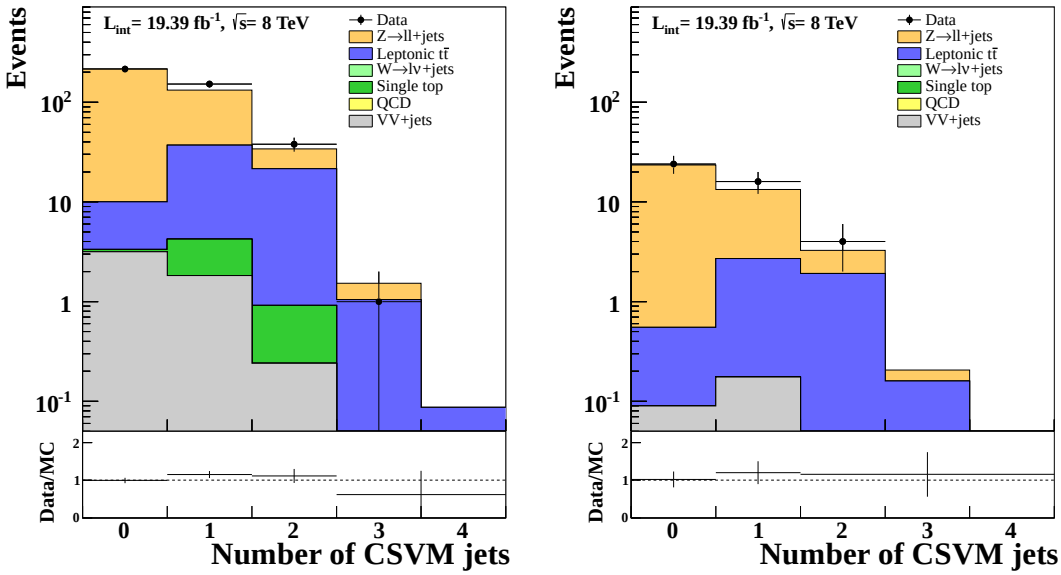

(a) $400 < H_{\mathrm{T}} < 800$ GeV (b) $H_{\mathrm{T}} > 800$ GeV

Figure 5.56: Number of CSVM b-tagged jets in the dilepton control sample. The black points are data, and the stacked histograms are from simulated events.

As with the properties of other hadronic quantities, the b-tag multiplicity of the dilepton control sample should be the same as $Z \to \nu\bar{\nu}$ in the analysis sample. Figure 5.56 shows the b-tag multiplicity distributions in the two H_{T} ranges of the control sample. When a jet with a CSV value above 0.679 (the medium working point selection used to define the signal regions) is required, the size of the sample is reduced and the proportion of $t\bar{t}$ events increases. The statistical power of the control sample is limited due to the relatively high H_{T} and jet cuts, so it is important to keep as many $Z \to l^+l^-$ events as possible. For this reason, the b-tag requirement is loosened to at least one jet with CSV >0.244 (as shown in Table 5.31), which has a misidentification rate of 10%. This sample relates to the signal b-tagged jet multiplicity bins in a way that can be determined from data, as described later in this section.

5.6.2 Method for predicting $E_{\mathrm{T}}^{\mathrm{miss}}$ shape

In a $Z \to \nu\bar{\nu}$ event, the decay products of the boson are not observed in the detector, and therefore are the dominant source of $E_{\mathrm{T}}^{\mathrm{miss}}$. Since the momentum spectra of the lepton decay products are the same, we add the transverse momenta of the observed electrons or muons in the dilepton control sample vectorally to the $E_{\mathrm{T}}^{\mathrm{miss}}$. This procedure provides an accurate shape of the $E_{\mathrm{T}}^{\mathrm{miss}}$ distribution in $Z \to \nu\bar{\nu}$ events.

When the value of $E_{\mathrm{T}}^{\mathrm{miss}}$ is modified by the lepton p_{T} in a dilepton event, the value of $\Delta\phi_N^{\mathrm{min}}$ is also modified. The distribution of the modified $\Delta\phi_N^{\mathrm{min}}$ is shown in Fig. 5.57. The shape of this distribution in the control sample is now broader. Because the $E_{\mathrm{T}}^{\mathrm{miss}}$ in

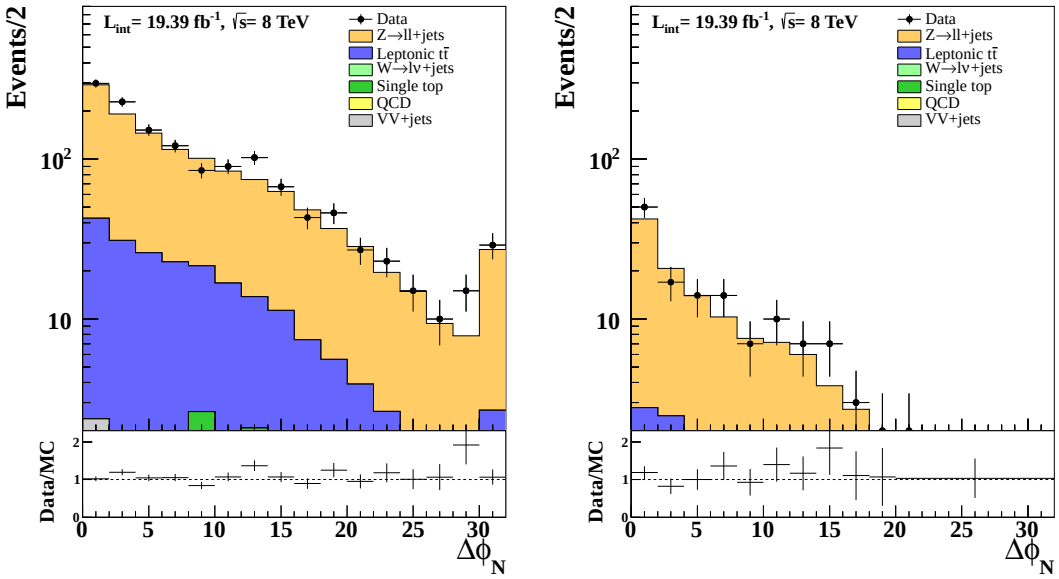

(a) $400 < H_{\mathrm{T}} < 800$ GeV (b) $H_{\mathrm{T}} > 800$ GeV

Figure 5.57: Distribution of $\Delta\phi_N^{\mathrm{min}}$ after modifyng $E_{\mathrm{T}}^{\mathrm{miss}}$ by the lepton momenta in the dilepton control sample, for low (left) and high (right) H_{T} bins. No cut on the modified $E_{\mathrm{T}}^{\mathrm{miss}}$ is applied. The black points are data, and the stacked histograms are from simulated events.

the event is no longer aligned with mismeasured jets, the modified $\Delta\phi_N^{\min}$ distribution is similar to $t\bar{t}$, in which $E_{\mathrm{T}}^{\mathrm{miss}}$ is genuine.

The $E_{\mathrm{T}}^{\mathrm{miss}}$ spectrum in the dilepton control sample is shown in Fig. 5.58, with and without the modification from observed lepton p_{T}. Before modification, the shape is peaked at zero, and the tail is dominated by $t\bar{t}$ contamination. After modification, the shape is spread out to 600 GeV, and is dominated by $Z \to l^+l^-$ for the entire range. The overlayed red histogram is the $E_{\mathrm{T}}^{\mathrm{miss}}$ shape from simulated $Z \to \nu\bar{\nu}$ events, normalized to the yield in data above 150 GeV. It shows that the modified $E_{\mathrm{T}}^{\mathrm{miss}}$ produces a shape in data that is very similar to what is expected from simulated events with two neutrinos.

A few other important quantities are checked with the new cuts on the modified $E_{\mathrm{T}}^{\mathrm{miss}}$ and $\Delta\phi_N^{\min}$. Figure 5.59 shows the mass of the dilepton pair in the control sample with and without the modification of the $E_{\mathrm{T}}^{\mathrm{miss}}$. Since the $E_{\mathrm{T}}^{\mathrm{miss}}$ cut selects leptons with higher momentum, we observe relatively fewer events at very low mass. However, this does not affect events at the Z peak or above, and the shape of the mass spectrum remains mostly unchanged. Figure 5.60 shows the distribution of CSV values for the three jets with the highest values after the modified selection. The first plot shows that the sample is dominated by $Z \to l^+l^-$ if a loose cut at 0.244 is applied. It is not possible to apply the medium working point cut (at 0.679) to even a single jet and still maintain a large, $Z \to l^+l^-$ dominated control sample. Instead, we must rely on an alternative procedure to reproduce the effect of applying medium CSV requirements on the $Z \to \nu\bar{\nu}$ background. This is described in the following subsection.

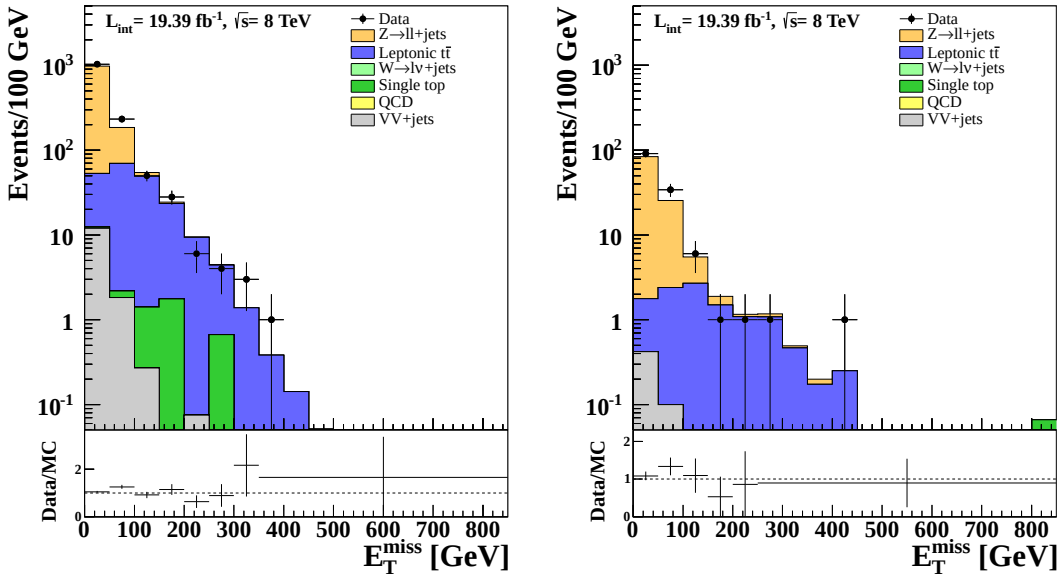

(a) $E_{\mathrm{T}}^{\mathrm{miss}}$, $400 < H_{\mathrm{T}} < 800$ GeV

(b) $E_{\mathrm{T}}^{\mathrm{miss}}$, $H_{\mathrm{T}} > 800$ GeV

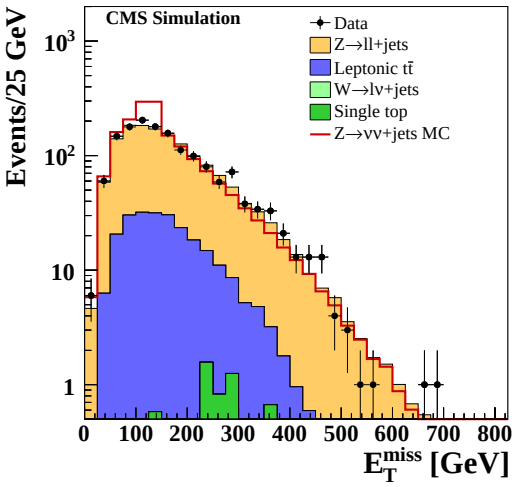

(c) $E_{\mathrm{T}}^{\mathrm{miss}}$, $H_{\mathrm{T}} > 800$ GeV

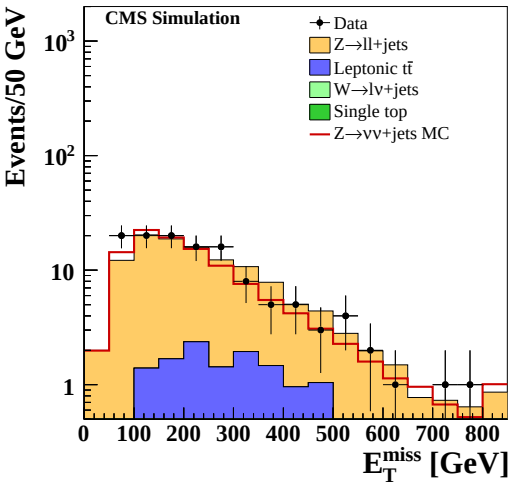

(d) $E_{\mathrm{T}}^{\mathrm{miss}}$, $H_{\mathrm{T}} > 800$ GeV

Figure 5.58: Distribution of $E_{\mathrm{T}}^{\mathrm{miss}}$ before and after modifying it by the lepton momenta in the $Z \to l^+l^-$ dilepton control sample. The top row shows the $E_{\mathrm{T}}^{\mathrm{miss}}$ spectra for low (left) and high (right) H_{T} bins. The bottom row shows the $E_{\mathrm{T}}^{\mathrm{miss}}$ spectra after adding the lepton momenta for the low (left) and high (right) H_{T} bins. The quantity $\Delta\phi_N^{\mathrm{min}}$ is calculated with the modified $E_{\mathrm{T}}^{\mathrm{miss}}$, and a cut at 4.0 is applied. The black points are data, and the stacked histograms are from simulated events. The red overlayed histogram represents the shape from simulated $Z \to \nu\bar{\nu}$ events, normalized to the yield in data.

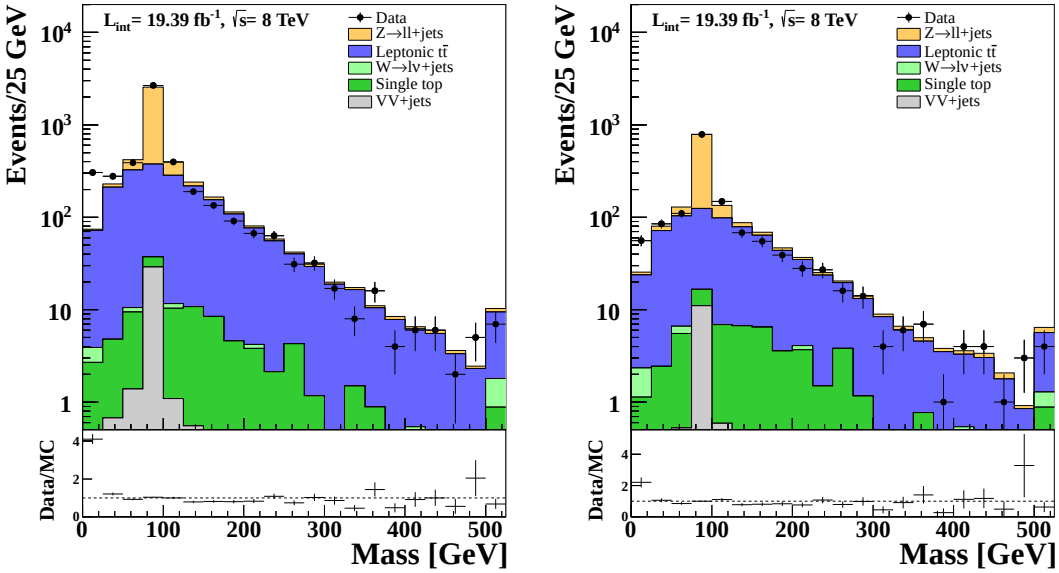

(a) Only control sample cuts applied.

(b) Modified cuts on $E_{\mathrm{T}}^{\mathrm{miss}}$ and $\Delta\phi_N^{\mathrm{min}}$ included.

Figure 5.59: Distribution of the mass of charged lepton pairs before and after modifying the $E_{\mathrm{T}}^{\mathrm{miss}}$ and $\Delta\phi_N^{\mathrm{min}}$ quantities by the lepton momenta in the $Z \to l^+l^-$ dilepton control sample. The black points are data, and the stacked histograms are from simulated events.

5.6.3 Method for correcting predicted yields

The previous subsection describes the method used to obtain a good description of the $Z \to \nu\bar{\nu}$ $E_{\mathrm{T}}^{\mathrm{miss}}$ shape from data for two ranges of H_{T} and a loose CSV requirement. This subsection describes how the yields in data from $Z \to l^+l^-$ events are adjusted to represent the yields of $Z \to \nu\bar{\nu}$ events. The equation below shows how the yields of $Z \to \nu\bar{\nu}$ in bins of b-tag multiplicity (Nb) are obtained from other control samples ($Z \to l^+l^-$, QCD), with a loose b-tag selection ($1Lb$). For each H_{T} and $E_{\mathrm{T}}^{\mathrm{miss}}$ bin,

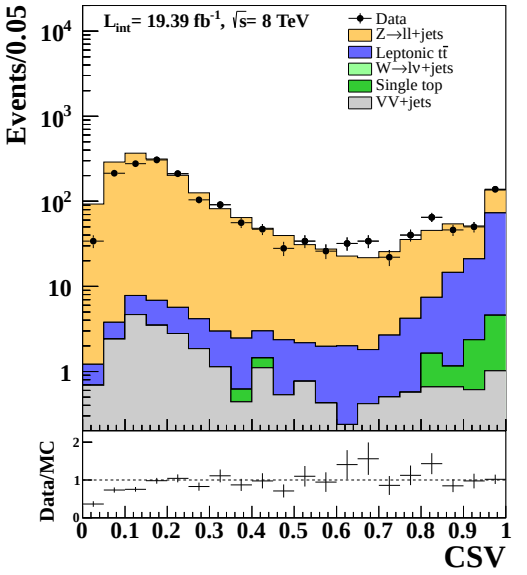

(a) Jet with highest CSV value.

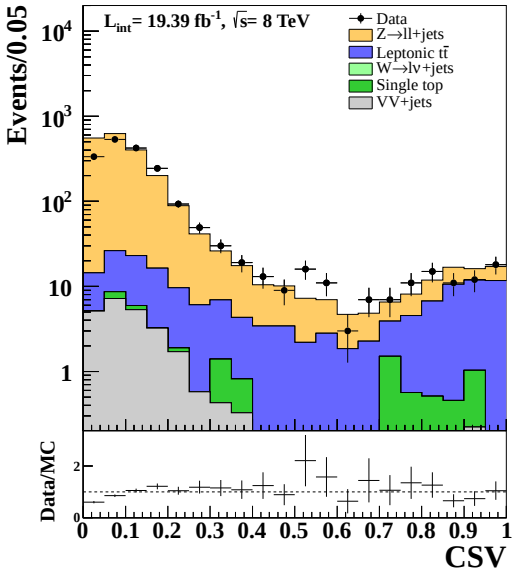

(b) Jet with second highest CSV value.

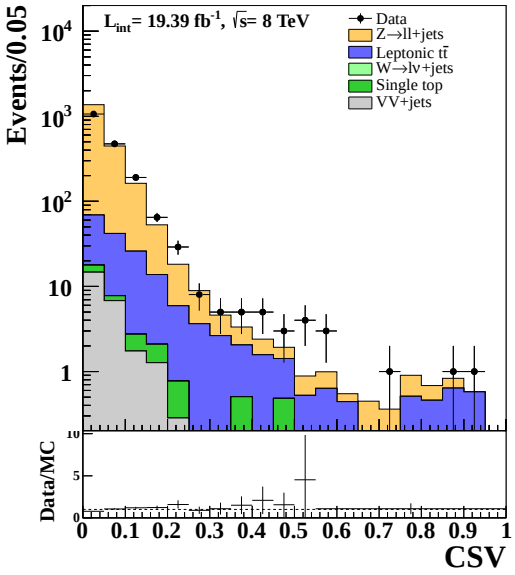

(c) Jet with third highest CSV value.

Figure 5.60: Distributions of CSV values for three jets with the highest CSV in a dilepton control sample event. The $E_{\mathrm{T}}^{\mathrm{miss}}$ and $\Delta\phi_N^{\mathrm{min}}$ quantities are modified by the lepton momenta, and cuts are placed on these values. The black points are data, and the stacked histograms are from simulated events.

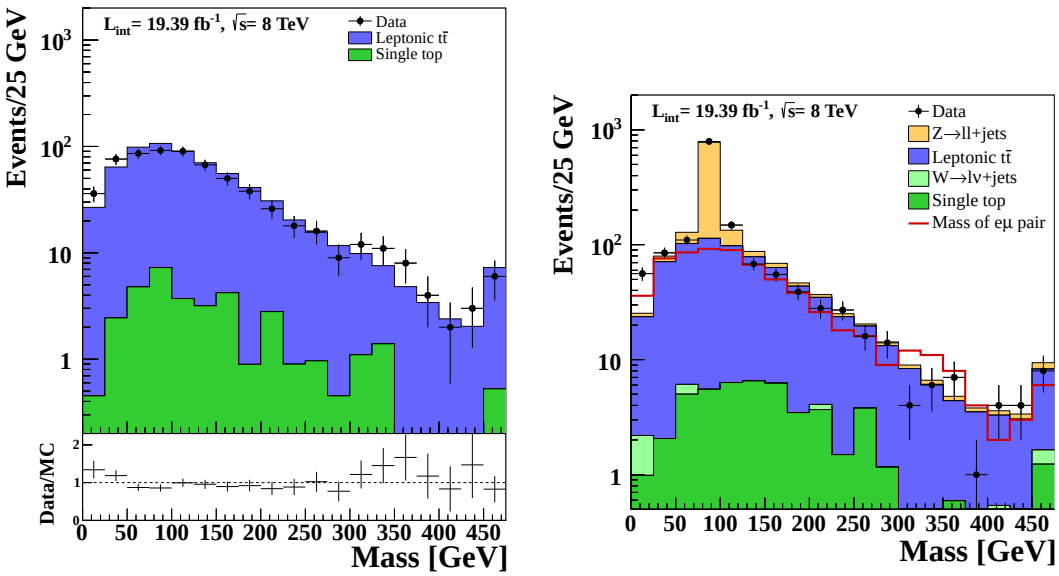

(a) Mass of $e\mu$ pairs.

(b) Mass of lepton pairs with the same flavor.

Figure 5.61: Subtracting $t\bar{t}$ contamination. Distribution of $e\mu$ pairs in data (left) is used to obtain the shape of the dilepton mass in $t\bar{t}$ events, which is compared with the $ee/\mu\mu$ sample (right). The black points are data, and the stacked histograms are from simulated events. The red overlayed histogram is the shape of $e\mu$ events in data from the left plot, normalized to the yield in the $Z \to l^+l^-$ control sample in data where $M_{l^+l^-}$ >110 GeV.

$$N^{DATA}(Z \to \nu\bar{\nu};\, CSVM) = N^{DATA}(Z \to l^+l^-;\, 1Lb) \times \frac{N^{MC}(Z \to \nu\bar{\nu};\, CSVM)}{N^{MC}(Z \to l^+l^-;\, CSVM)} \times \frac{N^{DATA}(QCD;\, CSVM)}{N^{DATA}(QCD;\, 1Lb)} \tag{5.9}$$

The events in the modified dilepton control sample have two ratios applied. One is purely from simulation comparing the rate of observed $Z \to l^+l^-$ with $Z \to \nu\bar{\nu}$, for which quantities such as branching fractions and detector acceptance are well known. The use of a ratio from simulation removes certain potential baises that might have been introduced by relying on simulated events. The other ratio is from a low $E_{\mathrm{T}}^{\mathrm{miss}}$ QCD-enriched control sample in data. This provides a relationship between the rate of one loose CSV tag and the rate of any other number of CSV medium tags.

Before we apply the corrections listed in Eq. 5.9, we reduce the effect of the presence of $t\bar{t}$ contamination in the $Z \to l^+l^-$ control sample. Since this method is based on the branching fractions of the Z boson, the presence of this contamination would cause predicted yields to be high. We use a data-driven method to estimate this contamination and subtract it from the yield in data to obtain the yield of $Z \to l^+l^-$ events. We begin with a sample of dilepton events from the analysis sample with exactly one muon and one electron with p_{T} greater than 17 GeV. The mass spectrum of these leptons are shown in Fig. 5.61. As expected, this sample is vastly dominated by $t\bar{t}$, and the shape is identical to the mass spectrum in $t\bar{t}$ in which the two leptons have the same flavor. This shape in data is normalized to the $Z \to l^+l^-$ control sample for $M_{l^+l^-}$ >110 GeV. The normalization

Table 5.32: Observed and predicted yields in the Z mass window from data and MC. Events have a loose CSV selection and are binned in H_{T} and $E_{\mathrm{T}}^{\mathrm{miss}}$.

H_{T}	400 – 800 GeV			$>$ 800 GeV		
$E_{\mathrm{T}}^{\mathrm{miss}}$	150 – 250 GeV	250 – 350 GeV	$>$ 350 GeV	150 – 250 GeV	250 – 350 GeV	$>$ 350 GeV
Obs. $ee/\mu\mu$	446	203	104	36	25	21
Obs. $e\mu$	52	38	9	1	4	3
Pred. $Z \to l^+l^-$	390 $\pm$ 23	162 $\pm$ 16	94 $\pm$ 11	34.9 $\pm$ 6.1	20.7 $\pm$ 5.5	17.7 $\pm$ 5.0
MC $Z \to l^+l^-$	371.2 $\pm$ 3.4	161.3 $\pm$ 2.2	84.9 $\pm$ 1.5	30.60 $\pm$ 0.91	19.6 $\pm$ 0.73	21.9 $\pm$ 0.77

Table 5.33: Simulation-based ratios relating the number of expected dimuon and dielectron events in the control sample to the corresponding number of $Z \to \nu\bar{\nu}$ events.

$400 < H_{\mathrm{T}} < 800$ GeV	5.185 ± 0.022
$H_{\mathrm{T}} > 800$ GeV	5.048 ± 0.059

factor applied to the $e\mu$ control sample is 1.085 ± 0.083. As a result, we obtain the number of $t\bar{t}$ events expected in the Z mass window between 76.2 and 106.2 GeV. The number of $Z \to l^+l^-$ events expected in each H_{T} bin for three ranges of $E_{\mathrm{T}}^{\mathrm{miss}}$ are shown in Table 5.32, along with the expected yield from simulation.

As mentioned above, the yield of $Z \to l^+l^-$ events in the control sample will not be equal to the number of $Z \to \nu\bar{\nu}$ events in the analysis sample for several reasons. First, the branching fractions for the two processes are dramatically different, with neutrino decay products occurring 20% of the time, and electron or muon decay products occuring 6% of the time. The yield of events in the control sample is further reduced by selection criteria imposed on the observed leptons. They must travel within the geometric acceptance of the detector, and pass minimum quality requirements. As a result, the control sample must represent a significantly larger yield, which is not desirable for obtaining a predicted yield. In other words, the statistical power of the control sample is less than the background present in the analysis. However, because $Z \to \nu\bar{\nu}$ is not a large background in this analysis, there are few other ways to model the $Z \to \nu\bar{\nu}$ background simply, and systematic uncertainties in this background prediction are minimized due to the use of data-driven techniques, the large scale factor is applied. Simulated events accurately model many quantities including

Table 5.34: Ratios of the number events with CSVM b-tagged jets divided by the number of events with at least one loose b-tagged jet. Yields are taken from events in the lepton-vetoed, low $E_{\mathrm{T}}^{\mathrm{miss}}$ (50 – 100 GeV) control sample from the prescaled dataset.

	1 CSVM b-tag	2 CSVM b-tags	$\geq$3 CSVM btags
Data, $E_{\mathrm{T}}^{\mathrm{miss}}$ 50–100 GeV	0.347 $\pm$ 0.011	0.0509 $\pm$ 0.0038	0.00274 $\pm$ 0.00087
QCD MC, $E_{\mathrm{T}}^{\mathrm{miss}}$ 50–100 GeV	0.342 $\pm$ 0.003	0.0498 $\pm$ 0.0012	0.00288 $\pm$ 0.00028
$Z \to \nu\bar{\nu}$ MC			
$E_{\mathrm{T}}^{\mathrm{miss}}$ 150–250 GeV	0.361	0.0485	0.00202
$E_{\mathrm{T}}^{\mathrm{miss}}$ 250–350 GeV	0.360	0.0463	0.00197
$E_{\mathrm{T}}^{\mathrm{miss}} > 350$ GeV	0.365	0.0415	0.00180

branching fractions and detector acceptance, therefore, a scale factor from the ratio of simulated yields with a large number of events is used to translate the yield of observed dilepton events into the yield of $Z \to \nu\bar{\nu}$. The yields in data are scaled according to its H_{T} bin, as listed in Table 5.33 .

To determine the yield of $Z \to \nu\bar{\nu}$ events in each b-tag multiplicity bin, we again make use of a control sample from data. We expect the rate of true and misidentified b-jets to be the same as for purely QCD events. Therefore, we use the QCD-enriched prescaled data control sample described in Sec. 5.5, in which the $E_{\mathrm{T}}^{\mathrm{miss}}$ is restricted to the range between 50 and 100 GeV. The selection criteria includes electron and muon vetoes, and all jet-based cuts. From this sample, we calculate the yield of each b-tag multiplicity, divided by the number of events having at least one CSV loose b-tag. Since this ratio does not depend on H_{T} or $E_{\mathrm{T}}^{\mathrm{miss}}$, the same value is used for all bins, which has the benefit of utilizing

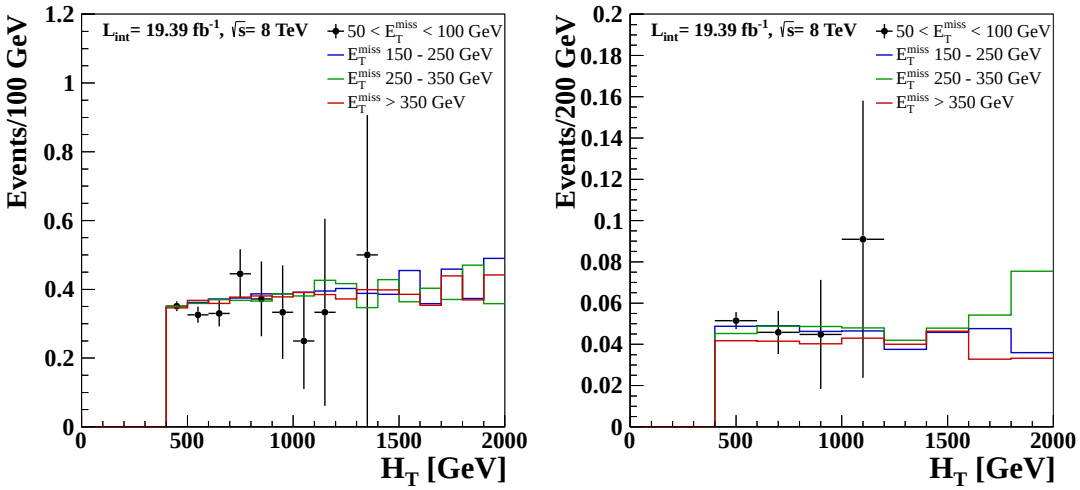

(a) Rate of =1 CSVM b-tag

(b) Rate of =2 CSVM b-tags

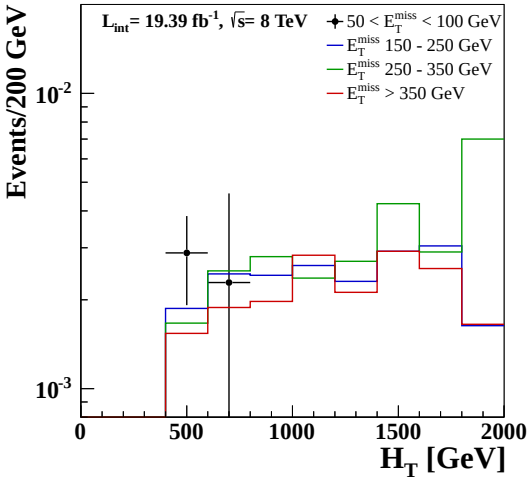

(c) Rate of $\geq$3 CSVM b-tags

Figure 5.62: Ratio of events with CSVM b-tagged jets with respect to events with at least one loose b-tagged jet, separated by H_{T} and $E_{\mathrm{T}}^{\mathrm{miss}}$. Black points with error bars are data from the lepton-vetoed, low $E_{\mathrm{T}}^{\mathrm{miss}}$ side-band (50 – 100 GeV). Colored lines are $Z \rightarrow \nu\bar{\nu}$ simulated events from the lepton-vetoed analysis sample, for three different $E_{\mathrm{T}}^{\mathrm{miss}}$ ranges.

the full statistical power of the prescaled control sample. The H_{T} and $E_{\mathrm{T}}^{\mathrm{miss}}$ dependence of this ratio is shown in Figure 5.62. For each b-tag multiplicity, the ratio from data is constant with respect to H_{T}. Furthermore, it is consistent with the ratios obtained from $Z \to \nu\bar{\nu}$ simulated events in the high $E_{\mathrm{T}}^{\mathrm{miss}}$ analysis sample. The simulated events are further separated according to $E_{\mathrm{T}}^{\mathrm{miss}}$, and all regions are consistent with each other and the observation in data in the low $E_{\mathrm{T}}^{\mathrm{miss}}$ sideband. This conclusion is shown quantitatively in Table 5.34. Since the data sample at low $E_{\mathrm{T}}^{\mathrm{miss}}$ is vastly dominated by QCD events, we expect the ratio obtained from data to be very close to the ratio calculated from QCD in the low $E_{\mathrm{T}}^{\mathrm{miss}}$ sideband. The table shows that the two samples agree within statistical uncertainty. In addition, the ratios from simulated $Z \to \nu\bar{\nu}$ events in the analysis sample, which are the ratios we are trying to model in data, are close to our observations. These three ratios representing the rate of one, two, or $\geq$3 CSVM b-tagged jets are applied to the control sample to obtain the predicted $Z \to \nu\bar{\nu}$ $E_{\mathrm{T}}^{\mathrm{miss}}$ spectrum in bins of b-tag multiplicity.

While the low $E_{\mathrm{T}}^{\mathrm{miss}}$ control sample has effectively the same CSVM b-tag rate as the high $E_{\mathrm{T}}^{\mathrm{miss}}$ $Z \to \nu\bar{\nu}$ sample, there are additional checks that can be performed with simulated events to build confidence in the flavor composition of QCD events. For each event in the low $E_{\mathrm{T}}^{\mathrm{miss}}$ control sample, the jet with the highest CSV value is selected. These jets are sorted according to the flavor of the corresponding parton at generator-level, either b, c, or everything else (*light flavor*). From these three flavor categories, three CSV shape templates are created. The relative contributions of each are fit to the distribution of the CSV of the highest valued jet in the low $E_{\mathrm{T}}^{\mathrm{miss}}$ data control sample. The fit range is restricted

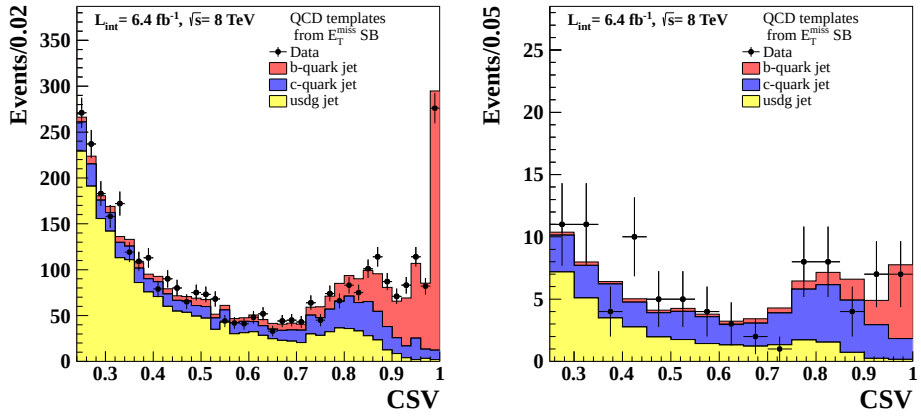

(a) $400 < H_T < 800$ GeV (b) $H_T > 800$ GeV

Figure 5.63: Distribution of CSV for the jet with the highest value in each event, showing the fit of jet flavor templates from simulated QCD events to data. Black points are data from the lepton-vetoed, low E_T^{miss} (50–100 GeV) control sample. Stacked, colored histograms are simulated QCD events from the low E_T^{miss} control sample, representing the parton associated with the jet. The normalization of each colored histogram is determined from a fit to the data.

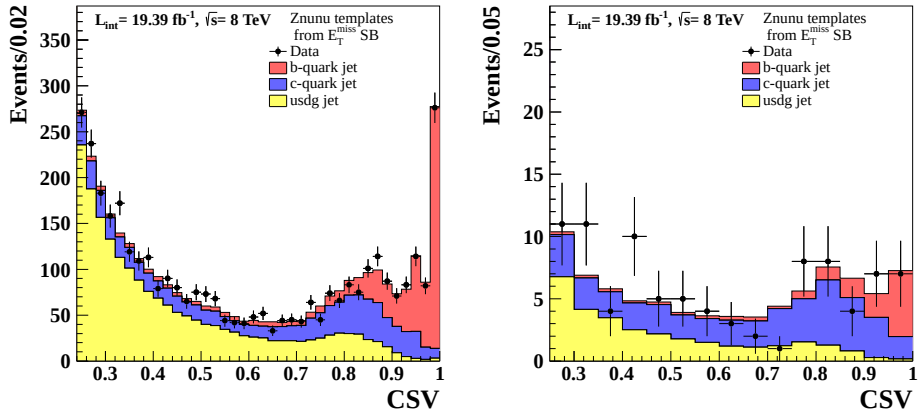

(a) $400 < H_T < 800$ GeV (b) $H_T > 800$ GeV

Figure 5.64: Distribution of CSV for the jet with the highest value in each event, showing the fit of jet flavor templates from simulated $Z \to \nu\bar{\nu}$ events to data. Black points are data from the lepton-vetoed, low E_T^{miss} (50–100 GeV) control sample. Stacked, colored histograms are simulated $Z \to \nu\bar{\nu}$ events from the low E_T^{miss} control sample, representing the parton associated with the jet. The normalization of each colored histogram is determined from a fit to the data.

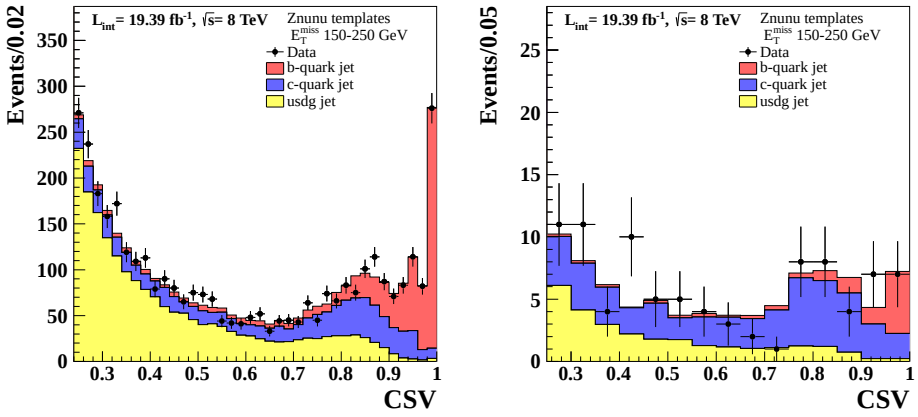

(a) $400 < H_{\mathrm{T}} < 800$ GeV, $150 < E_{\mathrm{T}}^{\mathrm{miss}} < 250$ GeV

(b) $H_{\mathrm{T}} > 800$ GeV, $150 < E_{\mathrm{T}}^{\mathrm{miss}} < 250$ GeV

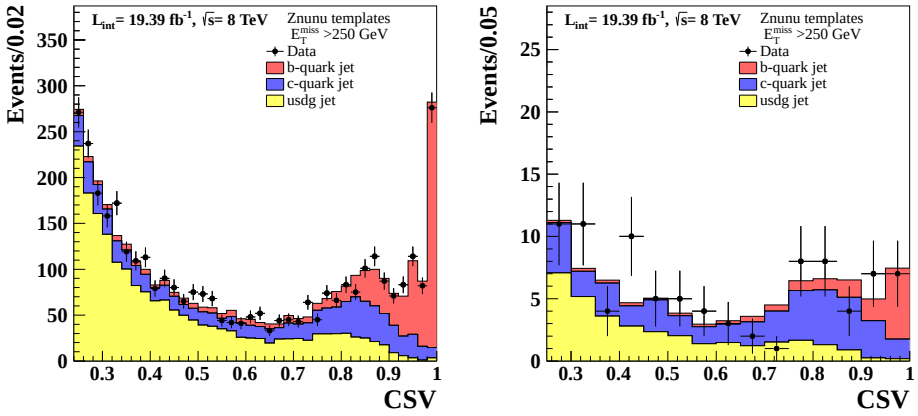

(c) $400 < H_{\mathrm{T}} < 800$ GeV, $E_{\mathrm{T}}^{\mathrm{miss}} > 250$ GeV

(d) $H_{\mathrm{T}} > 800$ GeV, $E_{\mathrm{T}}^{\mathrm{miss}} > 250$ GeV

Figure 5.65: Distribution of CSV for the jet with the highest value in each event, showing the fit of jet flavor templates from simulated $Z \to \nu\bar{\nu}$ events to data. Black points are data from the lepton-vetoed, low $E_{\mathrm{T}}^{\mathrm{miss}}$ (50–100 GeV) control sample. Stacked, colored histograms are simulated $Z \to \nu\bar{\nu}$ events from different regions in $E_{\mathrm{T}}^{\mathrm{miss}}$, representing the parton associated with the jet. The normalization of each colored histogram is determined from a fit to the data.

Table 5.35: Fitted fraction of the total yield, with at least one jet with CSV>0.244, according to the flavor of the jet with the highest CSV value. Each row is the result of a fit of templates from QCD or $Z \to \nu\bar{\nu}$ simulated events to the lepton-vetoed, low $E_{\mathrm{T}}^{\mathrm{miss}}$ control sample in data. The statistical uncertainty shown is dominated by the statistics of the data sample.

Sample	MET range [GeV]	light flavor	c-quark	b-quark
$400<H_{\mathrm{T}}<800$ GeV				
QCD	50 – 100	0.577 ± 0.019	0.172 ± 0.021	0.251 ± 0.012
$Z \to \nu\bar{\nu}$	50 – 100	0.555 ± 0.019	0.225 ± 0.021	0.220 ± 0.011
$Z \to \nu\bar{\nu}$	150 – 250	0.559 ± 0.018	0.219 ± 0.020	0.223 ± 0.011
$Z \to \nu\bar{\nu}$	>250	0.560 ± 0.019	0.208 ± 0.021	0.233 ± 0.012
$H_{\mathrm{T}}>800$ GeV				
QCD	50 – 100	0.42 ± 0.14	0.45 ± 0.18	0.130 ± 0.069
$Z \to \nu\bar{\nu}$	50 – 100	0.41 ± 0.15	0.46 ± 0.18	0.128 ± 0.072
$Z \to \nu\bar{\nu}$	150 – 250	0.37 ± 0.13	0.52 ± 0.17	0.107 ± 0.063
$Z \to \nu\bar{\nu}$	>250	0.45 ± 0.14	0.42 ± 0.17	0.131 ± 0.070

to events used in the control sample, with a CSV value greater than 0.244. Figure 5.63 shows flavor templates taken from simulated QCD events in the low $E_{\mathrm{T}}^{\mathrm{miss}}$ region, fitted to the data. These shapes describe well the observations from data. This is expected since the data represents a very pure QCD sample, and the composition determined from the fit is close to the flavor composition in QCD simulation. Next, flavor templates obtained from simulated $Z \to \nu\bar{\nu}$ events are fit to the data in the low $E_{\mathrm{T}}^{\mathrm{miss}}$ region. Figures 5.64 and 5.65 show these fits for three different $E_{\mathrm{T}}^{\mathrm{miss}}$ regions, the low $E_{\mathrm{T}}^{\mathrm{miss}}$ sideband 50 – 100 GeV, the validation region of the analysis sample 150 – 250 GeV, and the signal region >250 GeV. As in Fig. 5.63, the contribution due to jets associated with a c-quark is larger in the high H_{T} events than at low H_{T}. As expected, the shapes of each flavor template are very similar between QCD and $Z \to \nu\bar{\nu}$, even across $E_{\mathrm{T}}^{\mathrm{miss}}$ bins, indicating that the probability of a jet having a b-tag depends on the flavor of the parton, and mostly uncorrelated with $E_{\mathrm{T}}^{\mathrm{miss}}$.

Table 5.35 shows the fractional yields for each jet flavor from QCD and $Z \to \nu\bar{\nu}$ simulated events, after being fitted to data in the $E_{\mathrm{T}}^{\mathrm{miss}}$ sideband, for low and high H_{T} respectively. The results are consistent between the simulated samples, and across all $Z \to \nu\bar{\nu}$ $E_{\mathrm{T}}^{\mathrm{miss}}$ bins. Any deviations observed are negligible and do not effect the $Z \to \nu\bar{\nu}$ prediction.

The trigger efficiency for the dilepton control samples (listed in Table 5.30) is calculated from the *JetHT* dataset constructed from hadronic triggers. Dielectron and dimuon events in the Z mass window are selected, using the standard lepton quality criteria. The efficiency of the dielectron and dimuon triggers with respect to the p_{T} of the sub-leading

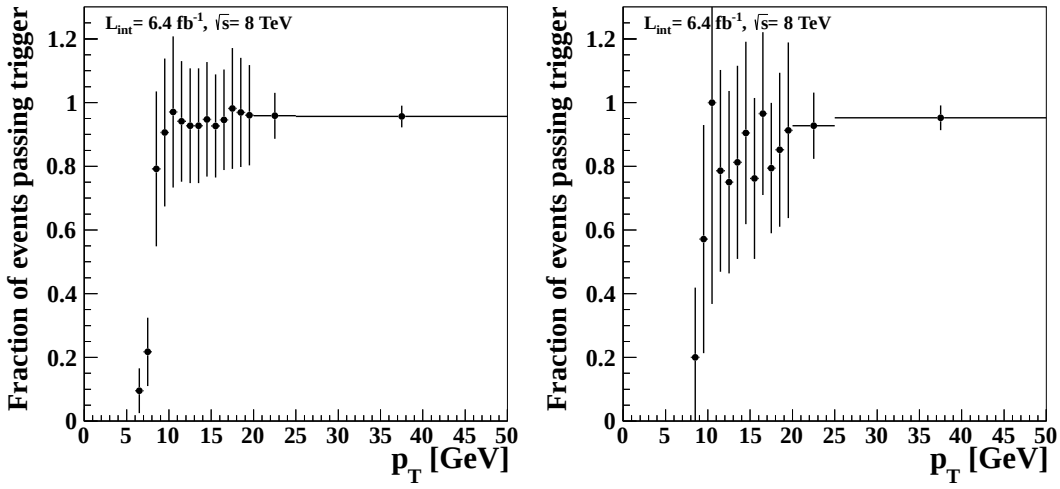

(a) Efficiency of $\mu\mu$ triggers.

(b) Efficiency of ee trigger.

Figure 5.66: Efficiency of dilepton triggers (listed in Table 5.30) with respect to the p_{T} of the sub-leading lepton. All events pass an H_{T}-based trigger, have a leading lepton with p_{T} >17 GeV, and dilepton mass 76.2< M_{ll} <106.2 GeV.

Table 5.36: Efficiencies, ϵ, of the dimuon and dielectron triggers. They are combined according to the proportion of flavors present in the Z mass window 76.2< M_{ll} <106.2 GeV.

	$\mu\mu$	ee
Dilepton ϵ	0.958±0.020	0.957±0.023
Ratio $\mu\mu/ee$	1.145 ± 0.044	
Combined ϵ	0.958 ± 0.015	

lepton are shown in Fig. 5.66, where the leading lepton p_{T} is greater than 17 GeV. The efficiency of the combined sample is shown in Table 5.36. Predicted yields are corrected for this effect.

As an additional check on the procedure of extrapolating the CSVM b-tag multiplicity yields from the QCD enriched control sample, we remove the simulation-based scale factor from the procedure. This results in predicted yields for $Z \to l^+l^-$ in each $E_{\mathrm{T}}^{\mathrm{miss}}$, H_{T}, and b-tag multiplicity bin, shown in Table 5.38. As expected, the yields from simulated events are close to the predictions from data, but consistently slightly higher.

5.6.4 Evaluation of systematic uncertainties

There are a limited number of sources of bias in the $Z \to \nu\bar{\nu}$ measurement. The potential effects of many sources of systematic uncertainty are reduced by using values of $E_{\mathrm{T}}^{\mathrm{miss}}$ and lepton p_{T} directly from data, and introducing corrections from simulation only as a ratio of yields. Table 5.39 shows the effect of the jet energy scale and resolution uncertainties. Varying the energy of jets in simulated $Z \to l^+l^-$ and $Z \to \nu\bar{\nu}$ events changes the simulation-based scale factor. As expected, this effect is very small, under 4%. Other sources of systematic uncertainty are negligible, and the effect of the uncertainty in the jet flavor composition in the low $E_{\mathrm{T}}^{\mathrm{miss}}$ control sample is addressed in the previous subsection.

In the $Z \to \nu\bar{\nu}$ method, the most important effect to consider is the somewhat arbitrary choice of the loose b-tag selection at a CSV value of 0.244. Especially in the less populated signal regions, choosing a higher or lower threshold could significantly change the result. Table 5.40 lists the percent difference with respect to the nominal selection

Table 5.37: Predicted yields of $Z \to \nu\bar{\nu}$ events from data and simulation, binned in H_{T}, $E_{\mathrm{T}}^{\mathrm{miss}}$, and b-tag multiplicity. Uncertainties are statistical, and include the statistical uncertainty on the scale factor from simulation.

H_{T}	400 - 800 GeV			$>$ 800 GeV		
$E_{\mathrm{T}}^{\mathrm{miss}}$	150 - 250 GeV	250 - 350 GeV	$>$ 350 GeV	150 - 250 GeV	250 350 GeV	$>$ 350 GeV
Prediction from data						
=1 b-tag	723 $\pm$ 50	304 $\pm$ 32	177 $\pm$ 21	64 $\pm$ 11	38 $\pm$ 12	32.4 $\pm$ 9.0
=2 b-tags	106 $\pm$ 11	44.6 $\pm$ 5.6	26.0 $\pm$ 3.6	9.4 $\pm$ 1.8	5.5 $\pm$ 1.6	4.8 $\pm$ 1.3
$\geq$3 b-tags	5.7 $\pm$ 1.9	2.40 $\pm$ 0.79	1.40 $\pm$ 0.47	0.50 $\pm$ 0.18	0.30 $\pm$ 0.12	0.26 $\pm$ 0.10
$Z \to \nu\bar{\nu}$ MC						
=1 b-tag	665.5 $\pm$ 2.3	253.2 $\pm$ 1.4	126.4 $\pm$ 0.9	63.27 $\pm$ 0.59	33.18 $\pm$ 0.43	37.36 $\pm$ 0.45
=2 b-tags	90.69 $\pm$ 0.91	32.63 $\pm$ 0.51	14.60 $\pm$ 0.32	7.397 $\pm$ 0.19	4.19 $\pm$ 0.15	4.01 $\pm$ 0.14
$\geq$3 b-tags	3.690 $\pm$ 0.086	1.326 $\pm$ 0.053	0.587 $\pm$ 0.042	0.400 $\pm$ 0.025	0.240 $\pm$ 0.020	0.219 $\pm$ 0.020

Table 5.38: Predicted yields of $Z \to l^+l^-$ events from data and simulation, binned in H_{T}, $E_{\mathrm{T}}^{\mathrm{miss}}$, and b-tag multiplicity. Uncertainties are statistical, and include the statistical uncertainty on the scale factor from simulation.

H_{T}	400 - 800 GeV			$>$ 800 GeV		
$E_{\mathrm{T}}^{\mathrm{miss}}$	150 - 250 GeV	250 - 350 GeV	$>$ 350 GeV	150 - 250 GeV	250 350 GeV	$>$ 350 GeV
Prediction from data						
=1 b-tag	141.1 $\pm$ 9.8	58.6 $\pm$ 6.2	34.1 $\pm$ 4.1	12.64 $\pm$ 2.3	7.5 $\pm$ 2.0	6.4 $\pm$ 1.8
=2 b-tags	20.7 $\pm$ 2.0	8.6 $\pm$ 1.1	5.01 $\pm$ 0.68	1.86 $\pm$ 0.36	1.10 $\pm$ 0.30	0.94 $\pm$ 0.25
$\geq$3 b-tags	1.11 $\pm$ 0.35	0.46 $\pm$ 0.16	0.27 $\pm$ 0.09	0.100 $\pm$ 0.035	0.059 $\pm$ 0.024	0.051 $\pm$ 0.021
$Z \to l^+l^-$ MC						
=1 b-tag	120.9 $\pm$ 1.1	51.62 $\pm$ 0.67	27.36 $\pm$ 0.45	10.78 $\pm$ 0.28	6.42 $\pm$ 0.22	7.31 $\pm$ 0.22
=2 b-tags	16.56 $\pm$ 0.40	6.06 $\pm$ 0.23	2.89 $\pm$ 0.14	1.23 $\pm$ 0.09	0.72 $\pm$ 0.07	0.76 $\pm$ 0.07
$\geq$3 b-tags	0.63 $\pm$ 0.04	0.23 $\pm$ 0.02	0.09 $\pm$ 0.01	0.06 $\pm$ 0.01	0.03 $\pm$ 0.01	0.04 $\pm$ 0.01

Table 5.39: Effect of jet energy uncertainties on the $Z \to \nu\bar{\nu}$ background predictions, calculated from simulated events.

	Jet energy scale	Jet energy resolution
$400<H_{\mathrm{T}}<800$ GeV	± 3.3	± 1.7
$H_{\mathrm{T}}>800$ GeV	± 2.8	± 0.3

Table 5.40: Effect of different definitions of the loose CSV selection on the final result in data.

	Increase to 0.344	Decrease to 0.144
$400<H_{\mathrm{T}}<800$ GeV		
$150<E_{\mathrm{T}}^{\mathrm{miss}}<250$ GeV	+2%	+13%
$250<E_{\mathrm{T}}^{\mathrm{miss}}<350$ GeV	-3%	+8%
$E_{\mathrm{T}}^{\mathrm{miss}}>350$	+8%	+4%
$H_{\mathrm{T}}>800$ GeV		
$150<E_{\mathrm{T}}^{\mathrm{miss}}<250$ GeV	-5%	+2%
$250<E_{\mathrm{T}}^{\mathrm{miss}}<350$ GeV	-1%	+22%
$E_{\mathrm{T}}^{\mathrm{miss}}>350$ GeV	+0.1%	-0.7%

Table 5.41: Effect of different definitions of the loose CSV selection on simulated events.

H_T range [GeV]	E_T^{miss} range [GeV]	Increase to 0.344	Decrease to 0.144
400<H_T <800 GeV			
150<E_T^{miss} <250 GeV		-7%	+11%
250<E_T^{miss} <350 GeV		-8%	+11%
E_T^{miss} >350 GeV		-7%	+10%
H_T >800 GeV			
150<E_T^{miss} <250 GeV		-2%	+7%
250<E_T^{miss} <350 GeV		-5%	+3%
E_T^{miss} >350 GeV		-3%	+9%

of thresholds at 0.144 and 0.344, binned in H_T and E_T^{miss} regions. Here, there are several competing effects. Both the observed $Z \to l^+l^-$ and opposite flavor dilepton control samples increase or decrease as expected as a result of the loosening or tightening the cut. However, the ratio of CSVM multiplicity with respect to the loose selection in the low E_T^{miss} control sample is inversely correlated with the dilepton yield. These effects partially cancel, and the result is sensitive to the statistical fluctuations in any of the samples. For the most part the result is within 10% of the nominal selection criteria, except for the high H_T region where 250<E_T^{miss} <350 GeV, where it is unexpectedly large.

For a measurement of the potential effect of changing the loose b-tag selection without sensitivity to the particular statistical limitations of this dataset, we perform the

Table 5.42: Predicted yields from $Z \to \nu\bar{\nu}$ events for each signal region. The first uncertainty is statistical, and the second is from systematic sources.

		250<$E_{\mathrm{T}}^{\mathrm{miss}}$ <350 GeV	$E_{\mathrm{T}}^{\mathrm{miss}}$ >350 GeV
400<H_{T} <800 GeV	=2 b-tags	44.6 ± 5.6 ± 5.1	26.0 ± 3.6 ± 2.8
	≥3 b-tags	2.40 ± 0.79 ± 0.3	1.40 ± 0.47 ± 0.15
H_{T} >800 GeV	=2 b-tags	5.5 ± 1.6 ± 0.3	4.8 ± 1.3 ± 0.4
	≥3 b-tags	0.30 ± 0.12 ± 0.02	0.26 ± 0.10 ± 0.02

same study on simulated events. The results are shown in Table 5.41 using simulated $Z \to l^+l^-$ events, and simulated QCD events for the low $E_{\mathrm{T}}^{\mathrm{miss}}$ control sample. Since positive and negative variations are similar, the larger of the two is applied to the predicted $Z \to \nu\bar{\nu}$ yields from data for each signal region.

5.6.5 Results

The yield of $Z \to \nu\bar{\nu}$ events in the signal regions are predicted from control samples in data. Along with their associated statistical and systematic uncertainties, they are listed in Table 5.42. In the regions with larger yields, the systematic uncertainty from jet p_{T} measurement and choice of CSV threshold for the control samples is comparable to the statistical uncertainty. The shape of the predicted $E_{\mathrm{T}}^{\mathrm{miss}}$ for these events is compared with simulation in Fig. 5.67. The shape is the same within each H_{T} bin, but with different normalizations due to the data- and simulation-based scale factors. Simulated events have a very similar shape to these results, but having a slightly lower yield in the lower H_{T} region, especially at high b-tag multiplicity. The method of treating the p_{T} of electrons and

muons in dilepton $Z \to l^+l^-$ events as missing transverse energy successfully reproduces the $E_{\mathrm{T}}^{\mathrm{miss}}$ shape of $Z \to \nu\bar{\nu}$ events and is included in the data-driven prediction of background yields in this analysis.

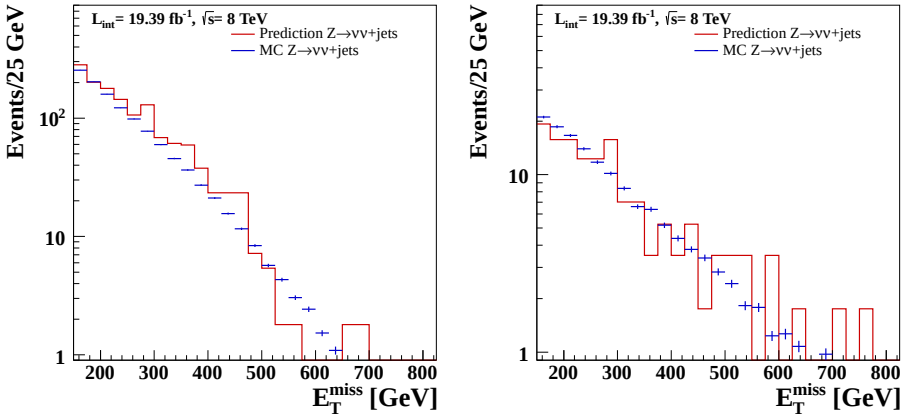

(a) 400<H_T <800 GeV, =1 b-tag (b) H_T >800 GeV, =1 b-tag

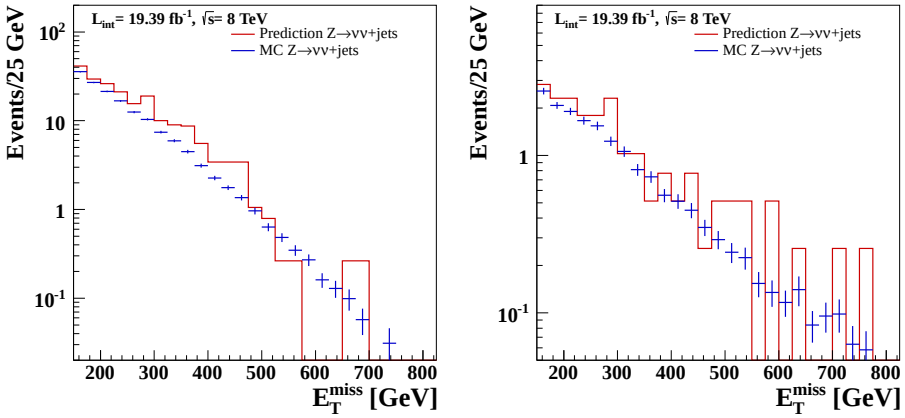

(c) 400<H_T <800 GeV, =2 b-tags (d) H_T >800 GeV, =2 b-tags

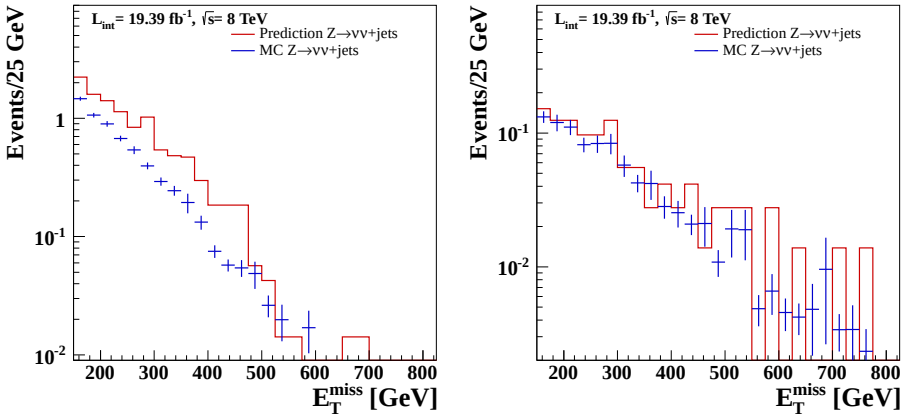

(e) 400<H_T <800 GeV, ≥3 b-tags (f) H_T >800 GeV, ≥3 b-tags

Figure 5.67: Predicted $E_{\mathrm{T}}^{\mathrm{miss}}$ spectrum of $Z \to \nu\bar{\nu}$ events. Solid red line is the data-driven prediction based on the modified $E_{\mathrm{T}}^{\mathrm{miss}}$ in the dilepton control sample. Blue points with error bars represent simulated events.

Chapter 6

Results and Interpretation

This chapter discusses how data-driven predictions of the Standard Model backgrounds compare with the observed data in this analysis. In the absence of unexplained excesses in any of the signal regions, the results are used to exclude regions of the T1bbbb parameter space.

6.1 Predictions of Standard Model processes

As discussed in Ch. 5, the data-driven methods used to predict the yields of Standard Model backgrounds in this analysis provide results at low $E_{\mathrm{T}}^{\mathrm{miss}}$ (150–250 GeV) and b-tag multiplicity (=1 b-tag). In both of these regions, any signal from supersymmetry is expected to be completely overwhelmed by Standard Model processes. Therefore, they provide validation samples in which the performance of the data-driven methods can be compared with the observation in data. Table 6.1 shows the predicted yields for each back-

Table 6.1: Comparison of data with yields from data-driven predictions of Standard Model backgrounds in the $E_{\mathrm{T}}^{\mathrm{miss}}$ 150-250 GeV validation regions.

	$400 < H_{\mathrm{T}} < 800$ GeV		$H_{\mathrm{T}} > 800$ GeV	
	=2 b-tags	$\geq$3 b-tags	=2 b-tags	$\geq$3 b-tags
$t\bar{t}/W/t$	2029 ± 57 ± 36	208 ± 15 ± 5	140 ± 12 ± 2	19.6 ± 4.1 ± 0.7
QCD	1243 ± 94 ± 67	89.7 ± 8.7 ± 4.8	254 ± 59 ± 36	22.9 ± 6.1 ± 3.3
$Z \to \nu\bar{\nu}$	106 ± 11 ± 12	5.7 ± 1.9 ± 0.6	9.4 ± 1.8 ± 0.7	0.50 ± 0.18 ± 0.04
Total	3380 ± 110 ± 77	303 ± 17 ± 7	403 ± 60 ± 36	43.0 ± 7.4 ± 3.4
Data	3391	345	363	33

ground source in the low $E_{\mathrm{T}}^{\mathrm{miss}}$ region. As expected, QCD events have a much higher relative yield with respect to the other backgrounds than with a tighter $E_{\mathrm{T}}^{\mathrm{miss}}$ selection. The total predicted yield is compared with data across the H_{T} and b-tag multiplicity bins, and they are, for the most part, in good agreement. Table 6.2 lists the predicted yields with the =1 b-tag selection. Again, we expect good agreement between the total predicted background and the data. This is true, except for a rather large discrepancy at low $E_{\mathrm{T}}^{\mathrm{miss}}$ and low H_{T}, however, it is the only large deviation observed.

The predicted $E_{\mathrm{T}}^{\mathrm{miss}}$ distributions for these backgrounds are shown in Fig. 6.1. It shows the $E_{\mathrm{T}}^{\mathrm{miss}}$ spectrum of data in the analysis sample. The predicted $E_{\mathrm{T}}^{\mathrm{miss}}$ spectra from Standard Model processes is shown in the stacked, colored histogram in the same figure. The size and shape of each contribution is determined from data-driven techniques described in Ch. 5. The violet region is the $E_{\mathrm{T}}^{\mathrm{miss}}$ spectrum obtained from a dilepton control sample in

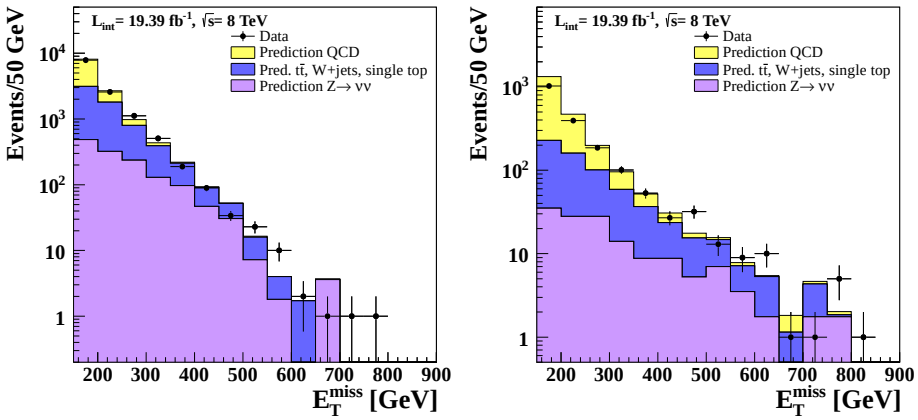

(a) 400<H_{T} <800 GeV, =1 b-tag

(b) H_{T} >800 GeV, =1 b-tag

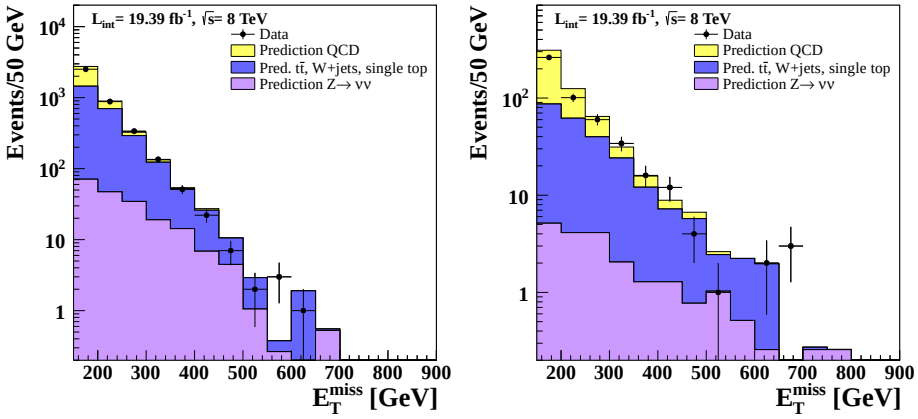

(c) 400<H_{T} <800 GeV, =2 b-tags

(d) H_{T} >800 GeV, =2 b-tags

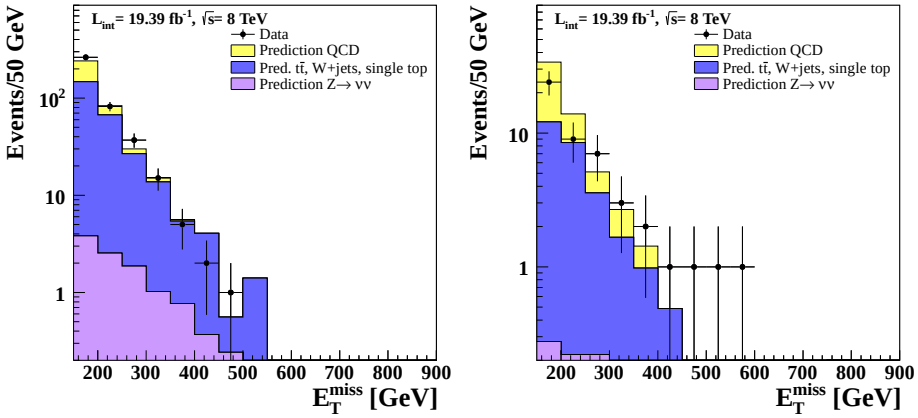

(e) 400<H_{T} <800 GeV, ≥3 b-tags

(f) H_{T} >800 GeV, ≥3 b-tags

Figure 6.1: Predicted $E_{\mathrm{T}}^{\mathrm{miss}}$ spectrum of Standard Model backgrounds. Black points with error bars indicate the analysis sample in data, with all selection criteria applied. The stacked, colored histogram indicates the shape of $E_{\mathrm{T}}^{\mathrm{miss}}$ derived from data-driven methods for $Z \to \nu\bar{\nu}$, $t\bar{t}/W/t$, and QCD processes.

Table 6.2: Comparison of data with yields from data-driven predictions of Standard Model backgrounds in the =1 b-tag validation regions.

H_{T}	400 – 800 GeV		> 800 GeV	
$E_{\mathrm{T}}^{\mathrm{miss}}$	250 – 350 GeV	> 350 GeV	250 – 350 GeV	> 350 GeV
$t\bar{t}/W/t$	821 ± 25 ± 13	193 ± 13 ± 3	118 ± 8 ± 4	72.2 ± 7.7 ± 2.4
QCD	194 ± 18 ± 10	7.2 ± 1.9 ± 0.4	124 ± 33 ± 18	23.0 ± 7.2 ± 3.3
$Z \to \nu\bar{\nu}$	304 ± 32 ± 35	177 ± 21 ± 13	38 ± 12 ± 2	32.4 ± 9.0 ± 3.0
Total	1319 ± 44 ± 39	377 ± 25 ± 13	280 ± 36 ± 19	128 ± 14 ± 5
Data	1624	350	287	153

data, described in Sec. 5.6. The blue region represents processes from $t\bar{t}$, W+jets, and single-top production, taken from a single lepton control sample upon which several techniques are employed to obtain the correct $E_{\mathrm{T}}^{\mathrm{miss}}$ shape, depending upon the decay product of the W boson. The yellow region is the $E_{\mathrm{T}}^{\mathrm{miss}}$ spectrum of a low $\Delta\phi_N^{\mathrm{min}}$ control sample, scaled according to a QCD-enriched low $E_{\mathrm{T}}^{\mathrm{miss}}$ sample, as described in Sec. 5.5.

As noted in the tables above, Fig. 6.1 shows the good agreement between the predictions in the validation regions and the observed data. Furthermore, one can determine visually if there are any anomalies that might indicate the presence of new physics in the sensitive regions. Figures 6.1(c) and (d) show no excess in the data with respect to the Standard Model background. When requiring at least 3 b-tagged jets, the same conclusion can be made regarding events at low H_{T} (Fig. 6.1(e)). However, at high H_{T}, Fig. 6.1(f), the high $E_{\mathrm{T}}^{\mathrm{miss}}$ tail contains approximately 4 events that were not modeled by the data-driven

background predictions. As discussed in Sec. 5.4, this may be due to an underprediction of the $t\bar{t}$ background, as the result of a fluctuation in the number of events in the single lepton control sample. We observe no pattern of unexplained excesses; this observation is also made in the published group result for a hadronic search with b-tags [13], and not seen in statistically independent searches.

Tables 6.3 and 6.4 list the predicted yields for each Standard Model background for each signal region. Despite a small excess observed in the high $E_{\mathrm{T}}^{\mathrm{miss}}$, $\geq$3 b-tags region, we conclude that there are no hints of supersymmetry signal. Therefore, we choose to set limits on the simple decay topology resulting from gluino pair production in the T1bbbb simplified model. The fluctuation in control sample events leading to an under-prediction in a sensitive signal region will reduce the scope of low cross-section processes that we are able to exclude.

Figure 6.2 shows the background predictions in a different way, showing the total yields of each signal region. The figure contains eight bins, corresponding to the eight signal regions of the analysis. From left to right, they are:

1. low H_{T} (400–800 GeV), low $E_{\mathrm{T}}^{\mathrm{miss}}$ (250 – 350 GeV), =2 b-tags
2. low H_{T}, low $E_{\mathrm{T}}^{\mathrm{miss}}$, $\geq$3 b-tags
3. low H_{T}, high $E_{\mathrm{T}}^{\mathrm{miss}}$ (>350 GeV), =2 b-tags
4. low H_{T}, high $E_{\mathrm{T}}^{\mathrm{miss}}$, $\geq$3 b-tags
5. high H_{T} (>800 GeV), low $E_{\mathrm{T}}^{\mathrm{miss}}$, =2 b-tags

Table 6.3: Data and estimated background yields in the =2 b-tags signal regions.

H_{T}	400 – 800 GeV		> 800 GeV	
$E_{\mathrm{T}}^{\mathrm{miss}}$	250 – 350 GeV	> 350 GeV	250 – 350 GeV	> 350 GeV
$t\bar{t}/W/t$	362 ± 17 ± 7	57.9 ± 7.4 ± 1.0	57.8 ± 6.1 ± 2.5	26.5 ± 4.2 ± 1.0
$Z \to \nu\bar{\nu}$	44.6 ± 5.6 ± 4.9	26.0 ± 3.6 ± 2.6	5.5 ± 1.6 ± 0.3	4.8 ± 1.3 ± 0.4
QCD	31.7 ± 4.4 ± 1.7	2.7 ± 1.0 ± 0.1	25.3 ± 6.9 ± 3.7	4.3 ± 1.9 ± 0.6
Total Pred.	438 ± 18 ± 9	86.6 ± 8.3 ± 2.8	88.6 ± 9.3 ± 4.5	35.6 ± 4.8 ± 1.2
Data	472	86	94	38

Table 6.4: Data and estimated background yields in the $\geq$3 b-tags signal regions.

H_{T}	400 – 800 GeV		$>$ 800 GeV	
$E_{\mathrm{T}}^{\mathrm{miss}}$	250 – 350 GeV	$>$ 350 GeV	250 – 350 GeV	$>$ 350 GeV
$t\bar{t}/W/t$	37.6 $\pm$ 4.9 $\pm$ 0.7	8.0 $\pm$ 3.1 $\pm$ 0.1	4.9 $\pm$ 1.6 $\pm$ 1.2	1.40 $\pm$ 0.67 $\pm$ 0.07
$Z \to \nu\bar{\nu}$	2.4 $\pm$ 0.8 $\pm$ 0.3	1.4 $\pm$ 0.5 $\pm$ 0.1	0.30 $\pm$ 0.12 $\pm$ 0.02	0.26 $\pm$ 0.10 $\pm$ 0.02
QCD	3.4 $\pm$ 1.2 $\pm$ 0.2	0.21 $\pm$ 0.26 $\pm$ 0.01	1.8 $\pm$ 0.8 $\pm$ 0.3	0.41 $\pm$ 0.33 $\pm$ 0.06
Total Pred.	43.4 $\pm$ 5.1 $\pm$ 0.8	9.6 $\pm$ 3.2 $\pm$ 0.1	7.0 $\pm$ 1.8 $\pm$ 1.2	2.07 $\pm$ 0.75 $\pm$ 0.09
Data	52	8	10	6

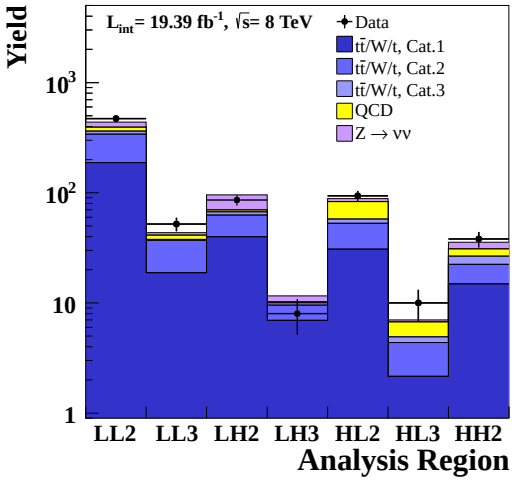

Figure 6.2: Data yields (black points with error bars) and data-driven predictions (colored, stacked histograms) for each signal region. The first four bins are the low H_{T} (400–800 GeV) region, with low (250–350 GeV, "LL") or high (>350 GeV, "LH")$E_{\mathrm{T}}^{\mathrm{miss}}$ range, with either =2 or ≥3 b-tags respectively. The last four bins have high H_{T} (>800 GeV) and either low ("HL") or high ("HH") $E_{\mathrm{T}}^{\mathrm{miss}}$ and either =2 or ≥3 b-tags.

6. high H_{T}, low $E_{\mathrm{T}}^{\mathrm{miss}}$, ≥3 b-tags

7. high H_{T}, high $E_{\mathrm{T}}^{\mathrm{miss}}$, =2 b-tags

8. high H_{T}, high $E_{\mathrm{T}}^{\mathrm{miss}}$, ≥3 b-tags

The stacked, colored histograms represent the components of the data-driven backgrounds, and the black points with error bars are the observed yield in data. The data is under-predicted in the "LL3" and "HH3" bins. Figure 6.3 includes the yield of the T1bbbb simplified model for two different choices of gluino and neutralino masses. The stacked red histogram is the yield from T1bbbb simulation, based on the cross-section for gluino production for that mass, and including all analysis selection criteria. As expected, the scenario with lower gluino mass is more spread throughout the signal bins, whereas the

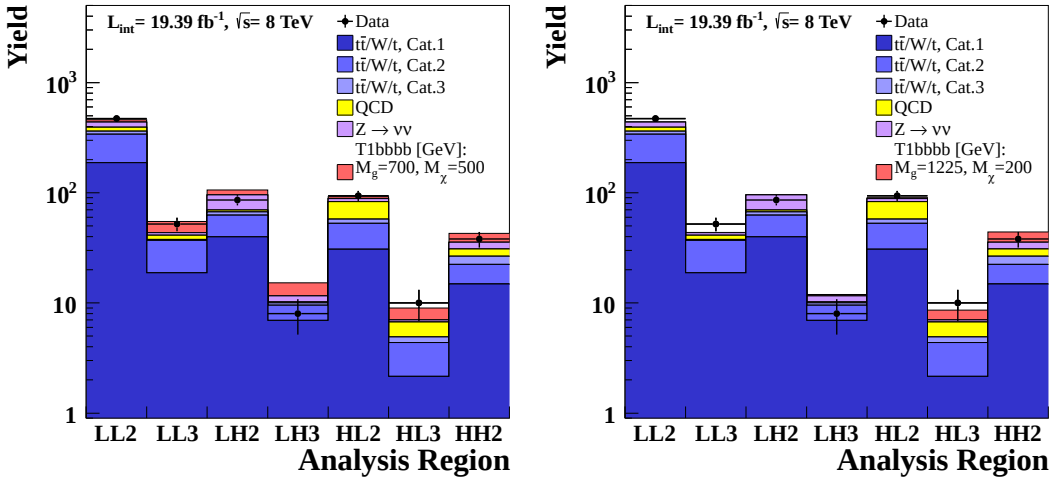

(a) $M_{\tilde{g}}$=700 GeV, $M_{\tilde{\chi}}$=500 GeV (b) $M_{\tilde{g}}$=1225 GeV, $M_{\tilde{\chi}}$=200 GeV

Figure 6.3: Data yields and data-driven predictions for each signal region, for two different T1bbbb scenarios. The first four bins are the low H_{T} (400–800 GeV) region, with low (250–350 GeV, "LL") or high (>350 GeV, "LH")$E_{\mathrm{T}}^{\mathrm{miss}}$ range, with either =2 or ≥3 b-tags respectively. The last four bins have high H_{T} (>800 GeV) and either low ("HL") or high ("HH") $E_{\mathrm{T}}^{\mathrm{miss}}$ and either =2 or ≥3 b-tags.

scenarios with higher gluino mass and high mass separation with respect to the neutralino are more concentrated at the highest kinematic regions. The additional yield from these T1bbbb scenarios are within reasonable deviations from the data. For this reason, these mass points are near the limits of the sensitivity of this analysis. The following section describes how this analysis evaluates the T1bbbb parameter space.

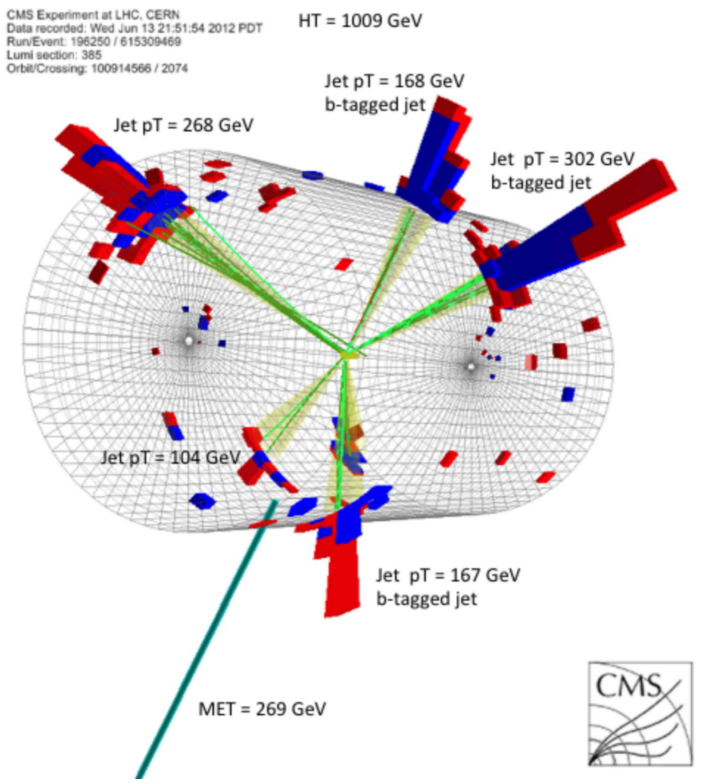

Figure 6.4: 3-dimensional visualization of an event from data in the signal region. Green lines are tracks from the tracker, and bars of blue and red demonstrate the amount of energy deposited in the ECAL and HCAL, respectively, according to its location in ϕ and z. Three of the jets pass the CSVM requirement, and there is large $E_{\mathrm{T}}^{\mathrm{miss}}$. [11]

6.2 Setting limits on the T1bbbb simplified model

Since this analysis targets the signature of b-quarks and dark matter candidates, the results are interpreted through the lens of a SMS T1bbbb decay, described in Sec. 2.2. To determine if a T1bbbb scenario is consistent with the data or not, we simultaneously fit all predicted backgrounds and potential signal, along with their respective uncertainties, to the observations in the six signal regions. This is done for a range of gluino and neutralino masses. The software to perform this complex task already exists, courtesy of the LHC Higgs Combination Group, which ensures that Higgs results from the CMS and ATLAS experiments follow the same statistical interpretation [33]. In order to calculate the significance of the Higgs discovery using several different decay channels, this analysis group created a tool to find the best fit to the data as a function of Higgs mass, and now provides documentation to allow other groups to use the software as well. The author uses this software for the limit-setting portion of the analysis, which is described below. It calculates the cross-section of each T1bbbb mass point that is excluded with 95% confidence, given the observations in data, the predicted backgrounds and their uncertainties, and the expected T1bbbb signal and its uncertainty.

There are eight channels which are being simultaneously fit to the observations in data. They are the eight signal regions defined by H_{T}, $E_{\mathrm{T}}^{\mathrm{miss}}$, and b-tag multiplicity bins. From the point of view of the fitter, there are 12 backgrounds which serve as inputs to fitting each channel. They are the five $\Delta\theta_T$ bins in the polarization method, four τ-jet bins (including dileptons), and one each for the e/μ dilepton, QCD, and $Z \to \nu\bar{\nu}$

backgrounds. The choice to separate the polarization method result into $\Delta\theta_T$ bins is to ensure the appropriate statistical uncertainty on the high $\Delta\theta_T$, low-yield portion of the single lepton control sample.

The uncertainties in the background predictions are included as nuisance parameters in the fit. Namely, the statsitical uncertainty on the size of the control samples used, the uncertainty on any scale factors applied, and additional systematic uncertainty. For the most part, the systematic uncertainties on any of the predictions, and even the simulated signal, are quite small. The exception is the uncertainty in the jet energy scale, which always has the largest effect in the resulting predictions. This uncertainty is included for the signal and each background, as determined from testing the effect on simulated events, and is fully correlated across all samples. (See relevent sections in Ch. 5.) The yields and systematic uncertainties on the T1bbbb signal across the gluino–neutralino mass plane are provided by collaborators. The nuisance parameters, their shapes, and their correlations are listed in Table 6.5.

The upper limits on the number of signal events are calculated using a modified frequentist method based on the prescription proposed by Feldman-Cousins [34] [35]. Among other reasons, this method is chosen because it provides sensible results for channels with small yields or cases in which the background estimate underpredicts the observed data. First, a test statistic is constructed as a measure of how signal-like or background-like an observation can be. It is a function based on the observables and nuisance parameters discussed above. It is determined from a profile likelihood ratio that is maximized as a

Table 6.5: Nuisance parameters entering into the calculation of the sensitivity of the analysis.

Category	Shape	Number	Correlation	Notes
Jet energy scale	lnN	1	All bins and channels	Calculated for each bin/channel from MC
$\Delta\theta_T$ SF	lnN	20	Shared value within H_{T}, Nbtag bin	Stat. unc. of SF for each $\Delta\theta_T$ bin from MC
Single lepton CS	gmN	40	Independent	CS yield in each $\Delta\theta_T$ bin
1 τ-jet SF	lnN	4	Shared value within H_{T}, Nbtag bin	Stat. uncertainty of SF from MC
τ-jet +lep SF	lnN	12	Shared value within H_{T}, Nbtag bin	Stat. uncertainty of SF from MC
1 τ-jet κ	lnN	2	Independent	Applies to the two high H_{T}, $E_{\mathrm{T}}^{\mathrm{miss}}$ bins
1 tight μ CS	gmN	8	Independent	Corresponds to calculated stat. unc.
Tight μ+lep CS	gmN	24	Independent	Corresponds to calculated stat. unc.
Dilepton SF	lnN	4	Shared value within H_{T}, Nbtag bin	Stat. uncertainty of SF from MC
Dilepton CS	gmN	4	Correlated within H_{T} bin, Nbtag bin	CS yield of dilepton sample
QCD κ	lnN	2	Shared value, within H_{T} bin	Stat. uncertainty of SF from MC
Low $\Delta\phi_N^{\mathrm{min}}$ CS	gmN	8	Independent	CS yield each bin w/ inverted $\Delta\phi_N^{\mathrm{min}}$ cut
$Z \to \nu\bar{\nu}/l^+l^-$ SF	lnN	2	Shared value within H_{T} bin	Stat. uncertainty of SF from MC
CSV SF	lnN	2	Shared value within Nbtag bin	Stat. unc. of low $E_{\mathrm{T}}^{\mathrm{miss}}$ SF from data
CSVL cut choice	lnN	1	Correlated within Nbtag bin	Calculated for each bin from MC
CSVL dilepton CS	gmN	4	Correlated within H_{T}, $E_{\mathrm{T}}^{\mathrm{miss}}$ bin	CS yield of CSVL in bins of H_{T}, $E_{\mathrm{T}}^{\mathrm{miss}}$

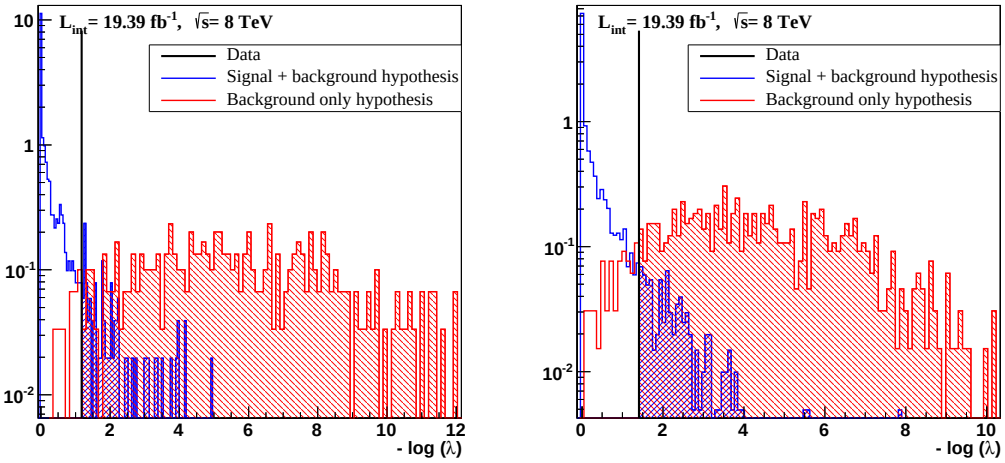

(a) $M_{\tilde{g}}$=700 GeV, $M_{\tilde{\chi}}$=500 GeV, r=1.3 (b) $M_{\tilde{g}}$=1225 GeV, $M_{\tilde{\chi}}$=200 GeV, r=1.0

Figure 6.5: Distributions of the test statistic (-logλ) for >100 pseudo-experiments, for the combination of signal and background (blue) and the background-only hypothesis (red), for two T1bbbb scenarios. The black line indicates the test statistic calculated from data.

function of the nuisance parameters (θ) and signal strength (r):

$$\prod_{i=1}^{6} \frac{max_{\theta_i}\mathcal{L}(\lambda|r \times s_i + b_i, \theta_i)}{max_{r',\theta_i}\mathcal{L}(\lambda|r' \times s_i + b_i, \theta_i)} \tag{6.1}$$

This equation shows that the test statistic λ is taken from the product of ratios for each signal bin, where s_i is the signal yield for that bin and b_i is the background yield. An additional constraint of $0 \leq r' \leq r$ ensures that the amount of signal can not be negative.

Figure 6.5 shows the distribution of the test statistic, λ, for the data and approximately 500 pseudo-experiments. The more signal-like the result is, the lower its value. The red distribution is the results from the background hypothesis (B), where the signal strength is set to r=0. The combination of signal and background (S+B) is shown in blue, and the value from the observed data is shown as a black line. The two T1bbbb mass points where chosen because they are close to the exclusion limit for this analysis.

Now, we need to specify a range of values of the test statistic for which we can make a conclusion about the S+B hypothesis. The significance of the exclusion (or discovery) is called the confidence level, CL. For the background hypothesis, it is calculated:

$$CL_B = P_B(\lambda \leq \lambda_{obs}) = \int_0^{\lambda_{obs}} \frac{dP_B}{d\lambda} d\lambda \tag{6.2}$$

This means it is a simple integral over the probability distribution function of the test statistic from the pseudo-experiments shown above. A similar integral is calculated from the S+B probability distribution function:

$$CL_{S+B} = P_{S+B}(\lambda \leq \lambda_{obs}) = \int_0^{\lambda_{obs}} \frac{dP_{S+B}}{d\lambda} d\lambda \tag{6.3}$$

The key element of this method is the normalization of the confidence level of the S+B hypothesis with respect to the background-only hypothesis. The ratio of these confidences gives the method its name, CL_S:

$$CL_S \equiv CL_{S+B}/CL_B \tag{6.4}$$

A signal hypothesis is considered excluded at a confidence CL when (1 - CL_S)$\leq$CL. For this analysis, we want to know the signal strength r at which 95% of the pseudo-experiments are more signal-like than it. Based on the yields attributed to background and signal, this is:

$$1 - CL_S = \frac{P(\lambda < \lambda_{obs}|r \times s + b)}{P(\lambda < \lambda_{obs}|b)} = 0.05 \tag{6.5}$$

In Fig. 6.5, the signal strengths being tested for the two mass points are at the limit of exclusion. This is because the integral of the background-only probability distribution above $-log\lambda_{obs}$, divided by the integral of (S+B), is about 0.05.

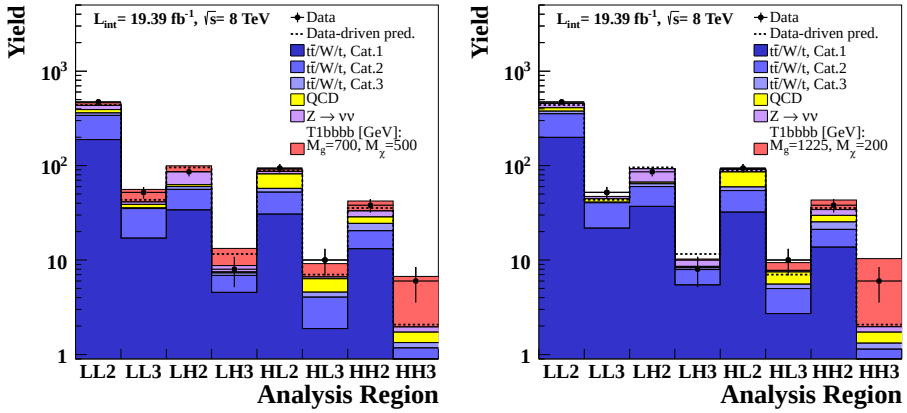

(a) $M_{\tilde{g}}$=700 GeV, $M_{\tilde{\chi}}$=500 GeV, r=1.3 (b) $M_{\tilde{g}}$=1200 GeV, $M_{\tilde{\chi}}$=550 GeV, r=1.0

Figure 6.6: Data yields (black points with error bars) and fit results for each signal region, for two different T1bbbb scenarios. The yield of signal events (red) is taken from the CL_S method, and the distribution of backgrounds (stacked, colored histogram) is from a maximum likelihood fit. For comparison, the total result of the nominal background prediction is shown as a dashed line. The first four bins are the low H_T (400–800 GeV) region, with low (250–350 GeV, "LL") or high (>350 GeV, "LH")E_T^{miss} range, with either =2 or ≥3 b-tags respectively. The last four bins have high H_T (>800 GeV) and either low ("HL") or high ("HH") E_T^{miss} and either =2 or ≥3 b-tags.

We now have a procedure for calculating the signal strength, r, of a T1bbbb model which is excluded at the 95% level by the CL_S method. Figure 6.6 shows the results of this procedure for the two T1bbbb scenarios that are at the edge of sensitivity for this analysis. Each bin of the histogram is one of the eight signal regions, showing the different channels as a colored, stacked histogram. The separate $\Delta\theta_T$ channels are combined and the dilepton channels are combined. The signal yield is taken from the result of the CL_S method, as the amount of signal that is just excluded by the analysis. The excess in the "HH3" region allows many signal events. In the low mass gluino scenario, the nuisance parameters allow the background yields to be lower than the nominal values, but overall are not unreasonable. The size of the signal yields are determined from $r \times s$, where r is the signal strength result

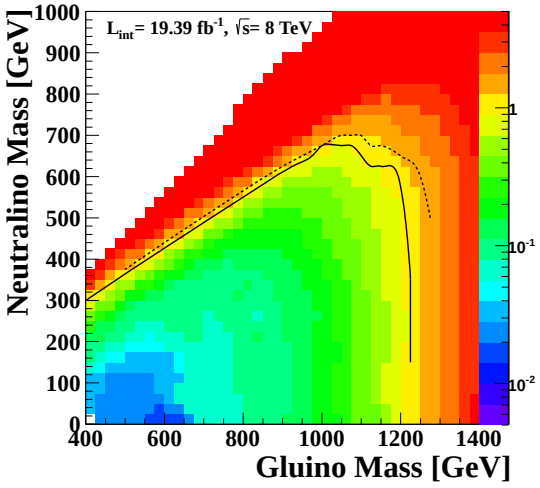

Figure 6.7: Signal strength, r, from CL_S calculation, in the gluino–neutralino mass plane. A value of 1 corresponds to a cross-section equal to the QCD production of gluinos, mass points with lower values are excluded, and mass points with higher values are not. The black line connects mass points along the limit of exclusion.

from the CL_S method, and s is the expected signal yield considering the QCD strength of gluino pair production, and the efficiency of the analysis for those particular gluino and neutralino masses. For M_{gluino}=700 GeV and M_{LSP}=500 GeV, r=1.3. Since the calculated r is greater than 1, the nominal production rate is not excluded for this T1bbbb scenario is not excluded by this analysis.

The following paragraphs describe what can collectively be called sensitivity diagrams. Results for simplified models are usually expressed as limits on the gluino production cross-section across the 2-dimensional M_{gluino} and M_{LSP} plane. Figure 6.7 provides the signal strength of each mass point on a color gradient. Each mass point has an intrinsic cross-section determined by the mass of the gluinos produced. If the signal rate can be greater than this cross-section without deviating significantly from observation, then this

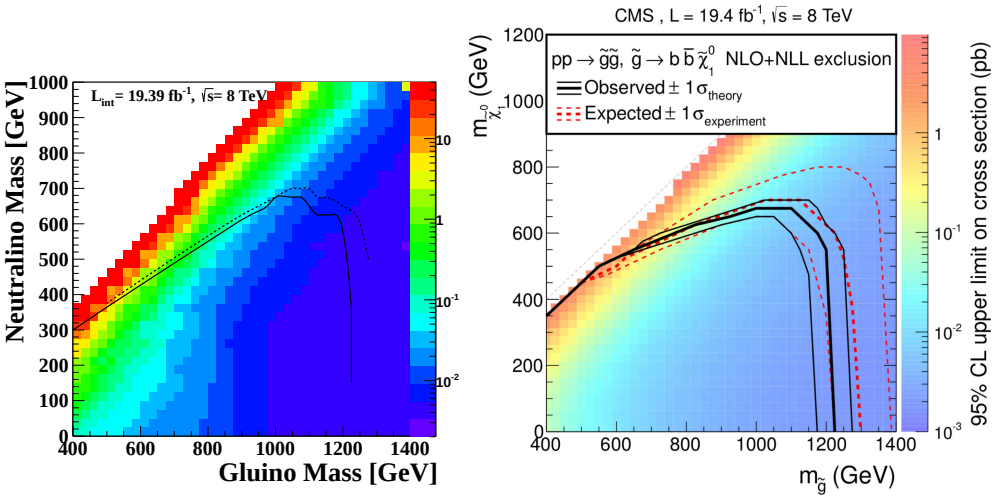

(a) Result from this analysis. (b) Result from hadronic search with b-tags. [13]

Figure 6.8: Results from the CL_S calculation, showing limits in the T1bbbb mass plane from this analysis and published results. The z-axis colors indicate the signal efficiency, based on the gluino production cross-section and effciency of analysis selection criteria.

analysis is not able to exclude the process. Unfortunately, a different technique must be used (perhaps without the troublesome single lepton control sample) in order to probe the possibility of these decays at such a low cross-section. On the other hand, if the gluino and neutralino masses were both low, we could easily observe an excess of events above the background. These mass points are excluded, having a best fit signal strength less than the nominal value. In Fig. 6.7, a relative signal strength close to unity is consistent with the gluino pair production cross-section, shown in shades of yellow. The redder region is beyond the sensitivity of this analysis, and the green to blue region is excluded by this analysis. The black line between these regions is the observed limit at 95% confidence.

Figure 6.8 again shows the 2-dimensional T1bbbb mass plane. In Fig. 6.8(a), the limit curve calculated by this analysis (and shown in Fig. 6.7) is overlayed with the

effective cross-section of each process. Even though the gluino pair production cross section decreases with gluino mass, there are other factors which influence the amount of observed signal events. The relative yield of signal events entering the analysis increases with the mass difference between the gluino and neutralino. The selection criteria for this analysis favors these events. For the T1bbbb signature, gluinos are excluded up to a mass of 1225 TeV, for neutralinos less than 350 GeV. The highest neutralino masses excluded are 650–675 GeV, in the gluino mass range 975–1125 GeV. The effect of removing the top-quark p_{T} correction in simulated events used for the background predictions was tested. It contributes an additional 22% uncertainty in the high $E_{\mathrm{T}}^{\mathrm{miss}}$, high H_{T}, $\geq$3 b-tags signal region, however, its affect on the final limit is small. The maximum neutralino mass excluded (for a gluino 1000–1050 GeV) would be restricted to 650 GeV. Figure 6.8(b) shows the limit and efficiency for the published group result. The results are very similar in their maximum reach in gluino mass and neutralino mass. However, the published result was able to exclude more parameter space in the range of low gluino mass at low mass splitting.

Figure 6.9 shows how the hadronic search with b-tags compares with other hadronic searches for supersymmetry at CMS in the T1bbbb simplifed model parameter space. The group result is shown as the red line in the figure. Each other method tries different techniques to try to distinguish signal from background. With many groups working largely independently to create analyses that explore an untouched region of the SMS parameter space, the topologies of many other SMS scenarios of supersymmetry have also been probed.

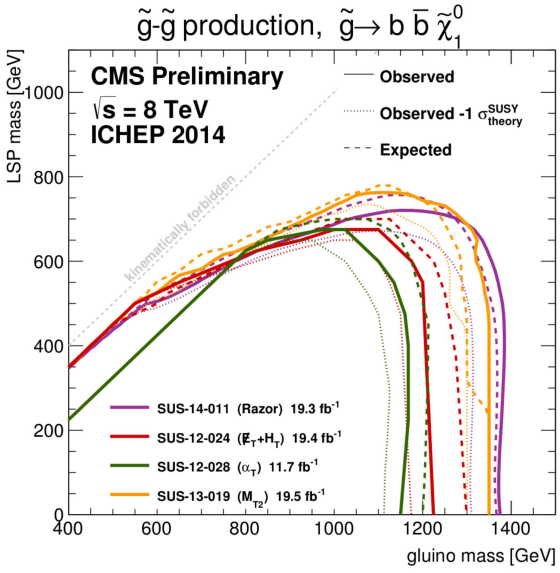

Figure 6.9: Results from the CL_S calculation, showing limits in the T1bbbb mass plane from several analysis efforts [12] [13] [14] [15].

Chapter 7

Conclusion

This dissertation presented a search for natural models of supersymmetry at CMS. The theory of supersymmetry provides an attractive solution to several puzzles vexing the particle physics community today Ch. 2. The data sample consisted of 19.39 fb^{-1} of proton-proton collisions at $\sqrt{s}$=8 TeV collected by the CMS experiment at the LHC.

The analysis described here is structured using the same selection criteria and signal regions as the general hadronic search using b-jet identification published in [13]. Using data-driven background predictions Ch. 5 and a robust hybrid-frequentist method of determining the compatibility of signal with data, limits are placed on the cross-section of gluino pair production that directly decays to four b-quarks and two neutralinos Ch. 6. This process is excluded for gluinos with mass up to 1225 GeV, and neutralinos less than 350 GeV, at 95% confidence. The highest excluded neutralino masses were 650–675 GeV, for

gluinos between 975–1125 GeV. The results are comparable to the latest limits calculated by other groups probing hadronic final states of gluino production [12] [13] [14] [15].

In 2015, the LHC will resume operations after its period of long shutdown, and begin colliding protons at $\sqrt{s}$=13 TeV. Analysts are preparing for the many challenges this new energy regime presents. For example, higher center of mass energies will create more boosted topologies for Standard Model processes, requiring new ways of handling jet counting and lepton isolation. In addition, as more bunch crossings are filled, methods for subtracting the thick underlying event and other forms of pile-up will need to be much more efficient. While this regime presents many interesting new challenges, nearly doubling the center of mass energy of the collisions provides an exiting new regime for exploring any potential new physics that may appear. It is an exciting time for scientists interested in probing the properties of the newly discovered Higgs boson, as well as those on the hunt for additional heavy bosons, black holes, extra dimensions, and supersymmetry.

Bibliography

[1] M. Papucci, J.T. Ruderman, and A. Weiler. Natural SUSY endures. *Journal of High Energy Physics*, 1209, 2012.

[2] CMS Collaboration. Interpretation of searches for supersymmetry. Technical Report Physics Analysis Summary SUS-11-016, CMS, 2011.

[3] CMS Collaboration. Operation and configuration of the LHC in Run 1. Technical Report Accelerator Note 2013-0041, CERN, 2014.

[4] CMS Collaboration. Description and performance of track and primary-vertex reconstruction with the CMS tracker. *J. Instrum.*, 9(P10009), 2014.

[5] CMS Collaboration. Pixel performance plots 2013. Technical Report CMS Performance Note DP-13-014, CMS, 2013.

[6] CMS Collaboration. 2012 ECAL detector performance plots. Technical Report CMS Performance Note DP-13-007, CMS, 2013.

[7] CMS Collaboration. Status of the 8 TeV jet energy corrections and uncertainties based on 11 fb^{-1} of data in CMS. Technical Report CMS Performance Note DP-13-011, CMS, 2013.

[8] CMS Collaboration. Single muon efficiencies in 2012 data. Technical Report CMS Performance Note DP-13-009, CMS, 2013.

[9] CMS Collaboration. Electron performance with 19.6 fb^{-1} of data collected at $\sqrt{s} =$ 8 TeV with the CMS detector. Technical Report CMS Performance Note DP-13-003, CMS, 2013.

[10] CMS Collaboration. Performance of b tagging at $\sqrt{s} = 8$ TeV in multijet, ttbar and boosted topologies. Technical Report CMS Physics Analysis Summary BTV-13-001, CMS, 2013.

[11] RA2b group. Search for supersymmetry in pp collisions at 8 TeV using the shape of the HT, MET, and b-quark jet multiplicity distributions. Technical Report Physics Analysis Note AN2012/081, CMS, 2012.

[12] RAZOR group. Interpretation PAS for the combination of SUS-13-004 and SUS-13-011. Technical Report CMS PAS SUS-14-011, CMS, 2014.

[13] CMS Collaboration. Search for gluino mediated bottom- and top-squark production in multijet final states in pp collisions at 8 TeV. *Phys. Lett. B*, 725, 2013. CMS PAS SUS-12-024.

[14] CMS Collaboration. Search for supersymmetry in hadronic final states with missing transverse energy using the variables α_T and b-quark multiplicity in pp collisions at $\sqrt{s} = 8$ TeV. *Eur. Phys. J. C*, 73, 2013. CMS PAS SUS-12-028.

[15] MT2 group. Search for SUSY in hadronic final states using MT2. Technical Report CMS PAS SUS-13-019, CMS, 2013. Submitted to JHEP.

[16] CMS Collaboration. *CMS Technical Design Report, Volume 1: Detector Performance and Software*. CERN, Geneva, 2006. CERN-LHCC-2006-001.

[17] CMS Collaboration. Search for supersymmetry in all-hadronic events with b-jets. Technical Report Physics Analysis Summary SUS-2011/006, CMS, 2011.

[18] CMS Collaboration. Search for supersymmetry in events with b-quark jets and missing transverse energy in pp collisions at 7 TeV. *Phys. Rev. D*, 86, 2012. CMS PAS SUS-12-003.

[19] F. Halzen and A.D. Martin. *Quarks and Leptons: An Introductory Course in Modern Particle Physics*. John Wiley & Sons, 1984.

[20] J.L. Feng. Dark matter candidates from particle physics and methods of detection. *Annual Review of Astronomy and Astrophysics*, 48, 2010.

[21] S.P. Martin. *A Supersymmetry Primer*, volume 21. Advanced Series on Directions in High Energy Physics, 2010.

[22] W. Herr and B. Muratori. Concept of luminosity. In *CERN Accelerator School: Intermediate Course on Accelerator Physics*, 2003.

[23] CMS Collaboration. CMS technical design report, volume II: Physics performance. *Journal of Physics G*, 34, 2007.

[24] CMS Collaboration. Particle-flow event reconstruction in CMS and performance for jets, taus, and ETmiss. Technical Report CMS Physics Analysis Summary PFT-09-001, CMS, 2009.

[25] CMS Collaboration. Performance of missing transverse momentum reconstruction algorithms in proton-proton collisions at $\sqrt{s} = 8$ TeV with the CMS detector. Technical Report CMS Physis Analysis Summary JME-12-002, CMS, 2013.

[26] C. Weiser. A combined secondary vertex based b-tagging algorithm in CMS. Technical Report CMS NOTE 2006/014, CMS, 2006. Submitted to Phys. Rev. Lett.

[27] CMS Collaboration. Identification of b-quark jets with the CMS experiment. *J. Instrum.*, 8, 2013. CMS PAS BTV-12-001.

[28] A. Czarnecki, J. Korner, and J. Piclum. Helicity fractions of W bosons from top quark decays at NNLO in QCD. *Phys. Rev. D*, 81, 2010.

[29] CMS Collaboration. Measurement of the polarization of W bosons with large transverse momenta in W+jets events at the LHC. *Phys. Rev. Lett.*, 107, 2011.

[30] CMS Collaboration. Measurement of the differential top-quark pair production cross section in the dilepton channel in pp collisions at$\sqrt{s} = 8$ TeV. Technical Report CMS Physics Analysis Summary TOP-12-028, CMS, 2013.

[31] CMS Collaboration. Search for new physics with jets and missing transverse momentum in pp collisions at $\sqrt{s} = 7$ TeV. *Journal of High Energy Physics*, 8, 2011.

[32] CMS Collaboration. Determination of jet energy calibration and transverse momentum resolution in CMS. *J. Instrum.*, 6, 2011.

[33] Higgs Combination Group. Procedure for the LHC higgs boson search combination in summer 2011. Technical Report CMS AN-11-298, LHC Higgs Combination Group, 2011.

[34] Gary J. Feldman and Robert D. Cousins. Unified approach to the classical statistical analysis of small signals. *Phys. Rev. D*, 57:3873–3889, 1998.

[35] A.L. Read. Modified frequentist analysis of search results (the CL_s method). In *1st Workshop on Confidence Limits*, 2000.